Modelling Multidimensional Seismic Wave Propagation Effects in Geotechnical Site Response Analysis by Incorporating Physics-Based Ground Motion Simulations and Soil Heterogeneity

A dissertation submitted to University of Canterbury in partial fulfilment of the requirements for the degree of Doctor of Philosophy

Christopher Alejandro de la Torre

November 2021

Department of Civil and Natural Resources Engineering,
University of Canterbury

Christchurch, New Zealand

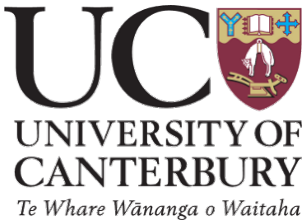

Abstract

The overarching goal of this dissertation is to improve predictive capabilities of geotechnical seismic site response analyses by incorporating additional salient physical phenomena that influence site effects. Specifically, multidimensional wave-propagation effects that are neglected in conventional 1D site response analyses are incorporated by: (1) combining results of 3D regional-scale simulations with 1D nonlinear wave-propagation site response analysis, and (2) modelling soil heterogeneity in 2D site response analyses using spatially-correlated random fields to perturb soil properties.

A method to combine results from 3D hybrid physics-based ground motion simulations with site-specific nonlinear site response analyses was developed. The 3D simulations capture 3D ground motion phenomena on a regional scale, while the 1D nonlinear site response, which is informed by detailed site-specific soil characterization data, can capture site effects more rigorously. Simulations of 11 moderate-to-large earthquakes from the 2010-2011 Canterbury Earthquake Sequence (CES) at 20 strong motion stations (SMS) were used to validate simulations with observed ground motions. The predictions were compared to those from an empirically-based ground motion model (GMM), and from 3D simulations with simplified V_{S30}-based site effects modelling. By comparing all predictions to observations at seismic recording stations, it was found that the 3D physics-based simulations can predict ground motions with comparable bias and uncertainty as the GMM, albeit, with significantly lower bias at long periods. Additionally, the explicit modelling of nonlinear site-response improves predictions significantly compared to the simplified V_{S30}-based approach for soft-soil or atypical sites that exhibit exceptionally strong site effects.

A method to account for the spatial variability of soils and wave scattering in 2D site response analyses was developed and validated against a database of vertical array sites in California. The inputs required to run the 2D analyses are nominally the same as those required for 1D analyses (except for spatial correlation parameters), enabling easier adoption in practice. The first step was to create the platform and workflow, and to perform a sensitivity study involving 5,400 2D model realizations to investigate the influence of random field input parameters on wave scattering and site response. Boundary conditions were carefully assessed to understand their effect on the modelled response and select appropriate assumptions for use on a 2D model

with lateral heterogeneities. Multiple ground-motion intensity measures (IMs) were analyzed to quantify the influence from random field input parameters and boundary conditions. It was found that this method is capable of scattering seismic waves and creating spatially-varying ground motions at the ground surface. The redistribution of ground-motion energy across wider frequency bands, and the scattering attenuation of high-frequency waves in 2D analyses, resemble features observed in empirical transfer functions (ETFs) computed in other studies.

The developed 2D method was subsequently extended to more complicated multi-layer soil profiles and applied to a database of 21 vertical array sites in California to test its appropriateness for future predictions. Again, different boundary condition and input motion assumptions were explored to extend the method to the in-situ conditions of a vertical array (with a sensor embedded in the soil). ETFs were compared to theoretical transfer functions (TTFs) from conventional 1D analyses and 2D analyses with heterogeneity. Residuals of transfer-function-based IMs, and IMs of surface ground motions, were also used as validation metrics. The spatial variability of transfer-function-based IMs was estimated from 2D models and compared to the event-to-event variability from ETFs. This method was found capable of significantly improving predictions of median ETF amplification factors, especially for sites that display higher event-to-event variability. For sites that are well represented by 1D methods, the 2D approach can underpredict amplification factors at higher modes, suggesting that the level of heterogeneity may be over-represented by the 2D random field models used in this study.

Acknowledgements

It was five years ago today that I first landed in New Zealand. The years at UC and in New Zealand have been an absolute pleasure, and I have many people to thank for that.

First and foremost, I would like to thank my mom, dad, and sister for supporting me through the decision to come here. It has not been easy, for any of us, being so far from each other, and I look forward to the day when NZ Immigration or viral diseases allow us to be closer together. I couldn't have asked for better parents and I am definitely a better person for your thoughtful and considerate guidance and support throughout my life. I love you guys!

My amazing and beautiful girlfriend, Jessica Allan, has been an incredible part of my experience in New Zealand. I love everything we do together from the craziest adventures to a lazy Sunday at home. I look forward to many more adventures. Her amazing and loving family, Ali, Stu, Scott, Tui and Emily have welcomed me in and made New Zealand feel more like home.

I would not be here, writing this dissertation, if it weren't for my supervisor Brendon Bradley. Thank you for giving me the opportunity to come here. You have opened more doors for me than I could have ever imagined. Despite your busy schedule, you have always made the effort to be involved and give me just the right amount of guidance to succeed. No one can interpret a figure as quickly or thoroughly as you, and while that is humbling sometimes it has greatly helped me in the interpretation of my results.

I would like to give my sincere thanks to Misko Cubrinovski for mentoring me in my teaching assistant and lecturing roles. I've learned a lot from you (technically and practically) and I'm a better teacher because of it. I cherish greatly our work together on CentrePort following the Kaikōura earthquake, and look forward to more collaborations with you in the future.

I am grateful for my supervisors, mentors, and professors from the University of Washington, Steve Kramer, Pedro Arduino, Bob Holtz and Joe Wartman, who helped me get where I am today. I'm convinced that some of the best lectures in the world on soil mechanics, earthquake engineering, and constitutive modelling take place within the old walls of More Hall. In honor of Holtz, lettuce all enjoy life and not take things too seriously, as you never know when you

will catch your last fish or run your last site response analysis.

My friends from all stages of life have always been one of the most important things in my life, and helped me maintain my sanity even through the most challenging and stressful times. I've been lucky to find a group of locals to call friends here. Cheers to Nikki Gosden, Kyle Sutherland, and Scott Allan (my first kiwi friends!), and Mark & Mel, Claire & Marcos, Penny & Ward, and Tom & Rachel.

My PhD experience would not have been the same without the great community we have among CNRE postgrads. These acquaintances, colleagues, "friends" or whatever you want to call them have been key to my everyday enjoyment at UC. A special shout out to members of the Coffee Time, FG, RFG, NFG, UFG, and all other group chats that have kept me entertained/distracted over the years. Thanks to Jay Bhanu, Brandy Alger, Jane Alexander, Fábio Silveira, Thomas Wallace, Alex Meredith, Francisco Gálvez, Forrest Bilek, Madeline Furness, Sky Halford, Tom Francis, Lizzy North, Justin Brown, Ana Sarkis, Connor Cleary, Karan Titus, and Yu Li for all the laughs and fun.

A special thank you to my dear office mates Vahid Loghman, Kevin Foster, Sarah Neill and Mohammad Eskandarighadi. It has been a pleasure sharing this office with you. My early days at UC were memorable because of the original BB (Brendon Bradley) Boys: Ethan Thomson, Robin Lee, Xavier Bellagamba, Karim Tarbali, and Kevin Foster. You've all moved on now but the memories of you remain. How could one forget our first QC annual meeting? Thank you for warmly welcoming me into the research group and the good times which followed.

It would be rude not to acknowledge the Pass People, Dyers Pass that is, for providing a wonderfully cozy, pleasant, and enjoyable flatting environment. Life in a hilltop mansion ain't always easy but we make it work. Thank you Jess Allan, Scott Allan, Meghan Kradolfer, and Damien Innes Taylor.

I am thankful for my dearest and wisest friend Shawn Jerrity. Even a simple mention of your name in my thesis is sure to discredit my life's hard work, but I will take the hit to my reputation to acknowledge our beautiful memories exploring the wild and remote wilderness of New Zealand. People foolish enough to crawl through impenetrable, wasp-infested Matagouri in steep terrain are hard to come by in today's snowflake generation; I hope those wounds have healed.

A big and special shout out to my homies back home: Patrick McDuffie, Erik Anderson, Alex Georges, Blake Polidore, Matt Kintz, Colin Caprara, Doug Lovell, Brett O'Brien, Will Fortini, and Brooke Henwood. Man, we've had some good times together. These memories will continue to bring joy and laughter to my life until the day I die. A special shout out to Nicholas Erler. More crazy, hilarious, silly, and epic times have been spent on the river with you than anyone else. I miss you all. Thank you for making time for me when I visit.

I'm grateful for all the riveting technical chats with Maxim Millen, Seokho Jeong, and Chris McGann. When it comes to the nitty gritty technical details, you're the people to talk to. Thank you Sean Reese and Claudio Cappellaro for getting me trained up the lab, and Andrew Stolte for showing me the ropes on surface wave testing; your attention to detail and technical knowledge do not go unnoticed.

I'm lucky to have worked at a place like Hart Crowser in Seattle that allowed me to pursue my passion in the seismic side of things and made a special effort to try to give me the work that interested me. Thanks to Madan Karkee, Doug Lindquist, Brice Exley, Garry Horvitz and many more. A special mention to the HC Volley Ball team and my friends Jamalyn Green, Jessica Blachette, Andrew Makdisi, Marissa Goodman, Andy Wade, Brigitte Brown, Alex Ciccone, Jeff Bruce, Dan Knapp, and Marc Miller.

Thank you to the QuakeCoRE computational/software team for their help with supercomputing and general coding. A special thanks to Viktor Polak for helping me in my early days of Python. I am thankful for the wonderful administrators of CNRE and QuakeCoRE, that make things happen around here, for putting up with me for five years. Thank you Elizabeth Ackermann, Veronika Letufuga, Catherine O'Shaughnessy, Emma Clark, Jennifer Clayton-Smith, Ruth Hartshorn, Rosemary Walton, Amy McGeddie, and Siew Lee O'Brien. I am also very grateful for our CNRE IT superstars Olive Dalton and Paul Strange for their constant help and support.

This PhD would not have been possible without funding from QuakeCoRE and UC which provided significant financial support and resources. I would also like to thank NeSI high performance computing for providing a wonderful resource to the research community. Thank you to Brendon Bradley, Chris McGann, Maxim Millen, Andrew Stolte, Felipe Kuncar, and Karan Titus for reviewing parts of this thesis and providing good feedback. Finally, I would like to thank my PhD examiners, Brady Cox and Eric Thompson, for their comprehensive review,

thoughtful discussion and feedback to improve current and future work.

Chris de la Torre

23th June 2021

To my sister, mother, father, girlfriend and close friends from all the stages of my life that helped me get through it all

Contents

List of Figures

List of Tables

Chapter 1

Introduction

1.1 Motivation

Seismic site response, also colloquially known as 'site effects', is a complex phenomenon that refers to the modification of seismic waves as they propagate through near-surface soils. Seismic waves can be significantly amplified or deamplified as they pass through the near-surface soil layers before reaching the ground surface. These effects are dependent on the geometry and characteristics of the soil/rock layers below a particular site (hence the name "site response"). The significance of such effects has been clearly observed in past events globally (e.g., Bolton Seed et al., 1987; Idris, 1993; Brando et al., 2020), but also in recent earthquakes of New Zealand, such as in Wellington from the 2016 Kaikōura Earthquake (Bradley et al., 2017b) and in Heathcote Valley, Christchurch from the 2010-2011 Canterbury Earthquake Sequence (Jeong and Bradley, 2017a; Bradley and Cubrinovski, 2011), among others.

It is the job of a geotechnical engineer to predict how the soil characteristics and basin geometry at their site of interest will modify the ground shaking using a site response analysis. While these analyses are commonplace, the uncertainty in them is high and many researchers have highlighted the shortcomings and limitations of these analyses when executed using convention assumptions (e.g., Thompson et al., 2012; Kaklamanos et al., 2015; Kokusho, 2017; Afshari and Stewart, 2019; Tao and Rathje, 2019). There is uncertainty associated with the input ground motion, the geometry, characteristics and constitutive response of the soil, and the

fundamental assumptions/simplifications of the methods used for these analyses. This dissertation focuses on addressing several of these limitations by incorporating more of the mechanisms that control the problem into these analyses.

The 2010-2011 Canterbury Earthquake Sequence (CES) produced strong shaking and significant damage across the city of Christchurch (Cubrinovski et al., 2011; Bradley, 2012; Bradley et al., 2014; Quigley et al., 2016). These ground motions are greatly influenced by the complex 3D geologic structure of the Canterbury basin (Browne et al., 2012; Lee et al., 2017b). By far the most common method for predicting shaking intensities from such earthquakes is using empirical ground motion prediction equations (GMPEs; e.g., Chiou and Youngs, 2008; Bradley, 2013; Campbell and Bozorgnia, 2014). While these models are on average globally unbiased, they represent the source, path, and site effects of an earthquake using average empirical correlations with simplified source parameters or site indices. Given these simplifications, which are inherent to an ergodic approach (Anderson and Brune, 1999), these equations cannot capture some of the salient complexities specific to every site/basin. As an alternative, the field of ground motion prediction using 3D physics-based simulations is rapidly evolving to be able to accurately represent event and location specific physical phenomena that contribute to ground motion characteristics (e.g., Graves and Pitarka, 2010; Bradley et al., 2017a). These simulations can account for the actual geometry and complexities of the subsurface geology for the region using 3D seismic wave velocity models (e.g., Thomson et al., 2020; Lee et al., 2017a).

The source and path components of 3D ground motion simulations are often complex and physics-based in nature, however, the conventional way to account for near-surface site effects is generally via empirical site amplification models (e.g., Graves and Pitarka, 2010). This empirical treatment of site effects is simple relative to the source and path modeling of simulations, and the state-of-the-art in geotechnical seismic ground response analysis (Stewart Annie On-Lei Kwok et al., 2008; Régnier et al., 2016; Stewart et al., 2017), suggesting that there is room for improvement in how site effects are modelled in the context of simulations. A few studies have investigated different ways to explicitly account for site response in 3D simulations (Hartzell et al., 2002; Bielak et al., 2003; Taborda et al., 2012; Roten et al., 2012) but never with a large database of recorded earthquakes with which to validate the approaches. By combining 3D simulations with wave-propagation site response analyses, complexities in the source, path,

and site effects can be modelled in a more rigorous and event/site-specific context.

While advancements in the field of physics-based ground motion simulation allow for extraordinary complexity to be captured in the prediction of earthquake ground motions, the conventional methods used for site response analyses that are commonly adopted still rely on fundamental assumptions that were developed more than 70 years ago. The overwhelming majority of site response analyses use a 1D assumption to predict how the ground motion is modified as it passes through near-surface soil layers. Since the early days of site response analyses in the 1960s, this assumption of 1D wave propagation has been widely used and accepted (Schnabel et al., 1972; Idris, 1993; Hashash and Park, 2001). In conventional 1D seismic site-response analysis, soils are modelled as horizontal, homogeneous, laterally infinite layers that are limited to shear deformation with only vertically propagating shear waves. These fundamental assumptions neglect important physical aspects of wave propagation through a soil deposit, which is a multi-dimensional phenomenon. It is well known that discrete soil layers are not perfectly homogeneous, but their properties vary spatially (Holzer et al., 2005; Wills and Clahan, 2006). While several studies have investigated incorporating soil heterogeneities into multi-dimensional site response analyses (e.g., Popescu, 1995; Nour et al., 2003; Assimaki, 2004; Thompson et al., 2009; Huang et al., 2019; El Haber et al., 2019), significantly more work is required to refine these methods, develop simplified workflows for practical applications of these approaches, and validate the methodology against site response observations.

Vertical arrays of seismic recording stations have been employed over the years to test the predictive capabilities of site response methods. A vertical array has instruments embedded in the soil at depth and also at the ground surface which allows for direct observation of site effects. Many of these studies have demonstrated the inability of 1D site response procedures to appropriately capture the site response at a large percentage of sites (Thompson et al., 2012; Kaklamanos et al., 2015; Zalachoris and Rathje, 2015; Afshari and Stewart, 2019; Pilz and Cotton, 2019; Tao and Rathje, 2020a). Specifically, the amplification at modal frequencies of the soil column are often strongly overpredicted when laboratory-based estimates of small-strain damping are used for elastic analyses. Some have attributed this overprediction, and overall inability to capture the observed response, to the fact that 1D analyses are incapable of representing soil heterogeneity and its effects such as wave scattering attenuation (Thompson

et al., 2009, 2012; Zalachoris and Rathje, 2015; Kokusho, 2017). Given this sentiment, an important research question is whether these phenomena can be appropriately captured using multi-dimensional site response analyses with soil heterogeneity.

1.2 Objectives

The objectives of this dissertation, which seek to improve predictive capabilities of site response models are the following:

(i) Combine 3D regional-scale physics-based ground motion simulations with 1D wave-propagation nonlinear site response analyses and validate the approach with a database of 11 Canterbury Earthquake Sequence events recorded at 20 Christchurch strong motion stations.

(ii) Develop a 2D site response platform that incorporates soil heterogeneity using spatially-correlated random fields, and rigorously assess the influence of these heterogeneities on the predicted site response with an extensive parametric analysis.

(iii) Validate the 2D site response method against a database of small-strain (i.e., weak) ground motions at 21 vertical array sites in California.

1.3 Organization

Chapter 2 presents the implementation and validation of an approach to incorporate nonlinear site response in the context of 3D regional ground motion simulations using a physics-based 1D wave-propagation site response approach. A database of 11 observed earthquakes from the CES at 20 strong motion stations is used to validate the methodology and compute statistically significant site- and event-specific bias and uncertainty. The more advanced site response approach was compared to a simplified V_{S30}-based approach for modelling the site effects of these simulated ground motions. The systematic performance of simulations with both

site response methods was compared to predictions from a conventional GMPE. Supplementary tables, figures and analysis interpretation are included in Appendix A, and are referenced throughout the main body of the paper accordingly.

Chapter 3 presents the development of a 2D site response approach for modelling soil heterogeneity in site response analyses via spatially-correlated random field. It describes features of the site-response models including model geometry, boundary conditions, and other modeling assumptions. The objective is to assess the influence of these heterogeneities, on site response and investigate the theoretical behavior of wave scattering in site response using an idealized viscoelastic single-layer soil profile. A comprehensive parametric analysis involving 5,400 2D model realizations was performed to determine the effects of random field parameters on the seismic ground response. For every 2D realization, randomized 1D V_S profiles are generated by extracting 1D vertical 'slices' from the 2D model at the location of ground surface recorder nodes. The influence of soil heterogeneities on IMs in a 1D and 2D context are compared to differentiate the effects from vertical heterogeneities on a 1D wave field, and 2D ground-motion phenomena such as wave scattering and surface wave generation. The results are normalized by, and compared to, those from a traditional deterministic 1D V_S analysis. Additional figures and discussion for this chapter, including the development of boundary conditions for 2D models, are in Appendix B

Chapter 4 extends the method developed in Chapter 3 to multi-layer soil profiles and vertical array boundary conditions. The method is applied to a database of 21 vertical array sites in California, developed by Afshari et al. (2019). The database is for small-strain (i.e., weak) ground motions and is intended for validation of the elastic behaviour of site response. This chapter tests the hypothesis that the overprediction of ground motion at the site modal frequencies is caused by the disregard of soil heterogeneity and 2D/3D wave propagation effects, and that these effects can be appropriately captured in a 2D analysis using spatially-correlated random fields to perturb soil properties. This is the most extensive application of a 2D site response method with spatially varying soil properties to multi-layered profiles and vertical array sites which can be used for direct validation of the approach. The implications of using different coupled input motion and base boundary condition assumptions are investigated due to the significant influence on results and the long-standing issues related to the downgoing wave effects

and pseudo-resonances in vertical arrays. ETFs from vertical arrays are compared to TTFs from 2D and 1D deterministic analyses, and residuals of various intensity measures (IMs) for the surface motion are computed. Estimates of uncertainty in surface IMs are analysed to identify frequency-dependent trends with respect to impedance ratio (R_V), 30-meter time-averaged shear wave velocity (V_{S30}), fundamental frequency of the soil column (f_0) and higher mode frequencies (f_1 to f_3), and depth to the downhole instrument (z_{DH}). Additional figures and metadata to supplement the discussion in this chapter are available in Appendix C.

Chapter 5 summarizes the key contributions from this dissertation to the fields of geotechnical site response analysis and physics-based ground motion simulation. Limitations of each study and possible avenues to continue improving these methods via future research are discussed.

This dissertation is a collection of chapters which were developed as stand-alone publications. Each chapter is self-contained and includes its own literature review, description of the method, and detailed conclusions. For more details on the motivation, methodology and conclusions of each study, the individual chapters should be referenced.

Chapter 2

Modeling Nonlinear Site Effects in Physics-Based Ground Motion Simulations of the 2010-2011 Canterbury Earthquake Sequence

C. A. de la Torre, B. A. Bradley, R. L. Lee (2020). Modeling Nonlinear Site Effects in Physics-Based Ground Motion Simulations of the 2010-2011 Canterbury Earthquake Sequence. *Earthquake Spectra*, 36(2): 856-879.

Abstract

This study examines the performance of nonlinear total stress 1D wave propagation site response analysis for modeling site effects in physics-based ground motion simulations of the 2010-2011 Canterbury, New Zealand earthquake sequence. This approach explicitly models 3D ground motion phenomena at the regional scale, and detailed site effects at the local scale. The approach is compared to a more commonly used empirical V_{S30}-based method of computing site amplification for simulated ground motions, as well as prediction via an empirical ground motion model. Site-specific response analysis is performed at 20 strong motion stations in

Christchurch for 11 earthquakes with $4.7 \leq M_W \leq 7.1$. When compared to the V_{S30}-based approach, the wave propagation analysis reduces both overall model bias and uncertainty in site-to-site residuals at the fundamental period, and significantly reduces systematic residuals for soft or "atypical" sites that exhibit strong site amplification. The comparable performance in ground motion prediction between the physics-based simulation method and empirical ground motion models suggests the former is a viable approach for generating site-specific ground motions for geotechnical and structural response history analyses.

2.1 Introduction

3D physics-based ground motion simulation methods are being increasingly used to predict ground motion intensity, with accuracy and precision that rivals conventional empirical models (e.g., Taborda and Bielak, 2013; Bradley et al., 2017a). Limitations associated with computation, modeled physics, and data availability often result in the use of "hybrid" simulations which involve a comprehensive solution of the 3D wave equation for low frequencies (LF), and a simplified-physics approach for high frequencies (HF). The transition between the low and high frequency approaches varies across research efforts, but is commonly $f = 1\ Hz$ (Graves and Pitarka, 2010; Razafindrakoto et al., 2016), which implies a spatial discretization in the velocity model on the order of 100 m, with additional factors being the minimum shear wave velocity, and specific numerical method adopted. In addition, the comprehensive 3D solution commonly models the 3D medium as viscoelastic, although recent attempts have also explicitly considered plasticity (Taborda et al., 2012; Roten et al., 2016), albeit without direct validation against observations and only at low frequencies (i.e., coarse spatial scales).

Given the sentiments above, near-surface nonlinear site effects in broadband ground motion simulations must therefore, at present, be computed separately from the regional 3D simulation. Four methods have been used or proposed to incorporate nonlinear soil response into 3D ground motion simulations: (1) fully-coupled low-frequency (i.e., coarse grid) 3D simulation models that explicitly consider soil nonlinearity in surficial soils (e.g., Taborda et al., 2012; Restrepo et al., 2012), (2) the domain reduction method for decomposing the physical domain into multiple subdomains for separate simulation (e.g., Bielak et al., 2003; Yoshimura et al., 2003),

(3) conventional 1D wave propagation site response analysis uncoupled from the simulations (e.g., Hartzell et al., 2002; Roten et al., 2012), and finally, (4) the use of simple empirically-based site amplification factors (e.g., Graves and Pitarka 2010, 2015). The most common way to do so is via empirical V_{S30}-based site effects models (i.e., Method 4. e.g., Graves and Pitarka, 2010; Razafindrakoto et al., 2018). This empirical treatment of site effects in ground motion simulations is simple relative to the physics-based source and path modeling of simulations, and the state-of-the-art in geotechnical seismic ground response analysis (Stewart Annie On-Lei Kwok et al., 2008; Régnier et al., 2016; Stewart et al., 2017), suggesting that there is room for improvement in how site effects are modeled in the context of simulations.

Hartzell et al. (2002) and Roten et al. (2012) are examples of where the more comprehensive physics-based 1D nonlinear wave propagation site response analysis was used for modeling site effects in ground motion simulations. These studies performed simulations of potential future earthquakes on the Seattle and Wasatch Faults, respectively, and therefore lack direct validation against observed ground motions. The nonlinear ground response was computed at hundreds of sites across the region using generalized regional subsurface data primarily based on geology, and hence soil stratification, shear wave velocity profiles, and constitutive model inputs were idealized. The results of these studies were not benchmarked against empirical site amplification functions or ground motion models.

As in Hartzell et al. (2002) and Roten et al. (2012), this study also explicitly models nonlinear site response in the context of 3D regional ground motion simulations using a physics-based 1D wave propagation site response approach. It is distinct in that it analyzes 11 observed earthquakes at 20 strong motion stations to validate the methodology and compute statistically significant site- and event-specific bias and uncertainty. The events and sites considered are described in Section 2.2. The strong motion stations are well-characterized geotechnically and geophysically, and therefore, detailed and representative soil profiles are used for each site. The methodology for the alternative site response approaches is given in Section 2.3. Sections 2.4 and 2.5 present results in terms of intensity measures and systematic prediction residuals. Finally, in Section 2.6, the systematic performance of simulations with both site response methods is compared to prediction from a conventional empirical ground motion model (GMM). Supplementary tables, figures and analysis interpretation are included in Appendices A.2 - A.6, and

are referenced throughout the main body of the paper accordingly.

2.2 Earthquakes and Sites Considered

2.2.1 Events from the 2010-2011 Canterbury Earthquake Sequence

Figure 2.1 illustrates the eleven moderate-to-large magnitude (i.e., $4.7 \leq M_W \leq 7.1$) earthquakes and 20 strong motion stations considered for this study, with additional date and M_W information in Table A.1 of Appendix A.2. Ten of the events occurred during the 2010-2011 Canterbury, New Zealand earthquake sequence and were simulated by Razafindrakoto et al. (2016). The eleventh event was the M_W5.8 Valentine's day earthquake from 2016 and was simulated by Razafindrakoto and Bradley (2016). These 11 events generated ground motions of engineering significance that may have been influenced by nonlinear soil response in Christchurch (Bradley, 2015). The largest magnitude, and most economically and environmentally destructive events were the 4 September, 2010 M_W7.1 Darfield earthquake and the 22 February, 2011 M_W6.2 Christchurch earthquake (Cubrinovski et al., 2011; van Ballegooy et al., 2014; Cubrinovski et al., 2014; Quigley et al., 2016).

In the context of kinematic rupture descritption, as elaborated in Razafindrakoto et al. (2016), for the four largest magnitude events (i.e., Events 1, 4, 7, and 10 in Table A.1), the geometry of the finite fault source models from Beavan et al. (2011) and Beavan et al. (2012) was used. The two M_W5.8 earthquakes (i.e., Events 9 and 11) used finite faults generated as a plane of appropriate along-strike length and down-dip width centered about the earthquake centroid. The remaining 5 events were modeled as point sources because of their small magnitudes (and therefore rupture area).

2.2.2 Christchurch strong motion stations considered

In order to compare and validate simulated ground motions with observations, the site response analysis was performed at 20 strong motion stations (SMS) that recorded the sequence of events. Figure 2.2 shows the location of sites, grouped for analysis interpretation by geo-

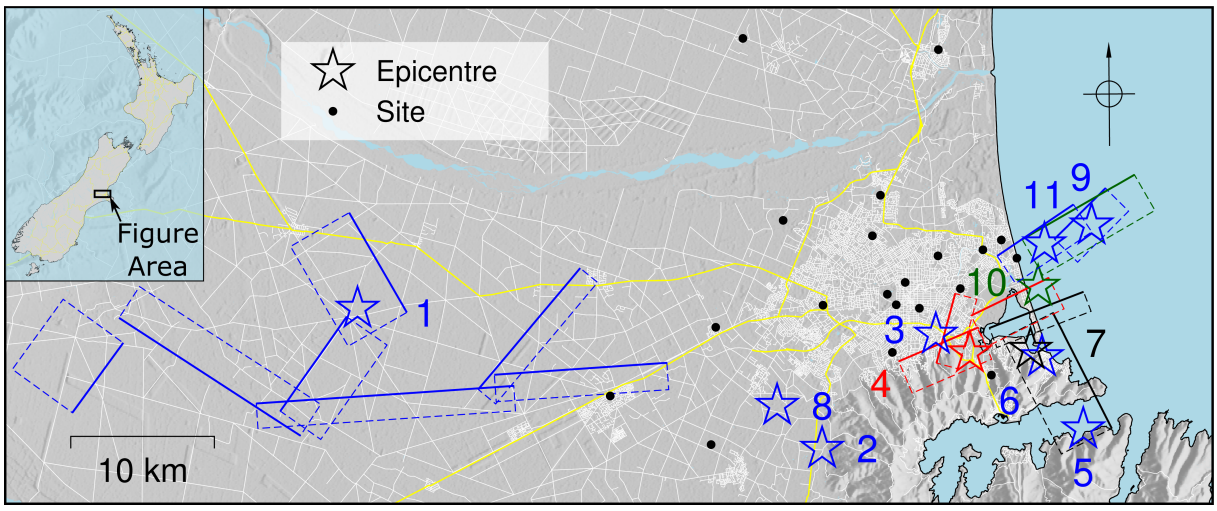

Figure 2.1: Illustration of simulated rupture models for 11 events, listed in Table A.1 labeled by Event ID, and location of 20 strong motion stations considered. Events 2, 3, 5, 6, and 8 were modeled as a point source and therefore no rupture plane is shown. The inset shows New Zealand with the vicinity of the region of this study marked by a black rectangle.

graphic region, site conditions, and site response characteristics into Central Business District (CBD), Eastern suburbs, Western stiff gravel, and 'other sites', which do not conform to these classifications, as annotated in the figure legend. Also included in Figure 2.2 is surface geology by Brown et al. (1995) which is discussed in the last paragraph of this section with regards to the shear wave velocity profiles in Figure A.1 of Appendix A.2.

Table A.2 in Appendix A.2 presents the observed geometric mean peak ground accelerations (PGAs) for the considered stations and events. The PGA values range from from 0.01 to 1.36 g, with a mean PGA of 0.17 g.

Figure A.1 illustrates shear wave velocity (V_S) profiles of the 20 sites based on site investigation results from Wotherspoon et al. (2014), Deschenes et al. (2018), and Jeong and Bradley (2017a). Wotherspoon et al. (2014) also performed detailed site investigations at most of the sites, including surface wave testing (using active and passive methods), cone penetration tests (CPTs), standard penetration tests (SPTs), and laboratory index tests. The velocity profiles in these studies were obtained from surface wave inversions with constant V_S values within each layer. Pressure dependence (i.e., depth dependence) was subsequently applied to the shear wave velocity of each layer in such a way as to maintain equal travel time between the published pressure-independent and pressure-dependent profiles used in this analysis. The pressure

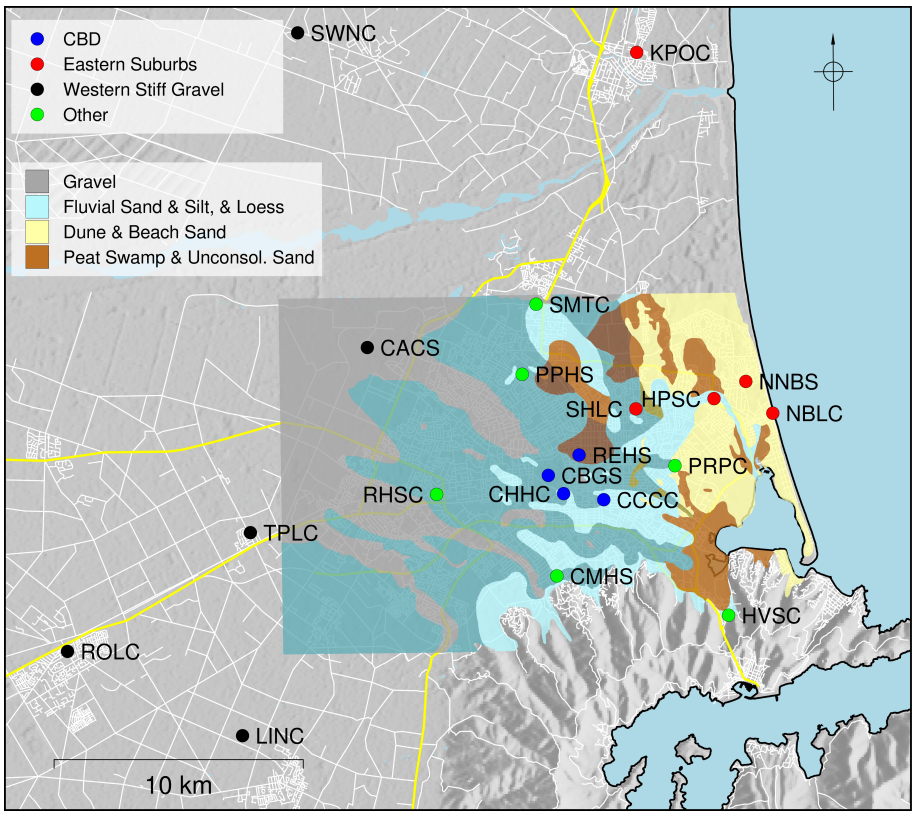

Figure 2.2: Location of the 20 strong motion stations analyzed in this study relative to the Christchurch urban area. Sites are grouped by geographic region and site response characteristics. Surface geology following Brown et al. (1995) is also included in the map. The darker shades of each color in the geologic descriptions indicate that gravel deposits are present at depths greater than 3 m.

dependence is applied using the formulation of the constitutive model which is described in Section 2.3.4. The corresponding "profile periods" (T_1^*) of the sites in Figure A.1 and the V_{S30} values used to compute empirical site amplification are given in Table A.2. T_1^* is computed as the fundamental period of the pressure independent V_S profiles above the halfspace used in the analyses (i.e., the same profiles in Figure A.1 albeit without pressure dependence). Importantly, it differs from the site period which is typically defined as the period of the entire soil profile above bedrock, which is not reached in these analyses due to the great depth of the Canterbury basin (the Methodology section should be referenced for more details on site response analysis).

In examining Figure A.1, while the near surface velocities are similar between CBD and Eastern Suburbs (about 150-200 m/s), the Eastern Suburbs profiles generally have thicker soil deposits above the stiff gravels that were used as the half space (i.e., total depths of 29 - 46

m compared to 20 - 25 m in CBD). From surface geology on Figure 2.2, the CBD sites are primarily fluvial sands and silts except for REHS which is a peat swamp deposit. As indicated by the darker shades of the respective colors in these geologic regions, some gravels are present at depths greater than 3 m at these sites. The Eastern Suburbs sites are dune and beach sands with no gravels present at shallow depths, except for SHLC which sits on fluvial sand and silt. The Western Stiff Gravel sites all have gravel up to or near the ground surface with higher velocities, and are therefore shallower profiles (i.e., 14-20 m deep). Many of the profiles have velocity inversions (i.e., layers of lower velocity below layers of higher velocity) due to interbedded sand/gravel and silt/clay layers. This is consistent with the interbedded nature of the geology in the Canterbury basin which generally alternates between terrestrial gravel and marine sediment deposits (Lee et al., 2017b).

2.3 Methodology

Two common methods for modeling site response are adopted for the context of ground motion simulations: an empirical V_{S30}-based site amplification function, and physics-based 1D wave propagation. These two simulations that account for site effects are also compared to a reference viscoelastic simulation that neglects near-surface site effects and soil nonlinearity. The specific methodologies for all analyses are provided in the following subsections.

2.3.1 Reference viscoelastic condition without site response

Simulated ground motions that do not account for shallow site response are used as a reference result. As presented in Razafindrakoto et al. (2016), these are simulations performed using the Graves and Pitarka (2010) methodology without modification for site response. To resolve the comprehensive low frequency component of the ground motion simulations at 1 Hz, a velocity model grid spacing of 100 m was used with a minimum shear wave velocity of 500 m/s in the simulations (Razafindrakoto et al., 2016), despite the near-surface shear wave velocities at deep sedimentary sites being lower than 500 m/s in reality. Because the simulations are viscoelastic, soil nonlinearity is not considered. In addition to these simulations being used

as a reference result, they are also the 'input' motions for site response analysis methods as described in the next two subsections. In figures throughout the paper, this analysis is referred to as "No Site Response" to highlight the fact that no site effects analysis was performed.

2.3.2 Site effects via empirical V_{S30}-based site amplification

V_{S30}-based site amplification functions from published empirical GMMs are commonly used to compute site amplification factors that can be applied to the reference simulated ground motions (e.g., Graves and Pitarka, 2010). Figure 2.3a shows an example of frequency (i.e., vibration period)-dependent nonlinear site amplification factors from the empirical GMM used in this study (Campbell and Bozorgnia, 2014). This function is then truncated at short and long periods, as in Figure 2.3a, following recommendations by Graves and Pitarka (2010), for two different reasons. Long period (i.e., low frequency) site amplification is truncated because the 3D LF component of the simulation should, to some extent, account for deep site response which would influence long period ground motion amplitudes. Short periods (i.e., high frequencies) are truncated because empirical GMM amplification functions are developed to be applied to response spectra, but in this context they are applied to Fourier spectra in the frequency domain (Graves and Pitarka, 2010). The short period truncation is applied to partially resolve this inconsistency. Bora et al. (2016) discuss the relationship between Fourier and response spectra in the context of ground motion amplification.

2.3.3 Site effects via physics-based 1D wave propagation analysis

1D wave propagation ground response analysis enables explicit modeling of the soil stratigraphy and dynamic response at each site. As shown schematically in Figure 2.3b, reference viscoelastic simulated ground motions are extracted at each site considered, deconvolved, and then used as input to a nonlinear 1D site response analysis. Ground motions are extracted from the simulation at the ground surface, rather than at depth, so that 3D ground motion phenomena, such as basin effects and surface waves, are present given the subsequent use of 1D analyses to model surficial site response.

Because the regional ground motion simulations are viscoelastic, they are deconvolved in the frequency domain using a transfer function for damped soil over an elastic halfspace (e.g., Kramer, 1996) with a 1D V_S profile representative of the velocity model used for the simulation. Ground motions are deconvolved to a depth where nonlinear soil behavior is considered practically negligible. In Christchurch, this typically corresponds to the depth of the Riccarton gravels formation, with a V_S of approximately 400 m/s at depths ranging from 20 to 40 meters (deepening to the east; Wotherspoon et al., 2014; Lee et al., 2017b; McGann et al., 2017). In this particular application, because the simulation grid is coarse (i.e., 100 m spacing), and the depth of deconvolution is relatively shallow (i.e., 20-40 m), the V_S profile for deconvolution is simply a single uniform layer (with $V_S = V_{S,min}$ [i.e., typically 500 m/s in Christchurch]) over a halfspace. The methodology for the nonlinear convolution (i.e., site response analysis) is described in the next subsection.

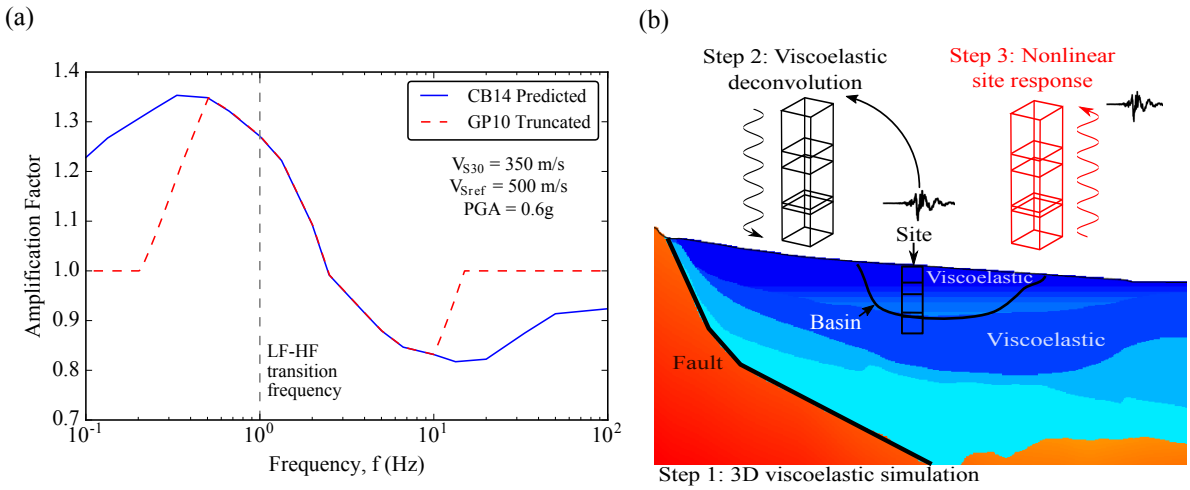

Figure 2.3: Two methods considered in this study for modeling nonlinear site effects in simulated ground motions: (a) Empirical V_{S30}-based nonlinear site amplification factors from Campbell and Bozorgnia (2014) (i.e., CB14) GMM truncated following Graves and Pitarka (2010) (i.e., GP10), applied to simulated ground motions in the frequency domain, and (b) 1D wave propagation site response in which simulated ground motions are extracted from 3D simulation model, deconvolved, and convolved via nonlinear wave propagation site response analysis.

2.3.4 Methodology for nonlinear wave propagation site response analysis

Site response analyses were performed with the nonlinear finite element software OpenSees (Mazzoni et al., 2007). One-dimensional (i.e., vertical) shear wave propagation for a single

930 horizontal component of ground motion was used with two-dimensional nine-noded quadratic
931 elements constrained to deform in horizontal shear. Geometric mean intensity measures were
932 computed from the two simulations with each horizontal component. Elements were sized for
933 each layer to resolve a maximum frequency of 25 Hz based on linear stiffness. The model uses
934 a single-element-wide soil column with periodic boundary conditions on the lateral boundaries
935 of the model, and a compliant base. The pressure-dependent multi-yield (PDMY02) constitu-
936 tive model (Yang et al., 2003) was used to represent nonlinear soil behavior. 1D site response
937 analysis was used because of its widespread adoption in practice and research although we
938 acknowledge the commonly stated limitations of this methodology as demonstrated through
939 validation studies (e.g., Thompson et al., 2009; Kaklamanos et al., 2013).

940 CPTs in the vicinity of each site (Wotherspoon et al., 2014) were used for determining
941 detailed stratigraphy, and the strength and relative density of each soil layer. Parameters esti-
942 mated using CPT data were unit weight, friction angle, relative density, and undrained shear
943 strength. In cases where geotechnical investigations showed the presence of interbedded softer
944 silt layers that were not identified in the V_S profiles from surface wave inversions, a CPT-V_S cor-
945 relation (McGann et al., 2017) was used to estimate the velocity of these layers. Friction angle
946 and undrained shear strength estimates from SPT data were also used to verify and supplement
947 CPT-based estimates.

948 Wotherspoon et al. (2014) performed CPT-based liquefaction triggering analysis (Robert-
949 son and Wride, 1998), and we additionally performed SPT-based liquefaction analysis (Idriss
950 and Boulanger, 2008) to identify soils susceptible to liquefaction (for the purpose of examining
951 subsequent analysis results). While liquefiable soils are present at some sites, the large majority
952 of the events were not severe enough to trigger liquefaction. In this study, the hydraulic conduc-
953 tivity of each soil layer is set artificially high to prevent generation of pore pressure, therefore,
954 the contraction and dilation parameters of the constitutive model have a negligible impact on
955 the response. Future work is intended to directly examine the differences between total and
956 effective stress analyses

2.3.5 Decomposition of prediction residuals

One of the novelties of this work is the validation of simulation results against observed ground motions from multiple earthquake events and stations, enabling repeatable prediction effects to be estimated. Using similar notation as Al Atik et al. (2010) and Bradley (2015), the total prediction residual, Δ, for a given intensity measure can be expressed as:

$$\Delta_{es} = ln(IM_{Obs})_{es} - ln(IM_{Sim})_{es} \tag{2.1}$$

where $ln(IM_{Obs})_{es}$ is the natural logarithm of the observed intensity measure for earthquake e at site s, and $ln(IM_{Sim})_{es}$ is the logarithm of the respective simulated intensity measure. The intensity measures considered in this study are 5%-damped geometric mean (from both horizontal components) response spectral accelerations at 200 vibration periods logarithmically spaced between 0.01 and 10 s.

To identify systematic trends in prediction bias for a given earthquake e, and specific site s, the prediction residual in Equation 2.1 can be partitioned as:

$$\Delta_{es} = a + \delta S2S_s + \delta B_e + \delta W_{es}^0 \tag{2.2}$$

where a is the constant systematic model bias for all earthquakes and sites considered, $\delta S2S_s$ is the systematic site-to-site residual for site s, δB_e is the between-event residual for earthquake e, and δW_{es}^0 is the "remaining" within-event residual for earthquake e at site s, that is apparently random. The sum $(a + \delta S2S_s)$ is the systematic portion of the residual for a given site and is herein referred to as the systematic residual.

The between-event (δB_e), site-to-site ($\delta S2S_s$), and "remaining" within-event (δW_{es}^0) residuals are assumed to be normally distributed with zero mean and variances of τ^2, ϕ_{S2S}^2, and ϕ_{SS}^2 , respectively. The total variance is then expressed as:

$$\sigma^2 = \tau^2 + \phi_{S2S}^2 + \phi_{SS}^2 \tag{2.3}$$

For an individual site, s, the variance in the within-event residuals (i.e., $\delta W_{es} = \delta S2S_s + \delta W^0_{es}$) at that site is represented by $\phi^2_{SS,s}$. The evaluation of Equation 2.2 for all events and sites considered is performed using linear mixed-effects regression with the lme4 package in R (Bates et al., 2015).

2.4 Qualitative comparison of observed and simulated ground motions

In order to illustrate the salient features of the analyses undertaken, this section provides a qualitative summary for a subset of results, while the subsequent section (Section 2.5) provides statistical analysis of results from all sites and events. Figure 2.4 plots response spectra of observed and simulated ground motions from all three methods for the 4 September 2010 M_W7.1 earthquake at the HVSC site, and the 13 June 2011 M_W5.3 earthquake at the RHSC site. Also included in the figure are acceleration time series for observed ground motions and the two simulations that model nonlinear soil response. These two examples are intended to illustrate relative differences between the various methods of modeling site effects.

Comparing the simulated response spectra in Figure 2.4 it is evident that for T $>$ 5 s all three analyses are essentially the same, suggesting the site response methods have little influence on the ground motion at long periods. Trends in response spectral accelerations seen in Figure 2.4, that are also generally visible across most of the data, are: (1) the empirical V_{S30}-based site amplification function results in greater amplification of long periods, (2) the wave propagation analysis results in greater amplification at short periods, and (3) the reference viscoleastic simulations that neglect shallow site effects greatly under-predict spectral accelerations near the profile period (0.39 and 0.29 seconds for HVSC and RHSC, respectively). These trends are discussed further with respect to observed-to-simulated residuals in subsequent sections.

Comparing the simulations with the observations, in both of these examples, the physics-based wave propagation method of modeling site response yields closer agreement to observations than the empirical V_{S30}-based method. Figure 2.4b is a good example of how there can be

imprecisions in the reference or input simulations used for subsequent site response analyses as seen by the large overprediction in the reference viscoelastic simulation without site response for T $>$ 1 s. Such imprecisions in the input motion will manifest as imprecisions in downstream analyses as shown in Figure 2.4b.

In general, the simulated acceleration time series for the 4 September 2010 event (Fig 2.4c) are consistent with observations in terms of frequency content and duration. However, the arrival time of the strongest shaking is different, which may be caused by the complex multi-fault rupture of this event. As also seen in the response spectra, there is significant underprediction in the amplitudes of simulations which is much more prominent for the empirical V_{S30}-based method. HVSC is a site that exhibits abnormally large ground amplification, as discussed in Section 2.5.3. For the 13 June 2011 event (Fig 2.4d) the simulated acceleration time series are relatively consistent with observations in amplitude and frequency content. The duration of shaking is clearly underestimated, which is consistent with results from Lee et al. (2018) who found that the HF path duration model was too short, resulting in underestimation of significant duration for small-to-moderate magnitude events. Also, simulations of this event show late, very low frequency arrivals not visible in observations. These late arrivals may be the cause of the large over estimation of long period energy seen in response spectra (Fig 2.4b).

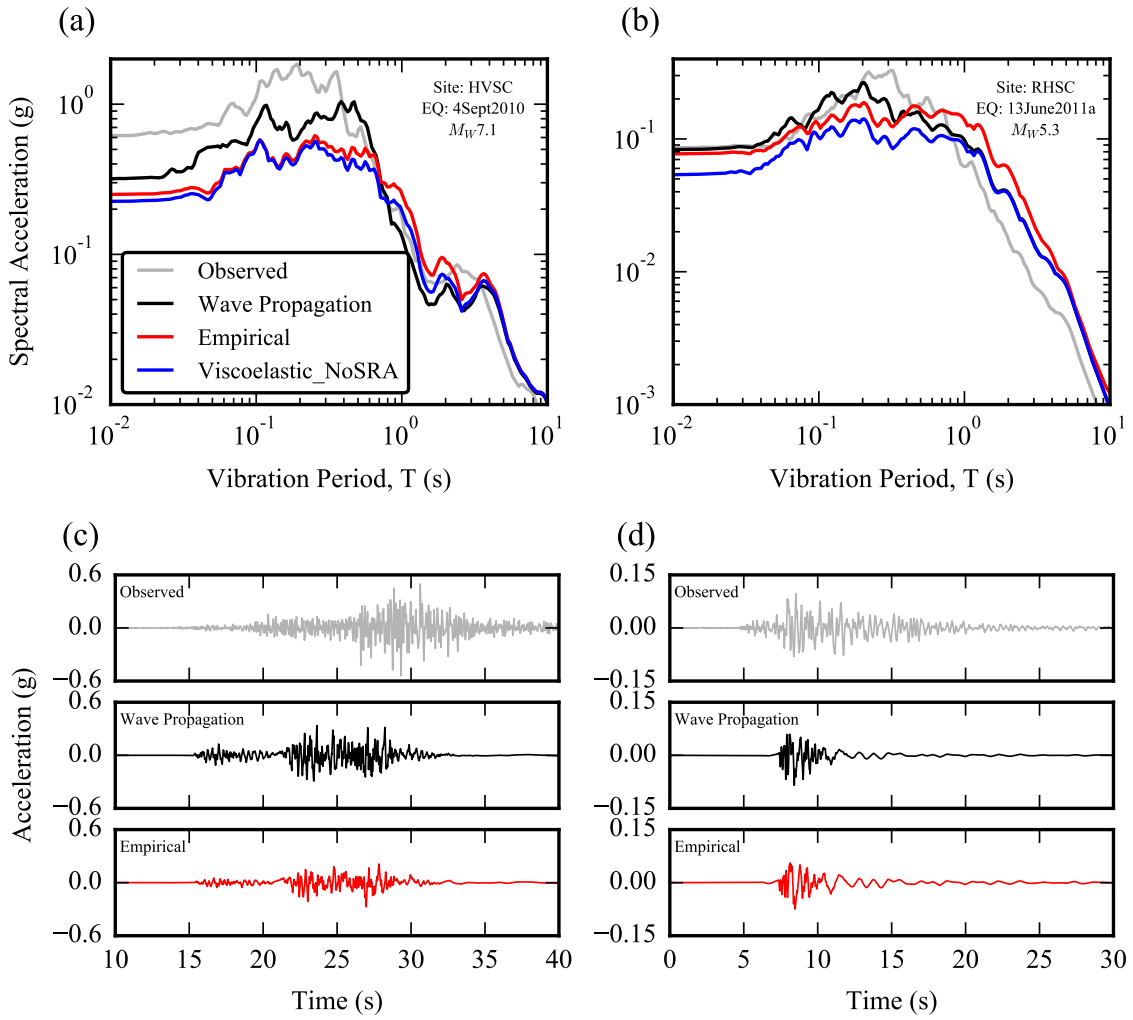

Figure 2.4: Comparison of 5%-damped geometric mean response spectra and acceleration time series for observed and simulated ground motions from (a and c) 4 September 2010 M_W7.1 earthquake at HVSC, and (b and d) 13 June 2011 M_W5.3 earthquake at RHSC. Note different y-axis scales between the left and right figures.

2.5 Systematic Prediction Residuals

Response spectra are computed for observed ground motions and all three simulation approaches discussed in Section 2.3. The partitioned residuals are then computed from the response spectra of all events at every site via Equations 2.1 and 2.2. The following subsections compare and contrast the computed residuals from the three simulation types.

2.5.1 Model systematic bias and total uncertainty for all events and sites considered

Figure 2.5 illustrates the systematic model bias, a (Fig 2.5a), and the total standard deviation, σ (Fig 2.5b), for all 20 sites and 11 earthquakes considered as a function of response spectral vibration period for all three analysis methods. Results from prediction via empirical GMM are not discussed until Section 2.6. Three average trends are identified in the results shown in Figure 2.5a: (1) For periods between approximately $T = 0.2 - 2$ s, consideration of site effects using both the empirical and wave propagation methods results in reduced bias (i.e., residuals closer to zero) relative to the reference viscoelastic simulations which ignore site effects and grossly under-predict spectral accelerations. (2) The empirical (V_{S30}-based) approach significantly over-amplifies the long periods (i.e., approximately 1-5 s) and the wave propagation method performs better in this period range, and (3) the empirical (V_{S30}-based) method results in slightly lower bias than the wave propagation approach at $T < 0.2$ s for which the wave propagation method over-predicts the ground motion. The subsequent three paragraphs discuss these trends in greater detail.

The first trend noted above is relatively self-evident. The significant underprediction by reference viscoelastic simulations without site response occurs near the range of profile periods for the sites (i.e., $T_1^* = 0.15 - 0.77$ s), at which large amplification occurs from near-surface soil response. The reference viscoelastic simulation neglects site effects and therefore fails to model this large amplification at the profile period.

The second trend noted above, over amplification by the empirical V_{S30}-based approach at $T = 1 - 5$ s, suggests that long period site effects are already being explicitly captured in the low frequency component of the ground motion simulations such that the empirical modification is, to some extent, effectively "double counting" the amplification. This result was also observed by Lee et al. (2018) using the same simulation methodology, albeit without wave propagation site response, on a dataset of 145 $M_W 3.5 - 5$ earthquakes in the same region. As previously noted, site amplification factors with truncation of long period amplification, as recommended by Graves and Pitarka (2010) (see Fig 2.3a), are intended to account for long period site effects when low-resolution velocity models are used that do not explicitly model these effects. How-

ever, the simulations used in this study are derived from a high-resolution Canterbury velocity model (Lee et al., 2017a) which explicitly models the basin, hence suggesting that the period range over which the site amplification function is heuristically truncated needs to be revised. In addition, the site amplification model from Campbell and Bozorgnia (2014) was developed primarily from California data, and therefore may not be appropriate for use in Christchurch.

Finally, regarding the third trend of overprediction of short period ground motion amplitudes, it is evident that the reference viscoelastic simulation (i.e., blue line in Fig 2.5a), which was used as an input motion for the wave propagation analysis, already overpredicts the observed ground motion at $T \approx 0.1$ s (relative to observed ground motions at $V_{S30} < 500$ m/s sites). This implies that periods close to 0.1 seconds would likely be further over-predicted for sites with near-surface shear wave velocities of less than 500 m/s when site effects are considered. Additionally, the 1D wave propagation based site response analysis may not properly attenuate high frequencies which leads to excessive site amplification. Other studies have found that 1D wave propagation analysis, which typically lacks heterogeneities present in natural soil deposits that scatter and attenuate high frequency waves, can 'underdamp' these frequencies (e.g., Afshari and Stewart, 2017).

Figure 2.5b shows that considering site effects via both the wave propagation and empirical methods reduces total uncertainty, σ, for $T < 2$ s relative to ignoring site effects in the case of viscoelastic simulations. As discussed in Appendix A.3, the reduction in uncertainty for $T < 1$ is attributed primarily to a reduction in between-event uncertainty, τ. Both site response methods have comparable uncertainty across the full period range. Reasons for this are discussed with regard to event- and site-specific uncertainty in Appendix A.3 and Section 2.5.2, respectively.

2.5.2 Site-to-site, $\delta S2S_s$, and within-event, δW_{es}, residuals

The site-to-site residual, $\delta S2S_s$ (Equation 2.2), represents the average difference between observed and predicted site amplification at a given site. Figure 2.6 plots the site-to-site residuals for the wave propagation analysis, and the site-to-site and within-event single-station standard deviations, ϕ_{S2S} and ϕ_{SS}, respectively, for all three methods. The residuals for the vis-

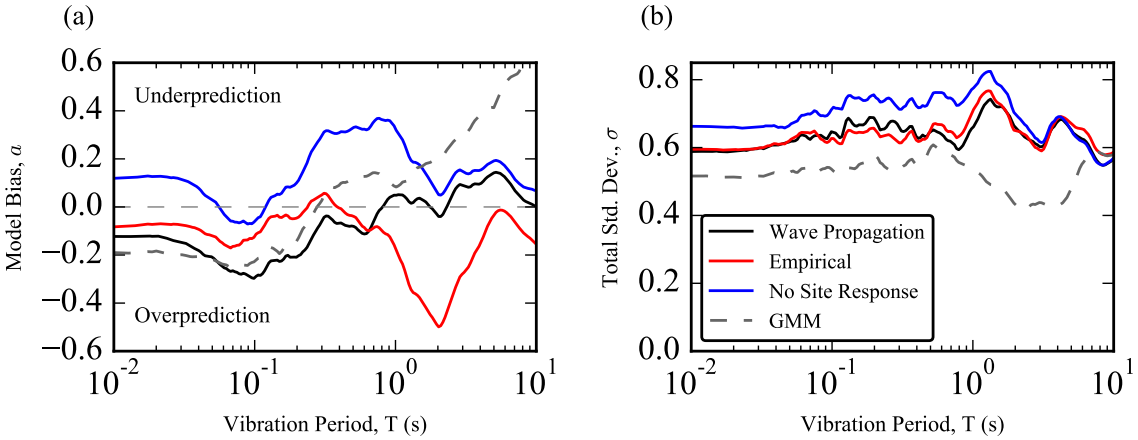

Figure 2.5: (a) Systematic model bias, a, and (b) total uncertainty, σ, for all events and sites considered.

coelastic reference simulations and simulations with empirical site response are plotted in Figure A.8 of Appendix A.6. The site-to-site residuals (Fig 2.6a) are color-coded by the site V_{S30}, which illustrates a dependence in the residual on V_{S30} at approximately $T = 0.5 - 3$ s. Generally, the stiffest sites are the most overpredicted, the softest sites are the most underpredicted, and intermediately stiff sites fall close to zero residual in this period range. This trend is even more notable for the $\delta S2S_s$ residuals of viscoelastic reference simulations that neglect shallow site response, which is reasonable as one would expect the softest sites, with the strongest site amplification, to be even more under-predicted when site effects are neglected. Two conclusions can be drawn from the fact that this trend is still visible in the wave propagation site response results: (1) Although the wave propagation site response analysis greatly reduces the large under-prediction at soft sites by modeling site response, the modeling assumptions mean the analysis does not fully capture the actual site amplification, resulting generally in a slight under-prediction (Fig 2.6a), or (2) the large majority of stiffer sites lie in the same region to the west of Christchurch in the Canterbury plains (Fig 2.2). This overprediction at moderate to long periods could alternatively be a regional effect caused by the 3D velocity model (i.e., path) for this region. Because the mean of all $\delta S2S_s$ must be zero, this regional over-prediction would cause an apparent under-prediction in the remaining sites, particularly for softer sites at which the observed site amplification is greater.

Theoretically, by perfectly modeling the site response, each individual site-to-site residual

($\delta S2S_s$) could be reduced to zero. The departure of $\delta S2S_s$ from zero is therefore indicative of both physics that is not adequately modeled in the site response analysis, and uncertainty in the geotechnical and geophysical site characterization. Additionally, because $\delta S2S_s$ represents the observed-to-simulated differences in site amplification, it is highly dependent on the input motion obtained from the regional ground motion simulation as nonlinear site response is greatly influenced by the amplitude and frequency content of the ground motion. Therefore, imprecision in the input motion will inevitably manifest as non-zero $\delta S2S_s$ residuals. While $\delta S2S_s$ is non-zero for the simulations with site effects modeling, it is evident from Figure 2.6b that a reduction in uncertainty is realized when site effects are considered.

Figure 2.6b shows that consideration of site effects via both the empirical and the wave propagation methods substantially decreases the site-to-site uncertainty, ϕ_{S2S}, for $T \approx 0.3 - 5.0$ s. This implies that the site amplification is predicted with less uncertainty when near-surface site effects are considered in physics-based ground motion simulation. Explicitly modeling site response via wave propagation reduces site-to-site uncertainty compared to the V_{S30}-based empirical method at $T = 0.2 - 1$ s, which is approximately the range of profile periods for the SMS considered (i.e., $T_1^* = 0.15 - 0.77s$; as defined in Table A.2). For $T = 1 - 5$ s, where the 1D wave propagation site response analysis has little influence on spectral accelerations for these sites, the V_{S30}-based empirical site amplification has slightly lower site-to-site standard deviation than the wave propagation method. One would expect that the site response approach which uses both significantly more information on soil type and stratigraphy, and also more comprehensive physics (i.e., the wave propagation analysis), would potentially result in less uncertainty in the site amplification. The fact that there is no appreciable difference in uncertainty for much of the period range between the two site response approaches suggests that, as alluded to previously, there is both uncertainty in the input motion, and potentially the assumptions in the 1D total stress site response analysis (including the determination of modeling parameters) is leading to significant imprecision. The total uncertainty is contributed to by both of these factors and further work is needed to untangle them, and thus isolate their relative contributions (this is discussed further in Appendix A.4).

As shown in Figure 2.6c, the within-event single station standard deviation (ϕ_{SS}) is practically the same for all three analyses over the entire period range. ϕ_{SS} represents the apparent

aleatory variability that is not systematically modeled by the physics used in these models, and includes effects from the source, path, and site. A reduction in ϕ_{S2S} with no change in ϕ_{SS} suggests that the mean site amplification is predicted with more accuracy when site response is explicitly modeled, however, at any given station, the uncertainty in the modeled site amplification is the same for all methods or is masked by apparently random uncertainties in the source, path, and site. Single station uncertainty is discussed further in Section A.4.0.1 of Appendix A.4.

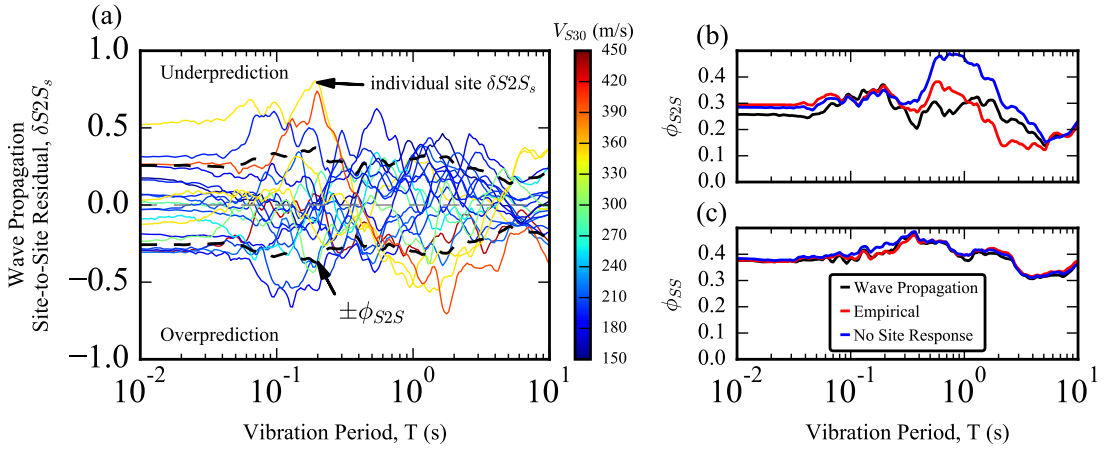

Figure 2.6: (a) Site-to-site residuals from wave propagation site response analysis for all 20 sites with lines colored by V_{S30}, and (b) site-to-site standard deviation, ϕ_{S2S}, and (c) within-event single-station standard deviation, ϕ_{SS}, respectively, for wave propagation, empirical, and reference viscoelastic (i.e., no site response) simulated ground motions.

2.5.3 Systematic residuals for individual sites

Figure 2.7 plots the average 1D wave propagation-based spectral acceleration amplification across the 11 events as a function of vibration period for each of the 20 profiles in Figure A.1. The amplification for an individual event is the ratio of the output motion at the ground surface to the input motion at the halfspace. It is apparent that sites REHS, HVSC, and CMHS have the largest average amplification, with amplification factors exceeding 2.5 at the profile period, while the western stiff sites profiles generate little amplification. The diamond on each curve indicates the profile period (i.e., T_1^*) as defined in Section 2.2.2.

To illustrate how the level of site amplification is manifested in the systematic residuals of each site, Figure 2.8 plots the systematic residual (i.e., $a + \delta S2S$) from all three analysis

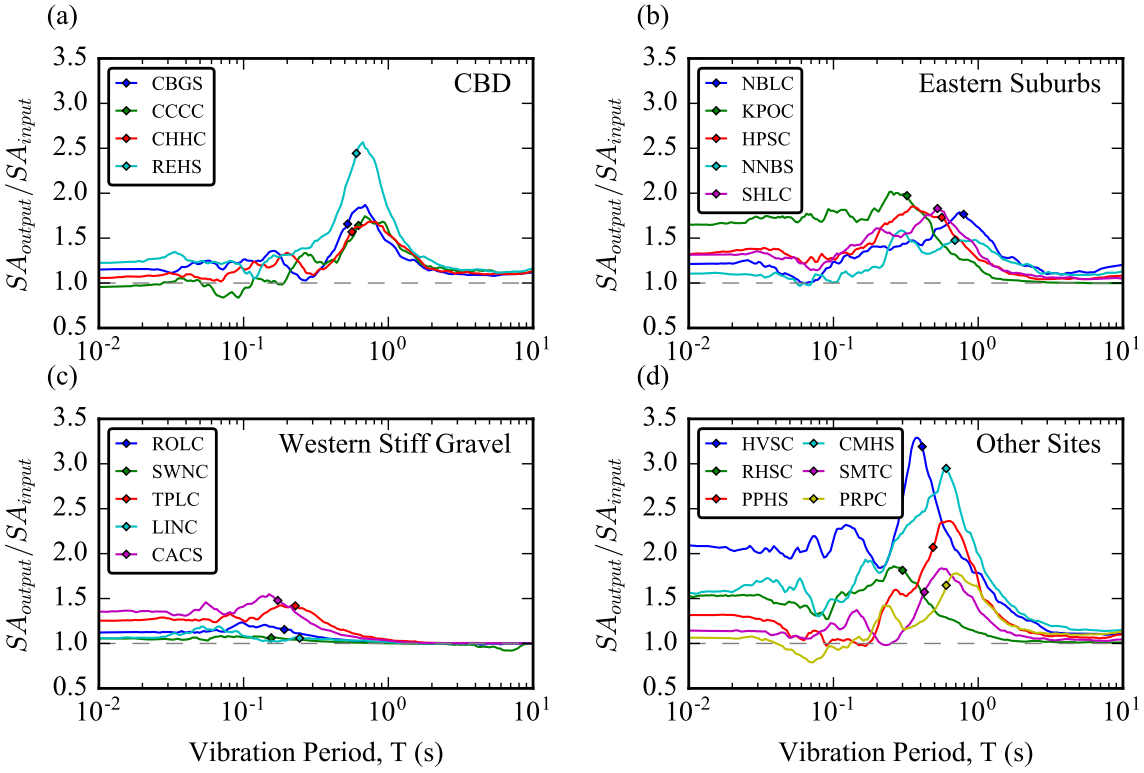

Figure 2.7: Spectral acceleration amplification functions (i.e., the ratio of computed ground surface motion over the input motion) from wave propagation site response analyses. The small diamonds indicate the small-strain, pressure-independent profile period (T_1^*) for each site.

methods for four sites. Figure 2.8a shows the results for HVSC, which consistently produced exceptionally strong ground shaking throughout the Canterbury Earthquake Sequence (Bradley, 2015; Jeong and Bradley, 2017a). This is evident from the large underprediction at $T < 1\ s$ when site effects are not considered (i.e., the reference viscoelastic simulations). The empirical V_{S30}-based amplification does not capture the strong site response and still severely underpredicts at short periods. The wave propagation site response analysis performs significantly better in this period range as a result of significant amplification being predicted (as shown in spectral amplification function of Fig 2.7d). Jeong and Bradley (2017a) found that this strong amplification can be attributed to 1D site effects from a large near-surface impedance contrast, and 2D/3D shallow basin response (Jeong and Bradley, 2017b). Since non-1D site response is not modeled in this study, further reduction in the systematic residual in Figure 2.8a would be possible using more comprehensive site effects modeling. It is also important to note that the 1D wave propagation method actually results in a slight overprediction due to the large amplification at T_1^* and

that this could be improved by a more complex site response model that yields amplification over a broader period range.

Figure 2.7a shows that REHS (a soft peat soil site; Fig 2.2) systematically produces large site amplification and strong ground motions. The systematic residual for REHS in Figure 2.8b illustrates that the reference viscoelastic simulation greatly underpredicts spectral accelerations at the profile period ($T_1^* \sim 0.6s$). The V_{S30}-based method does not fully capture the level of site amplification, and still results in substantial under-prediction at T_1^*. The wave propagation approach is better able to capture the strong amplification at the profile period and greatly reduces the systematic residual for this site.

As shown in Figure 2.8c, RHSC is yet another site at which the wave propagation site response analysis better predicts site amplification at the profile period. This site also demonstrates the overpredicting bias at short periods from the wave propagation analysis that is shown Figure 2.5 and discussed in Section 2.5.1 [i.e., trend (3)], which is likely a result of overprediction in the HF component of the reference simulations.

Finally, Figure 2.8d illustrates that at SWNC (a Western Stiff Gravel site; see Fig A.1) site response is negligible and therefore, all three analysis methods result in similar residuals. This trend is typical of all the Western Stiff Gravel sites. The large overprediction at $T = 0.5 - 3.0\ s$, which is discussed in detail in Section 2.5.2, is also typical of these stiff gravel sites.

While the 1D wave propagation site response analysis is better able capture the large site amplification at the profile period for these sites, accurately predicting the precise amount of amplification at the profile period and at other periods is more challenging. The features presented in Figure 2.8 are further discussed with respect to all sites in Appendix A.4. The systematic residual from all three analysis methods are plotted for every site in Figure A.9 of Appendix A.6.

Figure A.3 in Appendix A.4 plots the systematic residual for all sites divided into groups (as in Fig 2.2) for both wave propagation and empirical methods. It highlights the trends in bias that are discussed in Section 2.5.1. Figure A.4 directly compares the systematic residual at the profile period from empirical and wave propagation methods. The results indicate that for approximately 15% of sites, the wave propagation method greatly reduces the systematic

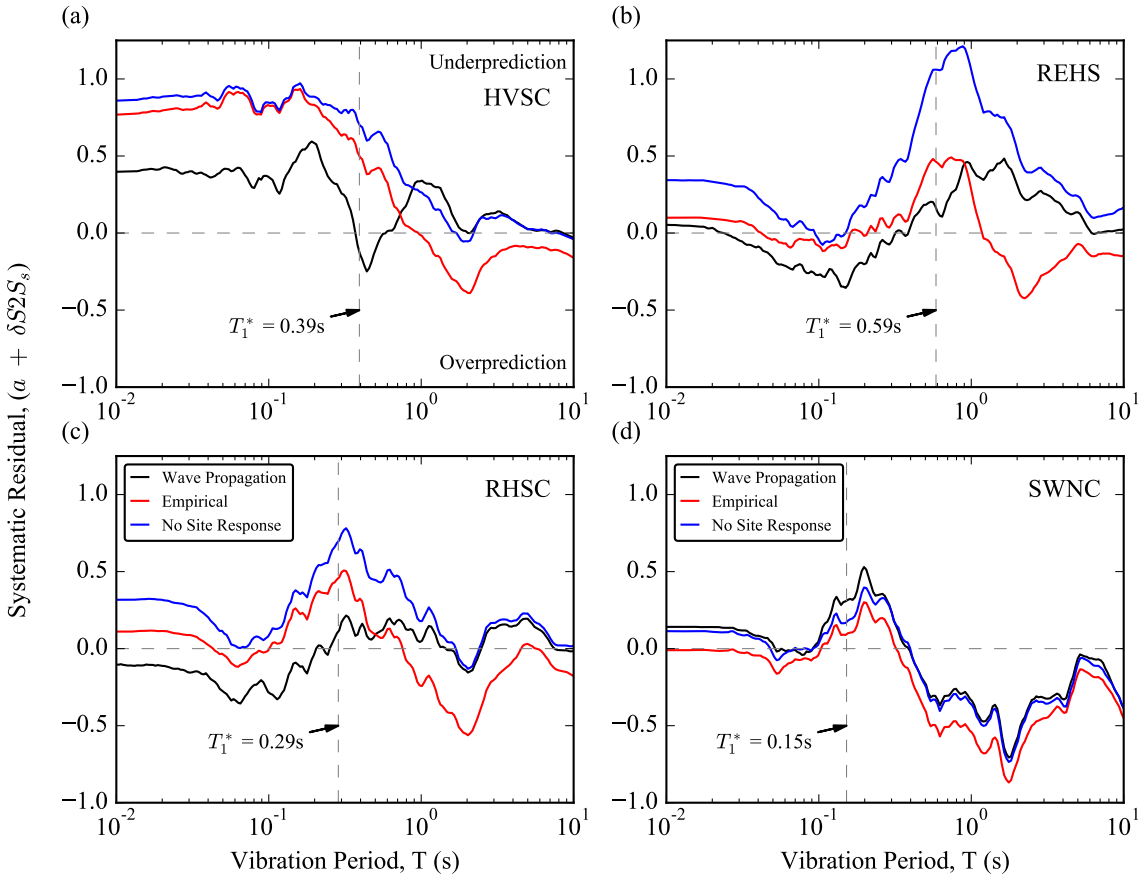

Figure 2.8: Comparison of systematic effect (i.e., $a + \delta S2S$) from three analysis methods for four sites: (a) HVSC, (b) RHSC, (c) REHS, and (d) SWNC.

residual. These sites are generally softer soil sites or sites with a large impedance contrast near the ground surface.

2.5.3.1 Comparison of observed and simulated response at nearby sites

This section compares the ground surface response of nearby sites within a group from both observed and simulated ground motions to examine whether the site response methods can capture local variability in ground motion that is presumably attributed only to near-surface site effects. Because the sites in the region considered here (i.e., CBD sites) are spatially close, this depiction of the data assumes that the incident ground motion below near-surface soils are practically similar. Spectral ratios are computed at every site and for every event as the ratio of the surface response spectrum for each site (i.e., $SA_{e,s}$) to the geometric mean response spectrum

for the full group of sites (i.e., $SA_{e,mean}$). At every site, the geometric mean spectral ratio is then computed across all 11 events. This computation is expressed in equation form in Equations 2.4 and 2.5. The average spectral acceleration for an event, e, across all four sites in the CBD group (i.e., $N_{sites} = 4$) is computed as:

$$SA_{e,mean} = \exp\left[\frac{1}{N_{sites}}\sum_{s=1}^{N_{sites}} \ln\left(SA_{e,s}\right)\right] \tag{2.4}$$

At each site, s, the ratio of spectral acceleration at that site to the average spectral acceleration for the group is computed for all events. The average ratio across all 11 events (i.e., $N_{events} = 11$) is expressed as:

$$\frac{SA_s}{SA_{mean}} = \exp\left[\frac{1}{N_{events}}\sum_{e=1}^{N_{events}} \ln\left(\frac{SA_{e,s}}{SA_{e,mean}}\right)\right] \tag{2.5}$$

The advantage of using this type of metric versus others examined thus far is that it does not require assuming that the simulated incident ground motion below sites is consistent with observed ground motions. Figure 2.9 plots these spectral ratios for the CBD group from (a) observed ground motions, (b) simulated ground motions that neglect site effects, and those that model site effects via (c) wave propagation and (d) empirical V_{S30}-based site response. The observed ground motion ratios clearly illustrate strong amplification in the REHS ground motion relative to the other sites at periods $T = 0.5 - 2$ s, as well as weaker shaking in this period range for CBGS. REHS is the softest of all 20 sites with the lowest V_{S30} (i.e., 155 m/s), as it has approximately 9 meters of peat and soft silt below the ground surface (Wotherspoon et al., 2014). Other studies have also identified REHS as a site of exceptionally large site amplification (Bradley, 2015, and Bradley et al., 2015).

As expected, because the distance between the sites is less than 2.5 km, the reference viscoelastic simulations with no site effects are similar across all CBD sites (Fig 2.9b). On the contrary, the wave propagation site response analysis does a reasonably good job of capturing many of the relative differences in observed ground motions between sites (Fig 2.9c). Most notably, the wave propagation method captures the strong amplification near the profile period of REHS, although not to the full extent across the entire period range (i.e., $T = 0.5 - 2$ s). At short

periods, the below average and above average amplitudes at CCCC and REHS, respectively, are also captured by the models. Additionally, the below average amplitudes at $T \approx 0.2 - 3$ s at CBGS are also seen in the wave propagation analysis. Some of the features that are inconsistent between the observed ratios and the wave propagation ratios can be attributed to the reference viscoelastic simulation (i.e., imprecision in the input motion) such as the strong relative deamplification in CCCC at about $T = 0.6$ s, again illustrating that imprecision in the input motion will manifest as unfavorable bias in the computation of residuals.

Unlike the wave propagation method, the empirical V_{S30}-based method (Fig 2.9d) fails to capture all of the aforementioned trends in ground motions at nearby sites. This is most evident in the REHS ratios at which the relative amplification from this method is not nearly as large or broad as the observations. This exercise reiterates the significance of explicitly modeling site response for sites that are soft and/or exhibit strong site amplification as is discussed further in Appendix A.4, but elucidates the difficulty in accurately predicting the precise amplitudes and frequency-dependence of ground amplification.

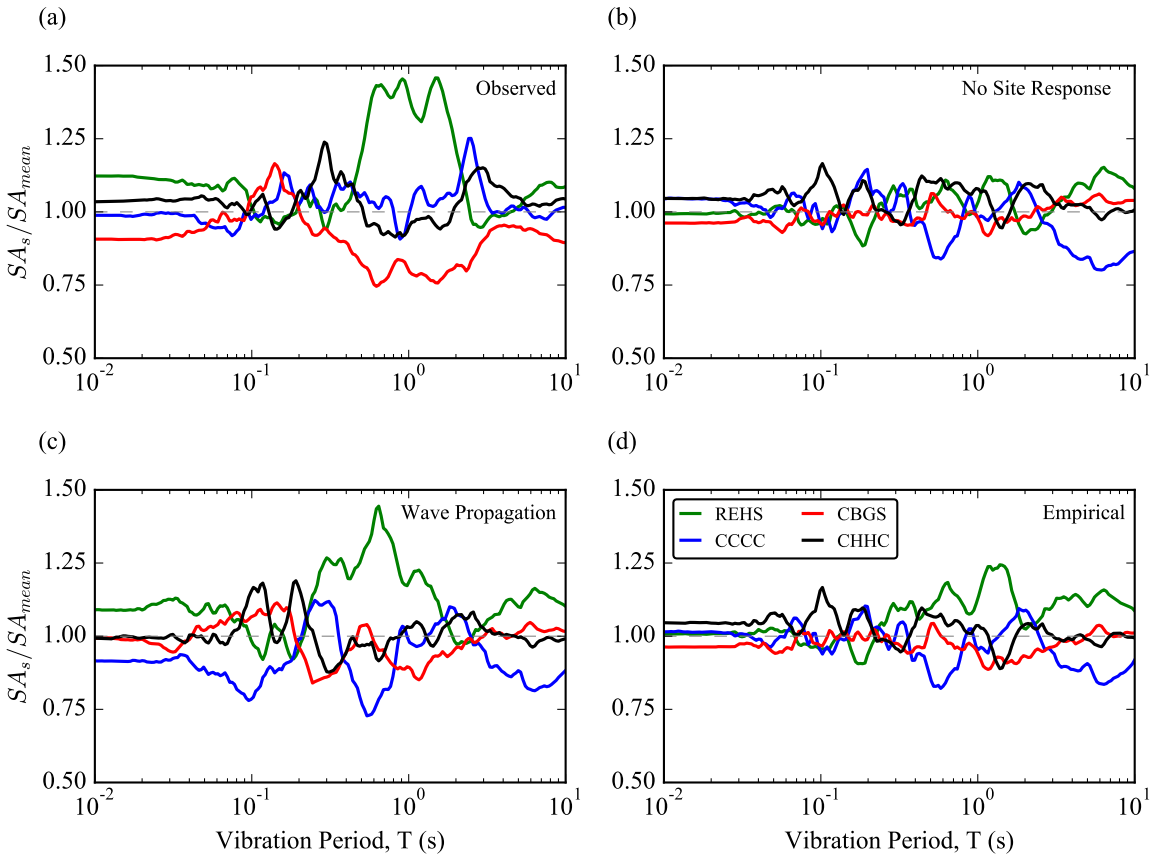

Figure 2.9: Response spectral ratios for sites within the Christchurch CBD from (a) observed ground motions, (b) reference viscoelastic simulations without site effects, (c) simulations with wave propagation site response and (d) simulations with empirical V_{S30}-based site response. The spectral ratio corresponds to the mean ratio for all 11 events where the ratio for an individual ground motion is the spectral acceleration for a given site over the mean spectral acceleration from all sites in the group.

2.6 Comparison with prediction from empirical ground motion model

Until now, focus has been on the use of simulated viscoelastic 'input' and alternative representations of surficial site response. In order to highlight the merit in this work presented to date, it is critical to benchmark results from these alternative physics-based ground motion simulations to conventional empirical ground motion models (GMM), which are the current standard of practice for ground motion prediction. For the purpose of illustrative compari-

son, predicted response spectra were computed for all events and sites considered using the Bradley (2013) New Zealand-specific GMM, and residuals computed and partitioned according to Equations 2.1-2.3. Figure 2.5 plots the systematic model bias and total standard deviation for all events and sites from the three physics-based ground motion simulation methodologies, and the empirical GMM which also utilizes V_{S30}-based site amplification (from Chiou and Youngs, 2008).

In examining Figure 2.5a, no notable differences in the magnitude of bias are observed for $T < 1$ s. For $T > 1$ s, the bias in the GMM prediction increases substantially with increasing period, such that the GMM greatly underpredicts the long period intensity and the bias is significantly greater than that from physics-based simulations for $T > 5$ s. Such long period bias has also been noted by Van Houtte (2017). Even for $T > 1$ s, the wave propagation method has substantially lower bias than the GMM.

Figure 2.5b illustrates that the total standard deviations show slightly less uncertainty for the GMM at $T < 1$ s, and moderately less uncertainty for $T = 1-5$ s. For $T > 5$ s, the empirical GMM predicts ground motion with similar uncertainty as the physics-based approaches. Figure A.6 in the Appendix A.5 compares the components of standard deviation from all analysis methods. Figure A.6 demonstrates that it is the between-event uncertainty, τ, that results in lower σ for $T = 1-5$ s, and the site-to-site uncertainty, ϕ_{S2S} that results in higher σ for $T > 5$ s from the GMM compared to the physics-based methods. Considering both the magnitude of bias and uncertainty, it can be concluded that for $T < 5$ s the physics-based simulation and empirical GMM methods predict ground motion with comparable performance while for $T > 5$ s the physics-based methods performs significantly better.

All components of standard deviation from this study are also compared to previously published values from empirical prediction models in Appendix A.5. Figure A.7 again shows that these physics-based simulation methods can predict ground motion with comparable uncertainty as empirical ground motion models.

2.7 Conclusions

This study compares and contrasts alternative approaches to modeling site response in physics-based ground motion simulations, and specifically highlights the benefits and hindrances of using a physics-based wave propagation site response methodology as opposed to the standard-of-practice empirical V_{S30}-based approach. In terms of the overall model bias across all events and sites considered, three notable observations are made: (1) Over a wide period range, consideration of site effects using both the empirical and wave propagation methods results in reduced bias (i.e., residuals closer to zero) relative to the reference viscoelastic simulations which ignore site effects and grossly under-predict spectral accelerations, (2) the V_{S30}-based approach significantly over-amplifies long period ground motions and the wave propagation method performs better in this period range, suggesting that the low frequency component of the ground motion simulation is capturing deep site effects reasonably well already, leading to a "double counting" of amplification, and (3) the empirical V_{S30}-based method performs slightly better than the wave propagation approach at short periods for which the wave propagation method overpredicts ground motions; This is also exacerbated by an over-prediction from the high frequency component of the simulation, as seen from the viscoelastic reference prediction for a reference shear wave velocity of 500 m/s. The total standard deviation is reduced for $T < 2$ s when site effects are considered, however, there is no notable difference in σ between the wave propagation and empirical site response methods. The site-to-site uncertainty, which reflects uncertainty in site amplification, is also greatly reduced at approximately $T = 0.3 - 5$ s by modeling nonlinear site effects. Explicit modeling of site response via wave propagation results in even greater reduction in site-to-site uncertainty near the profile periods of the SMSs considered (i.e., $T = 0.2 - 1$ s).

While the systematic residual in ground motion prediction at the profile periods from the physics-based wave propagation and empirical V_{S30}-based methods are comparable for the majority of sites, significant improvements are realized in some instances with the wave propagation method for very soft sites or sites that exhibit exceptionally large site response. For these sites, the empirical V_{S30}-based site amplification fails to capture the large amplification and greatly under-predicts. Comparisons of average amplifications from nearby sites indicates

that the wave propagation method is better able to model relative trends in site specific shallow ground response.

Investigation into systematic residuals and within-event single-station standard deviations for stiff gravel sites that have negligible impedance-based site response suggests that there is imprecision in the reference viscoelastic simulated motions which are used as input to the site response analyses. This likely limits the amount of improvement that can be realized by explicitly modeling nonlinear site effects.

Perhaps of utmost importance, these physics-based ground motion simulations with nonlinear site effects (especially the wave propagation method), can generally predict spectral accelerations with comparable bias and uncertainty, and with significantly lower bias at $T > 5$ s relative to empirical ground motion models. This suggests that these simulated ground motions are equally as appropriate as conventional empirical ground motion models for use in geotechnical and structural response history analysis. Additionally, because of the physics-based nature of wave propagation site response coupled with physics-based ground motion simulations, there is significant room for improvement. This could be via improvement of the simulations themselves (i.e., refinement of regional velocity models, and development and adoption of improved methodologies), or the site characterization and site response analysis.

2.8 Data and resources

Observed ground motions used for computing prediction residuals were downloaded from the GeoNet file transfer protocol (`ftp://ftp.geonet.org.nz/strong/`). The physics-based ground motion simulations were obtained from Hoby Razafindrakoto (Razafindrakoto et al., 2016). The simulations for the 2010 Darfield and 2011 Christchurch earthquakes are available on SeisFinder (`https://quakecoresoft.canterbury.ac.nz/seisfinder/`).

Figures 2.1 and 2.2 were generated using Generic Mapping Tools (`http://gmt.soest.hawaii.edu/`), and the remaining figures were generated in Python (`https://www.python.org/`) and Matplotlib (`https://matplotlib.org/`).

2.9 Acknowledgements

This work was financially supported by the University of Canterbury, and QuakeCoRE: The NZ Centre for Earthquake Resilience via the UC and QuakeCoRE PhD Scholarships. This is QuakeCoRE publication number 0371.

The authors would like to thank Hoby Razafindrakoto for providing the simulated ground motions used in this study, Christopher McGann, Liam Wotherspoon, Seokho Jeong, Jim Kaklamanos, Kevin Foster and Karim Tarbali for their technical and editorial support, and Viktor Polak for generating Figures 2.1 and 2.2.

Chapter 3

2D Geotechnical Site-Response Analysis including Soil Heterogeneity and Wave Scattering

C. A. de la Torre, B. A. Bradley, C. R. McGann (2021). 2D Geotechnical Site-Response Analysis including Soil Heterogeneity and Wave Scattering. *Earthquake Spectra* (Submitted).

Abstract

This study describes an approach for modeling wave scattering and the spatial variability of ground motion in geotechnical site-response analysis by modeling soil heterogeneity through 2D correlated random fields. Importantly, the required site-specific inputs to apply the proposed approach in a practical setting are the same as those associated with conventional 1D site-response analysis. The results, which are affected by wave scattering attenuation, are compared to those from conventional laterally homogeneous 1D site-response analyses and 1D analyses with randomized velocity profiles extracted from heterogeneous 2D velocity model realizations. A sensitivity study involving 5,400 2D model realizations investigates the influence of random field input parameters on wave scattering and site response. The computed ground surface acceleration waveforms and transfer functions show that this method is capable of scattering seis-

mic waves. Multiple ground-motion intensity measures are analyzed to quantify this influence, and distinguish between the effects of 1D vertical heterogeneities and averaging across many nodes and realizations, from the effects of wave scattering and 2D ground-motion phenomena. The redistribution of ground-motion energy across wider frequency bands and scattering attenuation of high-frequency waves in the 2D analyses resemble features observed in empirical transfer functions computed in other studies. While analyses with 1D randomized velocity profiles are able to replicate median results from 2D analyses for some low-frequency intensity measures (e.g., transfer functions at $f < 10$ Hz, and spectral acceleration at the fundamental period), medians and standard deviations of high-frequency intensity measures (e.g., transfer function at $f > 10$ Hz, *PGA*, and Arias intensity), which are influenced by wave scattering, are not appropriately captured. Given the equivalent input information requirements as conventional 1D analysis, and the availability of large computational resources, we advocate that the proposed 2D (and eventually 3D) approach is a fruitful path forward to improve the modeling of site-response physics and realize improved predictive capabilities.

3.1 Introduction

In conventional 1D seismic site-response analysis (SH1D), soils are modelled as horizontal, homogeneous, infinite layers and are limited to shear deformation with vertically propagating shear waves as the ground-motion excitation (Schnabel et al., 1972; Idris, 1993; Hashash and Park, 2001; Stewart Annie On-Lei Kwok et al., 2008). These basic assumptions, which were adopted in the late 1960s to early 1970s (e.g., Schnabel et al., 1972) for practical simplicity and computational efficiency, neglect important physical aspects of wave propagation through a soil deposit. In reality, the seismic wavefield and soil response is three-dimensional (3D), and heterogeneities are present within geologic deposits. While the use of these simplifications was required to perform site-response analyses 50 years ago, advancements in computational and modeling capabilities allow for extension to multi-dimensional analyses. This study focuses on the development of a practical approach for modeling soil heterogeneity and wave scattering in a 2D site-response analysis framework (which is conceptually extensible to 3D), based on nominally 1D site investigation information.

Numerous studies have compared 1D theoretical transfer functions (TTF) to empirical transfer functions (ETF) from vertical arrays and found that typical small-strain minimum damping ratios (D_{min}) from laboratory data underestimate the observed attenuation in ETFs, resulting in excessive amplification at modal frequencies in TTFs (e.g., Thompson et al., 2012; Kokusho, 2017; Afshari and Stewart, 2019; Afshari et al., 2019; Tao and Rathje, 2019). By increasing D_{min}, such studies have attempted to model the additional attenuation present from wave scattering, which is not present in dynamic soil laboratory tests nor SH1D analyses, via equivalent viscous damping.

Recent studies have shown the importance of accounting for uncertainty in shear wave velocity (V_S), and propagating this uncertainty through geotechnical site-response analysis and hazard analysis (Teague and Cox, 2016; Thompson et al., 2012; Griffiths et al., 2016a). Two approaches are typically used in practice to account for uncertainty in V_S for 1D site-response analysis: (1) developing a lower and upper bound profile by multiplying the median or "best estimate" profile by a constant factor (e.g., $\pm$ 20%), and (2) generating randomized V_S profiles that are probabilistically consistent with the "best estimate" profile using a statistical method such as that proposed by Toro (1995). These methods may produce V_S profiles that are inconsistent with the seismic site signature, producing site amplification significantly different than that observed at well-characterized and instrumented sites (Teague and Cox, 2016; Griffiths et al., 2016a). More recently, surface wave V_S testing methods have been applied to obtain an ensemble of V_S profiles that are all consistent with the site signature and produce more realistic site response (Griffiths et al., 2016b; Teague et al., 2018).

In contrast to SH1D site-response approaches that include V_S uncertainty (which still require the assumption of lateral homogeneity), modeling seismic site response in 2D or 3D with soil properties defined via spatially-correlated random fields can be used to explicitly account for spatial variability in the soil deposits, and appropriately model the scattering of seismic waves. Both of these aspects affect the seismic ground response, but are neglected in conventional 1D site-response analysis. Much of the work on wave scattering to date has been done in a seismological context, using heterogeneity length scales much larger (ranging from tens to thousands of kilometers) than those relevant to near-surface site response (Wu and Aki, 1988; Frankel and Clayton, 1986; Toksöz et al., 1988; Sato et al., 2012). Multiple studies

have evaluated the influence of 2D soil heterogeneity on site response in a viscoelastic or total-stress nonlinear context (Nour et al., 2003; Assimaki et al., 2003; Assimaki, 2004), while others have done so for liquefiable deposits including the effects of excess pore pressure generation (Popescu, 1995; Popescu et al., 1997; Lopez-Caballero and Modaressi-Farahmand-Razavi, 2010). Thompson et al. (2009) used 3D isotropic spatially-correlated random fields to predict site response at two downhole vertical array sites from the Kiban-Hyoshin network in Japan, and found better agreement between the TTF and ETF when soil heterogeneity was modelled. Most recently, El Haber et al. (2019) and Huang et al. (2019) performed parametric analyses to study the influence on ground-motion intensity measures (IMs), and their spatial distributions, from random field input parameters used in 2D site response of heterogeneous viscoelastic media.

This study expands on previous work by analyzing a larger dataset of random field model parameters, considering more IMs, and performing a statistically robust comparison between 1D and 2D heterogeneous V_S profiles. The objective is to assess the influence of soil heterogeneity, modelled via anisotropic spatially-correlated random fields, on site response and investigate the theoretical behavior of wave scattering in site response using an idealized viscoelastic single-layer soil profile. A comprehensive parametric analysis involving 5,400 2D model realizations was performed to determine the effects of random field parameters on the seismic ground response. For every 2D realization, randomized 1D ($1D_{Rand}$) V_S profiles are generated by extracting 1D vertical 'slices' from the 2D model at the location of ground surface recorder nodes. The influence of soil heterogeneities on IMs in a 1D and 2D context are compared to differentiate the effects from vertical heterogeneities on a 1D wave field, and 2D ground-motion phenomena such as wave scattering and surface wave generation. The results are normalized by, and compared to, those from a traditional deterministic 1D V_S analysis ($1D_{Det}$).

The organization of this paper is as follows. First, the Methods section describes features of the site-response models including model geometry, boundary conditions, and other modeling assumptions. The methodology for generating V_S perturbations using spatially correlated random fields, an explanation of the input excitation, and the definitions for IMs used to scrutinize results are also included in the Methods sections. The Results and Discussion section provides illustrative examples for individual realizations/permutations, an assessment of trends in median results for all parameter permutations, and a comparison between results of $1D_{Rand}$ and

2D analyses. As described in Section 3.5 section, four sub-appendices, that include additional results and discussion, are in Appendix B.

3.2 Methods

3.2.1 Site-Response Model

For the purpose of the sensitivity analysis, a simple model with a single viscoelastic soil layer over bedrock is considered. The upper layer has a constant median V_S, which is varied as part of the sensitivity study, and a compliant base is used to model a halfspace representative of soft rock (i.e., $V_{S,\,\text{halfspace}} = 760$ m/s). These simplifications are adopted so that the theoretical behavior is well understood before proceeding to more complex stratigraphy and constitutive response in future work.

Figure 3.1 schematically illustrates many of the features of the site-response model including boundary conditions, the Subdomain of Interest (SOI), location of surface recorder nodes, and an example of a 2D velocity model with anisotropic spatially correlated V_S perturbations. The soil layer above the halfspace is 50 m thick, and the total model width is 1,000 m (1,000 1-m-wide elements). To enforce the free-field 1D deterministic ($1D_{Det}$) response on the lateral boundaries of the model, a massive free-field column is included on each side. The columns are 10 elements (10 m) wide and 10,000 m thick in the out-of-plane direction (i.e., in OpenSees the mass of the elements is automatically scaled proportionally to the defined out-of-plane thickness). Each column is supported using periodic boundaries on the lateral extents of each column. As shown in Figure 3.1, the base is fully complaint in the horizontal and vertical directions by connecting each base node to two dashpots. Additionally, each base node has the appropriate vertical reaction force applied to it so that the model is freely suspended. This vertical compliance is required to prevent spurious reflection of vertical motion generated by wave scattering. These boundary conditions were selected based on a rigorous examination of different boundary conditions (for lateral boundaries and the base of the model). The results of this study and a thorough description of the adopted boundaries are in Appendix B.2.

Spatial variability in local V_S values in the 2D domain is applied to the upper soil layer based on a spatial random field model, as discussed in further detail in a subsequent subsection. The SOI is taken as the center 30% of the model domain (i.e., 300 m) to minimize boundary effects. Within the SOI, 10 equally spaced nodes at the ground surface are used to record results and compute site amplification relative to the base excitation. To further reduce the effects of the lateral boundaries: (i) a 100 m-wide zone of homogeneous soil is included at both lateral extents of the model (i.e., the zero-variance zone); and (ii) the soil V_S variability near the zero-variance zones exponentially reduces to zero.

2D viscoelastic site response can be performed in a number of wave propagation codes. OpenSees (McKenna, 2011) was chosen in this study so that complex nonlinear constitutive models can be used in future applications with ease. For computational efficiency, single-integration-point, 4-noded quadratic SSPquad elements (McGann et al., 2012) were used. Elements are sized in the vertical direction such that there are 8 nodes per wavelength at $f = 25$ Hz (based on the median V_S, i.e., $V_{S,0}$), however, a maximum element height of 1 m was prescribed so that when the vertical correlation length of the spatially correlated random field is as low as 3 m there is still sufficient discretization. It is acknowledged that the applied velocity perturbations may result in localized zones with V_S significantly lower than $V_{S,0}$. However, given that only 5 nodes are required to resolve a frequency, and that the highest frequency used for interpretation is 20 Hz (generally lower for the IMs considered) the mesh should be discretized enough to provide robust results within the frequency range considered.

With the large number of models generated for this study, parallelization of OpenSees and high-performance computing resources were instrumental in executing the analyses. To reduce computation time, each model realization was parallelized over 8 CPUs using OpenSeesSP. The initial goal was to perform the analyses in 3D, however, the presently poor scalability of OpenSees made it unfeasible to run so many models in 3D (de la Torre et al., 2019). Nonetheless, the sentiments offered in this paper are equally applicable to 3D implementations, which are seemingly inevitable for improving site-response predictive capability, and increasingly practiced as computational resources continue to increase exponentially.

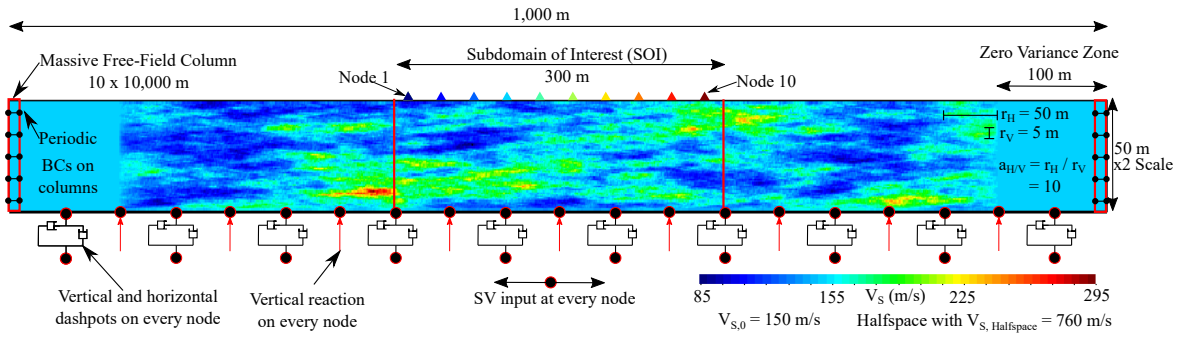

Figure 3.1: Schematic of site-response model illustrating a 2D shear wave velocity model with heterogeneity, boundary conditions, surface recorder node locations, the Subdomain of Interest (SOI), and zero variance zones. This example uses $V_{S,0} = 150$ m/s, $\sigma_{lnVs} = 0.175$, $r_H = 50$ m, and $a_{H/V} = 10$. All variables in figure are defined in Table 3.1. Note that the vertical scale is stretched by a factor of 2.

3.2.1.1 Extraction of $1D_{Rand}$ Profiles and 1D Site-Response Method

To differentiate between the effects of vertical heterogeneities in a 1D profile and 2D heterogeneities which have the ability to scatter waves, 1D randomized ($1D_{Rand}$) profiles are extracted from the 2D model. This is done by taking vertical 'slices' through the 2D model at the X-positions corresponding to the 10 SOI recorder nodes. The thickness of each 'layer' for the $1D_{Rand}$ profiles corresponds to the height of each element along the vertical slice. Because V_S is assigned to elements and not to the nodes, the V_S of each layer for the $1D_{Rand}$ profiles is taken as the average of the V_S from two adjacent elements that straddle a column of nodes directly beneath an SOI node.

For all 1D analyses (i.e., $1D_{Det}$ and $1D_{Rand}$) OpenSees is also used with the same modeling assumptions described for 2D analyses. Standard SH1D boundary conditions are implemented using periodic boundary conditions (i.e., equalDOF in OpenSees) on lateral boundary nodes, and base nodes are fixed in the vertical direction (e.g., McGann and Arduino, 2011).

3.2.2 Modeling Soil Heterogeneity via Spatially-Correlated Random Fields

Soil heterogeneity is modelled using anisotropic spatially-correlated random fields to perturb the model based on its mean V_S at a given location. The marginal distribution of V_S at a point is considered as lognormal, with a lognormal mean $\mu_{lnV_{S,0}}$ (or, equivalently, a median

$V_{S,0}$), and standard deviation σ_{lnVs}. The spatial correlation for random field generation is represented with an Exponential correlation function, which is a special case of the Matérn model (with shape parameter exponent, $\nu = 0.5$). Appendix B presents results considering Gaussian and Matérn (with $\nu = 0.2$) correlation functions (Figures B.9 and B.10). It was found that the Gaussian model was not as effective in scattering high-frequency waves, resulting in less attenuation of high frequencies and less generation of vertical motion. This is consistent with findings of Frankel and Clayton (1986) and Sato et al. (2012), who state that the Matérn model can more realistically model heterogeneities in natural deposits and scatter seismic waves. In this application, a negligible difference in IMs was observed between the Exponential model and the Matérn model with $\nu = 0.2$ (Figures B.11 and B.12).

Other input parameters of this model include the horizontal correlation length (r_H), and the anisotropy factor ($a_{H/V}$) to compute the vertical correlation length (r_V). The values of random field parameters used for the sensitivity study are based on previously published empirical values (Popescu, 1995; Toro, 1995; Fenton, 1999; Assimaki et al., 2003; Assimaki, 2004; Holzer et al., 2005; Wills and Clahan, 2006; Thompson et al., 2009; Bombasaro and Kasper, 2016) and listed in Table 3.1. Wills and Clahan (2006) computed σ_{lnVs} values for many soil deposits in the San Francisco Bay Area and found a range of 0.135 – 0.357 (excluding values proposed for rock deposits), while Holzer et al. (2005) propose average values of 0.16 for the entire geologic unit and up to 0.22 for a 2-m interval. Toro (1995) computed values of σ_{lnVs} ranging from 0.27 to 0.37 depedending on mean velocity of the profile (i.e., site class). An r_V of 5 m was calculated by Thompson et al. (2009) from suspension log V_S measurements at one site, and they assumed anisotropy factors of 10 – 20 to compute r_H. Popescu (1995) and Assimaki et al. (2003) used r_H and r_V ranges of approximately 12 – 16 m and 0.5 – 2.5 m, respectively, for generating heterogeneous V_S models for dynamic analysis based on CPT soundings at two sites (one with medium dense hydraulic fill and the other with a dense natural sand deposit). Also using CPT soundings, Fenton (1999) calculated vertical scales of fluctuation ranging from 0.22 – 13.8 m with an average of 2.3 m from 143 soundings in highly variable glacifluvial deltaic sands, gravels and silty-sands, and Lloret-Cabot et al. (2014) found vertical and horizontal fluctuation scales ranging from 0.4 – 0.44 m and 1.69 – 15.86 m, respectively, for three cross-sections of soundings in a sand fill. Bombasaro and Kasper (2016) compare their computed correlation lengths to those

from seven other studies and report values ranging from about 0.1 – 4 m vertically and 3 – 80 m horizontally in the literature for sedimentary soils. The selected values in Table 3.1 generally encompass these values. The r_H and $a_{H/V}$ values in Table 3.1 imply a range of r_V from 0.25 to 100 m. Given the height of the model considered (50 m) and the maximum element height (1 m), only permutations with $1 \leq r_V \leq 25$ m were analyzed. In total, 180 different analysis model permutations were considered from the Table 3.1 combinations.

The range of $V_{S,0}$ values was selected to represent a range of soft to very stiff soils. The fundamental frequencies, f_0, for the three median V_S profiles are 0.75, 1.25, and 2 Hz for $V_{S,0} =$ 150, 250 and 400 m/s, respectively. With a Poisson's ratio set to 0.25 for both the soil layer and underlying soft rock halfspace, the corresponding P-wave velocities are approximately 260, 433, and 693 m/s for $V_{S,0}$ = 150, 250 and 400 m/s, respectively, and 1,316 m/s for the halfspace with $V_{S,\text{ halfspace}} = 760$ m/s. Mass densities of 1.8 and 2.2 Mg/m^3 were assigned to the soil layer and halfspace, respectively.

Table 3.1: Random field parameters considered in parametric sensitivity study.

Parameter Name	Symbol	Values Used in Sensitivity Analysis
Median Shear Wave Velocity	$V_{S,0}$	150, 250, 400 m/s*
Standard Deviation of $ln(V_S)$	σ_{lnVs}	0.1, 0.175, 0.25, 0.325
Horizontal Correlation Length	r_H	5, 25, 50, 75, 100 m
Anisotropy Factor	$a_{H/V}$	1, 5, 10, 20
Vertical Correlation Lenth	r_V	1 – 25 m†

* These velocities result in nominal fundamental frequencies of $f_0 = 0.75$, 1.25, and 2 Hz, respectively.

† The implied range of r_V is 0.25–100 m, however, only permutations with $1 \leq r_V \leq 25$ m were analyzed.

3.2.3 Input Excitation

A simple Ricker wavelet (Ricker, 1943; Wang, 2015) with SV polarization is used as the input excitation, with velocity time series and acceleration Fourier amplitudes shown in Figure 3.2. The wavelet is a velocity pulse with $t_0 = 0.15$ s and $f_0 = 10$ Hz, and is applied as a force at every node of the model base simultaneously to simulate a vertically incident excitation.

The velocity pulse in Figure 3.2 is treated as an outcrop motion and is divided by 2 to obtain an equivalent incident motion. To fully capture the scattered wavefield, allow coda waves to attenuate, and enable accurate computation of Fourier Spectra and resulting transfer functions for frequencies as low as 0.5 Hz, the total duration of the input signal was extended to 15 s.

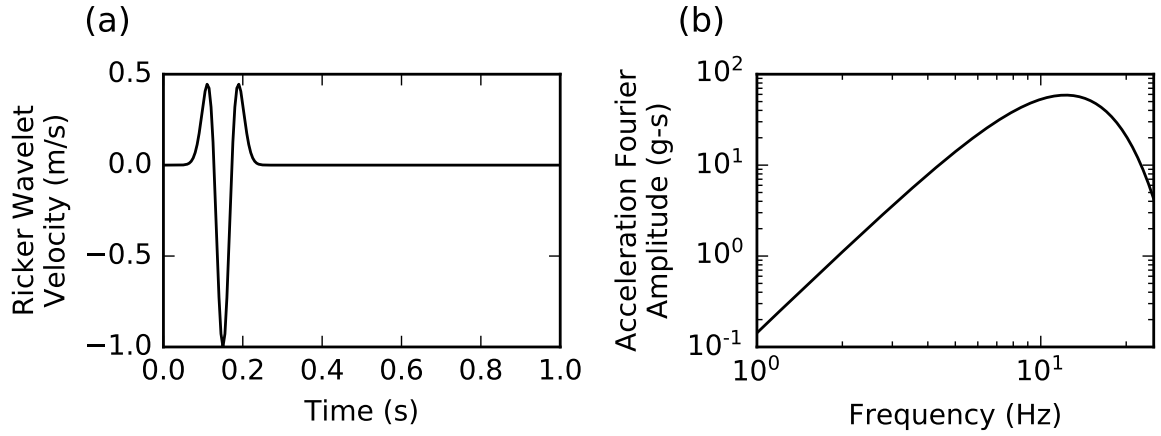

Figure 3.2: (a) Velocity time series (for $t = 0$ – 1.0 s) and (b) acceleration Fourier amplitudes of Ricker wavelet input excitation with $t_0 = 0.15$ *s* and $f_0 = 10$ Hz.

3.2.4 Intensity Measures (IMs)

To scrutinize results, assess the influence of random field input parameters on site response, and compare between 1D randomized ($1D_{Rand}$) and 2D methods for modeling soil heterogeneity, many ground-motion intensity measures (IMs) are computed from the acceleration time series extracted at ground surface recorder nodes. The following IMs are presented and discussed throughout this paper:

- TF: Outcrop transfer function, equal to the ratio of the Fourier Amplitude Spectrum (FAS) of surface motion to the FAS of the input excitation (Figure 3.2);
- f_0, f_1, f_2, and f_3: The first to the fourth modal frequencies of the soil column (i.e., the first four peaks in the transfer function). For 2D and $1D_{Rand}$ analyses these are computed as the local maxima between corresponding troughs of the $1D_{Det}$ TF;
- $AF(f_0)$: the amplification factor (i.e., the value of TF) at f_0;

- $SA(T_0)$: spectral acceleration at a vibration period of $T_0 = 1/f_0$;
- PGA: Peak ground acceleration;
- $I_{a,hor}$: Arias intensity of the horizontal component;
- $I_{a,vert}$: Arias intensity of the vertical component;
- IM^N: Any IM with superscript ^{N} implies normalization by the respective quantity from the 1D deterministic ($1D_{Det}$) analysis.

3.2.4.1 Differentiation Between Nodal, Realization Median, and Permutation Median IMs

In order to facilitate the interpretation of the results and differentiate between nodal, realization and permutation median IMs, the following notation is defined. The quantity computed at an individual node i (i.e., a "nodal IM") from V_S realization j is given the subscript i, j (e.g., $TF_{i,j}$ or $PGA_{i,j}$). The geometric mean of all 10 nodes for realization j is referred to as a "realization IM" and given the subscript j (e.g., $\overline{TF_j}$ or $\overline{PGA_j}$; Eq. 3.1). Finally, the geometric mean of all 300 nodes (i.e., 10 nodes from 30 realizations) is referred to as a permutation median, or simply the median IM and is written with an overline (e.g., $\overline{TF}$ or $\overline{PGA}$; Eq. 3.2). For any IM, $\overline{IM_j}$ and $\overline{IM}$ can be expressed mathematically as:

$$\overline{IM_j} = \exp\left[\frac{1}{N_{nodes}}\sum_{i=1}^{N_{nodes}} \ln\left(IM_{i,j}\right)\right] \tag{3.1}$$

$$\overline{IM} = \exp\left[\frac{1}{N_{realiz}}\sum_{j=1}^{N_{realiz}} \ln\left(\overline{IM_j}\right)\right] = \exp\left[\frac{1}{N_{realiz}N_{nodes}}\sum_{j=1}^{N_{realiz}}\sum_{i=1}^{N_{nodes}} \ln\left(IM_{i,j}\right)\right] \tag{3.2}$$

where N_{nodes} is the number of recorder nodes for a given realization (i.e., 10 nodes), and N_{realiz} is the number of realizations for a given parameter permutation (i.e., 30 realizations).

3.2.4.2 Standard Deviations of IMs

In addition to the median quantities described above, three standard deviations are defined for each IM. The within-realization standard deviation, $\sigma_{W,j}$ (Eq. 3.3), is the natural log standard deviation of the 10 nodal IMs (i.e, $IM_{i,j}$) for realization j and reflects the variation in IM due to spatial variability (i.e., $\sigma_{W,j} = 0$ for a 1D model). The between-realization standard deviation, σ_B (Eq. 3.4), is the natural log standard deviation of the 30 realization IMs (i.e., IM_j) for a given parameter permutation. The total standard deviation, σ_T (Eq. 3.5), is the natural log standard deviation of all 300 $IM_{i,j}$ for a given permutation. These can be expressed mathematically as follows:

$$\sigma_{W,j} = \sqrt{\frac{1}{N_{nodes}} \sum_{i=1}^{N_{nodes}} (\ln IM_{i,j} - \ln \overline{IM_j})^2} \tag{3.3}$$

$$\sigma_B = \sqrt{\frac{1}{N_{realiz}} \sum_{j=1}^{N_{realiz.}} (\ln \overline{IM_j} - \ln \overline{IM})^2} \tag{3.4}$$

$$\sigma_T = \sqrt{\frac{1}{N_{realiz} N_{nodes}} \sum_{j=1}^{N_{realiz.}} \sum_{i=1}^{N_{nodes}} (\ln IM_{i,j} - \ln \overline{IM})^2} \tag{3.5}$$

Additionally, the mean within-realization standard deviation, σ_W, is the mean of all realization $\sigma_{W,j}$ computed as:

$$\sigma_W = \frac{1}{N_{realiz}} \sum_{j=1}^{N_{realiz}} \sigma_{W,j} \tag{3.6}$$

The standard error in the mean transfer function is proportional to $\sigma_T/\sqrt{N}$. With $N = 300$ (i.e., 10 nodes and 30 realizations), the standard error in the resulting mean is $\approx \sigma_T/17$ which is considered sufficiently small to enable robust inferences from the results presented here.

3.2.4.3 Convergence of IMs

In order to generate perturbed V_S models and site-response IMs that are statistically representative of the distributional properties, the model domain must not only be large relative to the correlation lengths of the random field, but many realizations of the V_S model must be generated. A convergence study using bootstrap sampling was performed to test how many realizations are required for site-response IMs to converge. It was found that with 30 realizations of the random field, mean and standard deviation values of IMs had sufficiently converged to reduce the sample-size error to an acceptably low value. The results of this convergence study are summarized in Appendix B.4. Given the 180 parameter combinations from Table 1, and 30 realizations for each parameter combination, a total of 5,400 simulations were performed in the results presented herein.

3.3 Results and Discussion

The results in this section are based on the acceleration time series extracted at ground surface nodes. In the first subsection (Section 3.3.1), an initial assessment is carried out on results for individual realizations to build an intuition for how intensity measures (IMs) are computed at individual nodes and illustrate the influence of spatial variability and wave scattering on ground surface accelerations. Next, in Section 3.3.2, all nodal and realization transfer functions for selected permutations are shown, and trends in the medians and standard deviations are discussed. Then, in Section 3.3.3, permutation median IMs (i.e., $\overline{IM}$) from all 2D models are analyzed using a dimensionless parameter $k_0 r_V$ (the wave number of the fundamental mode frequency times the vertical correlation length) to assess the influence of various random field input parameters on site-response. This dimensionless parameter allows for all permutations to be compared directly independent of $V_{S,0}$ and r_V. Finally, in Section 3.3.4, median IMs from 2D and $1D_{Rand}$ are directly compared to distinguish between the effects of 1D vertical heterogeneities and averaging across many nodes and realizations, and those from wave scattering and 2D ground-motion phenomena.

3.3.1 Illustrative Examples for Individual Realizations

To provide intuition for how the ground motion is influenced by local heterogeneity and to further illustrate the utilized numerical model configuration, Figure 3.3 plots acceleration time series at ground surface nodes normalized by peak acceleration of the input excitation (i.e., normalized acceleration) for $V_{S,0} = 150$ (left) and 400 m/s (right). The top panels are for $\sigma_{lnVs} = 0.175$ and the bottom panels for $\sigma_{lnVs} = 0.325$. This figure illustrates the local variations in V_S and their subsequent effect on the wavefield, particularly scattered body waves and surface waves. Areas in which V_S is locally lower have later arrivals of the wave packet, and conversely areas with higher V_S have earlier arrivals. This causes lateral variations in stress and strain between nearby nodes leading to scattering of the original wavelet. As identified in the top right panel, surface waves can be seen travelling across the surface of the model which are generated from the refraction of waves to non-vertical incidence at the ground surface, and the presence of localized areas of lower or higher stiffness (i.e., V_S).

The effects of increasing σ_{lnVs} are also visible in Figure 3.3. Increasing σ_{lnVs} results in stronger soil heterogeneity, and therefore more wave scattering, such that in the $\sigma_{lnVs} = 0.325$ cases (i.e., bottom subplots) the second pulse arrival (i.e., the first reflection) is practically impossible to observe visibly amongst the scattered waves from the first arrivals.

As shown in Figure 3.3, spatial variation leads to different ground-motion outputs across the ground surface of the model. While this illustration is useful to gain an overall understanding/intuition of the problem and its mechanisms, all subsequent analyses in this paper use only the results from 10 surface nodes within the SOI. Figure 3.4 demonstrates how results are extracted at 10 surface nodes for calculating transfer functions. It plots accelerations and transfer functions at SOI nodes from one of the models in Figure 3.3 for 2D and $1D_{Rand}$ results. V_S profiles that are directly extracted from the 2D model at the location of surface recorder nodes are also provided as an example of how these $1D_{Rand}$ profiles are generated. It is evident that the soil heterogeneity causes spatial variability in acceleration time series, and therefore, in nodal transfer functions at the recorder nodes.

In the time domain (top panel of Figure 3.4), it is possible to see differences in arrival times

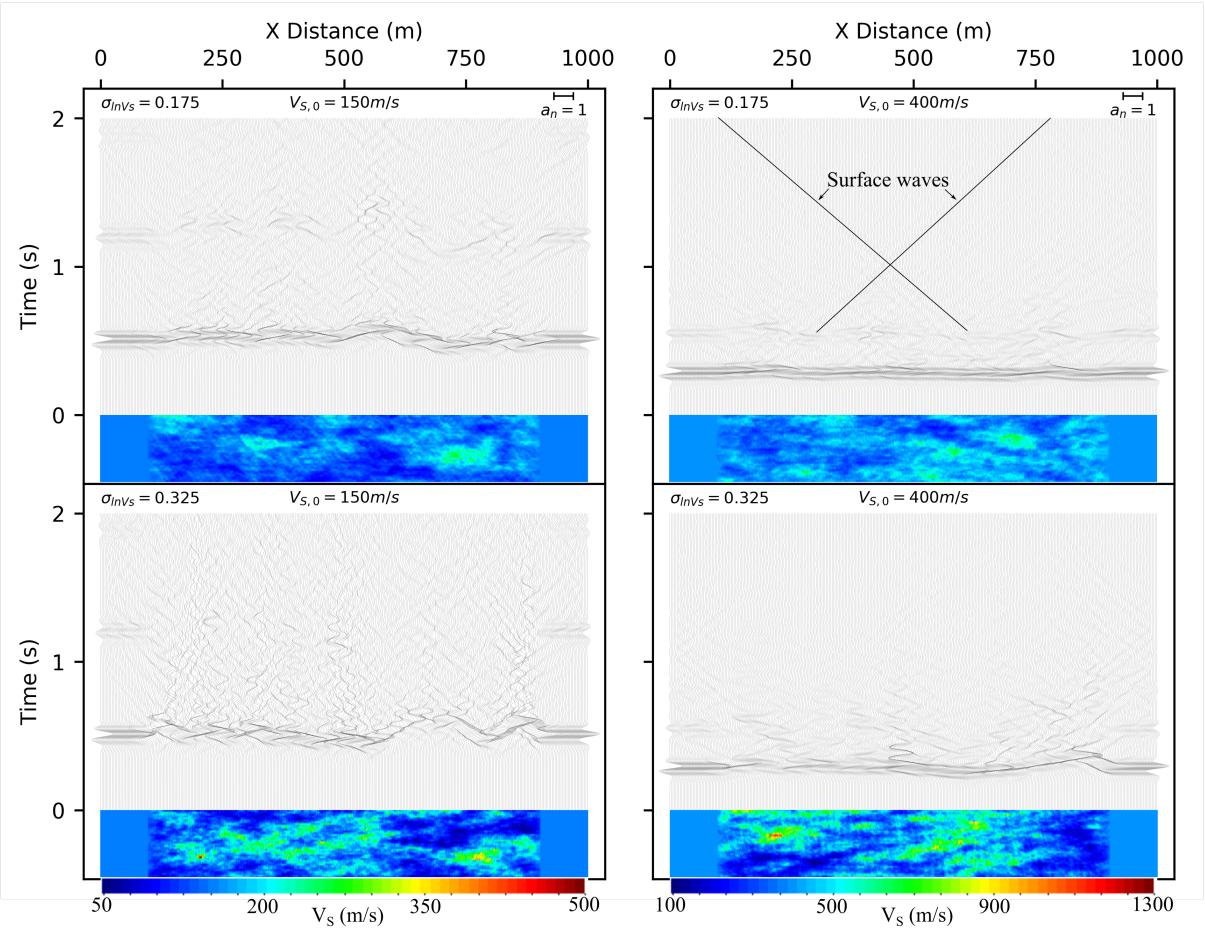

Figure 3.3: Acceleration time series at surface nodes normalized by peak acceleration of the input excitation for Realization 1 of permutations with $V_{S,0} = 150$ (left) and 400 m/s (right). The top and bottom panels are for $\sigma_{lnVs} = 0.175$ and 0.325, respectively. For all cases, $r_H = 50$ m and $a_{H/V} = 10$. The insets show respective V_S models that are stretched by a factor of 3 in the vertical direction for visual illustration. Note that V_S color scales are different between models with $V_{S,0} = 150$ and 400 m/s . Acceleration time series are extracted at 1 in every 4 surface nodes.

of the original and reflected wavelets between different nodes and the $1D_{Det}$ results. The time series from the 2D and $1D_{Rand}$ analyses, with the presence heterogeneities, are significantly more complex than those from the $1D_{Det}$ analysis. While the first arrivals of 2D and $1D_{Rand}$ generally display equal arrival times and similar amplitude, there are clear differences between the two methods, particularly in the phase and amplitude of later arrivals and coda waves. From the first-arrival times and $1D_{Rand}$ V_S profiles it is evident that the V_S profiles at the locations of Nodes 7–9 are, on average, slower than the $1D_{Det}$ profile. This lower average V_S is also visible in $1D_{Rand}$ transfer functions with a notable shift in the fundamental frequency (f_0) to lower

frequencies. Interestingly, this shift does not occur in 2D analyses suggesting the the system "responds as a whole" and the fundamental frequency is less influenced by local heterogeneities, which primarily affect high-frequency response.

Looking at nodal transfer functions in Figure 3.4, it is evident that the frequency-to-frequency correlation is much higher for the $1D_{Det}$ and $1D_{Rand}$ cases than the 2D. The ground-motion amplification is spread over wider frequency bands, particularly at high frequencies, unlike $1D_{Det}$ TFs with very discrete and narrow-banded amplification peaks. The smoothing of peaks and troughs from averaging of the transfer functions results in an even broader distribution of amplification across frequencies ($\overline{TF_j}$; grey lines in Figure 3.4).

Figure 3.5 plots normalized nodal IMs for the $V_{S,0} = 150$ m/s realizations in Figure 3.3. These figures show the variability in $IM_{i,j}$ across the width of the model and realization medians for both 2D and $1D_{Rand}$ analyses. Within-realization standard deviations for individual realizations ($\sigma_{W,j}$) are given in the top right corner of each panel. While some trends are maintained between 2D and $1D_{Rand}$ (i.e., the above average values of PGA^N, $SA(T_0)^N$, $I^N_{a,hor}$ at Node 5) it is clear that there are differences between the two methods which may be attributed to 2D wave propagation phenomena. Conclusions cannot be drawn from a single realization, however, one interesting feature that is visible in these results, and is true on average across all results, is that the within-realization standard deviation of f_0 is lower for the 2D analyses, as was discussed above in regards to Figure 3.4. As the strength of the heterogeneity increase, the variability in $IM_{i,j}$ across the ground surface increases, as indicated by the higher $\sigma_{W,j}$ values for $\sigma_{lnVs} = 0.325$ (right panels).

The nodal IMs in Figure 3.5 show that high variability in V_S results in the potential for significant localized reductions and increases in certain intensity measures relative to a conventional $1D_{Det}$ analyses. For the given $\sigma_{lnVs} = 0.325$ example, $SA(T_0)$ and $I_{a,hor}$ are more than 2 times greater than the $1D_{Det}$ case at node 5 (i.e., $SA(T_0)^N$ and $I^N_{a,hor} > 2$) and less than half of the $1D_{Det}$ value at Node 10.

As indicated in Equation 3.2, all nodes are treated equally, and results are averaged across all nodes and realizations, rather than treating each SOI node independently. This approach is reasonable because, as shown in Figure B.14 of Appendix B.5, no systematic bias was observed

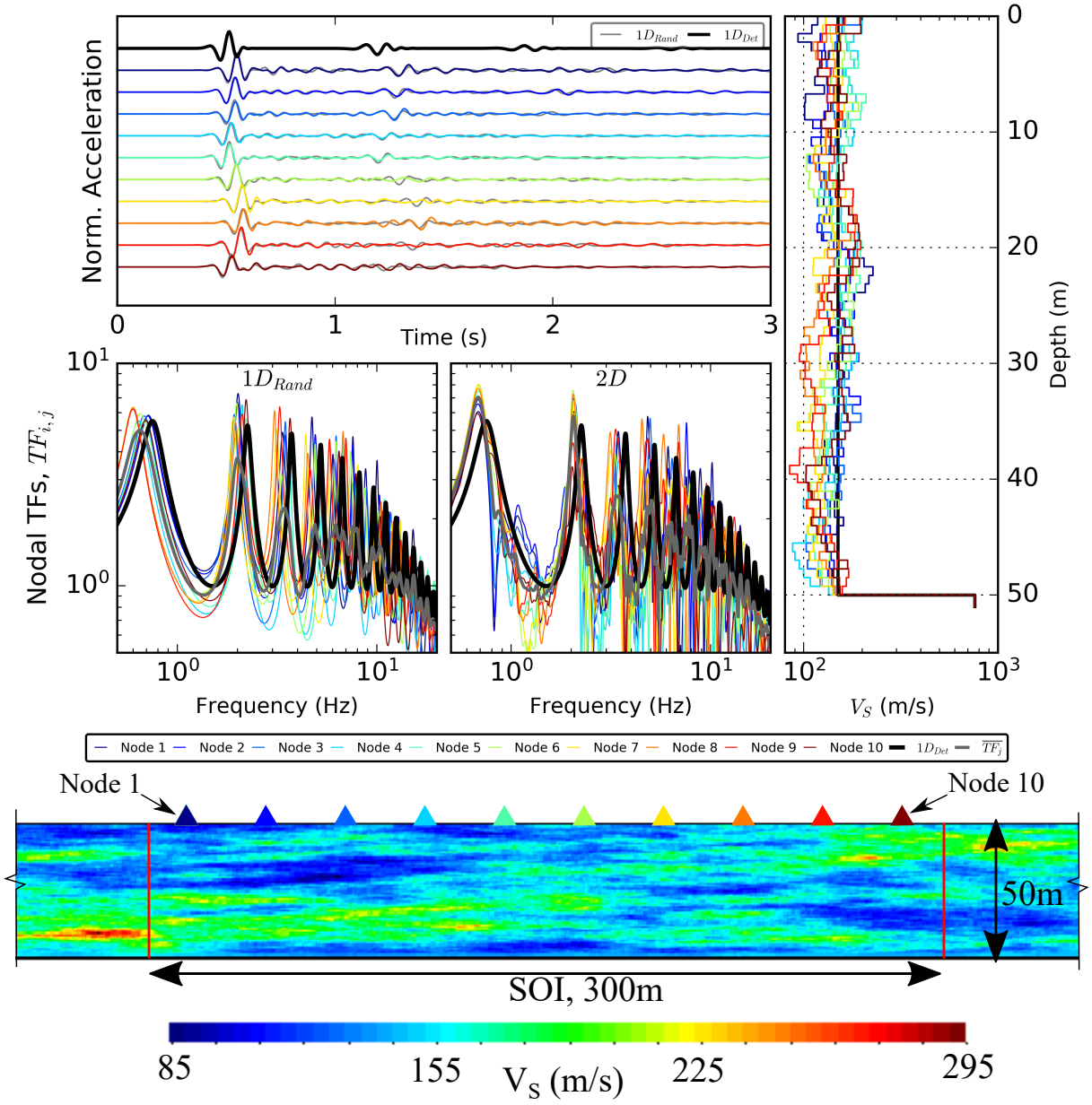

Figure 3.4: Comparison of nodal normalized acceleration time series and transfer functions between 2D and $1D_{Rand}$ models for Realization 1 of the permutation with $V_{S,0} = 150$ m/s, $\sigma_{lnVs} = 0.175$, $r_H = 50$ m and $a_{H/V} = 10$. The 2D velocity model and $1D_{Rand}$ velocity profiles extracted at the location of recorder nodes are also provided as reference.

at different nodes across all realizations. This figure compares, for two permutations, permutation median IMs to median IMs of individual nodes and shows that the median value of each IM is not dependent on the node position.

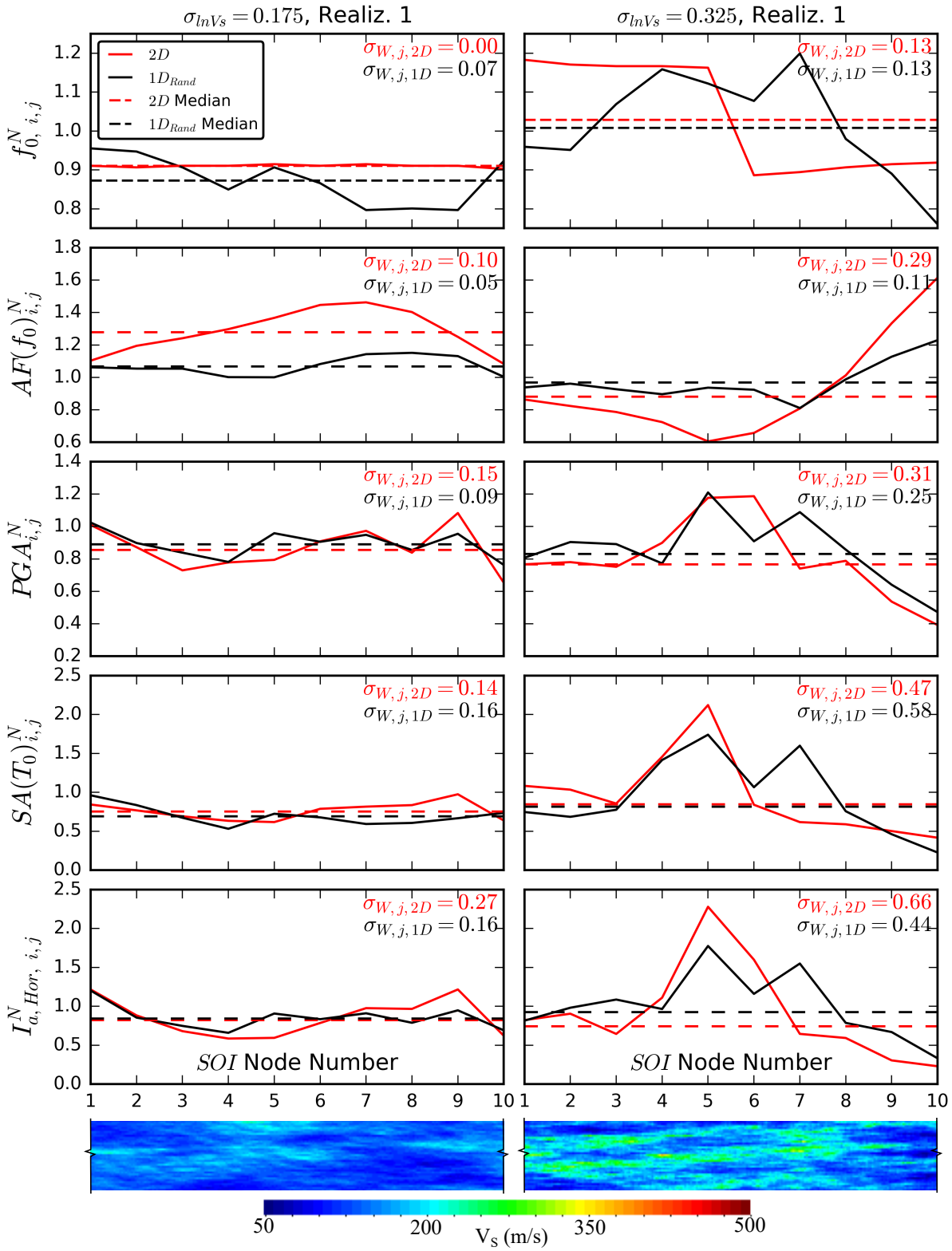

Figure 3.5: Comparison of normalized nodal IMs for 2D and $1D_{Rand}$ analyses for two realizations with $\sigma_{lnVs} = 0.175$ (left) and 0.325 (right). As in Figure 3.3, $V_{S,0} = 150$ m/s, $r_H = 50$ m and $a_{H/V} = 10$. The bottom inserts show the SOI of V_S models for these realizations.

3.3.2 Transfer Functions

Extending from previous illustrative examples, Figure 3.6 illustrates the computation of realization and permutation medians, and standard deviations of transfer functions represented by Equations 3.1–3.5. The top panels show all nodal transfer functions ($TF_{i,j}$) and within-realization stardard deviation ($\sigma_{W,j}$) for realization 5 with σ_{lnVs} increasing from 0.175 (left) to 0.325 (right). The middle panels show all 300 $TF_{i,j}$ from the 30 realizations and the total standard deviation (σ_T), and the bottom panels show all 30 realization median transfer functions ($\overline{TF_j}$) with the between-realization standard deviation (σ_B). Clearly, as σ_{lnVs} increases, $\sigma_{W,j}$, σ_B and σ_T increase, which is expected based on prior discussion.

Median $\overline{TF_j}$ and $\overline{TF}$ for $1D_{Rand}$ are also plotted over 2D results. The $1D_{Rand}$ analysis is able to replicate median transfer functions for frequencies up to about 10 Hz. At higher frequencies, the 2D analysis experiences higher effective damping due to scattering attenuation which is not present in $1D_{Rand}$. This effect is especially pronounced when $\sigma_{lnVs} = 0.325$ because more scattering occurs as was shown previously in Figure 3.3. The frequency dependent values of $\sigma_{W,j}$, σ_B, and σ_T corresponding to the transfer functions in Figure 3.6 are explicitly plotted in Figure 3.7. Here, is it evident that at $f > 10$ Hz there is more variability in $TF_{i,j}$ (i.e., higher $\sigma_{W,j}$ and σ_T) for 2D analyses which results in the decrease of the median observed in Figure 3.6.

Of the three different standard deviations in Figure 3.6, σ_B is the smallest because it is a standard deviation of realization medians which are already smoothed due to averaging, while σ_W and σ_T are standard deviations of nodal transfer functions. The total standard deviation is larger than the median within-realization standard deviation suggesting that there is more correlation in the transfer functions between nodes of the same realization than between nodes of different realizations. While σ_B is fairly constant as a function of frequency, σ_W and σ_T increase up to about the fourth mode of vibration (~ 5 Hz for $V_{S,0} = 150$ m/s) and then begin to drop slightly. This decrease in standard deviation with increasing frequency is more pronounced for the $1D_{Rand}$ case than for the 2D case, especially for higher values of σ_{lnVs}.

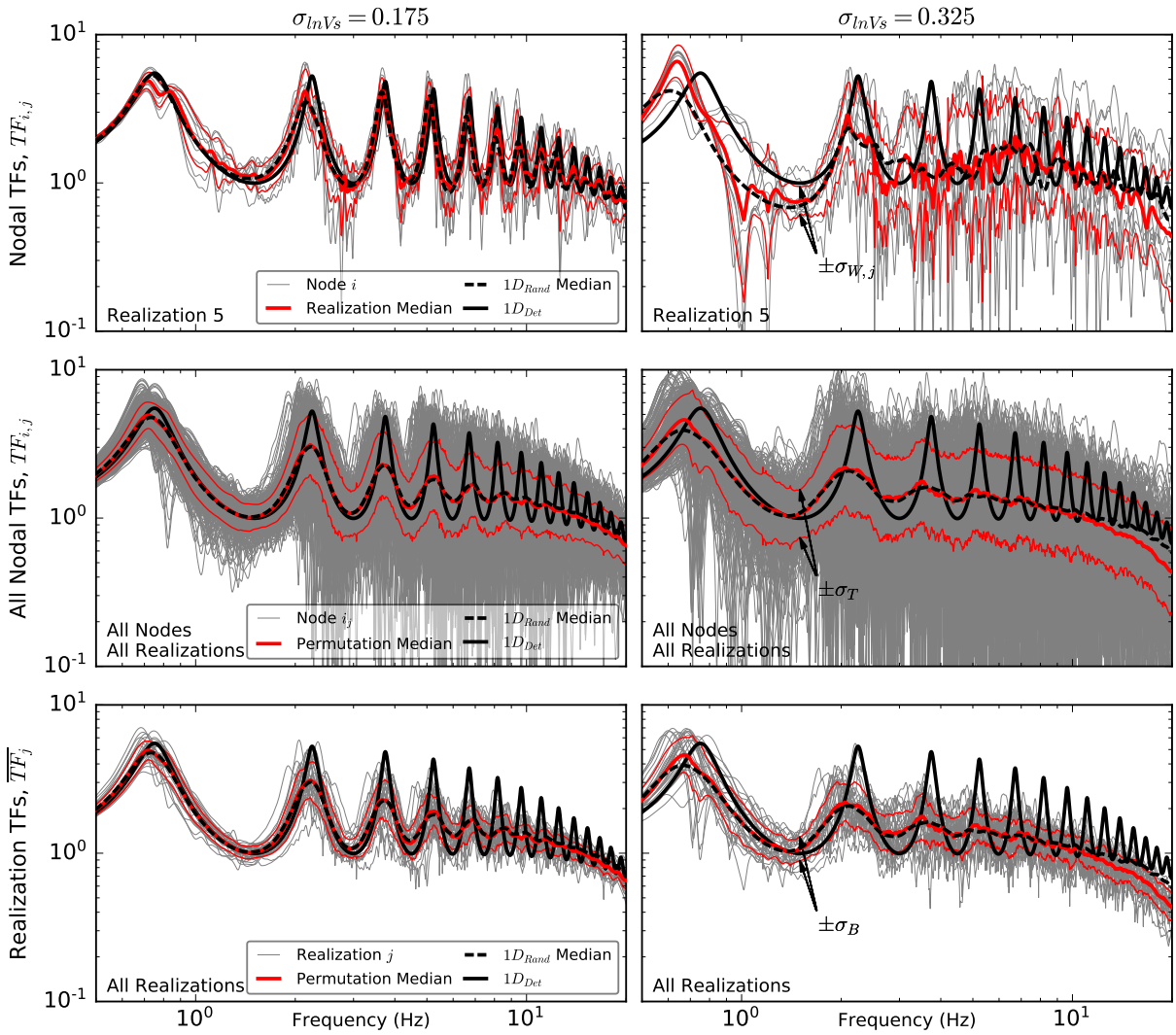

Figure 3.6: Nodal, realization median, and permutation median transfer functions with corresponding standard deviations for permutations with $\sigma_{lnVs} = 0.175$ (left) and 0.325 (right). Individual results are for 2D analysis but median $1D_{Rand}$ results are provided for comparison. As in Figures 3.3–3.5, $V_{S,0} = 150$ m/s, $r_H = 50$ m, and $a_{H/V} = 10$.

3.3.3 Evaluation of Median IMs for All Permutations

Results from all permutations are now aggregated and evaluated using a dimensionless parameter kr_V (often referred to as ka in seismological literature) to assess the influence of random field input parameters on median site-response IMs. First, an example for a suite of permutation median transfer functions ($\overline{TF}$) and total standard deviations (σ_T) in Figure 3.8 shows general trends with increasing σ_{lnVs}. As σ_{lnVs} increases, from 0.1 to 0.325, there is greater reduction in peak-to-trough ratios. This occurs for two reasons: (1) the models with higher variance in the V_S

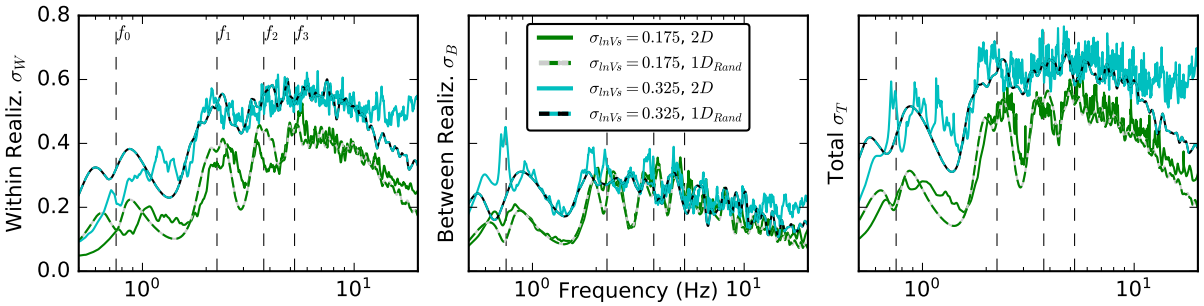

Figure 3.7: Comparison of mean within-realization, between realization and total standard deviations between 2D and $1D_{Rand}$ analyses for transfer functions in Figure 3.6. $V_{S,0} = 150$ m/s, $r_H = 50$ m, and $a_{H/V} = 10$. Dashed vertical lines reflect the first four modal frequencies from the $1D_{Det}$ profile (i.e, $f_0 - f_3$).

random field (i.e., stronger heterogeneity) experience stronger scattering of waves, resulting in more redistribution of energy across wider frequency bands at an individual node, and (2) there is greater node-to-node (within-realization) and realization-to-realization (between-realization) variability resulting in more averaging or smoothing of the computed $\overline{TF}$. The effects of (1) are seen in ground surface acceleration time series of Figure 3.3 and in nodal transfer functions of Figure 3.6. The effects of (2) are visible in Figure 3.6 in which nodal and realization transfer functions are much more variable for a higher value of σ_{lnVs}. Figure 3.8 quantifies this effect showing greater values of σ_T with increasing σ_{lnVs}. It is also evident that there is greater variability in the transfer functions at $1D_{Det}$ fundamental modes (peaks), and less variability at troughs.

In addition to greater reductions in peak-to-trough ratios, as σ_{lnVs} increases there is a net reduction in $\overline{TF}$ (i.e., higher equivalent damping that results in reduced amplification factors) at high frequencies relative to the $1D_{Det}$ analysis. It is worth noting that while $\sigma_{lnVs} = 0.1$ causes significant reduction in the peak-to-trough ratios, there is negligible reduction in the median amplification at high frequencies relative to the $1D_{Det}$ TF. On the contrary, for higher values of σ_{lnVs} the median amplification at high frequencies decreases with increasing σ_{lnVs}. As shown in Figure B.15 and discussed previously with regards to Figure 3.8, this effect is much more prominent for 2D analyses that are influenced by scattering attenuation unlike $1D_{Rand}$.

The corresponding medians and standard deviations of transfer functions for $V_{S,0} = 250$ and 400 m/s are in Appendix B.5 Figure B.15. These results show similar trends as $V_{S,0} =$ 150 m/s, however, they occur at relatively higher frequencies as a result of the increase in

fundamental frequency of the deposit. This illustrates that the effects of soil heterogeneities are dependent not only on the characteristics of the random field but on the relationship between the wavelength and the length scales of the heterogeneities. For this reason it is useful to evaluate results in terms of the dimensionless quantity $k_0 r_V$ so that results can be directly compared independently of the median velocity. This assessment in the frequency domain, as in Figure B.15, does however highlight that within the frequency range of interest for most engineering applications, lower velocity soil profiles will be influenced most significantly by the presence of heterogeneities.

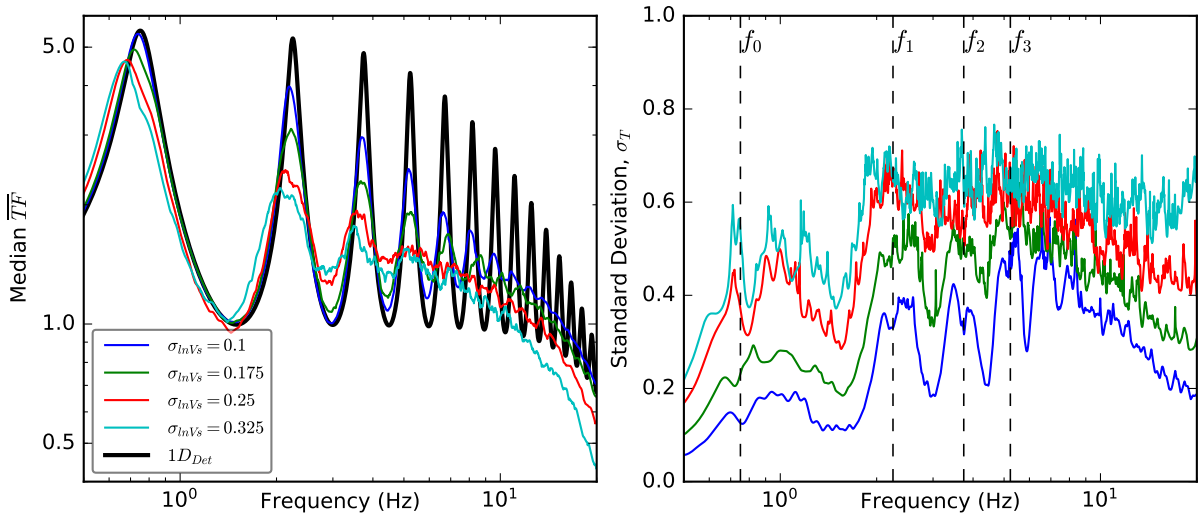

Figure 3.8: Comparison of median transfer functions and total standard deviations for various σ_{lnVs} values for all permutations with $V_{S,0} = 150$ m/s, $r_H = 50$ m, and $a_{H/V} = 10$. Each curve represents the median and standard deviation, respectively, of 300 transfer functions (i.e., 10 nodal transfer functions from 30 realizations).

As it is not feasible to concisely present transfer functions of all 180 permutations in this paper, other IMs are thus used to summarize the results and assess the influence of soil heterogeneity on site-response. Figure 3.9 plots normalized (by $1D_{Det}$) median IMs as a function of $k_0 r_V$ with corresponding total standard deviations in Figure 3.10. The advantages of plotting $\overline{IM}^N$ as a function of $k_0 r_V$ is that results for all $V_{S,0}$ collapse on top of each other as the effect of wavelength is removed, and that the influence of the vertical correlation length is explicitly shown. The normalized IMs and σ_T in Figure 3.9 and 3.10 are color-coded by σ_{lnVs}, which clearly show a dependence on the strength of the heterogeneity for all IMs.

The stronger scattering and increased ground-motion variability with increasing σ_{lnVs} leads

to a significant decrease in median PGA, $SA(T_0)$, and $I_{a,hor}$. From Figure 3.9 it is evident that these three IM^N reduce from approximately 1 (i.e., equal to the respective $1D_{Det}$ value) at a low value of $\sigma_{lnVs} = 0.1$, to 0.6 – 0.8 at a high value of $\sigma_{lnVs} = 0.325$. This reduction of 20 – 40% in the median values from 2D analyses comes with a significant increase in the standard deviations (Figure 3.10). With the decrease in PGA and I_a of the horizontal component as the strength of heterogeneity increases, comes an increase in $I_{a,vert}$. Higher σ_{lnVs} causes waves to be more refracted from vertical incidence resulting in higher energy in the vertical component; This phenomenon, along with the scattering in time of the wave packet's arrival at the ground surface, contribute to the reduction in intensity measures of the horizontal component. f_0 and $AF(f_0)$ are less influenced by the heterogeneities and therefore less sensitive to σ_{lnVs}. f_0 is generally within 5% of the $1D_{Det}$ value, however f_0^N is as low as 0.9 for $\sigma_{lnVs} = 0.325$ at low values of r_V. A slight increase, up to about 1.2 is observed in $AF(f_0)^N$ for the highest value of σ_{lnVs}. It should be noted that the median $AF(f_0)$ is not necessarily representative of the amplification factor of the median $\overline{TF}$ as it is computed as the median of all individual $AF(f_0)_{i,j}$ which will likely be higher than that of $\overline{TF}$. The minimal influence to f_0 and $AF(f_0)$ is likely because the length scales of the heterogeneities are relatively small compared to the fundamental wavelength of these shallow profiles (i.e., $k_0 r_V << 1$). On the contrary, PGA, and $I_{a,hor}$ are controlled by higher frequencies with wavelengths closer to r_V. The fact that $SA(T_0)$ responds similarly to PGA and $I_{a,hor}$ suggests that it is controlled by a wide range of frequencies, and not just $f = f_0$, which is consistent with findings in Bora et al. (2016). It is well understood that the strongest scattering occurs at wavelengths equal to the length scale of heterogeneities (i.e., kr_V [or ka] $= 1$; Frankel and Clayton, 1986; Sato et al., 2012). The effect of wavelength (which is also discussed above with reference to transfer functions in Figure B.15) is visible in Figure B.16, in which permutations with lower $V_{S,0}$, on average, have a greater reductions in PGA, $SA(T_0)$, and $I_{a,hor}$ because the corresponding wavelength of high frequencies will be shorter.

The standard deviations for all IMs (Figure 3.10) generally increase with increasing length scale of the heterogeneities (i.e., increasing $k_0 r_V$). This trend is particularly pronounced for $SA(T_0)$, f_0, and $AF(f_0)$. As discussed above, these are IMs that are influenced or controlled by lower frequencies (longer wavelengths) and therefore more variability would be expected

as the r_V increases. The higher frequency IMs, such as *PGA* and I_a, are less sensitive to r_V as they already experience significant variability even at the smallest length scales analyzed ($k_0 r_V < 0.01$). σ_T for f_0 and $AF(f_0)$ increases from about 0 (for all σ_{lnVs}) at small length scales to 0.25 and 0.4, respectively, at larger length scales, while the maximum values at the largest r_V and σ_{lnVs} for $SA(T_0)$, *PGA*, $I_{a,hor}$, and $I_{a,vert}$ are 0.71, 0.49, 0.75, and 0.78, respectively.

The interested reader is directed to Figures B.17 and B.18 in Appendix B.5, which directly compare the within-realization standard deviation to the between-realization and total standard deviations to analyze how some of the IMs are correlated within and between realizations.

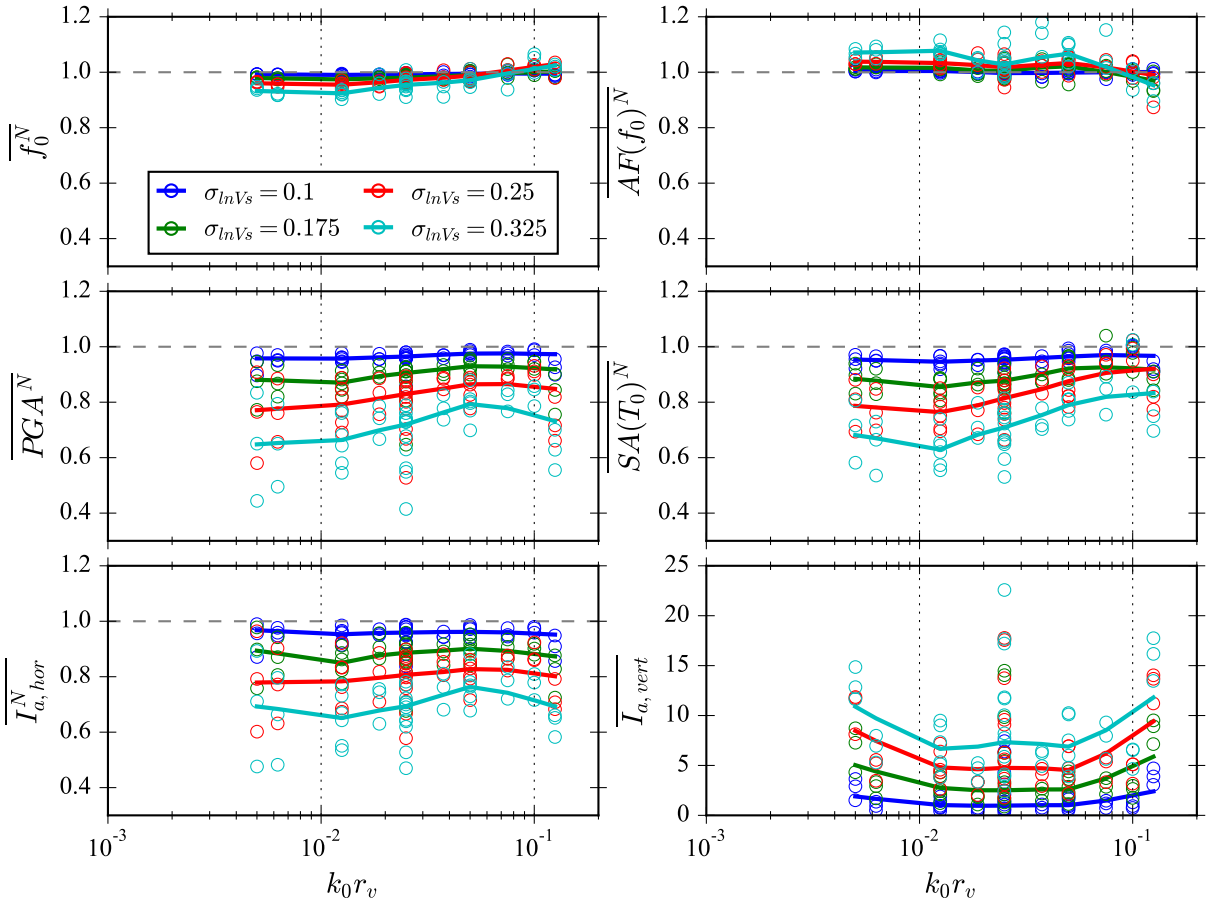

Figure 3.9: Normalized median IMs for all permutations plotted as a function of $k_0 r_V$ and color-coded by σ_{lnVs}. Note that $I_{a,vert}$ is not normalized as there is no vertical component to $1D_{Det}$ analysis.

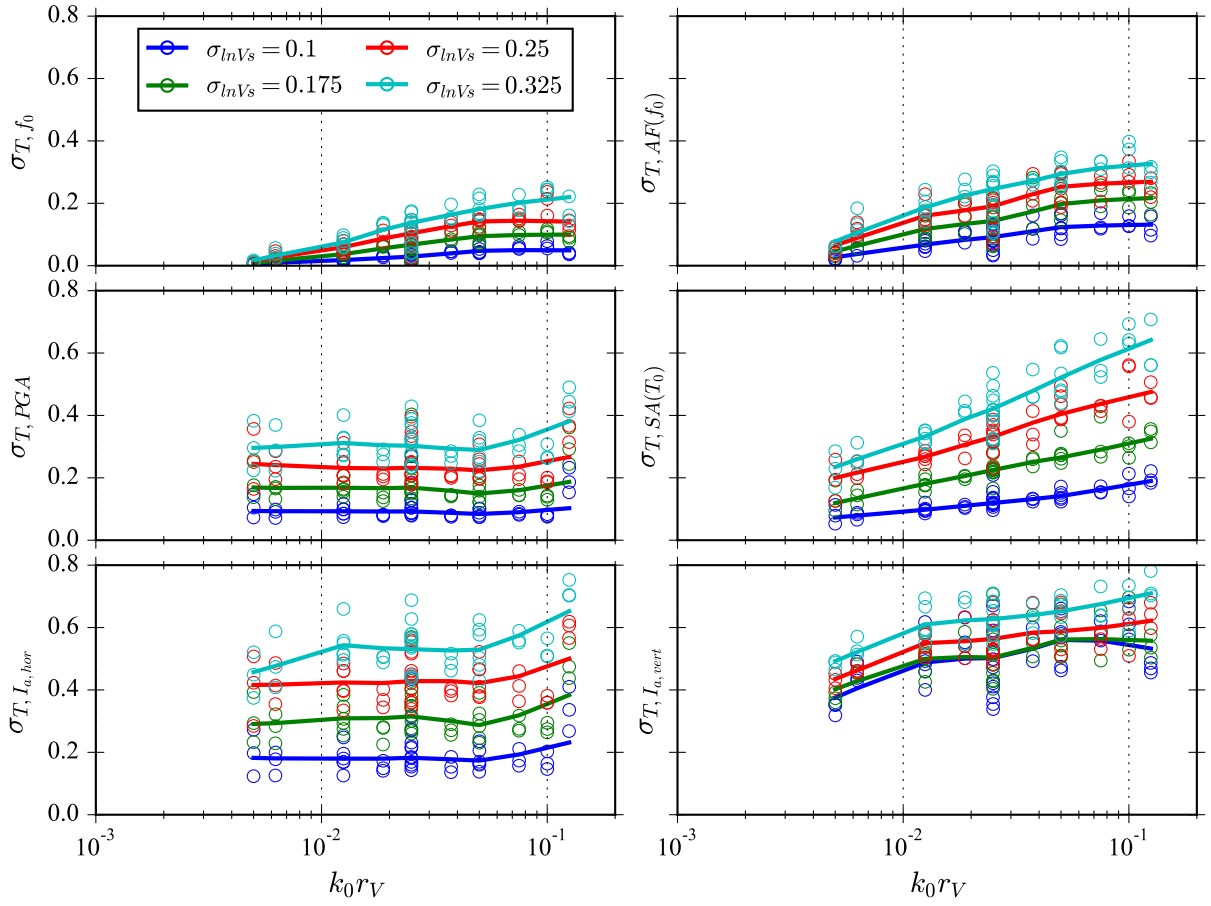

Figure 3.10: Total standard deviations of IMs for all permutations plotted as a function of $k_0 r_V$ and color-coded by σ_{lnVs}.

3.3.4 Comparison of $1D_{Rand}$ and 2D results for All Permutations

It was previously shown in Figure 3.6 that, for two example permutations, $1D_{Rand}$ could generally match the median TF up to about 10 Hz, where the 2D $\overline{TF}$ began to decrease more rapidly due to higher scattering attenuation not present in a $1D$ analysis. In order to fully evaluate the performance of the $1D_{Rand}$ models it is important to look at other IMs and their standard deviations. Figures 3.11 and 3.12 plot median IMs and total standard deviations, respectively, for 2D analyses versus the corresponding value for $1D_{Rand}$. The same comparison for within-realization standard deviations is in Figure B.19. Unsurprisingly, given the match of $\overline{TF}$ observed previously, f_0^N, f_3^N, and $AF(f_0)^N$ are comparable between 2D and $1D_{Rand}$ analyses and plot near the 1:1 line, although, on average, $AF(f_0)$ is approximately 5% higher for $1D_{Rand}$ analyses. $SA(T_0)$ also falls on the 1:1 line. For both PGA and $I_{a,hor}$, the $1D_{Rand}$ analy-

sis is consistently higher, which is likely due to the refraction of horizontal energy to generate vertical motion and the scattering in time of the wave packet as was discussed in the previous subsection in reference to Figure 3.9.

The total standard deviation in f_0 and f_3 is generally higher in the $1D_{Rand}$ cases, and can be as high as 2–3 times higher than that of the 2D analysis for some permutations (Figure 3.12). This is especially pronounced for within-realization standard deviation of f_0 in Figure B.19 in which many of the permutations fall on or above the 2:1. This effect was observed previously in Figure 3.4, in which a much higher correlation in f_0 was observed between nodes of the same realization from the 2D model than from individual randomized $1D$ V_S profiles which resulted in a significant shift of f_0 at certain locations. On the contrary, the standard deviation in the amplification at f_0 ($\sigma_{T,AF(f_0)}$) is significantly lower for $1D_{Rand}$ which is also visible in nodal $TF_{i,j}$ of Figure 3.4. In $1D_{Rand}$ models, $AF(f_0)$ is much more constant across different $1D$ realizations, whereas 2D ground-motion phenomena cause greater amplification or deamplification at f_0 relative to $1D_{Det}$. For $\sigma_{T,SA(T_0)}$ the results are similar and plot near the 1:1 line, however for $\sigma_{T,PGA}$ and $\sigma_{T,I_{a,hor}}$ the $1D_{Rand}$ values are significantly lower with most of the permutations falling between the 1:1 and 2:1 lines, and some even lower. As discussed previously, PGA and $I_{a,hor}$ are controlled by high frequencies which are most influenced by the length scales of heterogeneities considered. The refraction and scattering of these higher frequencies creates more variability in these IM.

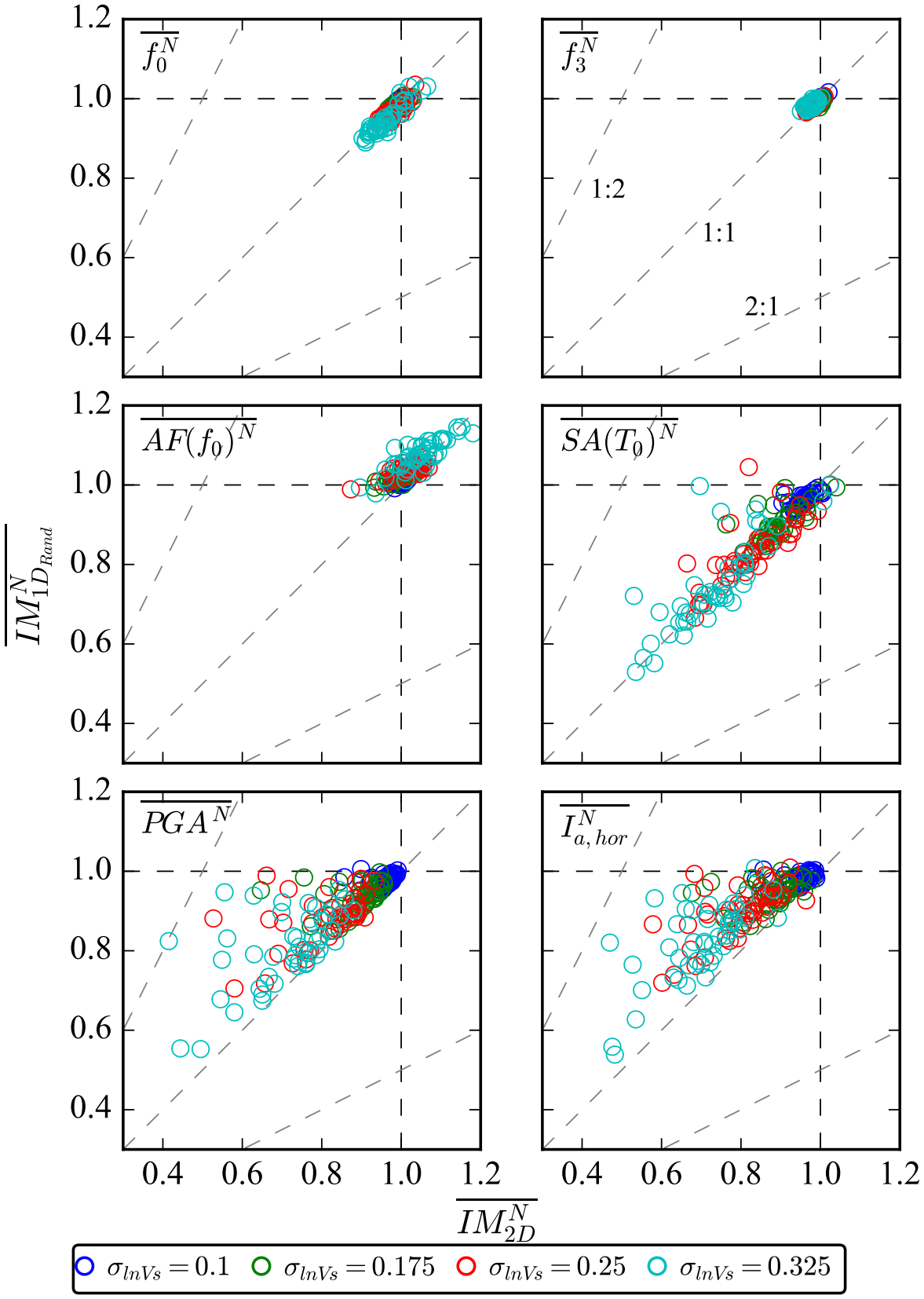

Figure 3.11: Comparison of median normalized *IM* between 2D and $1D_{Rand}$ analyses for all permutations color-coded by σ_{lnVs}.

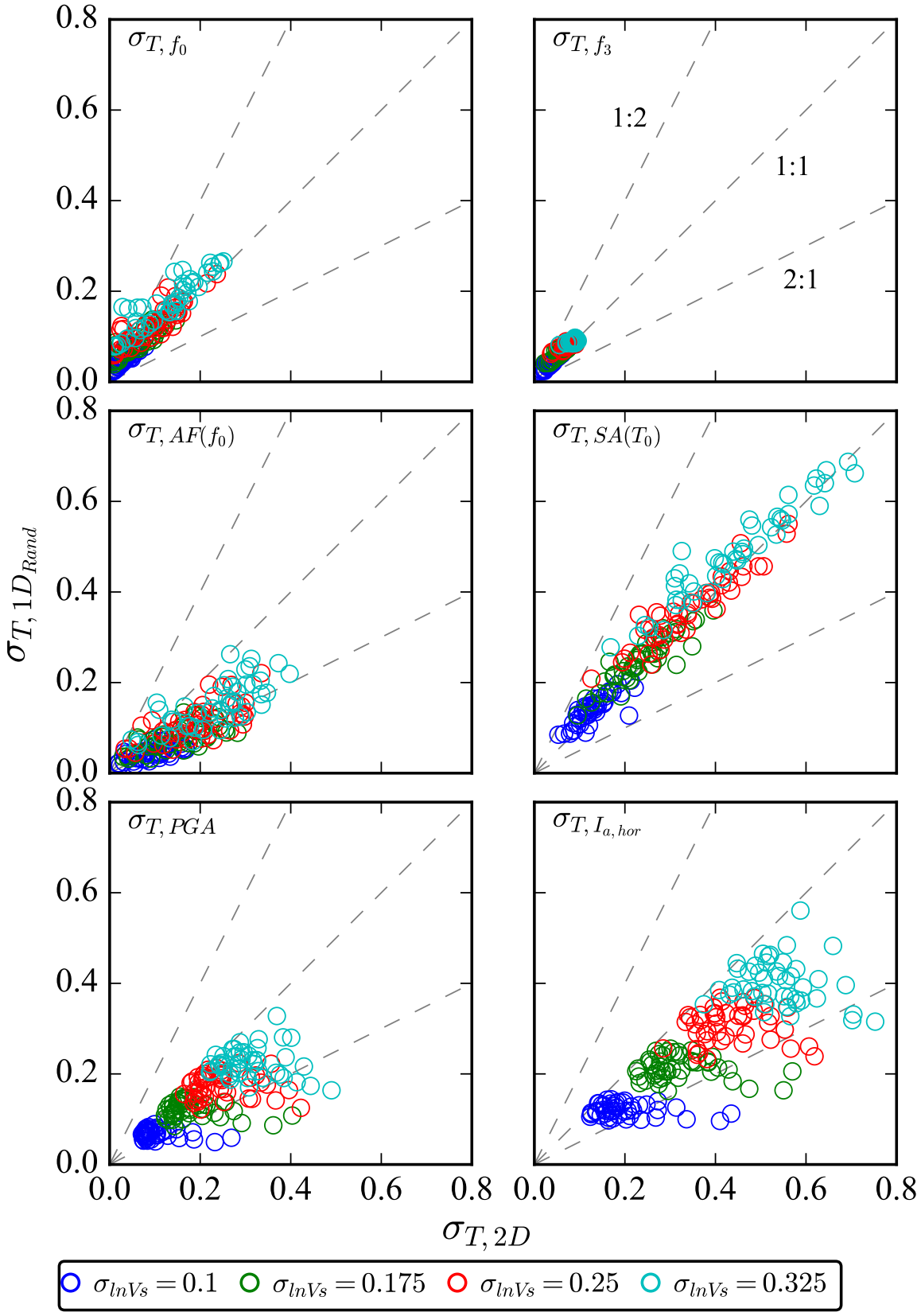

Figure 3.12: Comparison of total lognormal standard deviations between 2D and $1D_{Rand}$ analyses for all permutations color-coded by σ_{lnVs}.

3.4 Conclusions

A comprehensive parametric study was performed to investigate the effects of soil heterogeneity and wave scattering on geotechnical site response. The results demonstrate the ability of 2D site-response models with soil heterogeneity, modelled as anisotropic spatially correlated random fields, to cause scattering of seismic waves and impact several intensity measures (IMs) used to quantify the effects of site response. Relative to the conventional 1D site response with a deterministic V_S profile ($1D_{Det}$), acceleration time series and transfer functions from 2D analyses are significantly more complex. The frequency-to-frequency correlation in the transfer function reduces substantially, and ground-motion amplification is spread over wider frequency bands, particularly at high frequencies, unlike $1D_{Det}$ TFs with very discrete and narrow-banded amplification peaks.

The effectiveness of heterogeneities in scattering waves is highly dependent on the relationship between heterogeneity length scales and wavelength. For lower median V_S values and high frequencies (i.e., shorter wavelengths), and larger values of r_V (i.e., larger heterogeneity length scales) the influence of wave scattering becomes more pronounced and the variability in surface ground-motion increases. For this reason, wave scattering has more practical impact within the frequency range of engineering interest for softer soil deposits with lower V_S, and IMs that are influenced or controlled by higher frequencies such as TF for $f > 10$ Hz, PGA, $SA(T_0)$, and $I_{a,hor}$ are the most affected by heterogeneous deposits. For example, median values of PGA, $SA(T_0)$, and $I_{a,hor}$ experienced reductions of up to 20–40% relative to the $1D_{Det}$ results, while the effect on f_0 and $AF(f_0)$ was generally less than 10%. The maximum natural log total standard deviations observed (corresponding to the highest σ_{lnV_S} and largest r_V) for f_0 and $AF(f_0)$ were 0.25 and 0.4, respectively, but were significantly higher for $SA(T_0)$, PGA, $I_{a,hor}$, and $I_{a,vert}$ with values of 0.71, 0.49, 0.75, and 0.78, respectively. The variability in ground motion and other effects of randomizing V_S also become more pronounced as the strength of heterogeneity increases (i.e., increasing σ_{lnV_S}). The large decrease in PGA, $SA(T_0)$, and $I_{a,hor}$ can be partly explained by looking at trends in the vertical motion. Higher σ_{lnV_S} values cause waves to be more refracted from vertical incidence resulting in higher energy in the vertical component (i.e., higher $I_{a,vert}$).

While 1D randomized analyses ($1D_{Rand}$) are able to replicate median results from 2D analyses for some lower frequency IMs (e.g., median transfer functions at $f < 10$ Hz, f_0, and $SA(T_0)$), medians and standard deviations of high-frequency IMs (e.g., transfer function at $f > 10$ Hz, *PGA*, and Arias intensity) which are influenced by 2D ground-motion phenomena are not appropriately captured. In 2D results, for frequencies > 10 Hz, there is more variability in the transfer function and a reduction in the amplification factors (i.e., higher damping) due to scattering attenuation. Compared to the 2D analyses, the $1D_{Rand}$ models overestimate median *PGA* and $I_{a,hor}$ and underestimate their total standard deviations. The standard deviation of f_0 is larger for $1D_{Rand}$ cases, especially within a given realization, in which significantly greater correlation between adjacent recorder nodes is observed in a 2D model.

A detailed study to examine the influence of various boundary conditions was performed and is summarized in Appendix B.2. The results reveal that in order to prevent spurious reflections from the base, a vertically and horizontally compliant base must be used, and each node along the base must be allowed to respond independently with its own dashpot (i.e., base nodes cannot be tied to each other to respond in unison). Failure to implement such compliance and independence in the base nodes will result in overestimation of IMs (i.e., inefficient absorption of energy) because of the generation of vertical motion from refraction and wave scattering, and the lateral variation in arrival times of down-going waves at the base. The influence of different covariance models for random field generation on IMs was also investigated. Consistent with previous work by others, the Gaussian covariance model is not as efficient at scattering high frequencies and generating vertical motion. The difference between the Exponential model and Matérn model (with shape parameter exponent $= 0.2$) was insignificant for this application.

3.5 Appendices and Supplemental Material

Additional discussion and figures to supplement the content within the main body of the chapter, are included as appendices in Appendix B. Appendix B.2 provides the results of a thorough study to assess various boundary conditions for 2D site-response analysis. Appendix B.3 examines the influence of different commonly used covariance models for random field generation on site response. Appendix B.4 shows the results of a convergence study to determine

the number of random field realizations required for IMs to converge. Finally, Appendix B.5 provides additional figures to supplement the discussion throughout the text.

3.6 Data and resources

New Zealand eScience Infrastructure's (NeSI) high performance computing facilities and consulting support were used for all analyses and post-processing. More information is available at URL https://www.nesi.org.nz. All figures were generated in Python.

3.7 Acknowledgements

The authors thankfully acknowledge Alexander Pletzer, with NeSI, for his contribution in optimizing our OpenSees workflow, and Peter Stafford for his help in interpreting Fourier Spectra from 2D analyses. This work was financially supported by the University of Canterbury, and QuakeCoRE: The NZ Centre for Earthquake Resilience. This is QuakeCoRE publication number 0465.

Chapter 4

Can Modelling Soil Heterogeneity in 2D Site Response Analyses Improve Predictions at Vertical Array Sites?

C. A. de la Torre, B. A. Bradley, C. R. McGann, J. P. Stewart (2022). Can Modelling Soil Heterogeneity in 2D Site Response Analyses Improve Predictions at Vertical Array Sites? *in preparation*.

Abstract

This study uses a database of 21 vertical borehole arrays in California to examine whether a 2D site response analysis framework that accounts for soil heterogeneity via spatially-correlated random fields can explain misfits observed from prior 1D ground response modelling. The main hypothesis is that the overprediction of ground motion at site modal frequencies, consistently observed in many site response validation studies, is caused by soil heterogeneity and 2D/3D wave propagation effects that cannot be captured by 1D analyses. We apply classical 'within' boundary conditions for borehole input motion along with equivalent incident wave motions derived using a framework developed here to help elucidate effects of the down-going wave on observed first-model resonances. Results from 2D and 1D analyses are compared to ob-

servations using a transfer-function-based taxonomy and residuals of various other intensity measures (IMs) including response spectra. The uncertainty in predicted IMs is estimated from the many realizations of 2D models. We assess trends in median and standard deviations of IMs with respect to various site parameters (e.g., impedance ratios, shear wave velocities, frequencies of fundamental modes, and depth to the downhole seismic instrument). This 2D approach was found capable of scattering seismic waves and producing transfer function variability resembling the observed event-to-event variability in empirical transfer functions (ETF). For several sites that exhibit less down-going wave effects in ETFs (i.e., flatter peaks) and/or higher variability in ETFs, median transfer functions from 2D analyses provide a significantly better estimate of the median ETF than conventional 1D deterministic analyses, especially at fundamental modes. In contrast, for some of the sites that are well represented by 1D methods (e.g., Wildlife Liquefaction Array and Treasure Island), 2D methods with generic levels of spatial variability may over-represent the heterogeneity and consequently underpredict amplifications at higher mode frequencies.

4.1 Introduction

Vertical or borehole arrays of seismic recording stations, with instruments embedded at depth (often at, or near, the bedrock-soil interface) and at the ground surface, have been used to evaluate the performance of and estimate the uncertainty associated with site response methods. Most of these studies have used vertical arrays operated by KiK-net in Japan (e.g., Thompson et al., 2012; Pilz and Cotton, 2019; Tao and Rathje, 2020a), which mainly consist of firm soil or bedrock sites (the arrays were installed for source detection, and site response has been an ancillary benefit). As such, the findings from those studies are specific to those geological conditions. One recent study has used vertical arrays in California (Afshari and Stewart, 2019; Stewart and Afshari, 2021), primarily from bridge sites, and for which site conditions are on average softer.

The interpretation of data from the Japanese KiK-net and California arrays has focused on assessing the validity of the 1D assumption that is commonly used in site response analysis (e.g., Thompson et al., 2009, 2012; Afshari and Stewart, 2019; Pilz and Cotton, 2019; Tao

and Rathje, 2020a), determining the most influential parameters to site response, assessing the aleatory variability of site response given variability of soil properties and input motions (e.g., Rathje et al., 2010; Kaklamanos et al., 2013, 2015; Zalachoris and Rathje, 2015; Griffiths et al., 2016a; Li et al., 2018; Teague et al., 2018; Tao and Rathje, 2019; Hallal and Cox, 2021a) and estimating epistemic uncertainty associated with uncertain input parameters (e.g., Rodriguez-Marek et al., 2021; Ulmer et al., 2021) and modelling uncertainty (e.g., Stewart and Afshari, 2021). Two common themes were identified in the 1D ground response validation components of these studies: (1) the ground motion intensity at frequencies corresponding to fundamental modes of the modelled soil column is often overpredicted when using laboratory-based minimum damping ratios (D_{min}), and (2) a significant percentage of sites cannot be appropriately represented with the 1D assumption. However, these results are quite different for KiK-net and California sites such that relatively general patterns of behavior remain elusive.

By comparing 1D theoretical transfer functions (TTF) to empirical transfer functions (ETF) from vertical arrays for weak motions (e.g., $PGA < 0.1g$), it is possible to evaluate whether the attenuation characteristics of a particular damping model are in accord with the data. One of the first investigations identifying ground motion over-prediction (attenuation under-prediction) from geotechnical damping models was for the Service Hall Array in Japan (Yee et al., 2011, 2013), which was later confirmed for a larger series of KiK-net arrays by Thompson et al. (2012) and Cabas et al. (2017). Thompson et al. (2012) used a grid search for D_{min} to minimize misfit between TTF and median ETF, resulting in D_{min} values ranging from 1.4 to 10% with a median of 4% for 100 KiK-net sites (note that these values are provided as intrinsic attenuation of S waves ($^{i}Q_{s}^{-1}$) in Thompson et al., 2012). Recently, Tao and Rathje (2019) identified that a factor of 3-6 increase in D_{min} is required to directly match 1D site response predictions to median ETFs at 4 sites. Afshari and Stewart (2019) and Afshari et al. (2019) developed site-specific κ_0 values to adjust D_{min}, which also resulted in an increase in D_{min} for California vertical array sites. Also using California vertical arrays, Boore et al. (2020) estimated effective hysteretic soil damping ranging from 1 to 10 % with a method developed by Gibbs et al. (1994).

The need for increased D_{min} values and variable input parameters, in conflict with the values directly obtained in lab experiments, to match empirical data suggests that important physics that influence site response and the attenuation of seismic waves are being omitted in the

conventional 1D site response framework. Several of these studies have concluded that one of the reasons for this underestimation of damping may be that the effects of soil heterogeneity and wave scattering are not accounted for in 1D site response analyses or laboratory tests to estimate soil damping (e.g., Rodríguez-Castellanos et al., 2006; Thompson et al., 2009; Kokusho, 2017), in addition to non-vertically incident ground motions and an incoherent wavefield.

A 1D site response analysis assumes that soil layers are laterally homogeneous, the mode of deformation is simple shear, and that the incidence angle and direction of propagation of shear waves is vertical. In recent years, taxonomies have been developed to distinguish sites that are empirically seen to be well represented by 1D site response analyses from those that cannot, and to identify contributing factors for this distinction to aid with interpretation of forward predictions. Typical criteria for a "well-behaved" 1D site have been defined as: (1) low event-to-event variability in borehole ETFs, and (2) high goodness-of-fit between ETFs and TTFs. One of the first such taxonomies was Thompson et al. (2012), finding that only 16/100 Japanese KiK-net sites fit their best classification for a good 1D site (i.e., LG site with Low event-to-event variability and Good fit to the 1D TTF), despite adjusting D_{min} to optimize the fit between TTF and ETF. Similarly, Pilz and Cotton (2019) found that 158/354 KiK-net sites (i.e., 45 %) show influence of 2D and 3D effects on site response and were not well represented by a 1D analysis. Tao and Rathje (2020a) were able to increase the percentage of good 1D sites to 69 % (for 34 mostly KiK-net sites), by neglecting pseudo-resonant frequencies in the comparison between TTFs and ETFs. Various studies (e.g., Kawase and Matsuo, 2004; Kaklamanos et al., 2015; Wu et al., 2017; Pilz and Cotton, 2019) have suggested that the uncertainty and/or lack of discretization in V_S profiles of KiK-net sites is a possible reason for the high degree of misfit for many sites. Afshari et al. (2019) and Afshari and Stewart (2019) developed a database of 21 vertical arrays in California, and determined that five sites were exceptionally well represented by 1D site response, however, approximately 50 % of sites had a good fit between ETF and TTF. This more favorable performance of 1D methods for California sites relative to findings from the various KiK-net studies may well be an outcome of the distinct geological conditions at the two sets of arrays.

One important issue highlighted by Thompson et al. (2012) is that the spatial variability in local shear wave velocity (V_S) of a site can significantly influence the appropriateness of a

1D site response approach. For two sites, one with a very high goodness-of-fit and one with a very low goodness-of-fit to 1D TTF, they performed four SASW surveys at each site. They found that the site with high goodness-of-fit had low variability in V_S (laterally and vertically) between the four locations, compared to the site with low goodness-of-fit which had much higher variability in V_S. Their conclusion is that sites with high vertical and lateral variability in soil properties can be influenced by multidimensional phenomena that make the site response poorly predictable by 1D methods. Given these sentiments, the quantification and incorporation of uncertainty and spatial variability of V_S in site response analysis is an important step in improving our forward predictive capabilities. There have been many efforts to characterize how soil properties (including V_S) vary spatially (e.g., Popescu, 1995; Toro, 1995; Holzer et al., 2005; Wills and Clahan, 2006), estimate the uncertainty in V_S measurements (e.g., Toro, 1995; Griffiths et al., 2016b,a; Stolte and Cox, 2019), and directly incorporate spatial variation of soil properties into site response analyses (e.g., Toro, 1995; Thompson et al., 2009; Griffiths et al., 2016a; Passeri et al., 2019; Rodriguez-Marek et al., 2021).

Given that a large percentage of sites have been empirically found to not behave one-dimensionally, and that the spatial variability of soil properties has been found to be significantly influential to site response, a logical next step is to incorporate multi-dimensional phenomena and spatial variability into site response analyses. Some of the early pioneering efforts to assess the influence of spatial variability of soil properties on 2D site response include Popescu (1995), Nour et al. (2003), Assimaki et al. (2003), and Assimaki (2004). More recently, Thompson et al. (2009), El Haber et al. (2019), Huang et al. (2019), and de la Torre et al. (2021) have assessed the influence on, and quantified the variability in, transfer functions and other intensity measures. These studies have found that incorporating the effects of spatial variability and wave scattering in 2D or 3D site response analyses has the potential to reduce amplification factors at fundamental modes for individual transfer functions (Thompson et al., 2009; Huang et al., 2019) and median transfer functions (Thompson et al., 2009; Huang et al., 2019; de la Torre et al., 2021), compared to 1D deterministic analyses with no variability in soil properties. Other high-frequency-controlled intensity measures, such as PGA and Arias Intensity, have been shown to be reduced as well (de la Torre et al., 2021). It is important to note that the spatial variability in soil properties considered in these studies is not related to actual measured

2D or 3D site conditions at particular sites. Rather, they are investigating effects of randomness in soil properties in what would nominally be considered a 1D profile.

Uncertainty and spatial variability of surface intensity measures can also be estimated with these 2D/3D models. While these studies have been useful to gain intuition for how various random field input parameters can influence site response characteristics, they have generally been limited to simple idealized single-layer profiles (e.g., El Haber et al., 2019; Huang et al., 2019; de la Torre et al., 2021). Other than Thompson et al. (2009), who compared TTFs from 3D models with spatial variability to ETFs for 2 sites, there have been little to no efforts to validate results from such analyses with observations of any kind (e.g., vertical arrays, H/V data, etc.).

This study expands on previous work validating site response analyses by applying a method for modelling soil heterogeneity and wave scattering in 2D site response analyses to a database of 21 vertical array sites in California. As in some prior work, the intent is not to capture actual 2D or 3D variations in material properties at the respective sites, which are unknown due to limited site characterization. Rather, the intent is to examine the impact of essentially random, but realistic, variations in soil properties on computed responses. The method for 2D site response was developed by and is thoroughly documented in de la Torre et al. (2021), and the ground motion and site database was compiled by Afshari et al. (2019). This paper tests the hypothesis that the overprediction of ground motion at the site modal frequencies is caused by the disregard of soil heterogeneity and 2D/3D wave propagation effects, and that these effects can be appropriately captured in a 2D analysis using spatially-correlated random fields to spatially vary soil properties. The 2D approach developed in de la Torre et al. (2021) for a single-layer profile was extended to take any multi-layered 1D V_S profile as the median profile in the generation of 2D randomized V_S models. In order to utilize the vertically and horizontally compliant base adapted in de la Torre et al. (2021), the incident motion was computed from the observed within-motion using transfer functions from 1D compliant base models. This facilitates investigation of different boundary condition assumptions and their relevance in site response predictions.

This paper is organized in the following manner: first, the methods are defined for the site

response model geometry and inputs, followed by an explanation of the outputs and intensity measures used for validation of the approach. The results and discussion are broken into two sections. The first section discusses transfer function (TF) amplitudes, comparing ETFs to TTFs, and TTFs from 1D and 2D analyses. Residuals of and variability in intensity measures (IMs) are also presented. The next section, includes results and discussion related to surface ground motion IMs. Finally, conclusions, limitations, and ideas for future extension of the method are provided in the Conclusions.

4.2 Methods

4.2.1 Site and Ground Motion Database Considered

V_S profiles and recorded ground motions from 21 vertical array sites in California from Afshari et al. (2019) (available from Afshari et al., 2018) were analyzed. The recorded ground motions had been corrected and filtered using an acausual Butterworth filter. Table 4.1 identifies the sites and lists relevant metadata that are discussed subsequently. V_S profiles for all sites are plotted in Appendix C.6. Using a similar convention to Zalachoris and Rathje (2015), sites are classified into three groups as follows:

- Group 1: Significant impedance contrast near the downhole (DH) instrument;
- Group 2: No significant impedance contrast and depth to downhole instrument (z_{DH}) $<= 90$ m;
- Group 3: No significant impedance contrast and $z_{DH} >= 90$ m.

This grouping also attempts to differentiate sites that likely have strong down-going-wave effects (Group 2), from those at which these effects may be less pronounced due to the depth of the instrument (Group 3) or a strong impedance contrast above the instrument (Group 1). As in Tao and Rathje (2020a), the sites are further characterized by the presence of a pseudo-resonance at the fundamental mode of the 1D within transfer function ($f_{0,within}$). This distinction

is made by visual comparison of 1D outcrop and within TFs. If the outcrop TF does not display a prominent peak at $f_{0,within}$ but is prominent in the within TF, then the peak is considered to be a pseudo-resonance (Tao and Rathje, 2020b). Sites with a pseudo-resonance at f_0 are given an additional 'P' after the group number (e.g., Group 2P). Note that all Group 2 and 3 sites fall into this category except one site in each. No Group 1 sites fall into this category as the resonance at f_0 is controlled by a strong impedance contrast near the DH instrument.

Table 4.1: Metadata for 21 California vertical array sites.

SSN*	Site ID	Group^P	$f_{0,1D}$** (Hz)	V_{S30} (m/s)	V_{SDH} (m/s)	R_V	z_{DH} (m)	σ^M_{lnETF}	N_{EQ}
1	Borrego Valley	1	0.75	340	3227	12.2	238	0.82	16
21	Treasure Island	1	0.76	157	2400	16	122	0.58	11
7	Hollister Digital Array	1	1.19	385	2547	10.4	188.8	0.69	23
5	Garner Valley	1	1.68	265	2500	14.5	150	0.78	10
18	Foster City-San Mateo	1	1.75	810	2800	22.4	38.3	0.54	7
15	Corona	1	3.15	321	3000	16.7	41.8	0.79	31
20	SF Bay Bridge	1	3.89	391	1700	6.6	40	0.73	9
10	LA Obregon Park	2P	1.86	452	600	1.3	69.5	0.69	23
11	San Bernardino	2	2.51	252	675	4.9	35	0.73	5
3	Crockett-Carquinez Br 1	2P	2.91	335	600	3.1	45.7	0.67	8
12	Vallejo - Hwy37/Napa River	2P	3.88	528	738	1.5	44.7	0.8	17
2	Benicia-Martinez S	2P	4.48	547	600	1.5	35	0.74	10
13	Wildlife Liquefaction Array	3P	0.69	200	257	1.4	100	0.57	21
4	El Centro-Meloland	3P	0.69	238	594	4.4	195	0.62	19
6	Eureka	3P	0.89	160	608	6.3	136	0.69	14
8	Hayward-San Mateo	3P	0.89	185	348	3.1	91	0.66	5
17	Coronado West	3	1	214	620	4.5	109	0.71	19
14	Antioch-San Joaquin S	3P	1.1	253	504	3.8	102.4	0.53	4
9	LA La Cienega	3P	1.2	242	485	3.6	100	0.66	20
16	Coronado East	3P	1.33	329	620	1.9	91	0.64	10
19	Hayward-I580 W	3P	2.04	489	787	0.9	91	0.58	5

* Site serial numbers (SSN) from Afshari et al. (2019).

** f_0 from 1D within transfer function.

^{P} P indicates that the amplifications at $f_{0,within}$ are likely caused by a pseudo-resonance.

$V_{SDH} = V_S$ at downhole instrument, R_V = impedance ratio, z_{DH} = depth to the downhole instrument, σ^M_{lnETF} = mean standard deviation of ETFs over a given frequency range, and N_{EQ} = number of earthquakes recorded at the site.

4.2.2 Site-Response Model Geometry and Inputs

4.2.2.1 Model and Boundary Condition Assumptions

We follow the 2D site response approach outlined in de la Torre et al. (2021), with an extension to allow for a median V_S profile that is multi-layered and arbitrarily complex as a function of depth. Figure 4.1 schematically illustrates many of the features of the site-response model including boundary conditions, the Subdomain of Interest (SOI), location of surface recorder nodes, and an example of a 2D velocity model with anisotropic spatially correlated V_S perturbations. The total model width is 1,000 m (1-m-wide elements). The illustrated lateral and base boundary conditions were selected based on a rigorous examination of different assumptions (de la Torre et al., 2021). The SOI is taken as the center 30% of the model domain (i.e., 300 m) to minimize boundary effects. Within the SOI, 10 equally spaced nodes at the ground surface are used to record simulated motions and compute site amplification relative to the base excitation. 1D randomized ($1D_{Rand}$) V_S profiles extracted from the 2D model at vertical transects and within transfer functions for all 10 nodes are included in Figure 4.1.

2D viscoelastic site response was performed in OpenSees (McKenna, 2011). The ground motion database is for weak motions (Afshari et al., 2019), therefore, the elastic assumption is considered appropriate (Thompson et al., 2009; Kaklamanos et al., 2015). Mass densities were computed for every layer using a V_S-based correlation (Boore, 2007). Poisson's ratio of 0.25 was used for computation of elastic parameters in element and material definitions. Full Rayleigh damping was used with a target damping ratio of 1 % at frequencies corresponding to the first and fourth modes of the 1D TTF in order to approximately match laboratory-based D_{min} values, which typically range from 0.5 to 2 % (e.g., Darendeli, 2001; Vucetic and Dobry, 1991), over that frequency range. This damping formulation is consistent with recommendations from previous studies (e.g., Kwok et al., 2007; Stewart Annie On-Lei Kwok et al., 2008) for use in time-domain analyses. For compliant base analyses, V_S of the halfspace, $V_{S,HS}$, is assumed to be V_S at the depth of the downhole instrument ($V_{S,DH}$).

To reduce computational demands, single-integration-point, 4-noded quadratic SSPquad elements (McGann et al., 2012) were used. The height of each element is defined such that

there are 8 nodes per wavelength at $f = 25$ Hz (based on the median V_S), however, a maximum element height of 1 m was enforced so that the vertical correlation length is at least five times the element height (with $r_V = 5$ m). Analyses were parallelized over 8 CPUs using OpenSeesSP to reduce computation times. Because the 2D analyses are elastic, once transfer functions are computed for a given V_S model realization from a time-domain analysis for a single event, these same transfer functions can be used to perform frequency-domain analyses for the rest of the remaining ground motions. This frequency-domain analysis is explained further and verified in Appendix C.2.

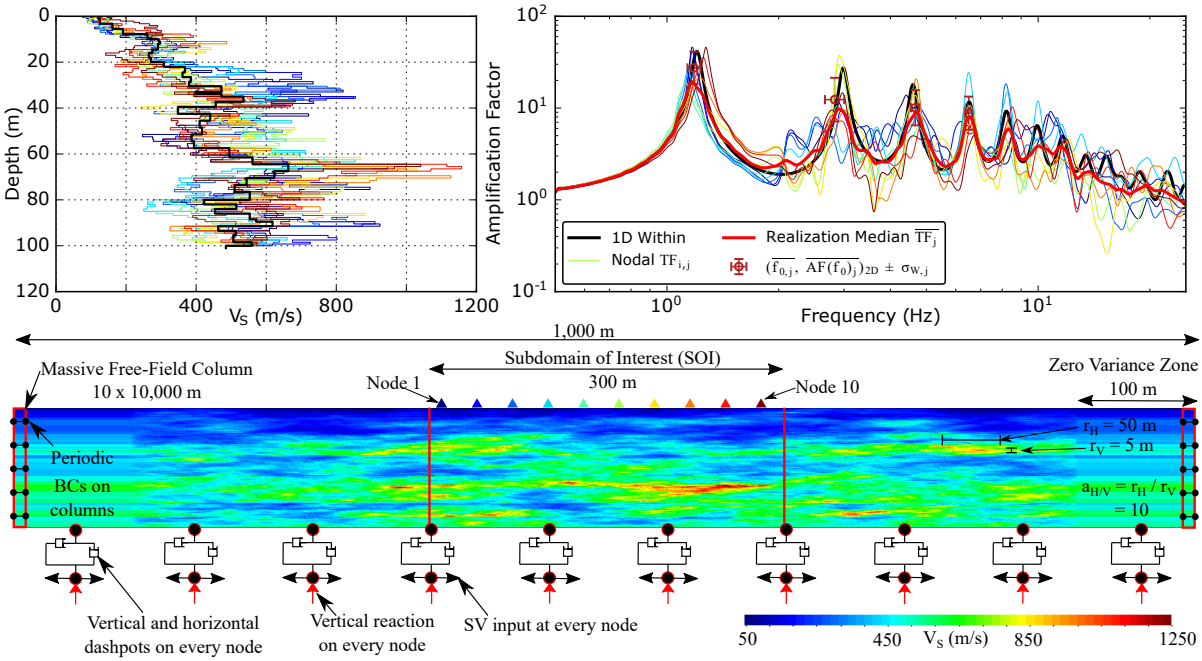

Figure 4.1: Schematic of compliant base site-response model illustrating a 2D shear wave velocity model with heterogeneity, boundary conditions, surface recorder node locations, the Subdomain of Interest (SOI), and zero variance zones. V_S profiles (top left) and nodal transfer functions (top right) are included for all 10 surface recorder nodes with the colors of curves matching those of the symbols in the schematic. This example is for Site 9, realization 13 with $\sigma_{lnVs} = 0.25$, $r_H = 50$ m, and $a_{H/V} = 10$. Transfer function IMs are defined in Section 4.2.3.

4.2.2.2 Modelling Soil Heterogeneity via Spatially-Correlated Random Fields

Soil heterogeneity is modelled using anisotropic spatially-correlated random fields to perturb the model based on its median V_S at a given depth. The marginal distribution of V_S at a point is considered as lognormal, with a lognormal mean $\mu_{lnV_{S,0}}$ (or, equivalently, a median

$V_{S,0} = \exp \mu_{lnVs,0}$), and standard deviation σ_{lnVs}. The spatial correlation for random field generation is represented with an Exponential correlation function (Frankel and Clayton, 1986; Sato et al., 2012), which is a special case of the Matérn model (with shape parameter exponent, $\nu = 0.5$). Other input parameters of this model include the horizontal and vertical correlation lengths, r_H and r_V, respectively.

Based on the parametric analysis presented in de la Torre et al. (2021), we adopted random field parameters $r_H = 50$ m and $r_V = 5$ m (i.e., $a_{H/V} = 10$) for all models and analyzed 30 random field realizations for parameter permutation. Analyses with $\sigma_{lnVs} = 0.15$ and 0.25 were performed and compared for a total of 2 random field parameter permutations. These values of σ_{lnVs} were selected because they are generally representative of values reported in previous studies, and values lower than this were shown to produce insignificant differences between 1D and 2D analyses (see de la Torre et al., 2021, for more details). With 10 nodal outputs from 30 realizations (i.e., 300 simulations for every observation), the standard error in the resulting simulated mean response is considered sufficiently small, allowing for robust conclusions.

4.2.2.3 Computation of Incident Motion for Input to Compliant Base Models

The theoretically correct way to model a vertical array in one-dimensional analysis, with recorded within motions, is using a rigid base and applying the recorded within motion as a uniform excitation (i.e., a global acceleration; Kwok et al., 2007). When extending this to 2D analyses, with spatially heterogeneous deposits, the rigid base can lead to unintended reverberations. Thus, it was desirable to use a fully compliant base as adopted in de la Torre et al. (2021). As demonstrated in Appendix C.4, the rigid base for 2D models reduces spatial variability in f_0, resulting in higher amplification factors of median transfer functions, and produces spurious nodal transfer functions in which the various fundamental mode peaks of different nodes appear to contribute to other adjacent nodes. On the contrary, nodal transfer functions from compliant base models appear to have more independent peaks.

The appropriate input motion for use with a compliant base is the incident motion only, however, the recorded downhole (DH) motions include both the upgoing incident wave and the down-going wave superimposed. It is possible to approximately isolate the incident motion

using a 1D incident-to-within motion transfer function. To accomplish this, 1D compliant base models in OpenSees were utilized. For each ground motion, the recorded within motion (i.e., the observed upgoing wave [A_o] + the observed down-going wave [B_o]) was first assumed to be the incident motion only (the modelled upgoing wave [A_m]) and was applied to the compliant base model of the corresponding site. The within motion was then computed at the complaint base of the model ($A_m + B_m$). It was then assumed that the ratio (in the frequency domain) of the upgoing wave (A) to the within motion ($A + B$) is the same for the real soil deposit in which the vertical array is embedded (subscript o for observed) and the 1D model (subscript m for model), that is:

$$\frac{A_o}{A_o + B_o} = \frac{A_m}{A_m + B_m} \tag{4.1}$$

With this assumption, the incident motion in the soil deposit can be calculated as:

$$A_o = (A_o + B_o)\frac{A_m}{A_m + B_m} = \frac{(A_o + B_o)^2}{A_m + B_m} \tag{4.2}$$

An example of the calculation of the incident motion from the within motion is illustrated in Figure 4.2. It should be noted that, for an elastic system, the ratio in Equation 4.2 is independent of the input motion used, therefore, the initially assumed input motion does not introduce error. In a 1D context, the surface motion calculated using a rigid base model with the within motion as input is identical to that calculated using a compliant base with the computed incident motion (as in Kwok et al., 2007). We acknowledge that by doing this "deconvolution" in 1D we are now relying on the 1D methodology that has already been found to underestimate the energy dissipation or "damping", and overpredict amplification factors from pseudo-resonances in elastic analysis with typical D_{min} values. This is one of the challenges in using vertical arrays and 1D within TFs, which overpredict the observed destructive interference of up-going and down-going waves for non-1D soil deposits, and not a problem with the 2D approach in general. Nonetheless, this provides an approach for using more realistic boundary conditions for 2D analysis that is equivalent to the rigid base with a within motion (excluding effects attributed to boundary conditions of 2D models).

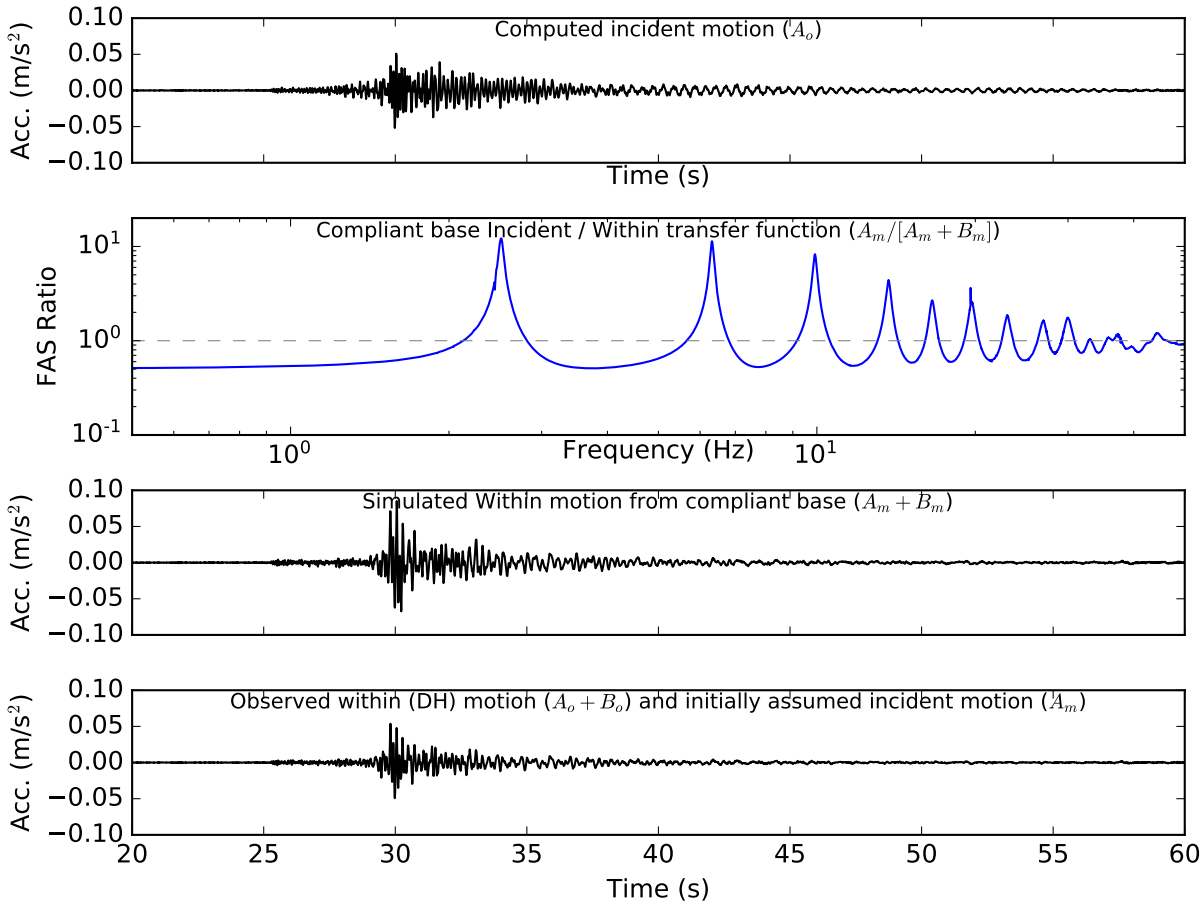

Figure 4.2: An example of computing the approximate incident motion using an Incident / Within transfer function from a 1D compliant base model.

4.2.3 Validation Study Metrics

4.2.3.1 Empirical and Theoretical Transfer Functions (ETF and TTF)

The within empirical transfer function (ETF) for an individual event component is computed as the ratio of the Fourier amplitude spectrum (FAS) for the ground surface motion by the FAS for the down-hole (DH) motion. The ETF was separately computed for each ground motion component of a site, and then the median ($\overline{ETF}$) and lognormal standard deviation (σ_{lnETF}) as a function of frequency were calculated for all events and components (i.e, two orthogonal components per event).

As shown in Figure 4.1, simulated accelerations are extracted at 10 nodes on the ground

surface of the model. Unless otherwise stated, all theoretical transfer function (TTF) shown and analyzed in this study are within transfer functions. 1D outcrop transfer functions are also computed from compliant base models and are shown in some figures as reference (e.g., Appendix C.6). Following the notation in Equations 4.1 and 4.2, the 1D outcrop transfer function is computed as:

$$TF_{1D,outcrop} = \frac{Sur_m}{2A_0} \tag{4.3}$$

where Sur_m and A_0 are the Fourier amplitude spectra of the computed surface motion from the 1D model and the incident input motion for the compliant base derived using Equation 4.2, respectively.

For rigid base 1D and 2D models, the TTF is computed as the FAS ratio of the simulated surface motion to the observed within motion (i.e., the input uniform excitation). For compliant base models that use an incident input motion, the within motion is recorded at 10 nodes along the compliant base directly below the surface recorder nodes to compute 10 independent within transfer functions for direct comparison with rigid base analyses.

It is common practice to smooth FAS or transfer functions (TF) for site response validation studies. To thoroughly understand the influence of the smoothing on median and standard deviations of TF, ETFs were calculated in three ways using Konno-Ohmachi smoothing with bandwidth coefficients (b-values) ranging from 20 to 100, as well as with no smoothing. Results of this smoothing study are documented in Appendix C.3. To preserve detailed features of the site response and the actual variability in ETFs and TTFs, for visual presentation we lightly smooth (i.e., b = 100) only the median and standard deviations (Method 3 in Appendix C.3). However, for computing transfer-function-based IMs (Section Intensity Measures (IMs)), more stable estimates can be made by lightly smoothing individual FAS prior to computing TFs (Method 1 in Appendix C.3)

4.2.3.2 Quantification of Within-Site Variability from ETF and TTF

Similar to Thompson et al. (2012) and Afshari and Stewart (2019), we estimate the within-site variability by calculating the mean standard deviations of ETFs and TTFs (σ^M_{lnETF} and $\sigma^M_{TTF,2D}$, respectively) over a given frequency range. For ETFs, σ^M_{lnETF} represents event-to-

event variability, and for TTFs $\sigma^{M}_{TTF,2D}$ represents location-to-location and realization-to-realization variability. For both ETF and TTF the frequency range over which the standard deviation values are averaged is between frequencies corresponding to the half-amplitude of the first mode peak (i.e., $\frac{1}{2} \times (1 + AF(f_0))$, and corresponds to a frequency $< f_0$) and the fourth mode peak (or 20 Hz, whichever is lower). Note that these ranges may vary between ETFs and TTFs as the respective peak frequencies are used for each. This bandwidth is the same as that used by Hallal and Cox (2021b), and was chosen because it includes the majority of the first-mode peak, unlike the range used in many previous studies which begins at f_0. For all sites, f_0 is listed in Table 4.1, and the frequency range is plotted in figures of Appendix C.

4.2.3.3 Intensity Measures (IMs)

The transfer function and surface ground-motion intensity measures (IMs) defined in Table 4.2 were computed for observed and predicted ground motions.

Figure 4.3 illustrates how transfer function-based IMs are computed for ETFs, by plotting individual recorded ground-motion transfer functions with modal peak picks [i.e., $(f_0, AF(f_0))$] for two sites. Wildlife Liquefaction Array (left) shows relative less variability in ETFs overall, and in frequencies and amplification factors of fundamental modes, compared to Borrego Valley (right).

Table 4.2: Definition of IMs for validation study.

IM symbol	**Definition**
f_0, f_1, f_2, and f_3	The first to the fourth modal frequencies of the soil (i.e., the first four peaks in the transfer function). For 2D analyses these are computed as the local maxima between corresponding troughs of the $1D_{Det}$ TF. For ETF, the ranges for selecting local maxima are based on $1D_{Det}$ troughs but adjusted manually to optimize peak selections
$AF(f_0)^*$	The amplification factor (i.e., the value of TF) at f_0
$SA(T)$	5%-damped pseudo-spectral acceleration at vibration period T for 200 logarithmically spaced periods between 0.01 and 10 s.
PGA	Peak ground acceleration
PGV	Peak ground velocity
I_a	Arias intensity
CAV	Cumulative absolute velocity
D_{S575}	Significant duration for 5 - 75 % I_a
D_{S595}	Significant duration for 5 - 95 % I_a
$(\overline{f_0}, \overline{AF(f_0)})$	The median f_0 and $AF(f_0)$ from individual nodal TTFs or individual event ETFs
$(f_0, AF(f_0))_{\overline{TF}}$	f_0 and $AF(f_0)$ or Median TTF of ETF

* $AF(f_0)$ and amplification factors at other frequencies represent a ratio between the motion at the ground surface and the downhole instrument (for both observations and simulations). All other IMs are used to compute residuals or ratios between observations and simulations at the ground surface.

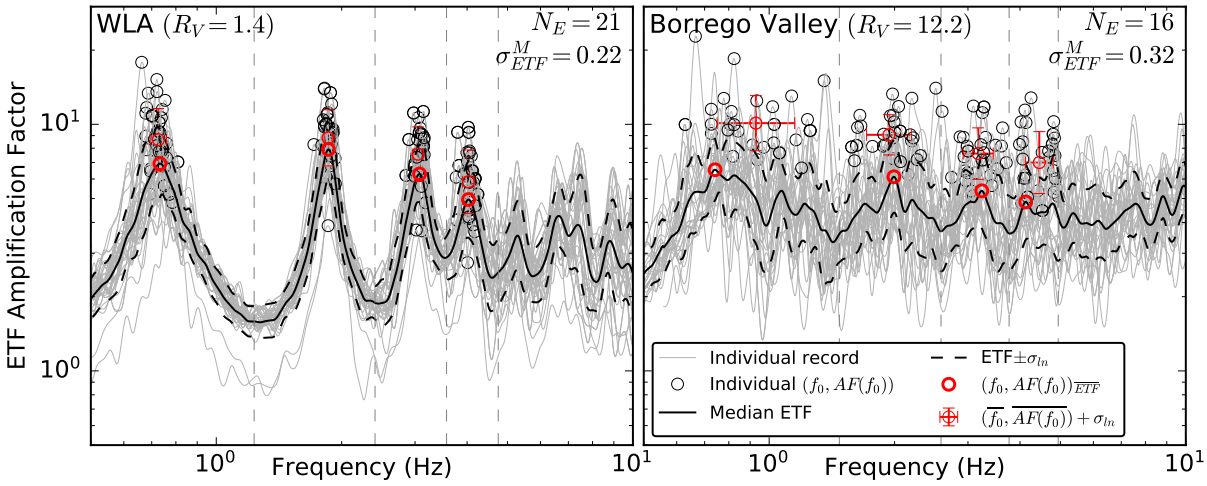

Figure 4.3: Example calculation of transfer-function-based IMs (e.g., f_0 and $AF(f_0)$) from ETFs for two sites. Wildlife Liquefaction Array (left) shows relative less variability in ETFs overall, and in frequencies and amplification factors of fundamental modes, compared to Borrego Valley (right). Individual FAS are smoothed (i.e., Method 1 from Section C.3) with b = 100. Note that the values of σ^M_{lnETF} reported here are different from those in Table 4.1 because of the different smoothing methods adopted for computing TF IMs (Method 1) versus computing median and standard deviation of TFs (Method 3).

4.2.3.4 Calculation of Residuals

To compare the predicted IM at each node to the corresponding observed IM, or median predictions to median observations, log residuals (Δ) are computed for all IMs. The residual is expressed as:

$$\Delta_{IMes} = ln(IM_{Obs})_{es} - ln(IM_{Sim})_{es} \tag{4.4}$$

where $ln(IM_{Obs})_{es}$ is the natural logarithm of the observed IM for a horizontal ground motion component of earthquake e at site s, and $ln(IM_{Sim})_{es}$ is the logarithm of the corresponding predicted IM. For a given event component, a residual is computed for all pairs of that one ground-motion recording at the surface and every simulated nodal result (i.e., 300 nodes).

The mean total site residual for a site s can then be approximated as:

$$\overline{\Delta}_{IMs} = \frac{1}{N_e}\sum_{i=1}^{N_e}\Delta_{IMes} \tag{4.5}$$

where N_e is the number of event components for site s. Using the same principles as Stewart and Afshari (2021), with notation from de la Torre et al. (2020), this mean total site residual can be further decomposed into an overall model bias, and a bias-corrected site term as follows:

$$\overline{\Delta}_{IMs} = a + \eta_s \tag{4.6}$$

where a is the overall model bias (i.e., the average of $\overline{\Delta}_{IMs}$ for all sites), and η_s is the bias-corrected site term.

4.2.3.5 Nodal, Realization, and Permutation IMs

We use the same notation developed in de la Torre et al. (2021) to differentiate between nodal, realization and permutation IMs, and their respective medians and standard deviations. For each ground motion component observation at the ground surface, the quantity computed at an individual node i (i.e., a "nodal IM") from V_S realization j is given the subscript i, j (e.g.,

$TF_{i,j}$ or $PGA_{i,j}$). We compute the geometric mean (i.e., the "realization median"; e.g., $\overline{TF_j}$) and lognormal standard deviation ($\sigma_{W,j}$) of all 10 nodes for realization j as in Equations 1 and 3 in de la Torre et al. (2021). The geometric mean of all 300 nodes (i.e., 10 nodes from 30 realizations) is referred to as a permutation median, or simply the median IM and is written with an overline (e.g., $\overline{TF}$ or $\overline{PGA}$; Eq. 2 in de la Torre et al., 2021). The total standard deviation (σ_T) of all 300 nodes and the mean within-realization $\sigma_{W,j}$ of all 30 realizations (σ_W) are also computed (Eq. 5 and 6 in de la Torre et al., 2021). The median of medians and standard deviations from all events are computed for all IMs except transfer functions as they are independent of the input motion.

4.3 Results and Discussion

4.3.1 Transfer Functions

4.3.1.1 Illustrative Examples of 2D Nodal Transfer Functions ($TF_{i,j}$)

To build intuition for results from 2D realizations and how median TTFs ($\overline{TTF}$s) are computed from the nodal TFs ($TF_{i,j}$) of all realizations, Figure 4.4 plots examples for four sites. For each site, Figure 4.4 has two panels, with top panels plotting all 10 $TF_{i,j}$ for a single realization and bottom panels plotting $TF_{i,j}$ for all realizations (i.e., 300 $TF_{i,j}$). Sites with low f_0 in Figure 4.4(a) have a low standard deviation of f_0 (i.e., σ_{f_0}), and $AF(f_0)$ similar to 1D analyses, i.e., little influence from heterogeneities, resulting in median TF amplitudes that are not significantly different than 1D at f_0. Sites with high f_0 in Figure 4.4(b) have higher σ_{f_0} and reduced $AF(f_0)$, on average, compared to 1D, indicating more influence from heterogeneities, and resulting in median TF amplitudes that can be significantly reduced at f_0. As identified in de la Torre et al. (2021), this is likely due to the relationship between correlation length and frequency. That is, the wavelength corresponding to sites with low f_0 are significantly longer than the vertical correlation length considered here ($r_V = 5$ m), and therefore, are not influenced by the spatial variability. As frequency increases for a given site (i.e., decreasing wavelength) or f_0 increases between sites, more influence from the heterogeneities is observed. For the SF Bay Bridge site (Site 20; Figure 4.4(a)), this reduction in $AF(f_0)$ results in a much better match

to the median ETF. These trends, as well as trends in higher mode frequencies (f_1 to f_3), are discussed in more detail for all sites in Section 4.3.1.4.

Treasure Island (Site 21) displays a clear double peak in ETFs at f_0 (Hallal and Cox, 2021b). Enough of the Treasure Island realization TTFs display this double peak (e.g., Figure 4.4a) that it is visible in the median TTF. This is one of the most pronounced double peaks in TTFs across all sites (only 4 display any double peak) which may suggest that it is features of the 1D median V_S profile (e.g., the V_S reversal just above the DH instrument) that cause this when 2D phenomena are considered.

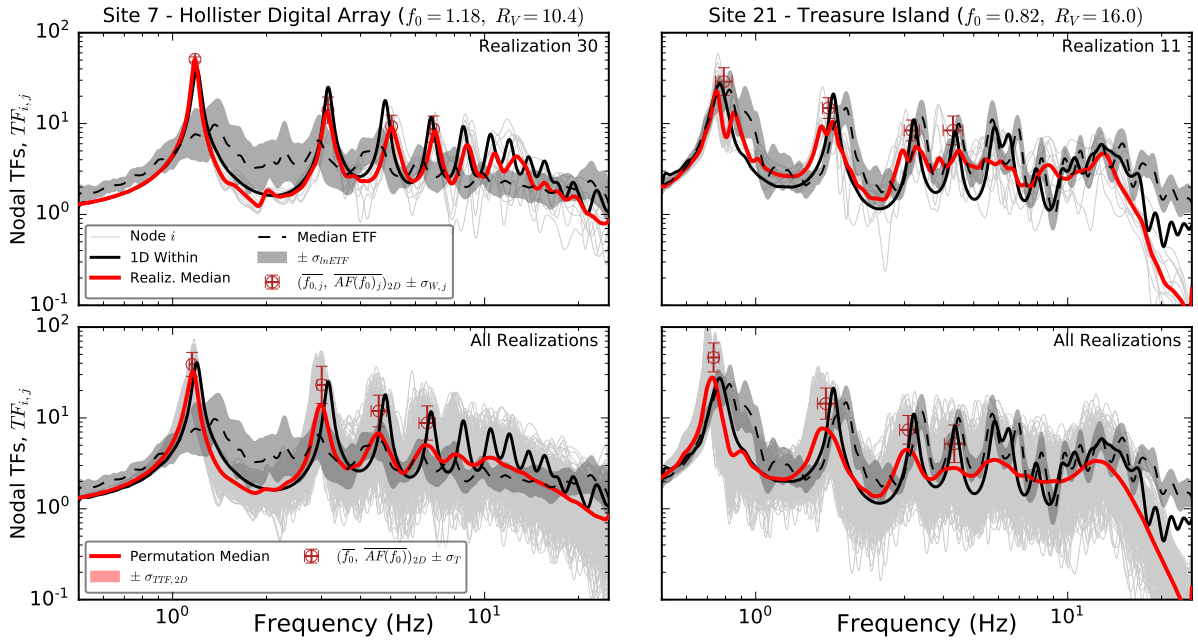

(a) Sites with a relatively low f_0 (Hollister Digital Array [left] and Treasure Island [right])

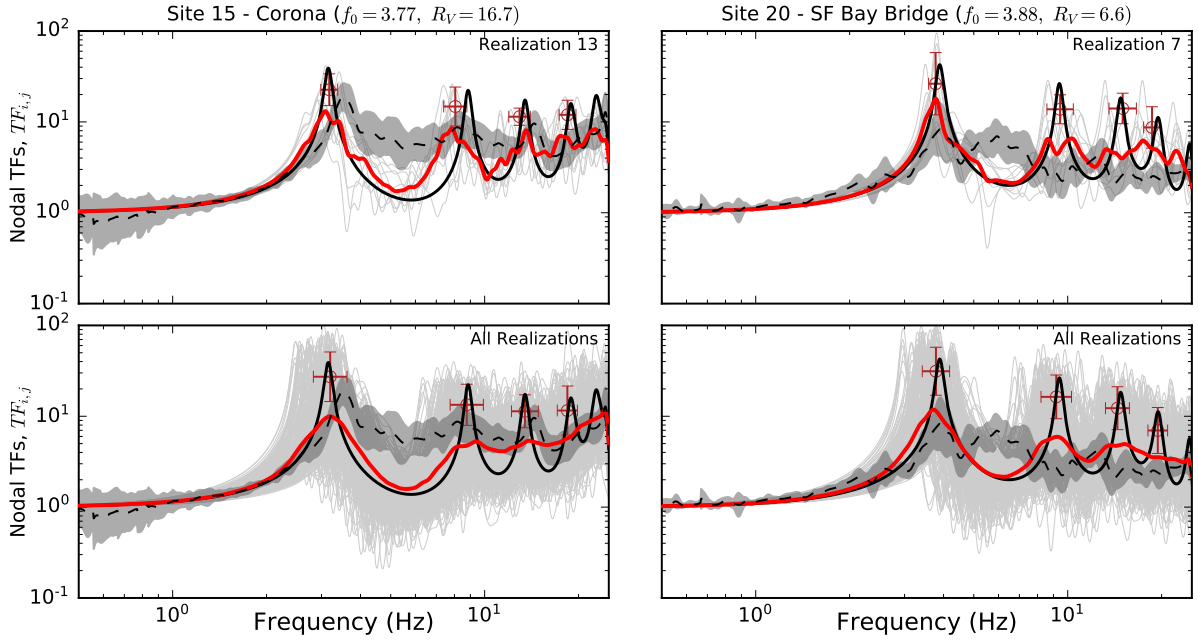

(b) Sites with a relatively high f_0 (Corona [left] and SF Bay Bridge [right])

Figure 4.4: Nodal transfer functions for one example realization and all realizations for four sites separated into sites with (a) relatively low f_0, and (b) relatively high f_0. 2D results are for $\sigma_{lnVs} = 0.25$

4.3.1.2 f_0 Ratios to Check Validity of 1D V_S Profiles

As suggested by Pilz and Cotton (2019), an important first step when comparing ETF to TTFs is to assess whether the 1D V_S profile used is representative of the actual site conditions. One way to test this is by comparing fundamental mode frequencies (f_0) from ETFs and TTFs. Ratios of observed to predicted f_0 for 1D and 2D analyses are plotted in Figure 4.5. f_0 for ETFs and 2D TTFs is taken as the first peak of the median TFs (i.e., $f_{0,\overline{TF}}$). As shown in Figure 4.5, all sites are well within the thresholds of 0.5 to 2.0 established by Pilz and Cotton (2019). Most are within approximately $\pm$ 20 % of observed f_0, with only Sites 12 (Vallejo) and 19 (Hayward I580 W) falling significantly outside this range. Generally, there appears to be a tendency for 1D velocity profiles to underpredict f_0 by about 5 to 10 % (i.e., ratios of about 1.05 to 1.1). This highlights that there is room for improving site response predictions (especially in terms of metrics such as Pearson's correlation coefficient) via refinement of the 1D V_S profiles, but that the majority of profiles are reasonable for site response assessment. For example, Teague et al. (2018) showed that the P-S logging V_S profile used in this study may not be an accurate representation of the site conditions, and that results can be improved using a V_S profile that accurately captures f_0. It may also be that the multi-dimensionality of the wave-field results on differences in f_0 between observations from earthquake recording and measurements from a 1D V_S investigation. Previous studies (e.g., Cheng et al., 2020) have found that f_0 from horizontal-to-vertical spectral ratios vary with azimuth, which may support this hypothesis.

The 2D analyses tend to shift f_0 by about 5 % to lower frequencies for most sites (points moving upward from 1:1 line on Figure 4.5). A rejection criterion, such as the one in Teague et al. (2018), could be implemented to exclude 2D realizations with f_0 significantly different than $f_{0,1D}$ to prevent this shift in f_0. Alternatively, a V_S distribution that prevents the generation of such realizations could be considered.

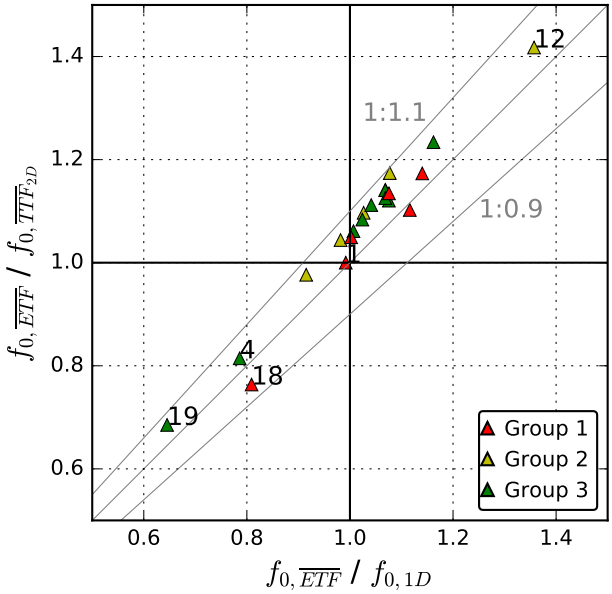

Figure 4.5: Ratios of f_0 from median ETF to f_0 from TTFs. Ratios from 2D TTFs are plotted against ratios from 1D TTFs. Annotations next to certain markers represent SSNs.

4.3.1.3 Residuals of Amplification Factors from Median TFs [$AF(f_0)_{\overline{TF}}$]

To begin aggregating results for all sites and identify trends as a function of site characteristics, Figure 4.6 plots residuals of amplification factors from median TFs. Residuals for the first and third modes are plotted against σ^M_{lnETF} (left panels) and $f_{0,\overline{ETF}}$ (right panels). Significant improvements in residuals of median TFs are observed when the 2D approach is used, albeit, there is still significant bias at f_0. However, the residuals for $AF(f_3)_{\overline{TF}}$ are centered around zero. Residuals using $\overline{AF(f_0)}$, instead of $AF(f_0)_{\overline{TF}}$ are given in Figure C.5 (Appendix C.5). These show similar trends but with more modest improvements to residuals, especially for $\overline{f_0}$. For $\overline{f_3}$ there is still significant improvement and residuals close to zero for many sites.

To further scrutinize results at individual sites, Figures 4.7 and 4.8 plot V_S profiles and median ETFs and TTFs for two groups of sites. Figure 4.7 includes sites that generally demonstrate significant improvements in prediction of median TFs and medians of TF-based IMs when 2D analyses are used. The event-to-event variability in ETF (σ^M_{lnETF}) is moderate to large for these sites. Very good agreement is observed between ETFs and 2D TTFs for amplification factors of TF peaks, especially at f_2 and f_3 (as in Figure 4.6). Sites 5 and 9 (Garner Valley and LA La Cienega, respectively) demonstrate this improvement for which predictions of median TFs

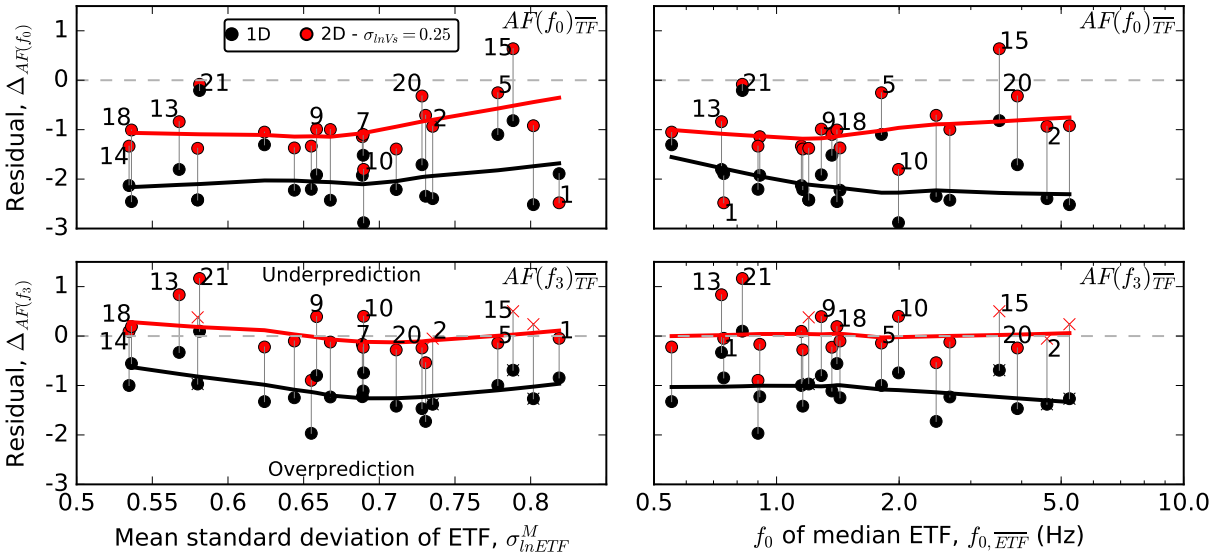

Figure 4.6: Total residuals of $AF(f_0)$ (top) and $AF(f_3)$ (bottom) for 1D and 2D analyses as a function of σ^{M}_{ETF} (left) and $f_{0,\overline{ETF}}$ (right). The 2D results are for compliant base models with the derived incident motion, and $\sigma_{lnVs} = 0.25$. Residuals are computed using amplification factors (i.e., peaks) of median TTFs and ETFs [i.e., $AF(f_0)_{\overline{TF}}$]. For sites with an 'x' symbol in $AF(f_3)$ plots, $AF(f_2)$ residuals are plotted because $f_3 > 20$ Hz or there is a large discrepancy between $f_{3,\overline{ETF}}$ and $f_{3,\overline{TTF}}$ (only site 19, see Section 4.3.1.2). Annotations next to certain markers represent site serial numbers.

and median TF IMs are very good for f_1 to f_3. Notable improvements are realized at f_0 as well, except for Site 1 (Borrego Valley; Figure 4.7a), for which the overprediction at f_0 and f_1 is more severe for 2D models than 1D analyses. This exacerbated overprediction at f_0 for 2D models occurs only at a two sites (SSNs: 1, 7) with large impedance ratios (R_V) and low f_0.

Borrego Valley demonstrates remarkable event-to-event variability in ETFs and ETF IMs (Figure 4.3), which results in a particularly "flat" median transfer function. This variability suggests that soil deposits at this site could be significantly heterogeneous or the wavefield incidence is not 1D/vertical. The fact that f_0 is so severely overpredicted could be an indication that the velocity contrast may not be as abrupt as represented in the V_S profile (i.e., $R_V = 12.2$), the velocity structure is oversimplified, or there are more complex 2D/3D phenomena that are not captured. This site is an example of how this 2D method is generally not capable of significantly scattering and influencing frequencies corresponding to such low frequencies and/or long wavelengths, especially because f_0 is often controlled by the depth to bedrock (or depth of the sensor for pseudo-resonances) which is assumed to be constant across the 2D model. The

phenomena that would influence this behaviour likely occur at length-scales much larger than the length-scales of heterogeneities considered here (i.e., $r_H = 50$ m and $r_V = 5$ m), such as phenomena attributed to the non-vertical incidence of wavefields. As discussed previously, the 2D models considered in this study do not capture deterministic 2D features of the site conditions, which may be influencing the observed site response. Therefore, this 2D method with randomized 2D spatial variability is not capable of resolving prediction issues related to these deterministic 2D/3D site complexities.

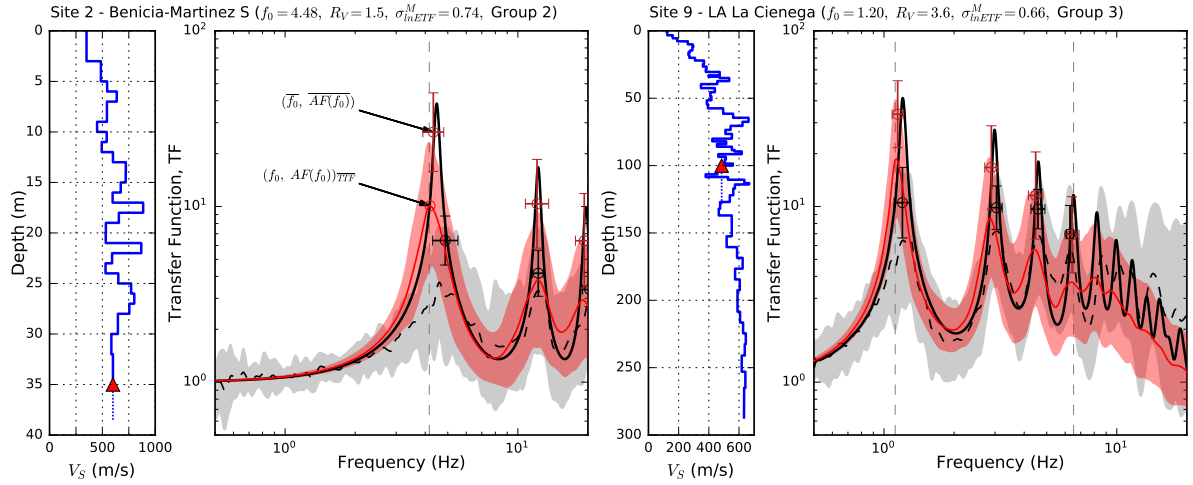

(a) Sites 2 (Benicia-Martinez; left) and 9 (LA La Cienega; right) with moderate values of σ^M_{lnETF}.

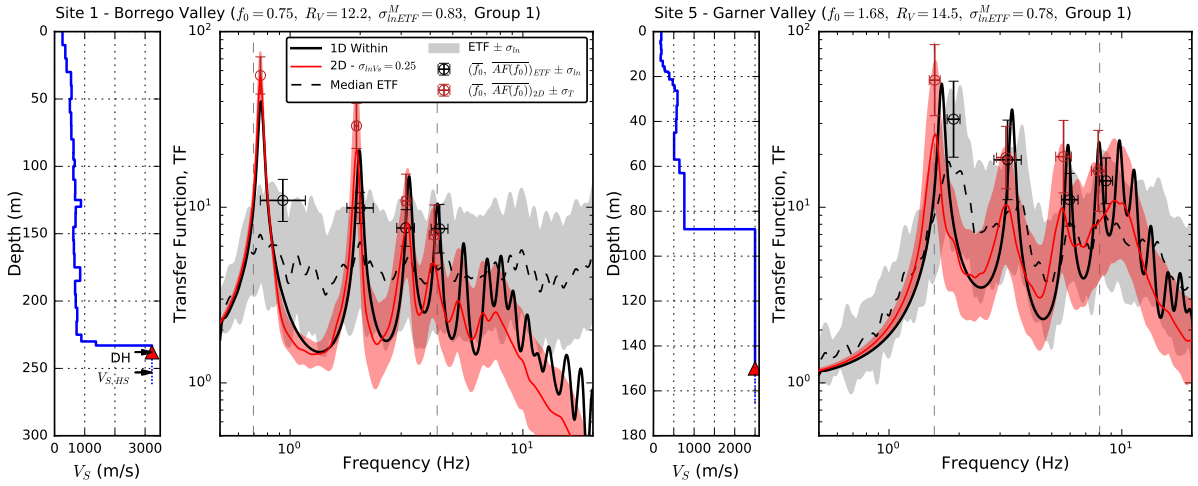

(b) Sites 1 (Borrego Valley; left) and 5 (Garner Valley; right) with high values of σ^M_{lnETF}.

Figure 4.7: V_S profiles and median TFs for sites where the 2D approach generally improves TF predictions (except for Site 1 at low frequencies). These sites have (a) moderate to (b) high values of σ^M_{lnETF}. $V_{S,HS} = V_S$ of the visco-elastic halfspace.

If σ^M_{lnETF} is indeed a good predictor of whether a site will behave one-dimensionally (e.g., Thompson et al., 2012; Pilz and Cotton, 2019; Afshari and Stewart, 2019), then an obvious question that arises when interpreting Figure 4.6 is: why do sites 13 and 21 demonstrate nearly 1D response while sites 14 and 18 are better represented by 2D analyses when they all have the lowest values of σ^M_{lnETF}? V_S profiles, and median TFs with TF IMs are plotted in Figure 4.8 to assess whether there are any distinct differences between these site pairs. V_S profiles for the "good" 1D sites (13 - Wildlife Liquefaction Array and 21 - Treasure Island; Figure 4.8a) are relatively less complex, and are some of the simplest profiles of the database (see Appendix C.6). Cheng et al. (2021) and Hallal and Cox (2021a,b) found relatively low values of spatial and temporal variability in f_0 from H/V data at Treasure Island, which is consistent with these observations.

For Treasure Island and Wildlife Liquefaction Array, the 2D method significantly under-predicts peaks of median TFs for higher modes (f_2 and f_3) suggesting that the level of heterogeneity considered in this study ($\sigma_{lnVs} = 0.25$ for Figure 4.8) over-represents the actual soil variability of these rather 1D and uniform sites. On the contrary, V_S profiles for sites 14 and 18 have visibly more complexity in soil (site 14) and bedrock (site 18) conditions. These sites have exceptionally flat ETFs, unlike sites 13 and 21. The lower amplitudes of $\overline{ETF}$ peaks are better represented by the 2D approach. While σ^M_{lnETF} is low for sites 14 and 18, they have above average standard deviations σ_{f_0} and σ_{f_1}, respectively. In contrast, sites 13 and 21 have rather low standard deviations of modal frequencies (e.g., σ_{f_3} and σ_{f_4} are nearly zero for Treasure Island). These findings suggests that there could be complexities in soil properties that are not fully represented by σ^M_{lnETF}.

An important detail to emphasize here is that, for all sites, only results of 2D analyses with $\sigma_{lnVs} = 0.25$ are shown in Figures 4.7 and 4.8. As σ_{lnVs} approaches zero (i.e., no heterogeneity is applied), the results from 2D analyses approach those from 1D analyses. The trend towards 1D results can be seen in Appendix C Section C.6, which plots results of analyses with $\sigma_{lnVs} =$ 0.15 and 0.25 for all sites. The strength of the V_S perturbations, σ_{lnVs}, and other random field input parameters (i.e., r_H and r_V) should be treated as site specific because, in reality, sites will display varying degree of influence from heterogeneities. Analyses of H/V spectral ratios by Hallal and Cox (2021a) (their Figure 12) indicate that σ_{f_0} is highly site dependent, which is

consistent with the sentiments described here. Whilst developing site-specific random field input parameters is the goal of many researchers (e.g., Popescu, 1995; Bong and Stuedlein, 2017; Ching et al., 2018), it is outside the scope of this study. Rigorous quantification of the level and nature of heterogeneities at a particular site from in-situ testing is a challenging undertaking, which could significantly improve results for these type of analyses.

The double f_0 peak of Treasure Island (Site 21; as discussed in Section 4.3.1.1), and the unusually flat ETFs for Foster City (Site 18) are both represented in TTFs to some extent, although not to the extent of ETFs. Treasure Island is one of four sites that displays a double peak in $\overline{TTF}$ and Foster City is the flattest of all $\overline{TTF}$s. This indicates that some of the 2D/3D phenomena caused by the inherent velocity structures of these 1D V_S profiles may actually be partially represented by allowing these multidimensional phenomena to take place in the 2D analyses. On the contrary, these complexities are not represented at all in 1D analyses.

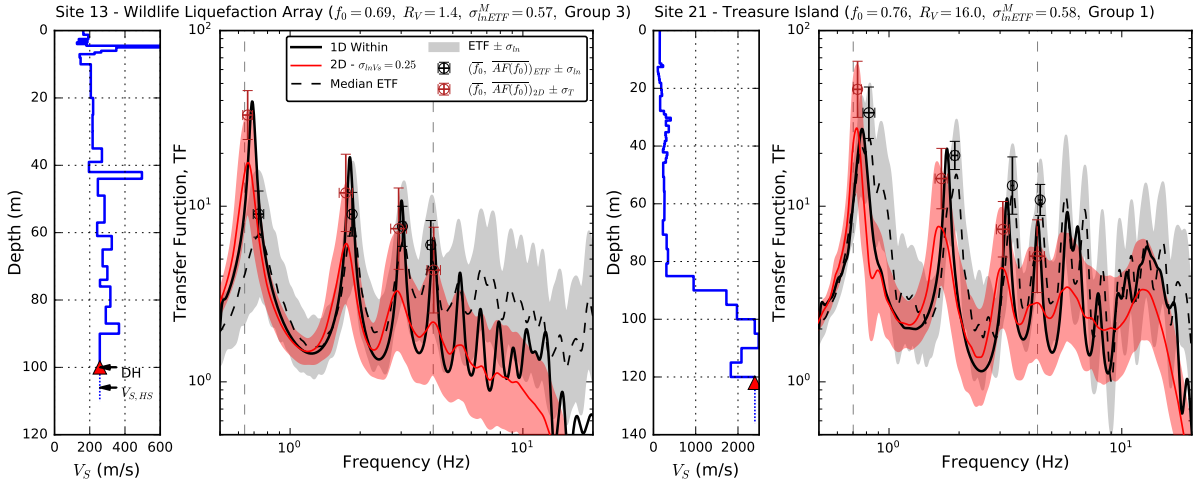

(a) Sites 13 (Wildlife Liquefaction Array; left) and 21 (Treasure Island; right) which display "1D" behaviour.

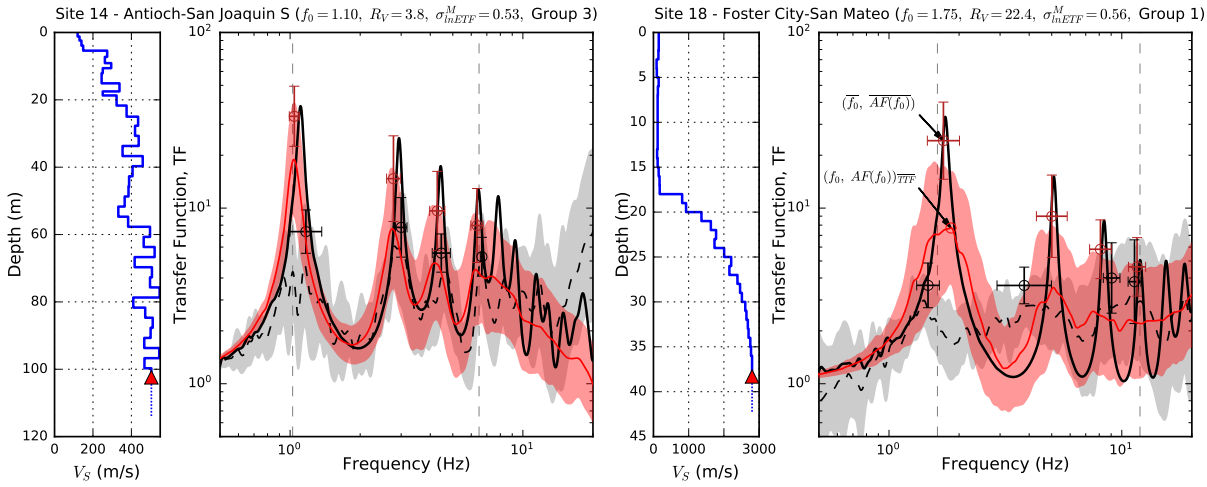

(b) Sites 14 (Antioch-SanJoaquin; left) and 18 (Foster City-San Mateo; right) which display behaviour significantly different from "1D".

Figure 4.8: V_S profiles and median TFs for sites with low σ^M_{lnETF} that display (a) good "1D" behaviour and (b) behaviour significantly different than the "1D" response.

4.3.1.4 Estimates of TTF and ETF Variability

Event-to-event variability of ETFs are compared to within-realization and total standard deviations from TTFs for all sites in Figures 4.9 and 4.10. While the sources of uncertainty are different for TTFs and ETFs, it is hypothesized here that these uncertainties are related and are controlled by the same phenomena of soil spatial variability. ETF variability arises because different earthquakes send waves through the site in different directions, thereby sampling variable soil properties. This mechanism is approximated in TTFs by varying the soil properties and sending 1D vertically propagating waves through the variable properties.

Standard deviations for modal frequencies (f_0 to f_3; Figure 4.9), and their respective amplification factors ($AF(f_0)$ to $AF(f_3)$; Figure 4.10) are plotted as a function of modal frequency. For example, in Figure 4.9 the top panels are for standard deviations of f_0, where σ_{f_0} is plotted against $\overline{f_0}$. The left column plots within-realization standard deviations (σ_{W,f_0}), and the right column total standard deviations (σ_{T,f_0}). The data for ETF are the same for both left and right columns. Each data point on the plots represents one site, and the trend lines indicate average trends across all sites.

In interpreting Figure 4.9, it is observed that for f_0 and f_1, the event-to-event variability in observations (ETFs) is significantly greater than σ_W and σ_T from TTFs. As discussed in previous sections, Borrego Valley (Site 1) has exceptionally large variability in ETF. This is shown here with it having a higher σ_{f_0} than any other site. This exceptionally high value of σ_{f_0} is caused because the actual f_0 peaks in individual ETFs are actually composed of at least two distinct peaks, and therefore the location of peaks around this frequency range vary greatly. This double peak and large variability in f_0 are suspected to be caused by phenomena that are not currently accounted for in the adopted 2D simulations (and may occur on much larger length scales than what are represented by the heterogeneities in this study).

The large discrepancy between σ_{f_0} of ETFs and TTFs is consistent with the fact that the TTF at f_0 significantly overpredicts amplification factors $AF(f_0)$. There is less influence from averaging and wave scattering in the 2D models at these long wavelengths, as indicated by the lower standard deviations. For higher modes (f_2 and f_3), there is a good match between ETF and TTF standard deviations. For both ETF and TTF, there is an increasing trend in σ_{f_0} with increasing f_0 which is consistent with the discussion in Section 4.3.1.1.

Figure 4.10 plots results in the same format, but for $\sigma_{AF(f_0)}$. There is more consistency between ETF and TTF standard deviations for amplification factors than was observed above for f_0 and f_1. However, while a strong increasing trend in $\sigma_{AF(f_0)}$ with increasing f_0 is seen in TTFs, there is essentially no trend for ETFs (i.e., the mean trend is nearly horizontal). Comparing between Figures 4.9 and 4.10, the standard deviations for amplification factors are approximately 5 to 10 times larger than those for frequencies.

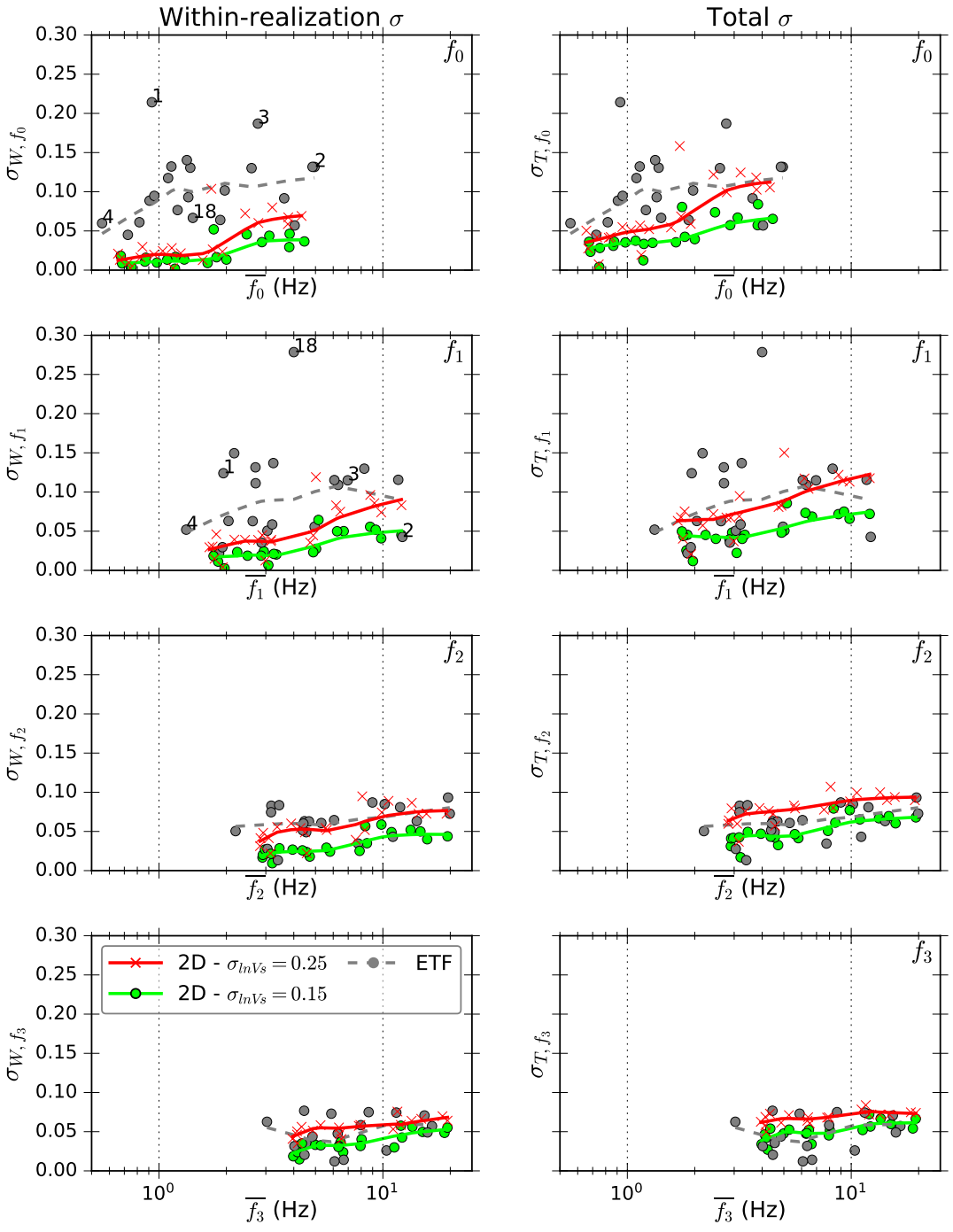

Figure 4.9: Comparison of event-to-event variability in ETF IMs to within-realization (σ_W; left) and total (σ_T; right) standard deviations of 2D TTF IMs. Standard deviations for f_0 to f_3 are plotted versus frequency. Results include 2D analyses with $\sigma_{lnVs} = 0.15$ and 0.25.

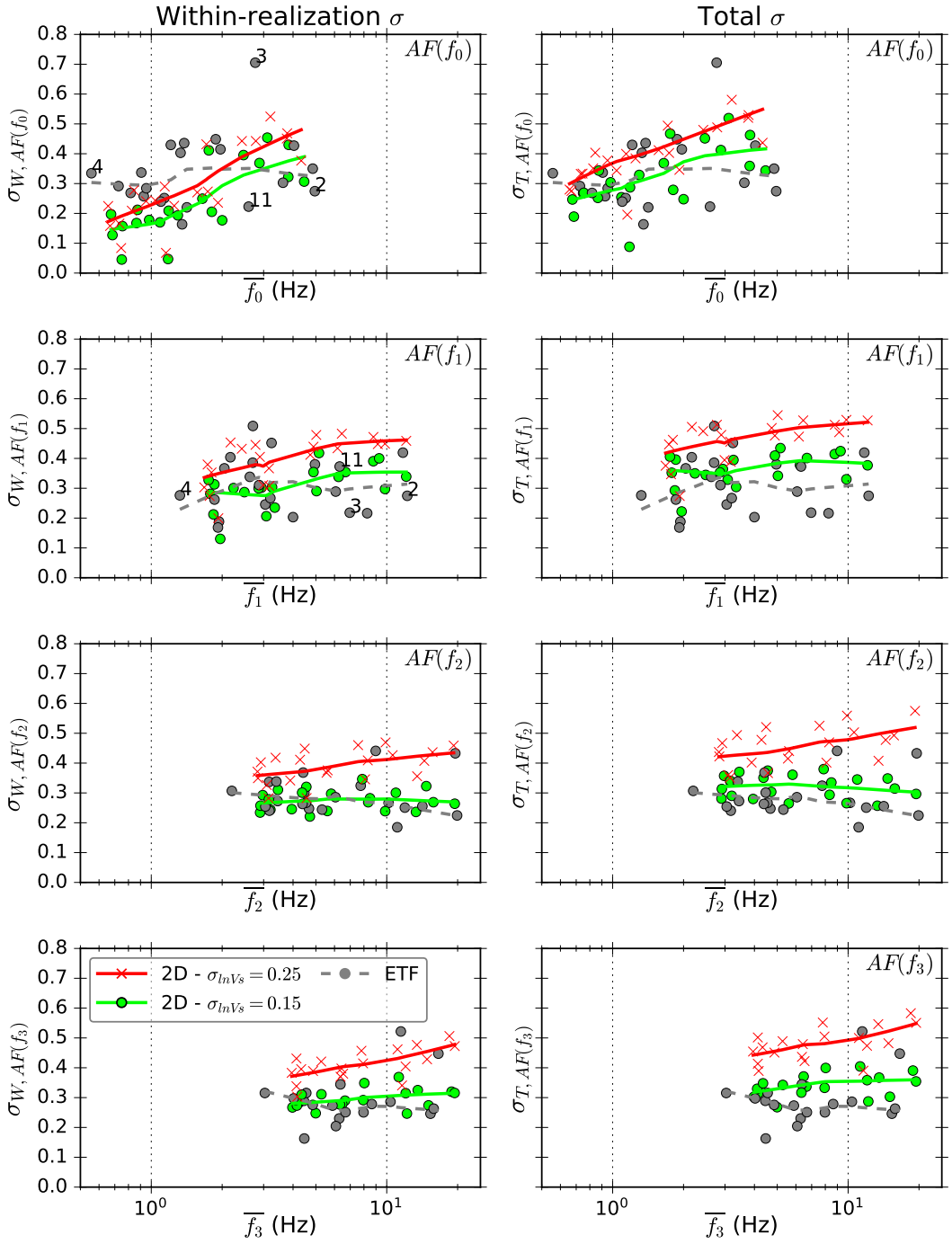

Figure 4.10: Comparison of event-to-event variability in ETF IMs to within-realization (σ_W; left) and total (σ_T; right) standard deviations of 2D TTF. Standard deviations for $AF(f_0)$ to $AF(f_3)$ are plotted versus the respective modal frequency. Results include 2D analyses with $\sigma_{lnVs} = 0.15$ and 0.25.

4.3.2 Residuals of Ground Surface IMs

4.3.2.1 Overall Model Bias

The overall model bias across all events and sites considered is plotted in Figure 4.11. The figure includes results for 1D analyses, and 2D analyses of compliant base models with the derived incident motion. Bias for spectral accelerations is in the left panel and on the right are several other IMs (PGA, PGV, I_a, CAV, D_{S575}, and D_{S575}). Both 1D and 2D models overpredict spectral accelerations over the full period range, and all other IMs (especially I_a and CAV). Stewart and Afshari (2021) also observed overprediction at $T < 0.1$ s when using laboratory-based D_{min} values. However, Stewart and Afshari (2021) have an average bias closer to zero for $0.1 < T < 10$ s. The frequency range of interest for most of the sites considered (i.e., f_{min} to f_{max} based on f_0 and f_3) lie between approximately $0.1 < T < 1$ s. The overprediction in this frequency/period range, which would also influence SAs at periods outside this range (see Bora et al., 2016), is likely due to the full Rayleigh damping formulation. The target damping ratio is set to 1 % at f_0 and f_3, but this would lead to damping values lower than lab-based D_{min} estimates between f_0 and f_3. These results, along with those of many other studies (e.g., Zalachoris and Rathje, 2015; Kaklamanos et al., 2015; Afshari and Stewart, 2019; Stewart and Afshari, 2021) show the significant influence of damping assumptions on SA predictions. Results in Zalachoris and Rathje (2015) and Kaklamanos et al. (2015), who used higher damping values to match median ETFs, show underprediction at short periods for Japanese KiK-Net databases. When Stewart and Afshari (2021) used the V_S-based damping values, which were comparably high, for their California database, they observed similar underprediction.

There is a negligible difference between the 1D rigid base analyses and 2D analyses with the computed incident motion. This is because the response in this 2D model is dominated by the input motion which used a 1D model to "deconvolve" the observed within motion into its corresponding incident motion. As Stewart and Afshari (2021) pointed out, further insights can be gained when vibration periods are normalized by each site's respective fundamental period. Conclusions based on biases averaged across all sites do not precisely reflect the actual trends for individual sites or the severity of bias at T_0. However, they can reflect overall trends in

prediction capability, such as the fact that there is clearly insufficient damping in these models.

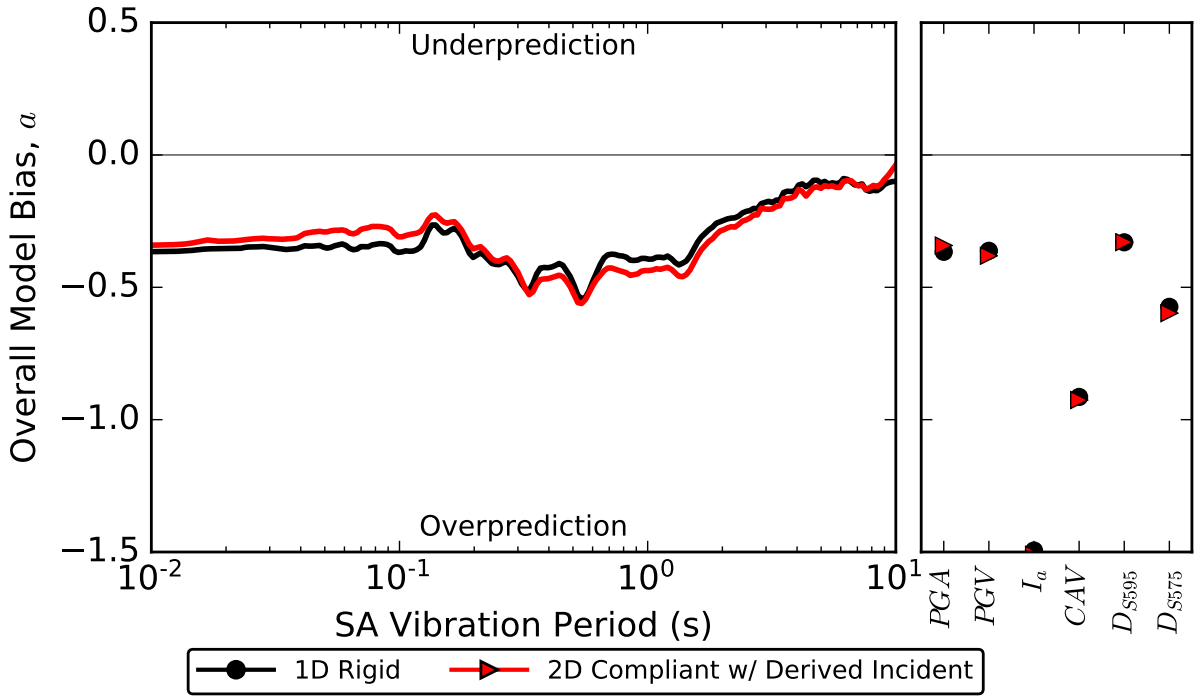

Figure 4.11: Overall model bias from 1D and 2D analyses for $SA(T)$ (left) and other IMs (right). Input motions for 2D compliant base analyses are: (1) the computed incident motion from DH motion (red) and (2) the DH motion used as incident motion (magenta).

4.3.2.2 Total Residuals for Individual Sites and Groups

In Figure 4.12, individual site total residuals are plotted versus normalized period (i.e., vibration period normalized by the site's T_0 based on its within TTF). The sites are subdivided into three groups (Table 4.1), and both individual site residuals and group medians are plotted. It becomes clear that the overpredicting bias discussed above (Section 4.3.2.1) was caused by severe overprediction at T_0 at most sites, which is consistent with the results of Stewart and Afshari (2021). As observed in the previous section, the differences between 1D and 2D analyses are minor, likely because the 2D analyses still rely on the 1D assumption, as 1D models were used to derive the input incident motions. Another reason for this negligible difference could be the inconsistency in f_0 between ETF and TTF (see Figure 4.5). This would result in slightly different positions (i.e., periods) of the peaks in response spectra of observed and predicted surface motions. This is one of the reasons for evaluating amplification factor residuals, independent of

the frequency at which they occur, in previous discussion sections related to Transfer Functions (Section 4.3.1).

For sites with pseudo-resonances at $T_{0,within}$, (i.e., Group 2 and 3 sites), the overprediction at T_0 is even stronger. One of the key identifying features of a pseudo-resonance is that an outcrop transfer function displays essentially no amplification at $f = 1/T_{0,within}$, while the within transfer function may display large amplification at this frequency (see Tao and Rathje, 2020a,b, for further details). This effect is clearly visible in the transfer functions plotted in Appendix C.6 for Group 2 and 3 sites (e.g., Figure C.28). The reason for this difference between outcrop and within transfer functions is that this frequency does not actually correspond to any particular impedance contrast in the soil profile, and therefore, the soil profile does not amplify these frequencies. The "amplification" at T_0 observed in within transfer functions is purely due to the destructive interference of up-going and down-going waves. While this large amplification observed at pseudo-resonances in within transfer functions may not be attributed to a significant velocity contrast, peaks are still generally observed in ETFs at $f_{0,within}$. This suggests that the destructive interference of up-going and down-going waves is a real phenomenon that occurs in the field, albeit not to the extent predicted by a 1D model. Tao and Rathje (2020a) developed a taxonomy to differentiate pseudo-resonances from true-resonances, and provide a more detailed discussion on this topic than is provided here.

For Group 1 sites (top panels in Figure 4.12) T_0 is controlled by a strong impedance and not a pseudo-resonance. For these sites we would also expect less down-going wave effects as down-going waves will reflect back up to the surface from these abrupt interfaces (e.g., Bonilla et al., 2002). Less bias is observed for these sites across the full period range, with significantly less bias at $T_{0,within}$. Much better agreement is also observed between the outcrop and within TTFs, due to the fact that the amplification at f_0 is controlled by an actual velocity contrast. In fact, it would appear that as the conditions become more favourable for destructive interference between up-going and down-going waves (from Group 1 to 3 to 2), there is more discrepancy between the outcrop and within TTFs. The 1D rigid base and within input motion combination appear to be more reasonable for sites with large impedance contrasts (i.e., Group 1) at which $f_{0,within}$ is controlled by a true-resonance and not a psuedo-resonance.

These destructive interference effects, which are much more exaggerated in 1D analyses than in observed ground motions, present a great challenge in the interpretation of vertical array observations and simulations. As alluded to previously, while the residuals in Figure 4.12 suggest large overprediction at T_0 for Groups 2 and 3, in forward analyses, which typically utilize a compliant base with an incident input motion, the pseudo-resonant frequencies will generally experience no amplification as they propagate through the soil column. Based on these results, it appears it is the rigid base assumption, or the method of computing input motions which relies on a 1D within TF, that produces excessive bias at T_0. This does not necessarily mean that the 1D method is unfit for modelling the site response at these sites, especially when the majority of practical site response applications use the compliant base and incident motion conditions. Previous studies of vertical array sites have generally ignored this and proceeded to compute goodness-of-fit parameters (e.g., Pearson correlation coefficient) between the ETFs and within TTF, even for sites that have a pseudo-resonance at $f_{0,within}$. This approach is justifiable given that the within boundary condition is theoretically the correct assumption for the vertical array conditions, however, the discrepancy between sites that have a pseudo-resonance at f_0 versus those that have a true resonance should be considered when judging the performance of site response techniques. Perhaps one way to account for this, while maintaining fidelity to the correct boundary condition assumptions (i.e., the within condition), is to ignore or exclude these pseudo-resonances when calculating goodness-of-fit parameters.

Additional insights into the performance of these site response models can be made by removing the overall model bias, a, from the mean total site residual (see Equation 4.6). Figure C.4, in Appendix C, plots these bias-corrected site terms in the same format as Figure 4.12. As discussed in Section 4.3.2.1, this overall model bias is likely significantly contributed to by underdamping from the Rayleigh damping formulation with a low D_{min} value of 1 % based on laboratory data. Once this bias effect is removed, some interesting trends are observed.

For Group 1, which was shown to have less down-going wave effects and not be controlled by a pseudo-resonance at T_0 (due to large a large impedance contrast), the site terms (top panels of Figure C.4) are close to zero at T_0. This suggests that the amplifications across these large impedance contrasts are actually captured relatively well when effects such as the underestimation of damping are removed. For forward predictions, this is perhaps the most significant

aspect to critique about these models. For Groups 2 and 3, which are generally controlled by a pseudo-resonance at T_0, there is still significant overprediction at T_0, which is expected based on interpretation of median ETFs and the previous discussion in this section. For all groups, the bias-corrected site terms indicate little prediction error for $T < T_0$, suggesting that predictions in this period range can be improved by correcting issues such as the low values of D_{min}.

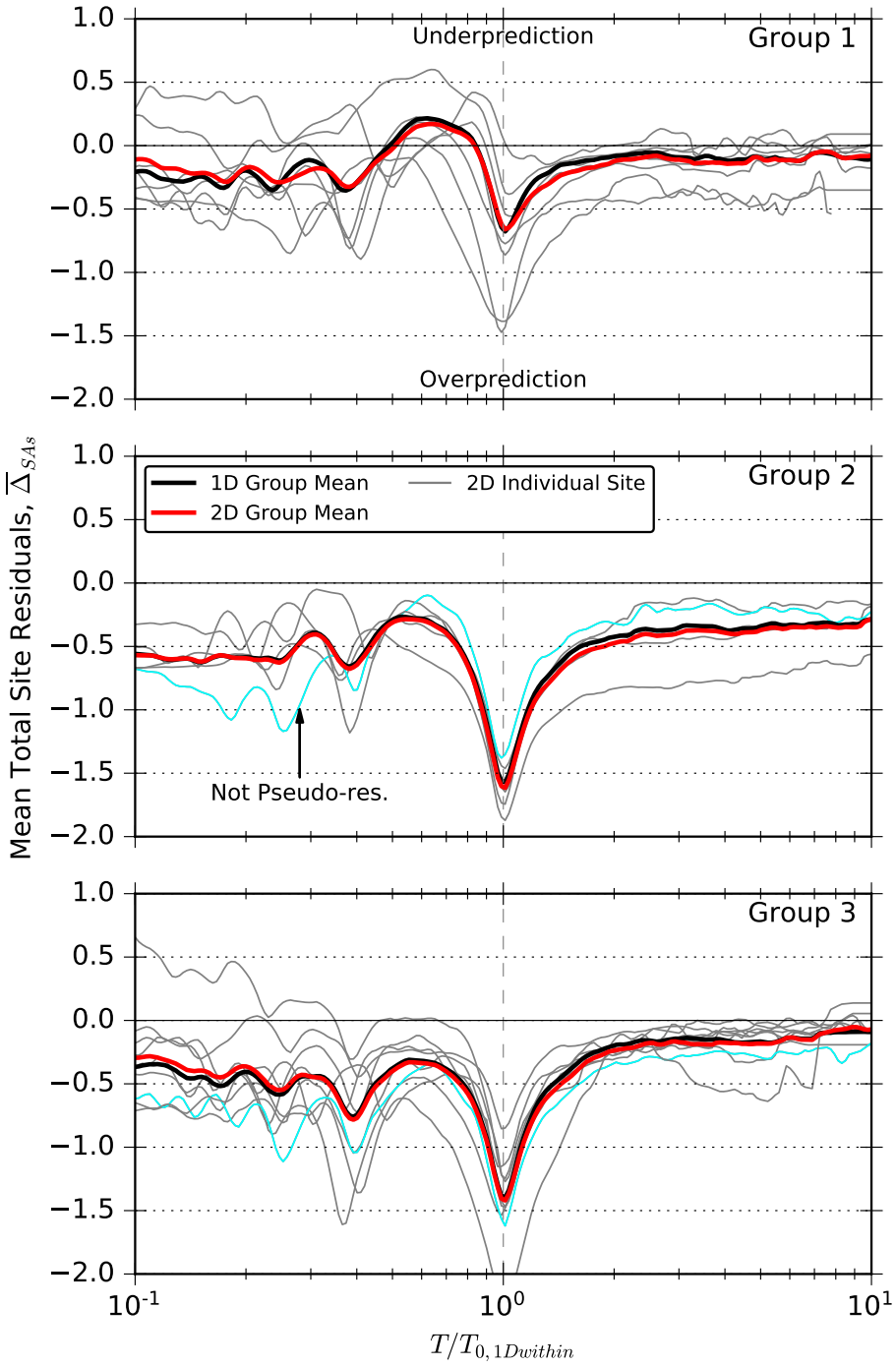

Figure 4.12: Mean total site residuals of spectral accelerations versus normalized period $T/T_{0,1Dwithin}$ for 1D and 2D analyses. The 1D analyses are rigid-base models with the recorded within (i.e., downhole) input motion, and 2D analyses are compliant-base models with the derived incident motion. All sites are divided by groups (Table 4.1) and group averages are plotted along with individual site residuals.

4.3.2.3 Estimates of Surface IM Uncertainty from 2D Models

Within-realization (σ_W) and total (σ_T) standard deviations for all IMs are plotted against impedance ratio (R_V) in Figure 4.13. All sites are included in each panel, with the left panels being for σ_W and the right panels for σ_T. These results quantify the spatial variability of IMs along the ground surface, and the epistemic uncertainty from V_S site characterization. As expected from previous studies (e.g., de la Torre et al., 2021), σ_W and σ_T increase with increasing strength of the heterogeneities (i.e., σ_{lnVs}). Note the different y-axis scales for each IM. The standard deviations for I_a, which range from about 0.2 to 0.4, are significantly greater than for other IMs which are closer to 0.1 to 0.2. In this study there are now many different site conditions, so results can be plotted as a function of various site parameters. A trend of increasing σ_W and σ_T as a function of R_V is visible in Figure 4.13. This may be because the reflections of down-going waves, off of bedrock or a large impedance contrast, back toward the surface may be complicating the response at the surface. No notable trend as a function of f_0 was predicted (See Fig C.8 in Appendix C).

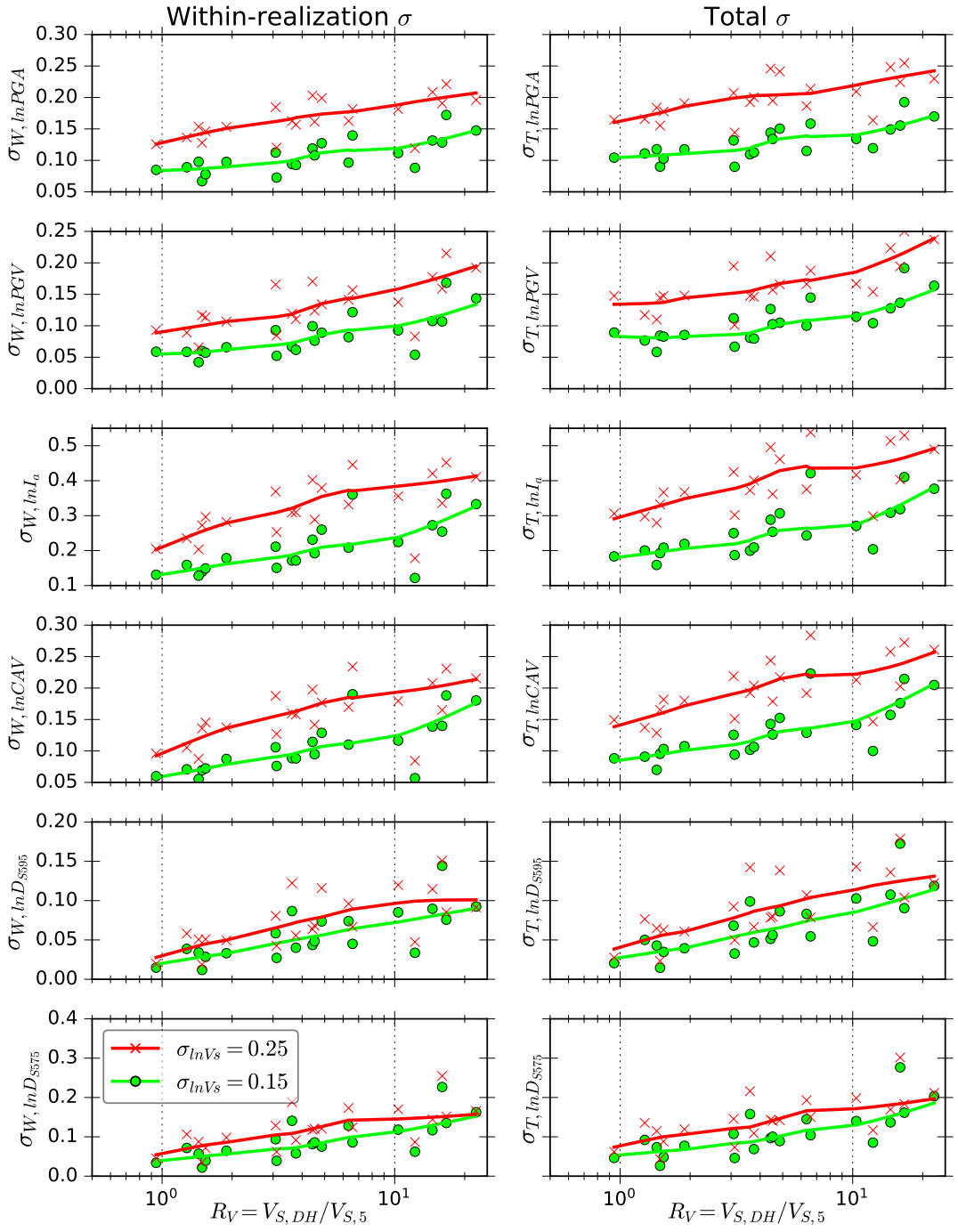

Figure 4.13: Within-realization (σ_W; left) and total (σ_T; right) standard deviations for surface motion IMs as a function of R_V for all sites with $\sigma_{lnVs} = 0.15$ and 0.25.

4.4 Conclusions

In this study, a method for modelling soil heterogeneity in 2D site response analyses via spatially-correlated random fields was applied to a database of 21 vertical array sites in California. Results were compared to those from conventional 1D analyses, and to observations recorded at the vertical arrays. The 2D method significantly improves predictions of median ETF peaks, especially for sites with a high f_0 and/or high variability in ETFs (i.e., high σ^M_{lnETF} or σ_{f_0}). This improvement is attributed to scattering of energy in time and space, as well as the spatial averaging of TTFs. The improvements to individual transfer functions (i.e., the average amplification factor at peaks of individual TFs, not the amplification factors of median TF peaks) is more modest. However, a reduction in amplification factors compared to 1D analyses is still realized. For sites that are especially-well modelled by a 1D approach, and appear to have relatively uniform and simple velocity structures (e.g., Wildlife Liquefaction Array and Treasure Island), 2D methods with generic levels of spatial variability may over-represent the heterogeneity and consequently underpredict amplifications at higher mode frequencies. This highlights the importance of developing site-specific random-field input parameters in future work, which was outside the scope of this paper.

The 2D analyses are capable of partially capturing some of the complexities, presumably attributed to multidimensional wave propagation, visible in ETFs. Examples of this are the double f_0 peak of Treasure Island (Site 21; as discussed in Section 4.3.1.1), and the unusually flat ETFs for Foster City (Site 18), which are both represented in TTFs to some extent, although not to the extent of ETFs. Treasure Island is one of four sites that displays a double peak in $\overline{TTF}$ and Foster City is the flattest of all $\overline{TTF}$s. Some of these effects visible in ETFs may be caused by the inherent velocity structures of these 1D V_S profiles, which may or may not be properly represented at all sites. On the contrary, these complexities are not represented at all in 1D analyses.

There are, however, complexities in ETFs at several sites that are not captured by this 2D method (e.g., the extremely high variability in f_0 at Site 1 - Borrego Valley). This has three implications regarding phenomena that are not adequately modelled. First, the 1D V_S profile

does not sufficiently represent the actual site velocity structure. Second, additional phenomena are not currently represented in these models (e.g., non-vertical incidence of wavefield). Third, other scattering phenomena are occurring at length-scales larger than what is modelled by the heterogeneities and domain extent of these 2D analyses. It is consistently observed that the 2D method has less influence on f_0 compared to higher modes. Interestingly, the opposite trend is observed in ETF, which have a higher standard deviation for f_0 than higher modes. This is likely because f_0 is often controlled or influenced by the depth to bedrock or the depth of the sensor. The disregard for fluctuations in bedrock depth or incidence-angle of the wavefield creates this limitation in modelling the observed variability in f_0.

Within-realization and total standard deviations of TTF IMs were compared to event-to-event standard deviations of ETF IMs. The former represents spatial variability (in the models), and the latter represents event-to-event variability (in the observations). However, it is likely that both are influenced by the phenomenon of waves propagating through complex and heterogeneous near-surface geologic structure. The observed and predicted standard deviations are generally consistent, except for σ_{f_0} which is greatly underestimated by 2D models. This again highlights that the 2D analyses do not greatly influence the phenomena that affects f_0 and that future work should consider these effects.

Residuals of surface ground motion IMs (including spectral accelerations) were also computed. Negligible differences were observed between 1D rigid base analyses and 2D analyses that use the derived incident motion. Most significantly, this is due to the reliance of computing the incident motion on a 1D transfer function, which greatly overpredicts the destructive interference of up- and down-going waves. Another reason could be the inconsistency in f_0 between ETF and TTF (see Figure 4.5). This would result in slightly different positions (i.e., periods) of the peaks in response spectra of observed and predicted surface motions. This is one of the reasons for evaluating amplification factor residuals, independent of the frequency at which they occur, in previous discussion sections related to Transfer Functions (Section 4.3.1).

The overall modal bias for spectral accelerations indicates a tendency for 1D and 2D models to overpredict over the full period range. This is consistent with previous studies that have found that using laboratory-based estimates of D_{min} underestimates the observed attenuation,

resulting in overprediction of the surface ground motion. Further investigation into total residuals for individual sites clearly shows that another significant contribution to the overpredicting bias is the overprediction at f_0 from the within TTF. This overprediction at $f_{0,within}$ is especially true for sites where this frequency corresponds to a pseudo-resonance (i.e., Groups 2 and 3 where the peak in the within TTF is due to destructive interference between up-going and down-going waves as opposed to impedance amplification from a large velocity contrast). As pointed out by Tao and Rathje (2020a), this overprediction at pseudo-resonances will not generally persist in practical applications of forward analyses, in which typically a compliant base with an incident input motion is used. This issue presents a challenge in interpreting vertical array observations and simulations, and should be considered when judging the performance of 1D and 2D site response modelling techniques.

4.5 Data and resources

The Afshari et al. (2018) database was downloaded from the DesignSafe-CI Data Depot. New Zealand eScience Infrastructure's (NeSI) high performance computing facilities and consulting support were used for all analyses and post-processing. More information is available at URL https://www.nesi.org.nz. All figures were generated in Python.

4.6 Acknowledgements

The authors thankfully acknowledge Kioumars Afshari for providing the data files of V_S profiles, and Peter Stafford for his input on the processing and interpretation of Fourier Amplitude Spectra. This work was financially supported by the University of Canterbury, and QuakeCoRE: The NZ Centre for Earthquake Resilience.

Chapter 5

Conclusions

In this dissertation, two distinct studies have been performed, both with the overarching goal of validating and improving site response predictions. The first (Chapter 2) relates to combining the results of 3D physics-based ground motion simulations with 1D nonlinear site response analyses. The objective was to incorporate 3D regional-scale wave-propagation phenomena in site response predictions, or, alternatively, to incorporate more rigorous site-specific effects into large scale 3D simulations. The second study (Chapters 3 and 4) was to incorporate the influence of soil heterogeneity and wave scattering on 2D site response. The following sections summarize the key contributions of this work and the implications for the field of site response analysis. Limitations of the studies and recommendations for future work to continue improving the methods are also provided.

5.1 Key contributions

5.1.1 Modeling Nonlinear Site Effects in Physics-Based Ground Motion Simulations of the 2010-2011 Canterbury Earthquake Sequence

Perhaps the most significant finding of Chapter 2 is that ground motion predictions using physics-based ground motion simulations rival those of conventional empirically-based ground

motion models (GMM). The overall model bias and uncertainty for a database of 11 events from the 2010-2011 Canterbury Earthquake Sequence at 20 strong motion stations are comparable between these two prediction methods, albeit, the GMM results in significantly more bias at periods longer than 5 seconds. Another benefit of the physics-based simulation method is that event- and site-specific time series for subsequent time history analyses are output, unlike predictions with a GMM which require a ground-motion selection process to identify candidate motions from historic events of other regions.

When comparing the wave-propagation site response method to the simpler empirical site amplification model for modelling site effects of simulated ground motions, significant improvements are only realized for a small number of sites that exhibit exceptionally strong site effects (e.g., sites HVSC and REHS). HVSC has a large impedance contrast close to the surface (Jeong and Bradley, 2017a), and REHS has a very soft organic silt layer approximately 8 m thick (Wotherspoon et al., 2014). For the remainder of the sites, the site response predictions are comparable and/or the improvements are clouded by uncertainty in the input motion (i.e., the simulated ground motions).

5.1.2 2D Geotechnical Site-Response Analysis including Soil Heterogeneity and Wave Scattering

This chapter developed a method for modelling soil heterogeneity in 2D site response analyses using spatially correlated random fields. A detailed parametric analysis was performed to understand the influence on the predicted site response from various random field input parameters, including standard deviation of V_S (σ_{lnVs}), vertical and horizontal correlation lengths (r_V and r_H), and the anisotropy factor ($a_{H/V} = r_H/r_V$). 1D randomized V_S profiles were also extracted from 2D V_S models and analysed in a 1D framework. By comparing results from 2D and 1D randomized analyses, the effects of 1D vertical heterogeneities, and smoothing of the median transfer function due to averaging can be isolated from those caused by 2D wave-propagation phenomena.

This method was found capable of scattering seismic waves and producing spatially varying ground motions along the ground surface. The effects of the heterogeneities increase with

increasing σ_{lnVs} as the heterogeneities become stronger. A clear relationship was observed between wavelength, length scale of the heterogeneities, and the potential for waves to be scattered. In the context of idealized single-layer soil profiles, for lower median V_S values and high frequencies (i.e., shorter wavelengths), and larger values of r_V (i.e., larger heterogeneity length scales) the influence of wave scattering becomes more pronounced and the variability in surface ground-motion increases. Given this relationship, IMs controlled by high frequencies (e.g., PGA and Arias intensity) were most influenced by the heterogeneities, and were generally reduced due to the energy of the ground motion being scattered in time and space.

While 1D randomized analyses ($1D_{Rand}$) were able to produce results that match 2D analyses for some lower frequency IMs (e.g., median transfer functions at $f < 10$ Hz, f_0, and $SA(T_0)$), medians and standard deviations of high-frequency IMs (e.g., transfer function at $f > 10$ Hz, *PGA*, and Arias intensity) were not appropriately captured. This is because these higher frequencies are influenced by 2D wave-propagation phenomena, such as wave-scattering, which are not accounted for in a 1D framework. The $1D_{Rand}$ models produce higher median values of *PGA* and Arias intensity, but underpredict their total standard deviations.

Overall, this method was considered a viable way to consider more complex multi-dimensional phenomena and improve site response predictions. Therefore, the method was extended to the validation study of Chapter 4.

5.1.3 Can Modelling Soil Heterogeneity in 2D Site Response Analyses Improve Predictions at Vertical Array Sites?

Chapter 4 extended the 2D site response approach developed in Chapter 3 to vertical array sites. A database of 21 sites in California was chosen to use for validation of the elastic behaviour of 2D site response including soil heterogeneities. Clear improvements in the prediction of median empirical transfer functions (ETF) were observed with the 2D method, especially for sites with high f_0 and/or high event-to-event variability in ETFs (i.e., high σ^M_{lnETF} or σ_{f_0}). For two sites that display exceptionally good 1D behaviour (Treasure Island and WLA), the 2D method actually performs worse than the 1D method. For these sites, higher modes (i.e., f_2 and f_3 are significantly underpredicted when the 2D approach is used, suggesting that the

level of heterogeneity considered in the models may overrepresent the spatial variability of soil properties in these more uniform sites. Event-to-event standard deviations of ETFs and ETF IMs are comparable to within-realization and total standard deviations of theoretical transfer functions (TTFs) and TTF IMs, except for σ_{f_0} which is greatly underestimated in 2D models. f_0 is typically controlled by the depth to bedrock or a large impedance contrast, and corresponds to larger wavelengths than what is modelled in 2D heterogeneities. The 2D models have less influence at f_0 than at higher modes because the depth to bedrock is maintained constant across the width of the model. For this reason, generally greater improvements are observed at higher mode frequencies.

To better understand down-going wave effects, such as the destructive interference observed in 1D within motions and pseudo-resonances, surface ground motions and IMs for 2D models were calculated using two input motion assumptions. The first used a 1D incident/within transfer function to approximate the observed incident motion, and the second assumes that the observed DH motion is the incident motion. The former input motion (which is equivalent to a 1D rigid base analyses without the presence of heterogeneities) severely overpredicts SA at T_0, especially for sites controlled by a pseudo-resonances. On the contrary, the later input motion results in essentially no bias at T_0. This highlights the great sensitivity of results to boundary condition assumptions, and the severity of the overprediction of the destructive interference in the within motion from 1D analyses. As suggested by Tao and Rathje (2020b), it is important to consider these differences and identify pseudo-resonances when interpreting the ability for site response methods to predict the surface motion. This is especially true because forward predictions of site response using outcrop motions generally do not rely on a rigid base or a 1D within TF, both of which predict near-perfect destructive cancellation of the up- and down-going waves resulting in severe over-amplification in a forward analysis.

The overall model bias indicates overprediction of spectral accelerations across the full period range and all other IMs. As many other previous studies have shown (e.g., Thompson et al., 2012; Kaklamanos et al., 2015; Kokusho, 2017; Afshari and Stewart, 2019; Tao and Rathje, 2019), laboratory-based minimum damping values (D_{min}), underestimate the attenuation observed in vertical arrays, even for weak elastic ground motions. The use of slightly higher D_{min} would undoubtedly improve predictions, but the aim of this study was to model such

energy dissipation or attenuation mechanisms explicitly by incorporating soil heterogeneity. Reductions in amplification factors of transfer functions are observed through modelling these heterogeneities, especially when averaging spatially across many locations. However, there is room for improvement through future work, such as accounting for fluctuations in bedrock depth and layer thickness, and the non-vertical incidence angle and spatial variability of the incident wavefield.

5.2 Recommendations for future work

5.2.1 Modelling Pore Pressure Generation at Liquefiable Christchurch Strong Motion Stations

As discussed in Chapter 2, only total-stress site response was considered in this study, that is, the influence of pore pressure generation and liquefaction was neglected. An obvious extension is to use effective-stress site response analyses to model these effects. While the large majority of sites did not display any manifestation of liquefaction in most events, there are sites that had minor to severe liquefaction manifestation in the Christchurch, 2011 M_W6.2 earthquake (Bradley, 2012; Wotherspoon et al., 2014). These sites were CHHC, CMHS, HPSC (severe in both Darfield and Christchurch earthquakes), PRPC, and SHLC. While the generation of pore pressure at these sites does not significantly influence the overall model bias (for all site and events considered), there may be room for considerable improvements at these sites by considering effective-stress site response. Phrased in a slightly different way: the question of whether the use of 3D simulated ground motions can improve effective-stress site response predictions at liquefiable sites is a topic that is definitely worth exploring.

5.2.2 Refinement of 3D Simulations and Extension to Other Regions

In Chapter 2, it was also found that the uncertainty in the input motions (i.e., the simulated motions) is large enough that it is difficult to truly perceive improvements from the specific method used to predict site effects at the majority of sites considered. Since the time the simu-

lations for this study were run, improvements and refinements have been made to the simulation methodology (e.g., Lee et al., 2020, 2021). It would be interesting to re-assess the results of this study using refined simulations, ideally with less bias and uncertainty, and considering the effects of pore pressure generation. Additionally, this study can be extended to other regions of interest, such as in Wellington, where the complex basin geometry and variable near-surface soils create highly spatially varying motions across the city.

5.2.3 Incorporating the Effects of Variable Bedrock Depth and Actual 2D Soil Layering in 2D Analyses

The 2D method implemented in Chapters 3 and 4 does not account for any lateral variations in the depth of each layer boundary, including the depth to bedrock. Hallal and Cox (2021a,b) have highlighted that the depth to bedrock has a significant influence on the average response of a site. These effects are especially pronounced at f_0, which is intuitive given that f_0 is often controlled by the depth to bedrock or a major impedance contrast. As discussed in Chapters 3 and 4, this 2D approach does not significantly influence the response at f_0 because the lengthscales of heterogeneities considered here are not large enough to influence the long wavelengths corresponding to f_0. Accounting for variability in bedrock depth in these 2D models is a relatively trivial extension, assuming that a 2D/3D velocity model, such as those in Hallal and Cox (2021a,b), is available for the site. It should be noted that developing such a 2D/3D V_S model is far from trivial, and requires significant experience and field data. However, a systematic study to understand the extend to which this may improve predictions would be valuable.

5.2.4 Incorporating the Effects of Non-Vertically Incident Wave-Fields and the Spatial Variability of Input Motion on 2D Site Response

While the extension discussed above to consider fluctuations in bedrock depth is a large undertaking, as it requires an accurate 2D V_S model, there are simpler ways to account for these large scale wave propagation phenomena in a 1D or 2D context. As in Thompson et al. (2009,

2012), the assumed incidence angle of the wavefield can be modified in a 1D or 2D framework to be non-vertical. Conventional site response analyses, including the 2D analyses performed in this dissertation, consider the incidence angle of the wavefield to be vertical. Thompson et al. (2009, 2012) have observed improvements in predictions by considering modifications in the incidence angle. The idea is that the incidence angle of the wavefield will not necessarily be perfectly vertical for all events and that slight variations in the incidence angle may help improve predictions at certain sites.

In a similar manner, the incident ground motion at the depth of the bottom of the model will not be perfectly uniform along a distance of 1 km (i.e., the width of the 2D models), as is assumed in these 2D models. Just like the ground motion varies along the surface of the 2D models analysed here, the incident motion at depth, in reality, would vary spatially. The spatial variability of the incident motion can be accounted for by modelling the incoherence of ground motions using a simplified model such as that presented in Ancheta et al. (2011).

5.2.5 Site-Specific Quantification of Soil Heterogeneity for Random Field Generation

As explained in Section 4.3.1.3, the level of heterogeneity varies from site to site, therefore, the random field input parameters (including the strength of the heterogeneity) should ideally be site-specific. This study only considers generic values of $\sigma_{lnVs} = 0.15$ and 0.25 for all sites. While developing site-specific random field input parameters was outside of the scope of this study, it is the goal of many research studies (e.g., Popescu, 1995; Bong and Stuedlein, 2017; Ching et al., 2018). Rigorous quantification of the level and nature of heterogeneities at a particular site from in-situ testing is a challenging undertaking, which could significantly improve results for these type of analyses.

Appendices

Appendix A

Appendix to Chapter 2

A.1 Summary

This section presents the appendix to Chapter 2: Modeling Nonlinear Site Effects in Physics-Based Ground Motion Simulations of the 2010-2011 Canterbury Earthquake Sequence.

A.2 Earthquakes and Sites Considered Supplementary Tables and Figures

Table A.1: Earthquake events considered from the 2010-2011 Canterbury Earthquake Sequence.

Event Date	M_W	Event ID
4 September 2010	7.1	1
19 October 2010	4.8	2
26 December 2010	4.7	3
22 February 2011	6.2	4
16 April 2011	5.0	5
13 June 2011 (1:01 p.m.)	5.3	6
13 June 2011 (2:20 p.m.)	6.0	7
21 June 2011	5.2	8
23 December 2011 (12:58 p.m.)	5.8	9
23 December 2011 (2:18 p.m.)	5.9	10
14 February 2016	5.8	11

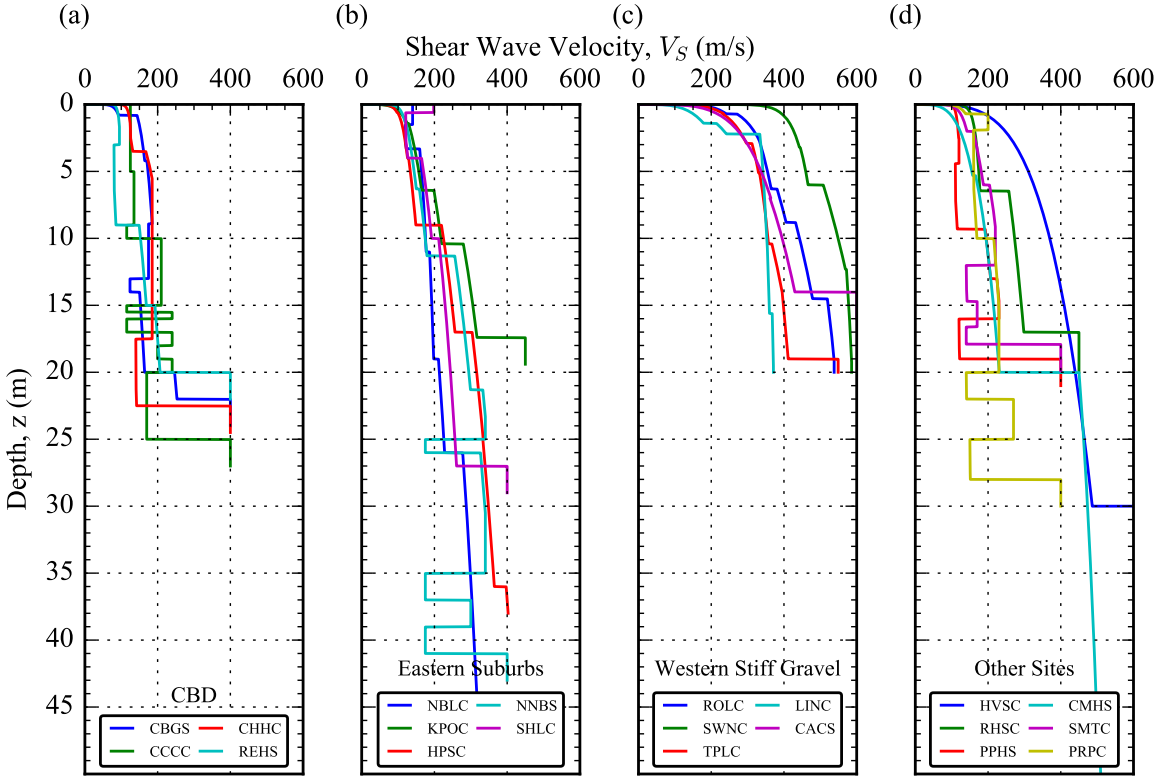

Figure A.1: Shear wave velocity profiles for the 20 sites considered separated by group as: (a) Central Business District (CBD), (b) Eastern suburbs, (c) Western stiff gravel sites, and (d) other sites. Locations of the sites are given in Figure 2.2

Table A.2: Geometric mean horizontal PGA observed at all strong motion stations from the 11 events considered. Event IDs listed in Table A.1, and SMS locations shown in Figure 2.2. The symbol "–" means the event was not recorded at that station.

			Geometric mean PGA for each event ID (g)										
SMS ID	$\mathbf{T_1^*}$ **(s)***	$\mathbf{V_{S30}}$ **(m/s)****	1	2	3	4	5	6	7	8	9	10	11
CACS	0.16	435	0.20	0.03	0.02	0.19	0.03	0.09	0.12	0.09	0.08	0.08	0.03
CBGS	0.51	197	0.16	0.07	0.27	0.51	0.07	0.18	0.17	0.08	0.16	0.21	0.10
CCCC	0.60	182	0.21	0.10	0.22	0.41	–	–	–	–	0.14	0.17	0.15
CHHC	0.54	196	0.17	0.09	0.16	0.37	0.15	0.19	0.21	0.11	0.17	0.22	–
CMHS	0.58	213	0.24	0.17	0.14	0.37	0.13	0.16	0.18	0.14	0.16	0.17	–
HPSC	0.55	206	0.15	0.04	0.05	0.20	0.14	0.18	0.26	0.07	0.21	0.26	0.20
HVSC	0.39	350	0.61	0.10	0.11	1.36	0.73	0.43	0.83	0.28	0.26	0.51	0.15
KPOC	0.32	257	0.32	0.01	0.01	0.20	0.05	0.20	0.10	0.07	–	0.29	–
LINC	0.24	300	0.47	0.03	0.02	0.12	0.03	0.03	0.07	0.11	0.05	0.07	0.03
NBLC	0.77	189	–	0.04	0.02	–	0.14	0.23	0.21	0.04	0.20	–	0.20
NNBS	0.66	204	0.20	0.04	0.04	0.61	0.16	0.22	0.18	0.06	–	–	–
PPHS	0.48	180	0.22	0.05	0.09	0.20	0.05	0.11	0.11	0.08	0.10	0.14	–
PRPC	0.57	196	0.21	0.05	0.09	0.62	0.22	0.31	0.34	0.09	0.29	–	–
REHS	0.59	155	0.25	0.08	0.25	0.52	0.10	0.19	0.26	0.09	0.20	0.26	0.16
RHSC	0.29	286	0.22	0.28	–	0.28	0.08	0.09	0.20	0.20	0.16	0.16	0.06
ROLC	0.19	350	0.40	0.01	0.02	0.17	0.01	0.04	0.04	0.12	0.12	0.06	0.02
SHLC	0.51	207	0.19	0.09	0.14	0.32	0.12	0.26	0.21	0.08	0.21	0.25	0.17
SMTC	0.41	219	0.17	0.02	0.03	0.17	0.03	0.13	0.08	0.08	0.06	0.15	–
SWNC	0.15	400	0.22	0.02	0.01	0.20	0.01	0.06	0.06	0.04	0.08	0.16	–
TPLC	0.22	350	0.28	0.06	0.03	0.11	0.03	0.03	0.07	0.23	0.07	0.08	0.02

* T_1^* = "profile period", the fundamental period of the pressure independent 1D V_S profile.

** V_{S30} values used to compute empirical site amplification.

A.3 Between-event residuals, δB_e

The between-event residual represents the event-specific deviation in residuals from the total model bias discussed in the previous section. Figure A.2 plots the between-event residual for all events, and the standard deviation in between-event residuals for all three methods as a function of vibration period. From Figure A.2(a, b, and c) it is evident that, for a given event, the between-event residual is nearly constant for $T < 1\ s$. By contrast, in the LF component (i.e., $T > 1\ s$), there is significant variability in the between-event residual across periods. A hypothesis for this observation is related to the modeling of event stress drop parameter. For simplicity, the high frequency simulations all use a constant stress drop in the source modeling. Although research has shown that there is variation in stress drop across events of the Canterbury Earthquake Sequence (Oth and Kaiser, 2014), there does not exist a non-constant predictive model for this parameter. A change in the adopted stress parameter value results in a near-uniform shift of acceleration response spectral amplitudes across the full period range (i.e., $T < 1\ s$ for the HF simulation). This suggests that the approximately constant imprecision for $T < 1\ s$ of an individual event seen in Figure A.2a may be a result of the assumption of constant stress drop across all events.

Because the mean of all δB_e is zero, a meaningful comparison between analysis methods is made by comparing the uncertainty or standard deviation in δB_e, or τ (Fig A.2d). For $T > 1\ s$, there is little difference in uncertainty between the three analysis methods, which is reasonable as the shallow site amplification (especially for the 1D wave propagation analysis) is negligible at periods longer than the profile period ($T_1^* = 0.15 - 0.77\ s$). A modest reduction in uncertainty is observed when nonlinear site effects are modeled in simulations using either site response method for $T < 1\ s$. The reduction in total uncertainty, σ, in this period range can be predominately attributed to this reduction in between-event uncertainty, τ. In this context, a reduction in τ suggest that, on average, the spectral acceleration amplitudes are more precisely predicted across all stations and events when site response is considered.

Further investigation into the residuals reveals there is no statistically significant dependence on magnitude in these between-event residuals. Particularly high residuals (large un-

derprediction) are observed for the offshore M_W5.9 earthquake from 23 Decemeber 2011 (i.e., event 10), which may suggest imprecision or incompleteness in the source modeling for this event. Although these unusually large residuals could also be influenced by source-to-site path effects (i.e., the velocity model in this region), there are two other events in this general offshore region (i.e., events 9 and 11; see Fig 2.1), for which this effect is not evident.

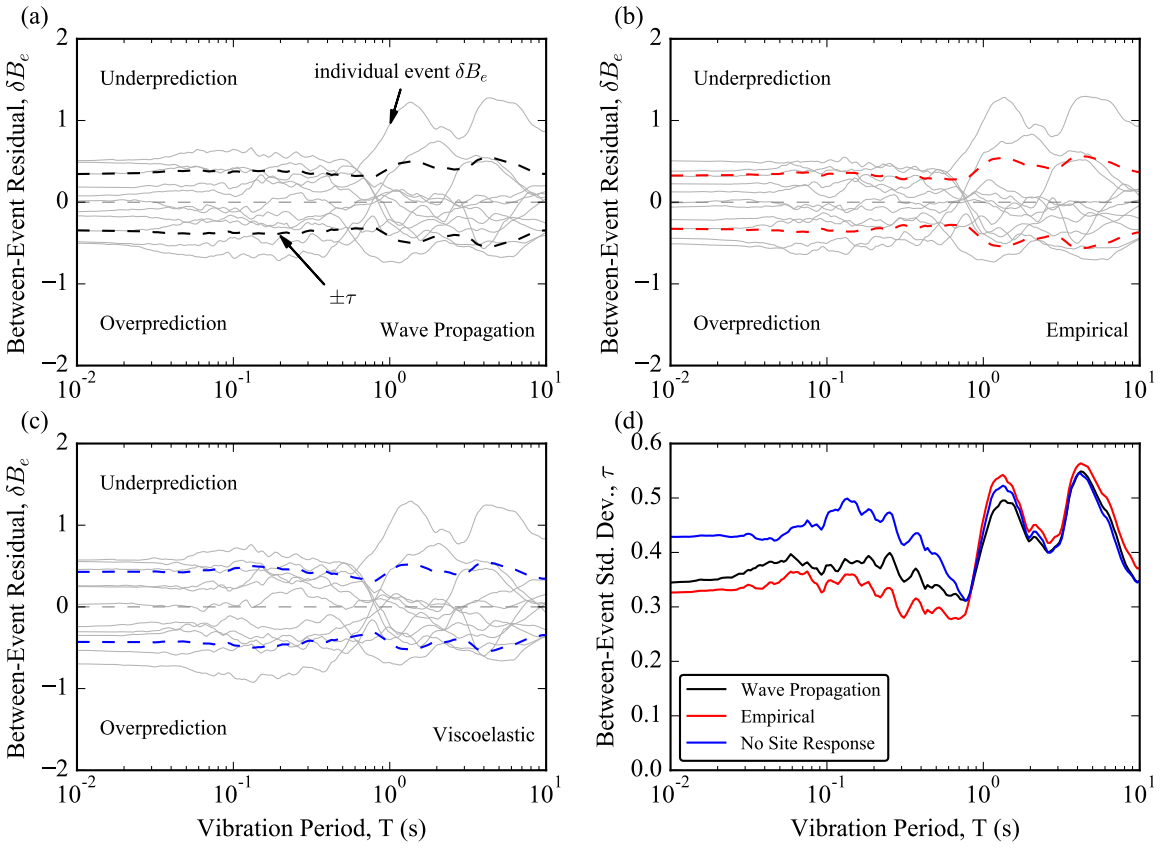

Figure A.2: Between-event residuals, δB_e, for all 11 events from (a) the wave propagation site response, (b) empirical site response and (c) reference viscoelastic simulations, and (d) standard deviation of between-event residuals, τ, for all three cases as a function of vibration period.

A.4 Systematic residuals for different sub-regions of Christchurch

To further illustrate potential reasons for systematic departures of predictions relative to observations, and determine possible avenues for improvement, the sites are divided into groups based on geographic region and site response characteristics as noted in Figure 2.2. The systematic residual for sites in three different regions of Christchurch (i.e., Central Business District, Eastern Suburbs, and Western Stiff Gravel sites) are in Figure A.3(a, c, and e) for the wave propagation analysis and in Figure A.3(b, d, and f) for the empirical method.

Figure A.3 (b, d, and f) clearly show the influence of the model bias (a; Figure 2.5a), in the systematic residual for all sites, which is especially pronounced at $T = 1 - 3$ s in the empirical method. As discussed in Section 2.5.1, the empirical method greatly overpredicts long periods. On the contrary, this systematic overprediction across all sites is not visible in the wave propagation results [i.e., Fig A.3 (a, c, and e)]. It is also apparent that for all regions there is a slight overprediction for $T < 0.2$ s which is greater for the wave propagation analysis and most pronounced at $T = 0.1$ s. This is likely attributed to overprediction from the reference input motions and insufficient damping of high frequencies in 1D wave propagation analyses (refer to Section 2.5.1 for further discussion).

Stiff gravel sites (Fig A.3e and f) at which shallow site response is expected to be trivial, can provide insight into the bias in the simulated input motions used for site response analyses. For these sites, as expected, all three analysis methods result in similar overall systematic bias (e.g., Fig 2.8d). Because site amplification quantified using conventional methods is negligible at these site, the reference viscoelastic simulations should closely reproduce observed ground motions if the underlying simulations were "perfect". The fact that there is bias in the reference simulations for a stiff site, suggests that there is imprecision in the input ground motions (i.e., the deconvolved reference simulations). This uncertainty is further analyzed in Section A.4.0.1 of this appendix in terms of within-event single-station standard deviations.

Another notable observation from Figure A.3c is that the overprediction at short periods is most pronounced for the wave propagation analysis at the Eastern Suburbs sites, some of

which are liquefiable and liquefied during some of the events considered (Bradley and Cubrinovski, 2011; Wotherspoon et al., 2014). It is important to consider what effect, if any, pore-water-pressure generation may have had on the short period spectral acceleration intensities and residuals for these sites. Stations HPSC, NNBS, and SHLC are considered liquefiable and had liquefaction manifestation (either by surface manifestation or in ground motion records) in one to three events of the 11 events considered. Further investigation into residuals shows that at HPSC and SHLC, four out of five of the strongest events (i.e., largest observed PGAs) were overpredicted at short periods. It is possible that consideration of pore-pressure generation with an effective stress analysis would result in deamplification at short periods and improve simulations for these particular cases by better capturing the near-surface response of liquefiable deposits. However, the number of ground motions for which pore-pressure generation was significant is small relative to the total number of ground motions used to generate Figure A.3c, and therefore, they would likely not greatly influence the mean systematic residual for the region. Additionally, another site in this region that did not manifest liquefaction (i.e., NBLC) also displays this overprediction of short periods, implying that this may be a regional effect in the reference input ground motions in combination with the limitations of the 1D wave propagation analysis discussed in Section 2.5.1.

To elaborate on the comparison between wave propagation and empirical systematic residuals made in Figure A.3, the systematic residuals from both analysis methods at the profile period, T_1^*, of each site are directly compared in Figure A.4. Points that fall on the 1:1 diagonals are sites for which the wave propagation and empirical methods have the same systematic residual. Points that plot in the left and right quadrants (i.e., green-colored regions in the color print) of the figure suggest that the wave propagation method improved the simulations when compared to simulations with V_{S30}-based site response, and the opposite is true for the top and bottom quadrants (i.e., red-colored regions in the color print). It is evident that the majority of points plot on or near the diagonals, suggesting that either (1) V_{S30}-based site response appropriately captures the response of these "standard" sites, (2) the uncertainty in the input motion is such that the models cannot effectively capture the site response and realize benefits from explicit modeling of site response, or (3) the assumptions in the 1D wave propagation model (including site characterization and constitutive model inputs) are not providing addi-

tional value.

It is, however, evident that three sites (i.e., REHS, HVSC, and RHSC) plot well off the 1:1 line into the right quadrant meaning that the residual from the wave propagation analysis is significantly smaller than from the empirical V_{S30}-based method. As discussed in the previous section (i.e., Sec 2.5.3) and shown in Figure 2.7, these sites exhibit strong site amplification at the profile period that is not captured using V_{S30}-based site amplification. On the contrary, there are only two sites (i.e., SWNC and CACS) that notably plot off the 1:1 lines into the top and bottom quadrant (i.e., the V_{S30}-based residual is smaller than the wave propagation residual). These two sites are Western Stiff Gravel sites for which the modeled site response is less pronounced than the remaining sites, suggesting that the imprecision may be in the input motions and not the site response for these two cases.

The results in Figure A.4 agree with recommendations from Campbell and Bozorgnia (2014) who suggest not using the generic V_{S30}-based nonlinear site response function for soft or atypical sites. It is indeed evident that using the simplified empirical V_{S30}-based site response is not appropriate for very soft sites or sites with large near-surface impedance contrasts. About 15% of the sites considered are substantially better represented by explicitly modeling site response using the wave propagation analysis while for the remaining sites there is no notable improvement from using wave propagation analysis.

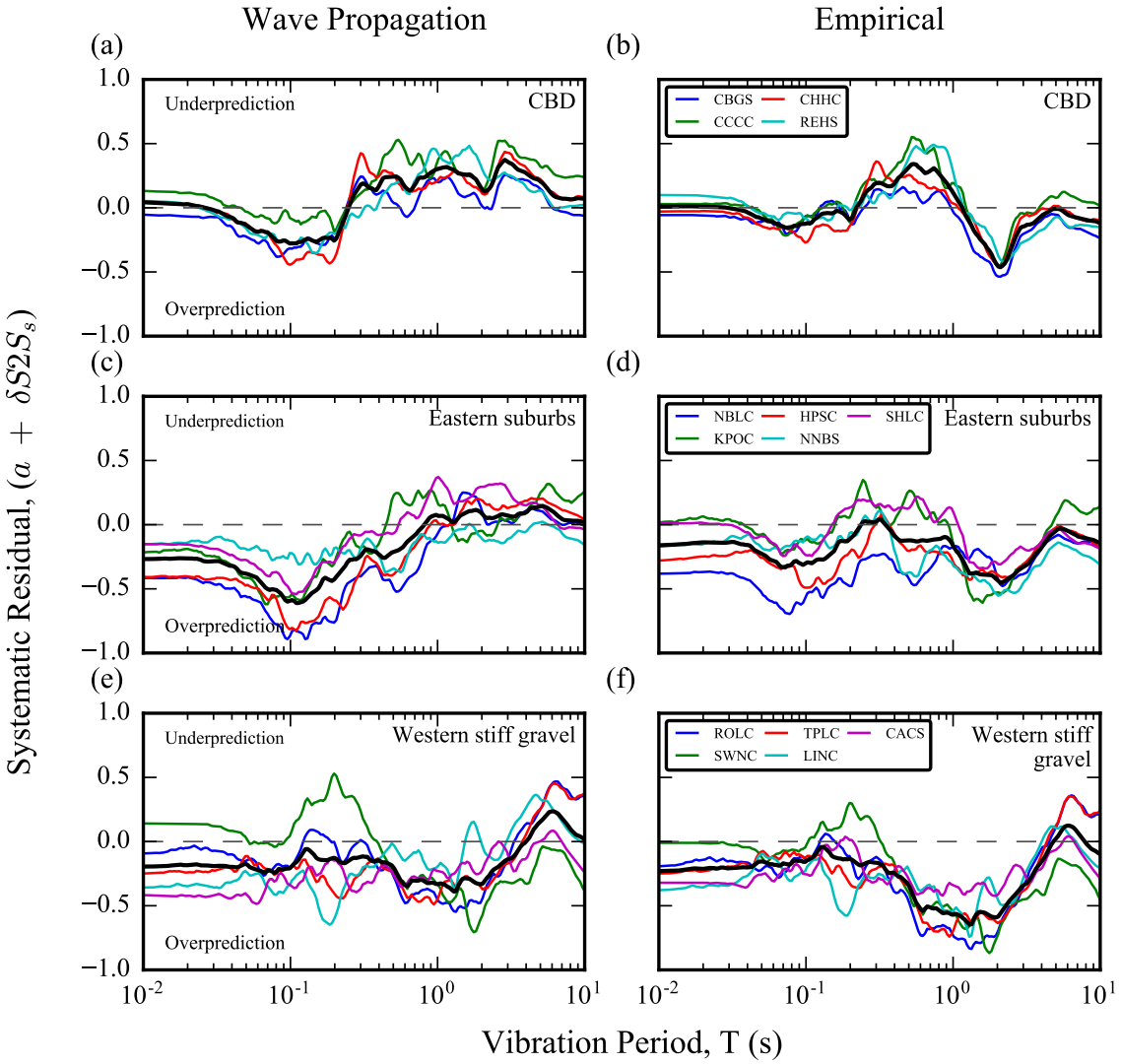

Figure A.3: Systematic portion of the spectral acceleration residual (i.e., $a + \delta S2S$) from wave propagation (left) and empirical (right) methods for sites in (a, b) Christchurch Central Business District, (c, d) Eastern suburbs, and (e, f) Western stiff gravel sites.

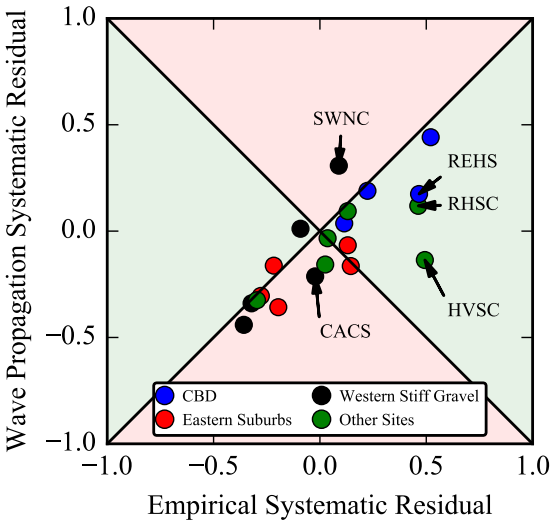

Figure A.4: Direct comparison of systematic effect at the profile period, T_1^*, of each site between wave propagation and empirical methods colored by group. The left and right axis quadrants (colored in green in the color print) represent smaller magnitude of residuals for the wave propagation site response analysis method than the V_{S30}-based empirical method.

A.4.0.1 Inference of uncertainty in input motion with analysis of reference stiff soil sites

To better understand the uncertainty in the simulated input motion and its potential influence on the results of the wave propagation site response analysis, the within-event single-station standard deviation with site and event term corrections for individual sites (i.e., $\phi_{SS,s}$; the standard deviation of δW_{es}) are compared. Figure A.5 plots $\phi_{SS,s}$ from the wave propagation analysis for all sites in the CBD, Eastern suburbs, and Western stiff gravel sites groups. One would anticipate that for stiff sites, for which near-surface site effects via impedance contrast are conventially considered negligible, the ground motion could be predicted with less uncertainty than for sites that include moderate to strong site amplification and uncertainty in the site response. However, Figure A.5 shows that for the Western stiff gravel sites (i.e., the stiffest sites with the least site amplification), the single-station uncertainty is generally similar to that for sites in other groups, and the mean across all sites in the group is larger for $T < 1$ s. This provides insight regarding the imprecision in the deconvolved reference simulations used as input motions which may be limiting the potential for the site-specific ground response analysis to improve simulations. Other research also provides insight to the outcomes in this study. For example, while there is certainly imprecision in the site characterization, development of shear wave velocity profiles, and determination of input parameters for site response modeling, Bazzurro and Cornell (2004) also found that the prediction of nonlinear site amplification is controlled more by the uncertainty or variability in input motions than the uncertainty in soil parameters. The results of previous studies along with the individual site $\phi_{SS,s}$ presented in this section suggest that imprecision in the simulated input motion may be a notable reason for not observing appreciable reduction in the overall event-corrected single-station standard deviations (ϕ_{SS}) when site response is modeled explicitly.

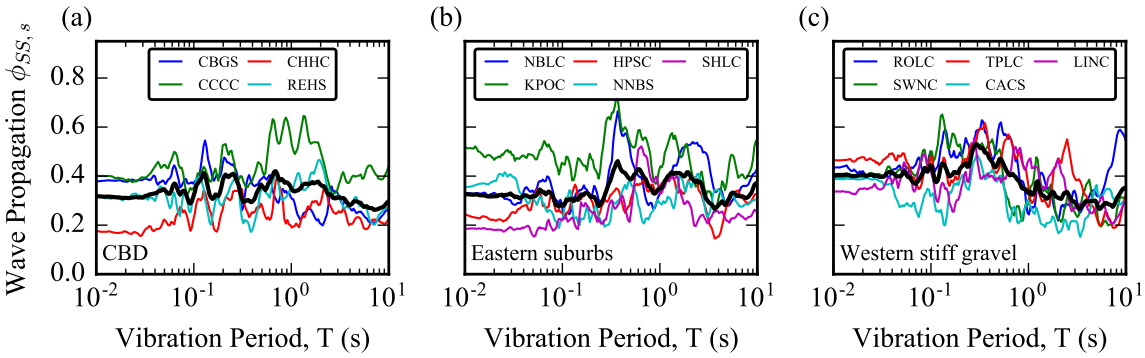

Figure A.5: Single-station standard deviations, $\phi_{SS,s}$, from wave propagation analysis for individual sites grouped into (a) Central Business District, (b) Eastern suburbs, and (c) Western stiff gravel sites. The solid black lines are the mean of all sites within each grouping.

A.5 Components of standard deviation compared with published empirical models

Elaborating on Section 2.6, Figure A.6 compares the components of standard deviation from the three physics-based simulation approaches to those from ground motion prediction by an empirical GMM (Bradley, 2013) for the same dataset of earthquakes and strong motion stations. The figure shows that the GMM generally has lower between-event uncertainty, τ, for the entire period range, and higher site-to-site uncertainty, ϕ_{S2S} for T $>$ 5 s.

To further scrutinize the magnitude of standard deviations from the physics-based simulations, Figure A.7 compares all components of standard deviation for PGA prediction from this study to those from other empirical models that use different datasets (presented in Lin et al., 2011). The results from this study include the wave propagation and empirical methods for modeling site response in simulated ground motions, the reference viscoelastic simulations without site response, and the purely empirical GMM prediction. The other studies presented include Lin et al. (2011), Chen and Tsai (2002), Atkinson (2006), and Chiou and Youngs (2008). The values of standard deviation from physics-based simulations (i.e., this study) are quite comparable to, and often slightly lower than, those of other published empirical models. The proportion of individual components of uncertainty to the total uncertainty for this study are also within expected ranges from other studies. This gives confidence that ground motion prediction can be achieved via physics-based simulations with comparable uncertainty to that of the standard of practice using empirical models.

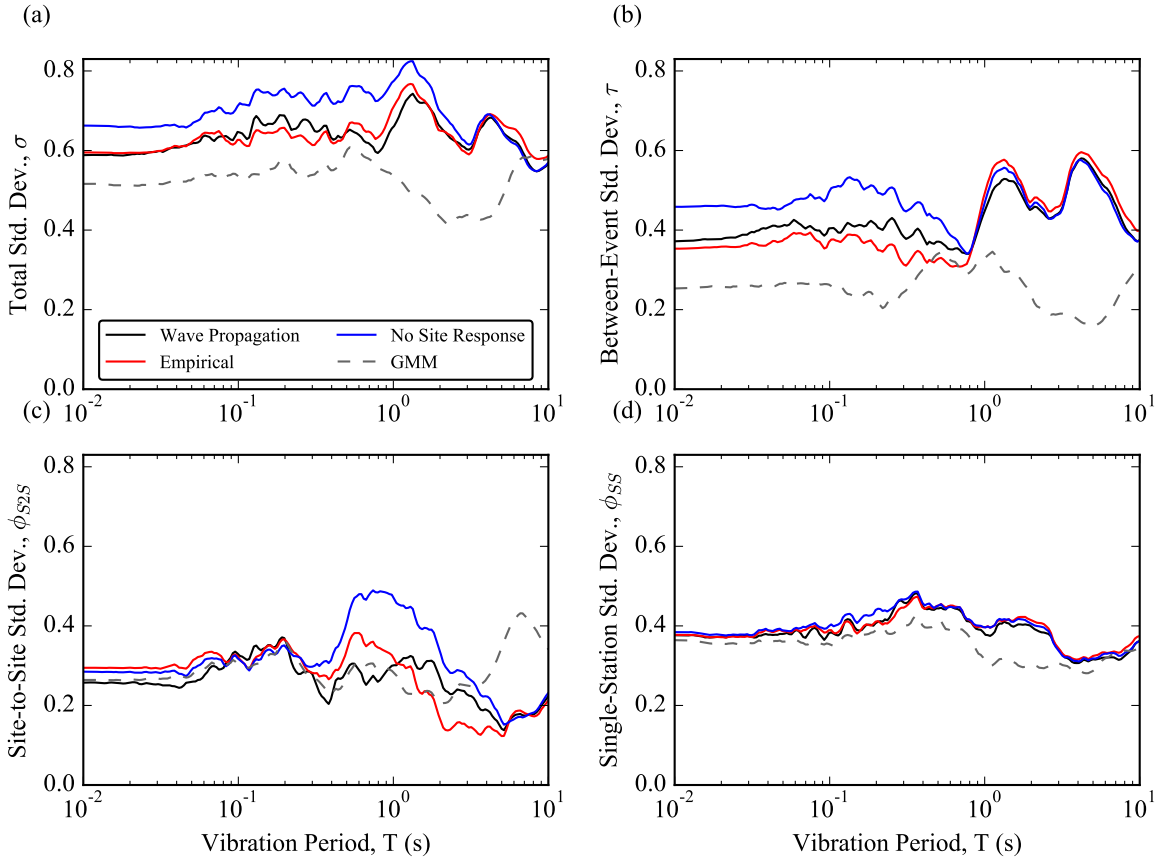

Figure A.6: Four components of standard deviation (σ, τ, ϕ_{S2S}, and ϕ_{SS}) as a function of vibration period for all four analysis methods.

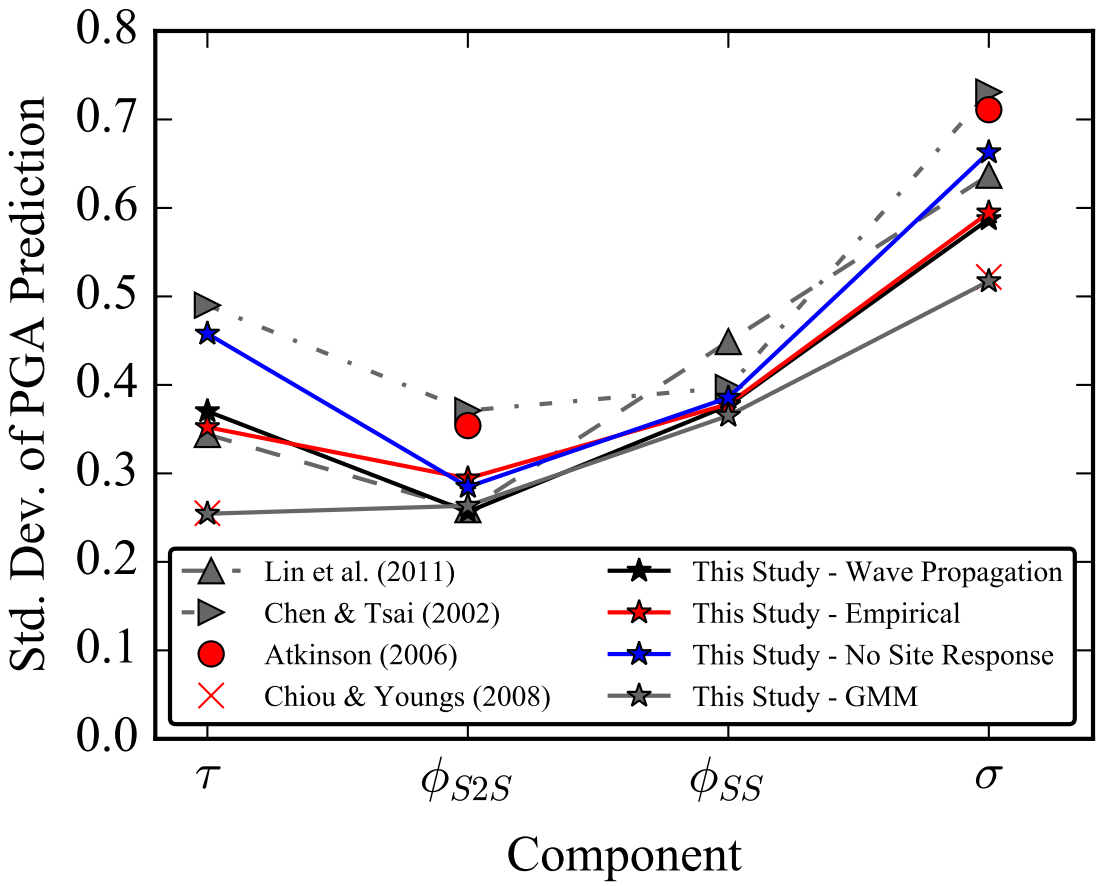

Figure A.7: Components of standard deviation from this study and other published empirical models for prediction of PGA. The results from this study include those from reference viscoelastic simulated ground motions, simulations with wave propagation and empirical site response, and empirical ground motion prediction with a GMM. Note Lin et al. (2011) only list ϕ_{S2S} and σ, and τ and σ for Atkinson (2006) and Chiou and Youngs (2008), respectively.

A.6 Miscellaneous Supplementary Figures

Figure A.8 shows site-to-site residuals as a function of vibration period for simulations with empirical V_{S30}-based site response (Fig A.8a) and for viscoelastic reference simulations (Fig A.8b) with curves color-coded by V_{S30} of each site. Figure A.9 plots systematic residuals (i.e., bias + $\delta S2S$) from all four analysis methods (wave propagation, empirical, reference viscoelastic, and GMM) for all 20 sites.

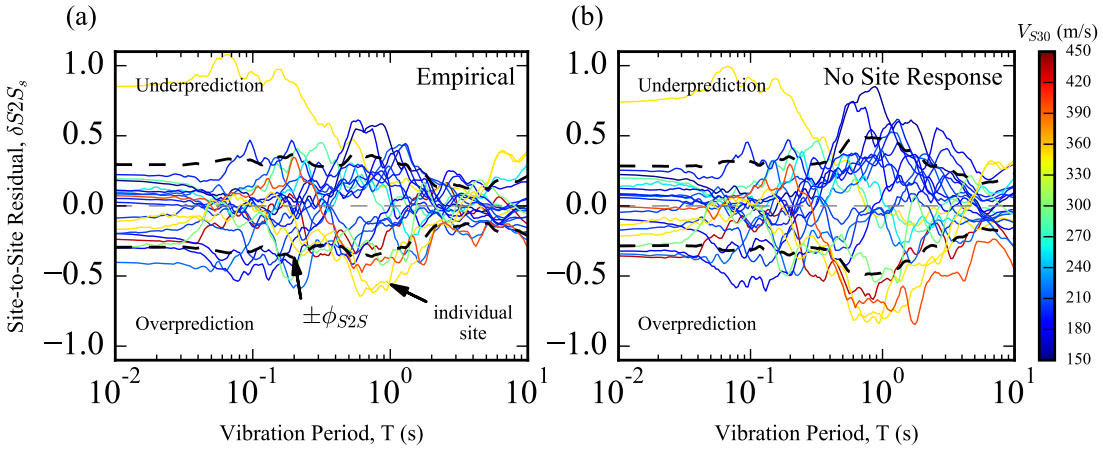

Figure A.8: Site-to-site residuals as a function of vibration period for (a) simulations with empirical V_{S30}-based site response and (b) viscoelastic reference simulations with curves color-coded by $VS30$ of each site.

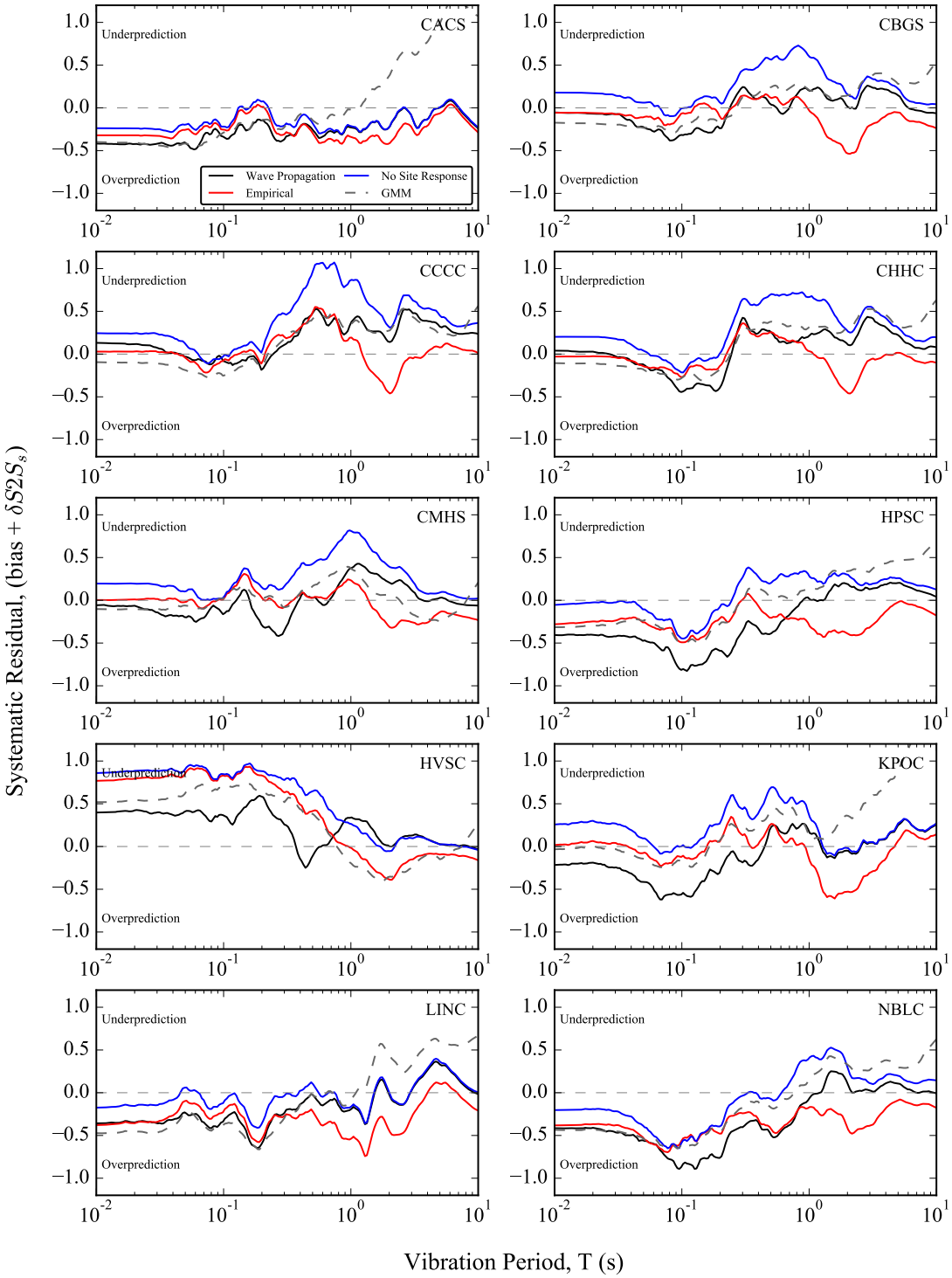
CACS
CBGS
CCCC
CHHC
CMHS
HPSC
HVSC
KPOC
LINC
NBLC
Underprediction
Overprediction
Wave Propagation
Empirical
No Site Response
GMM
Systematic Residual, (bias + $\delta S2S_s$)
Vibration Period, T (s)

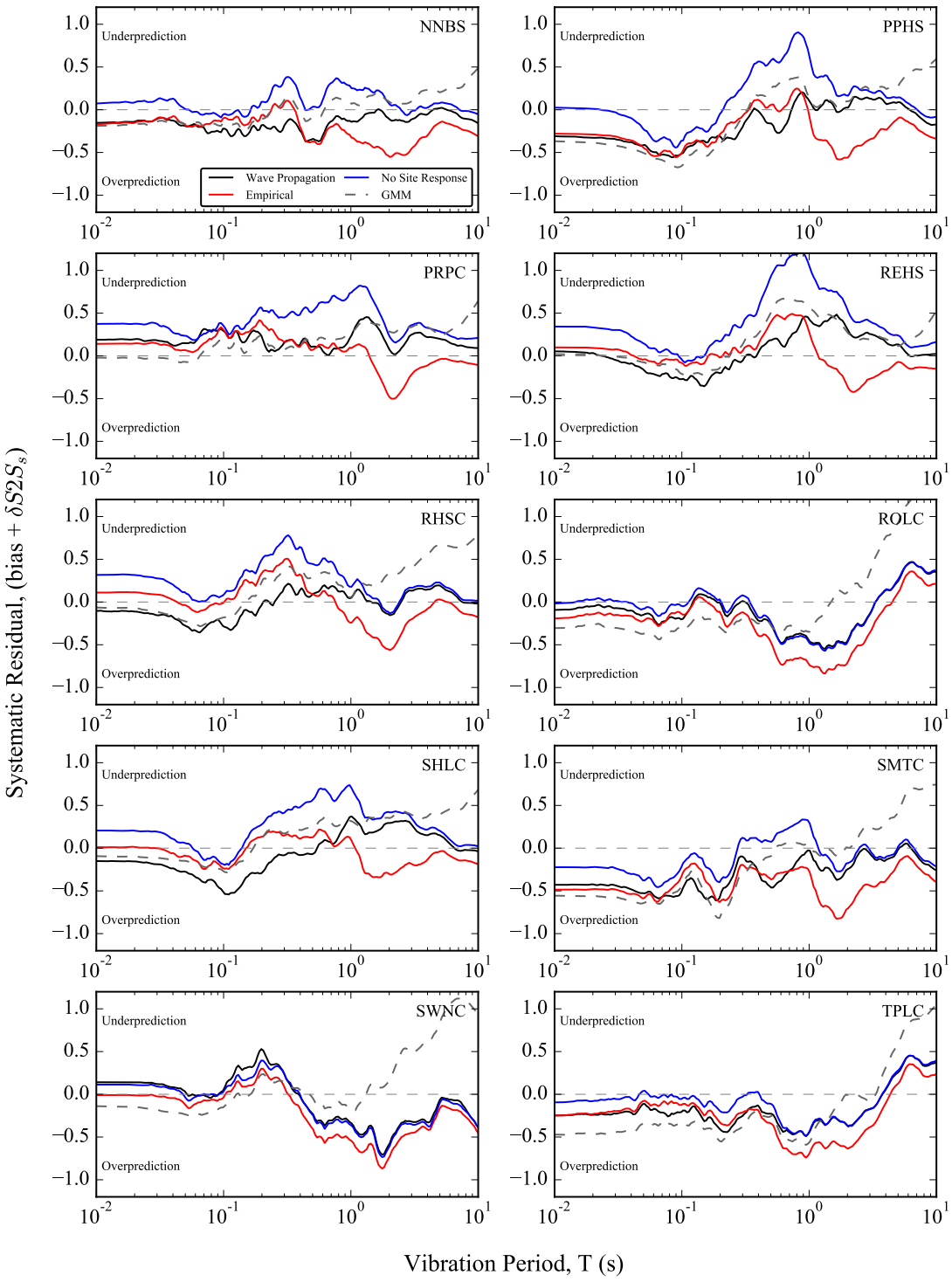

Figure A.9: Systematic residuals (i.e., bias + $\delta S2S$) as a function of period from all four analysis methods (wave propagation, empirical, reference viscoelastic, and GMM) for all 20 sites.

Appendix B

Appendix to Chapter 3

B.1 Summary

This section presents the appendices to Chapter 3: 2D Geotechnical Site-Response Analysis including Soil Heterogeneity and Wave Scattering.

The appendices contain additional figures, with interpretation, to supplement the discussion in the paper, and are referenced throughout the main paper. Appendix B.2 compares different boundary conditions in OpenSees and describes the implications of using each model assumption in the context of heterogeneous deposits, Appendix B.3 examines the influence of the covariance model used for random field generation on intensity measures (IMs), Appendix B.4 determines the number of random field realizations required for convergence of IMs, and Appendix B.5 provides additional figures to supplement the discussion throughout the text.

- **COMPARISON OF VARIOUS BOUNDARY CONDITIONS FOR 2D SITE-RESPONSE ANALYSIS IN OPENSEES**
- **INFLUENCE OF COVARIANCE MODEL FOR RANDOM FIELD GENERATION ON SITE-RESPONSE RESULTS**
- **CONVERGENCE OF IMs**
- **ADDITIONAL FIGURES TO SUPPLEMENT DISCUSSION**

B.2 Comparison of Various Boundary Conditions for 2D Site-Response Analysis in OpenSees

The standard boundary conditions for 1D site-response analysis using the finite element method with a purely horizontal input are periodic lateral boundary conditions (i.e., a node on the left boundary is tied to the corresponding node at the same elevation on the right boundary) and a base that is fixed in the vertical (Y) direction. As OpenSees does not have these boundary conditions included by default, the analyst is required to implement them, therefore, when 2D problems are analyzed, these simplifications that apply to 1D problems are often adopted. In particular, it is common for 2D dynamic models in OpenSees to be used with periodic boundary conditions ('tiedBoundaries'), a base that is fixed in the vertical direction ('fixedY'), and a base with nodes that are tied in the horizontal (X) direction (i.e., the entire base moves in unison; 'tiedX'). This was the 'control' case that was initially used for this study. Examples of previous studies that have adopted one or all of these boundary condition simplifications are Zhang et al. (2003), Karimi and Dashti (2016), Jeong and Bradley (2017c), Gobbi et al. (2017), and Ramirez et al. (2018)

Using this 'control' case with standard boundary conditions from 1D site response for 2D site response with soil heterogeneity resulted in strange behaviour observed in the frequency domain at the fundamental frequency of the soil deposit (f_0). Transfer functions appeared to be distorted (compared to 1D analyses) and showed significantly higher peak amplification at f_0 ($AF(f_0)$). This behaviour can be observed directly in nodal and realization transfer functions of Figures B.1, B.2, and B.3. To test whether this response was artificially introduced by the model configuration, a thorough study was launched to identify the cause of this behaviour. Initially, simple things were tested such as: increasing the width of the model (up to 3,000 elements), developing the zero-variance zones, introducing high viscous damping on boundary elements, increasing the duration of the analysis to 100 seconds, changing the fundamental frequency of the Ricker wavelet, increasing the total depth of the model, increasing the minimum damping ratio, and modifying how Fourier spectra were computed (e.g, adding more padding and not applying a smoothing function). None of these solutions solved the problem, they all still

displayed this odd behaviour in the transfer function, therefore, more significant changes to the boundary conditions were investigated.

In this appendix, five different model configurations are compared by making incremental modifications to the boundary conditions. This includes two variations on lateral boundary conditions (periodic versus massive free field columns) and four variations on base conditions (nodes fixed in vertical direction and tied to move horizontally uniformly). The most influential modification was releasing the base nodes so that they can each act independently in the horizontal direction and are not all tied to displace uniformly. A direct comparison between methods is made by running the different model configurations with the same random field seeds such that the resulting differences in ground response are only attributed to the boundary conditions and not the wave speed of the heterogeneous material. Ten random field seeds were analyzed (with Seed = 1, 2, 3, ..., 10) for all variations of the model. The features of the model that were varied incrementally are described in the following subsections.

B.2.1 Periodic lateral boundary conditions

The first significant modification to the model configuration was to change the lateral periodic boundary conditions. Rather than tying the lateral boundaries to each other ('tiedBoundaries'), a free field column was approximated on each side by including a massive column (the mass of each element was assigned a mass 10,000 times greater than a standard element by defining the thickness into the page as 10,000 m). These massive columns are within the zero-variance zone, therefore, they have a 1D deterministic velocity profile. The columns enforce this homogeneous "free-field" response on the main model by being significantly more massive than the elements within the main domain. This 2D configuration was verified using a homogeneous velocity model to ensure the response was identical to the control case with periodic boundary conditions. McGann and Arduino (2015), Chin et al. (2016) and de la Maza et al. (2017) are examples of studies that have implemented these massive free field columns in OpenSees.

Figures B.1 and B.2 compare results between the two lateral boundary conditions for 2D analyses with velocity perturbations. Figure B.1 plots nodal transfer functions ($TF_{i,j}$) for one

random field seed while Figure B.2 directly compares the resulting realization median transfer functions ($\overline{TF_j}$) from two random field seeds. While there are slight differences between the two lateral boundary conditions (i.e, the control with periodic boundaries versus the massive free field columns), the response is similar and the strange behaviour around f_0 is still visible. Constraints on the base nodes were analyzed next.

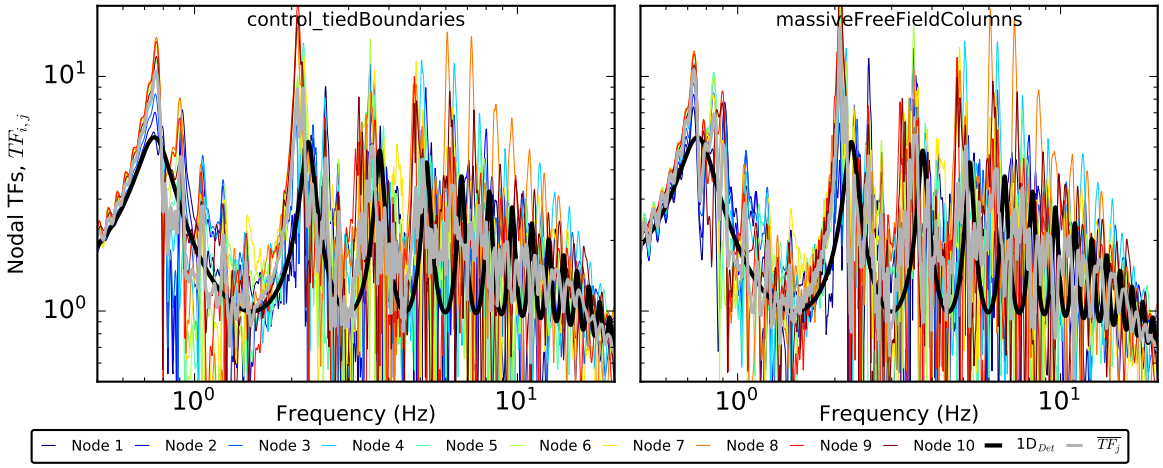

Figure B.1: Comparison of nodal transfer functions, $TF_{i,j}$, from one random field seed for two lateral boundary conditions: the control case ('control_tiedBoundaries') and the proposed modification ('massiveFreeFieldColumns'). $Seed = 5$, $V_{S,0} = 150$ m/s, $\sigma_{lnVs} = 0.175$, $r_H = 50$ m and $a_{H/V} = 10$.

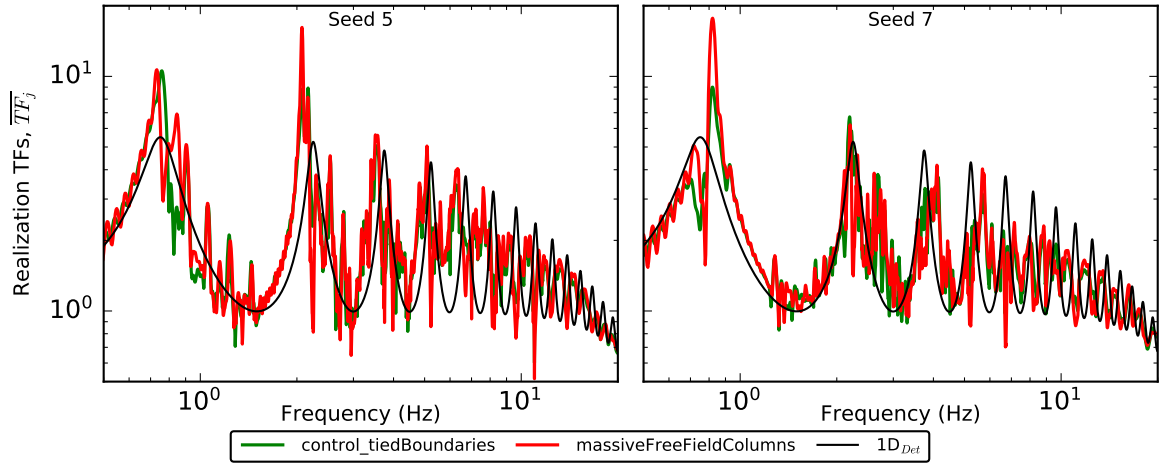

Figure B.2: Comparison of realization mean transfer functions, $\overline{TF_j}$, from two random field seeds for two lateral boundary conditions: the control case ('control_tiedBoundaries') and the proposed modification ('massiveFreeFieldColumns'). $V_{S,0} = 150$ m/s, $\sigma_{lnVs} = 0.175$, $r_H = 50$ m and $a_{H/V} = 10$.

B.2.2 Vertical fixity of base nodes

It is convenient to fix base nodes in the vertical Y direction ('fixedY'), and this idealization is reasonable when only horizontal motion is present in the model. However, the presence of soil heterogeneity generates parasitic vertical motion, including surface waves with a vertical component. In order to create a base that is compliant in the vertical direction, to prevent all vertical motion from being trapped in the model, the base nodes cannot be fixed in Y. This also allows for a vertical input motion which was not considered in this study. Releasing the fixity of base nodes ('freeY') requires a multi-step approach in OpenSees. First, the nodes must be fixed in Y and a gravity analysis must be performed to compute the vertical reactions on base nodes. Then the nodes are released, and a force equal to that of the vertical reaction is applied at each node and another gravity analysis is performed for the model to reach equilibrium. Next, dashpots are created at every base node by adding two nodes at the location of each base node. One of these two additional nodes is fully fixed and one is fully free. These dashpot nodes are connected using a zeroLengthElement with a linear viscous material and a dashpot coefficient equal to $\rho V_P A_{trib}$, where $\rho = mass\ density$, $V_P = compression\ wave\ velocity$, and $A_{trib} = tributary\ area\ of\ column\ base\ (i.e.,\ generally\ 1 - element\ wide)$. The free dashpot node is then tied to the corresponding main model node using the equalDOF command. Finally, the dynamic analysis can be performed. Note that in OpenSeesSP, when a model is parallelized, incorrect reactions may be recorded at nodes on the boundary of parallel partitions. This is because the nodes exist in two partitions and the reactions are stored as the correct value in one, and as zero on the other. Therefore, the first gravity analysis to record reactions should be performed on a single processor. The heterogeneity in soil stiffness creates non-uniform reactions along the base, therefore, the gravity analysis to record reactions must be performed for every random field realization.

Figures B.3 and B.4 plot nodal and realization transfer functions, respectively, for four model base node conditions. Figure B.5 plots other normalized (by $1D_{Det}$) nodal IMs as a function of node position. Comparing the 'fixedY_tiedX' and 'freeY_tiedX' cases allows for assessment of the influence of vertical fixity of base nodes on the response. Releasing the vertical fixities of base nodes has a negligible effect on horizontal IMs, such as transfer functions, the

fundamental frequency f_0 and amplification at f_0 ($AF(f_0)$), peak ground acceleration (PGA), spectral acceleration at $1/f_0$ ($SA(T_0)$), and Arias intensity ($I_{a,Hor}$). This is not unexpected as these measures are controlled by the horizontal component of motion. Changes are only visible in vertical IMs such as Arias intensity of the vertical component of accelerations ($I_{a,Vert}$; bottom panels of Fig B.5) which shows a notable decrease when the base is free. This effect would be even more pronounced with profiles that have a smaller impedance contrast at the base (currently 150 m/s over 760 m/s). This highlights the significance of considering a vertically compliant base when a 2D profile is not horizontally homogeneous and generates vertical motion.

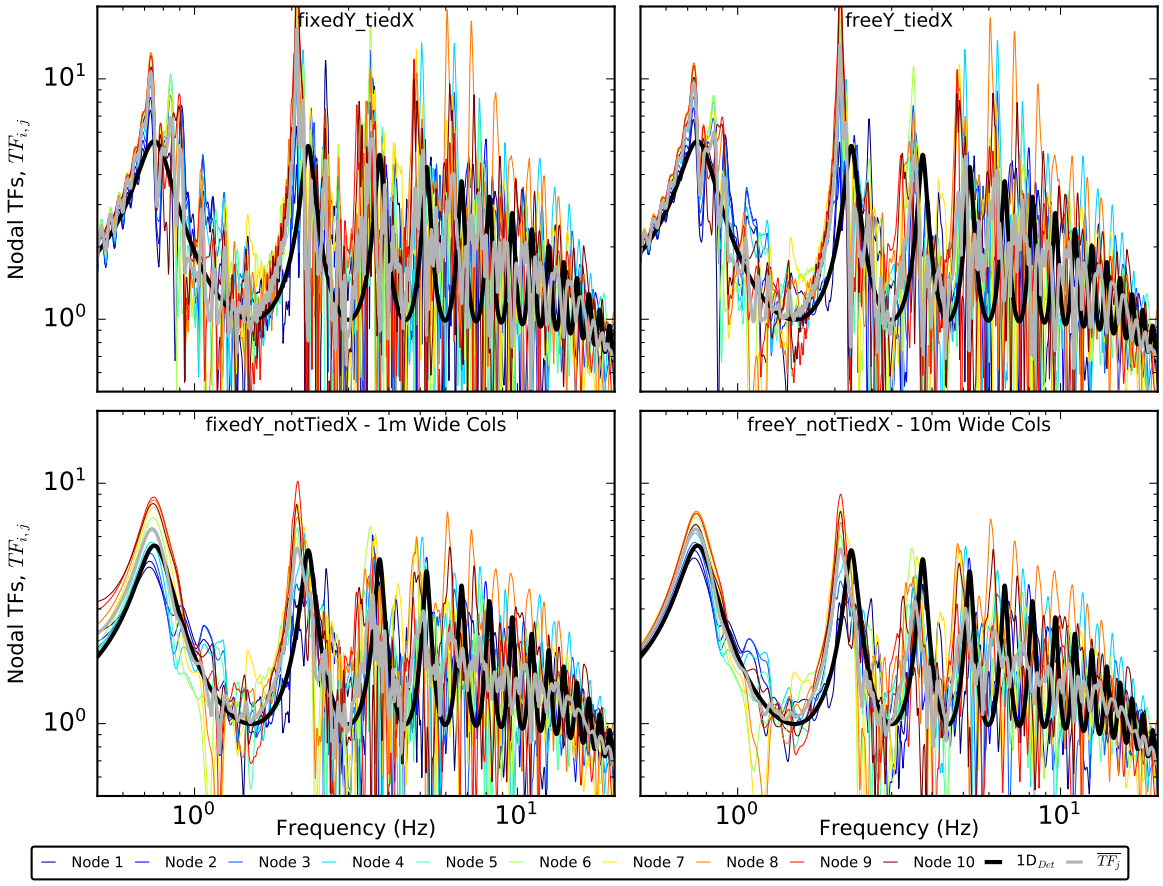

Figure B.3: Comparison of nodal transfer functions, $TF_{i,j}$, from one random field seed for four base conditions with massive lateral free field columns for lateral boundaries. $Seed = 5$, $V_{S,0} = 150$ m/s, $\sigma_{lnVs} = 0.175$, $r_H = 50$ m and $a_{H/V} = 10$.

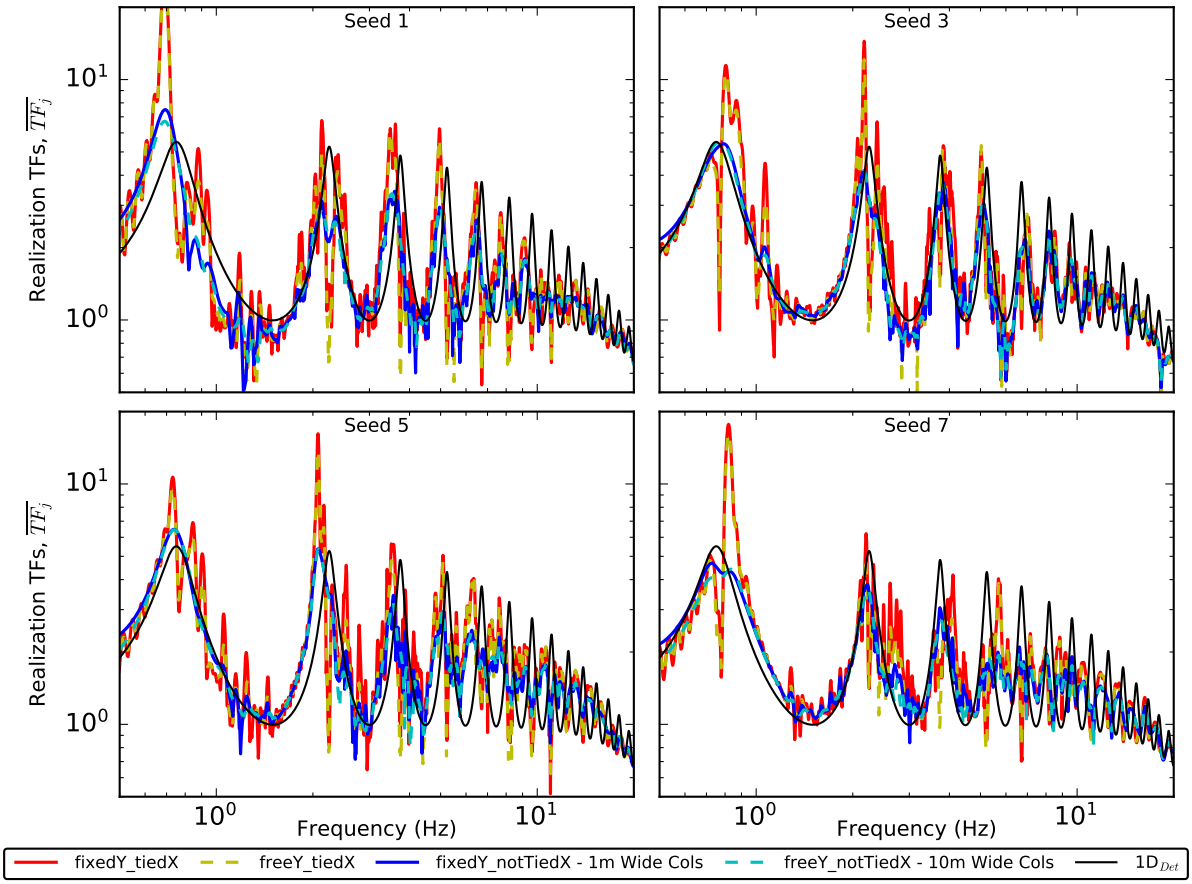

Figure B.4: Comparison of realization mean transfer functions, $\overline{TF_j}$, from four random field seeds for four variations on base conditions. $V_{S,0} = 150$ m/s, $\sigma_{lnVs} = 0.175$, $r_H = 50$ m and $a_{H/V} = 10$.

B.2.3 Uniformity of horizontal displacements along base nodes

Another simplification is to tie all base nodes together so that their response is uniform, and the input motion need only be applied at one location (the master or retained node). By far, this is the most influential assumption analyzed in this study. In order to release the base nodes so that they respond independently, each node must have its own horizontal dashpot. In the same manner as the vertical dashpots were created to make the base vertically compliant, a linear viscous material is applied to the zeroLengthElement connecting the dashpot nodes using a dashpot coefficient of $\rho V_S A_{trib}$. The input motion is then applied separately at each node as a dynamic force proportional to $\rho V_S A_{trib}$. Studies that have implemented model base conditions with individual horizontal dashpots on every base node to allow better base compliance include

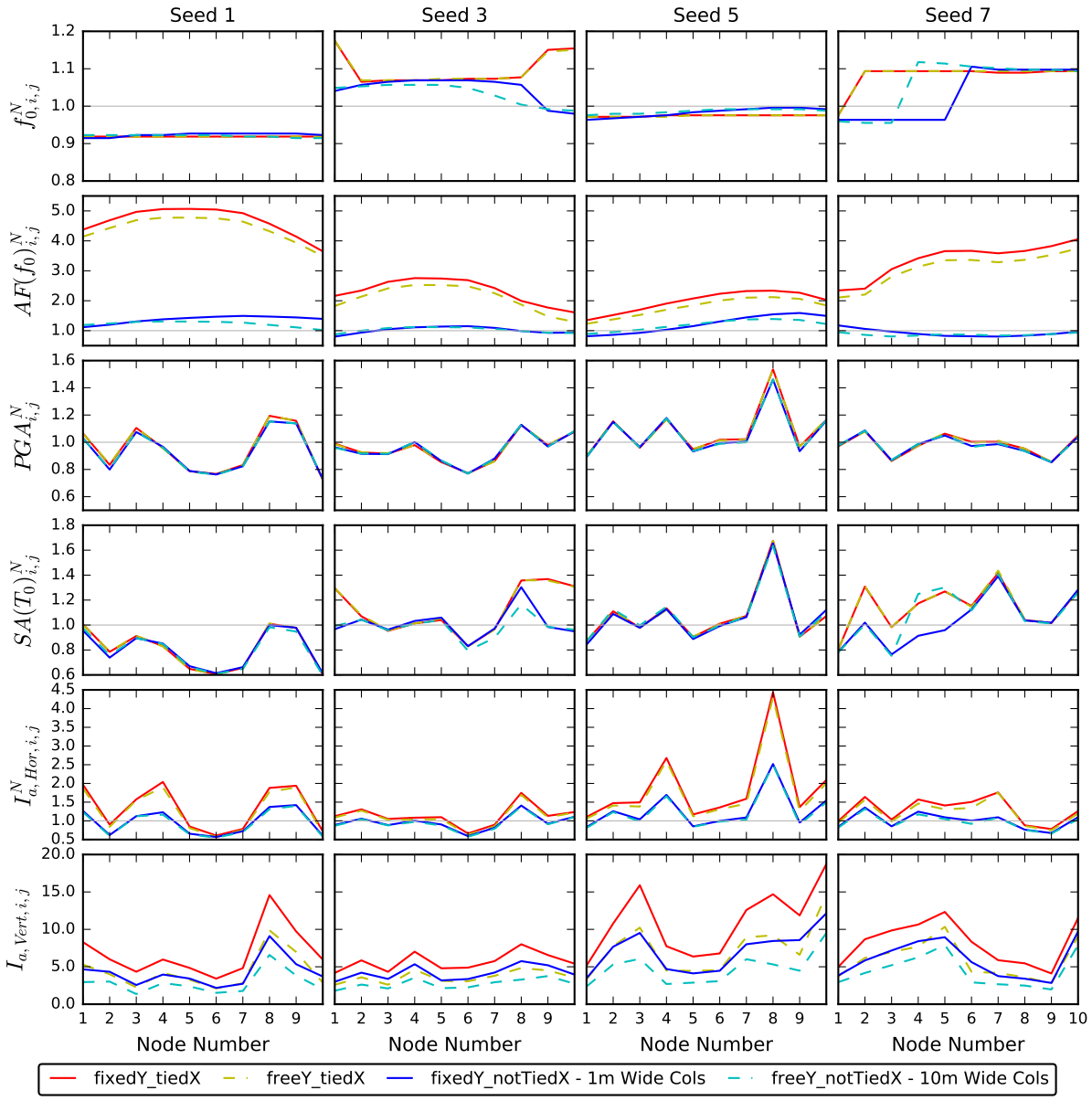

Figure B.5: Normalized ground surface nodal IMs from four random field seeds comparing results from four variations of base conditions. Results are normalized by the equivalent $1D_{Det}$ value, except for $I_{a,Vert}$ which is zero for $1D_{Det}$. As in Figure B.4, $V_{S,0} = 150$ m/s, $\sigma_{lnVs} = 0.175$, $r_H = 50$ m and $a_{H/V} = 10$.

Zhang et al. (2003), Assimaki (2004), Elgamal et al. (2008), Zhang et al. (2008), Chavan et al. (2017), and Vytiniotis et al. (2019).

While the simplification that all base nodes move horizontally uniformly is appropriate for a homogeneous and level deposit, this assumption is not appropriate for 2D models with randomized properties or other heterogeneities. The effect of this simplification is very visible in

the frequency domain when comparing the amplification at f_0 in transfer functions between the 'tiedX' and 'notTiedX' cases. $AF(f_0)$ is significantly larger for the model with a base tied horizontally (see Figs B.3 and B.4). This effect is also clearly visible in the time domain by directly comparing acceleration waveforms between the 'fixedY_tiedX' and 'freeY_notTiedX' cases in Figure B.6. Higher horizontal accelerations occur in second arrivals (i.e., reflections off base) and subsequent coda when the base nodes are tied to each other, however the first arrival amplitudes are not affected. Similar behaviour is observed in a comparison of base and boundary conditions by Zhang et al. (2003). Waves that are reflected back down from the surface will arrive at the halfspace at different times due to the heterogeneities. This non-uniform wavefield observes a base that behaves more as a rigid base because any force applied to the base must move the entire soil column (1,000 elements wide). This causes more energy to be reflected back into the model than is expected for a compliant base. Higher horizontal Arias intensity ($I_{a,Hor}$) for the 'tiedX' models, shown in Figure B.5, confirms the increase in total energy trapped within the model. Peak intensity measures that are controlled by the first arrival (e.g., *PGA* and $SA(T_0)$) are not sensitive to the modifications of vertical and horizontal constraint analyzed in this study (Fig. B.5).

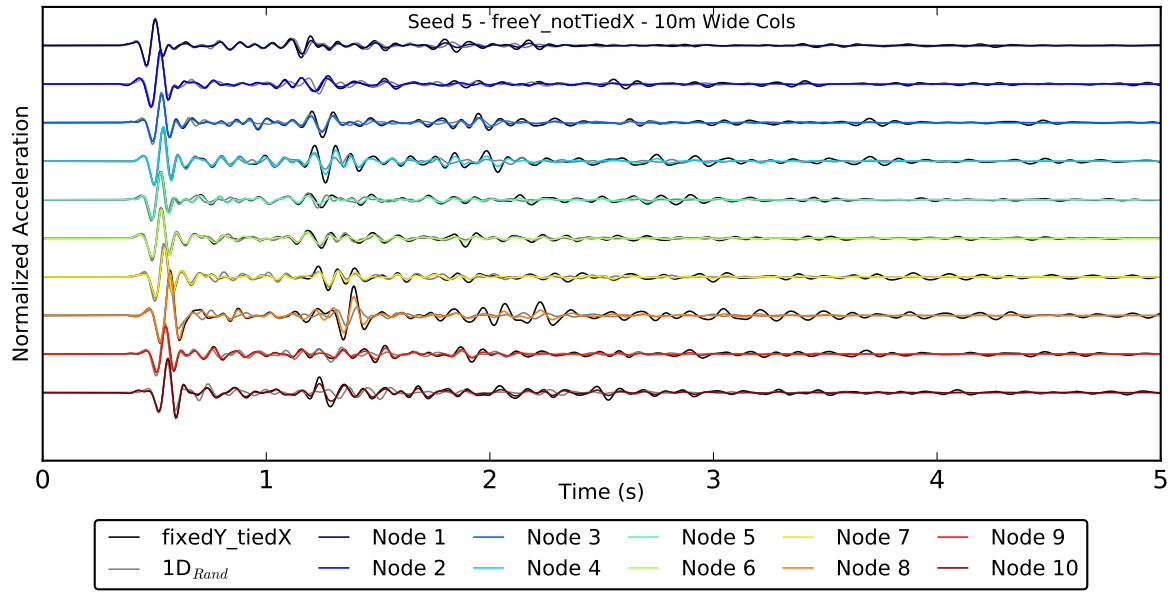

Figure B.6: Comparison of normalized acceleration time series from one random field seed for the final proposed model configuration ('freeY_notTiedX'), and the original fixedY_tiedX model. Time series from 1D randomized (1D_{Rand}) profiles are also plotted for reference. $Seed = 5$, $V_{S,0} = 150$ m/s, $\sigma_{lnVs} = 0.175$, $r_H = 50$ m and $a_{H/V} = 10$.

B.2.4 Width of massive free field columns

Initially, free field columns were only one-element-wide (i.e., 1-m-wide). This narrow column was insufficient to completely hold back soil pressures from the inner domain which caused bulging at the base of the columns and sagging of the base near the lateral extents. Widening the columns to encompass 10 elements significantly reduced the bulging and sagging that was observed. Figure B.7 plots horizontal and vertical (X and Y, respectively) displacements along all base nodes for the 1-m- and 10-m-wide free field columns. Gravity and dynamic displacements are superimposed, and every tenth time step is plotted with time increasing on the color scale from 0 (dark blue) to 30 s (dark red). These displacements show that the 1-m-wide columns were experiencing more horizontal displacements, indicating bulging, during the gravity analysis (time 0: dark blue), which continued to increase during the dynamic analysis. This bulging behaviour is not observed in 10-m-wide columns (right side of figure), however, some distortion along the base during the gravity analysis is unavoidable due to heterogeneities in soil stiffness which cause non-zero X-reactions in base nodes. The bulging and sagging of narrow columns was also influencing the response at low frequencies as observed in nodal transfer functions in the bottom left panel of Figure B.3.

B.2.5 Final proposed model

The final proposed model including all modifications discussed was verified with a 1D analysis using standard boundary conditions by running a 2D homogeneous profile (i.e., $\sigma_{lnVs} = 0$). As shown in Figure B.8, the $1D_{Det}$ model with periodic boundary conditions, the 2D 'control' case with periodic boundary conditions, and the final model with massive free field columns, and vertically and horizontally unconstrained base nodes all produce identical results for a homogeneous profile.

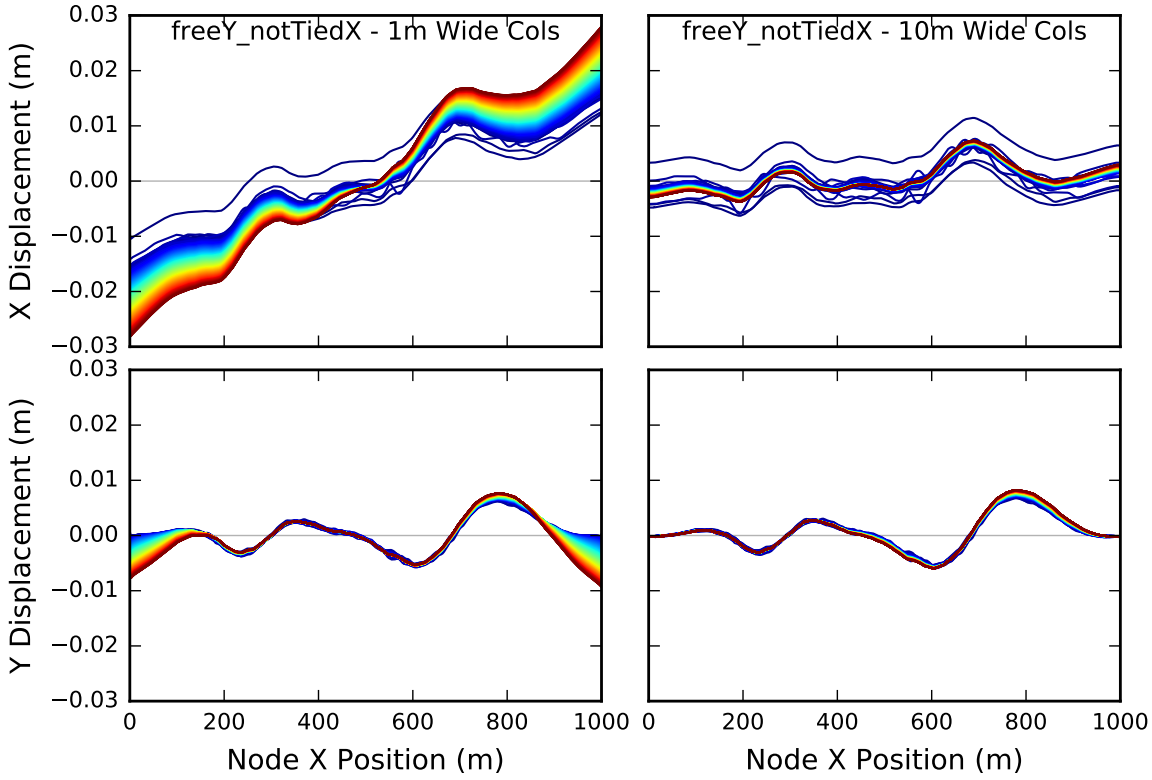

Figure B.7: X and Y displacements as a function of X position for all nodes along the base of the model for the final proposed model configuration ('freeY_notTiedX'). Left and right panels are for 1-m-wide and 10-m-wide massive columns, respectively. Every tenth time step is plotted, with the color scale representing time increasing from dark blue at 0.0 seconds and to dark red at 30 seconds (end of record). Note that dynamic and 'static' gravity displacements are superimposed. $V_{S,0} = 150$ m/s, $\sigma_{lnVs} = 0.175$, $r_H = 50$ m and $a_{H/V} = 10$.

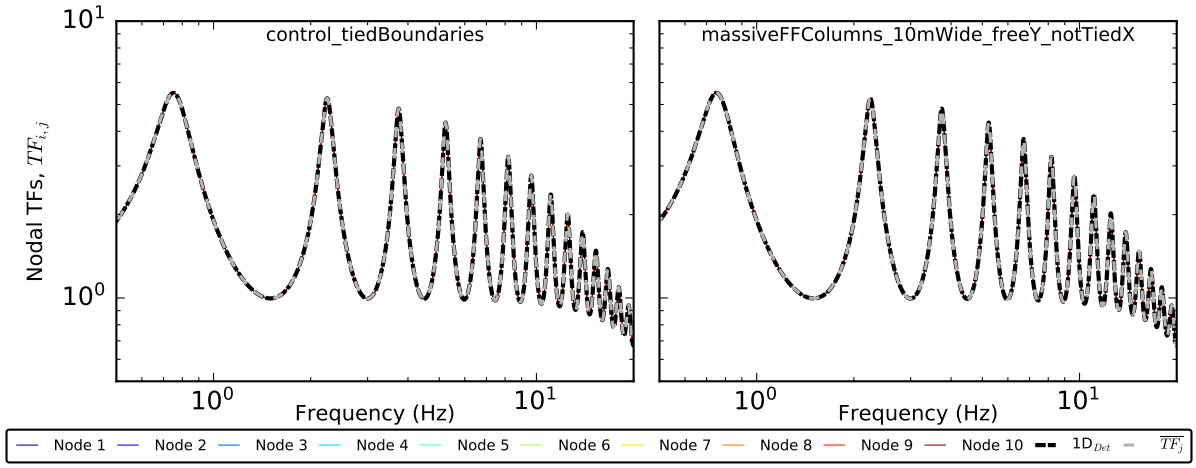

Figure B.8: Verification of the final proposed model configuration ('freeY_notTiedX'; right) with 1D model using a 2D homogeneous profile (i.e., $\sigma_{lnVs} = 0$). The control case (left) is shown for reference and utilizes identical model boundaries as $1D_{Det}$ albeit with 1,000 elements in the Y direction as opposed to 1 element. $V_{S,0} = 150$ m/s, $\sigma_{lnVs} = 0.0$, $r_H = 50$ m and $a_{H/V} = 10$.

B.3 Influence of Covariance Model for Random Field Generation on Site-Response Results

In order to gain an understanding of how the covariance model used for generation of the random field influences site-response results, 30 realizations of one permutation of random field parameters (i.e, $V_{S,0} = 150$ m/s, $\sigma_{lnVs} = 0.175$, $r_H = 50$ m and $a_{H/V} = 10$) were analyzed using three covariance models: Gaussian, Exponential, and Matérn (also know as Whittle-Matérn or Von Kármán). The Exponential model is a special case of the Matérn model with shape parameter exponent, $\nu = 0.5$. The Matérn model was run with the lowest available value in the Python package GSTools (Müller and Schüler, 2020), $\nu = 0.2$. As the shape parameter decreases, the roughness of the random field increases, particularly at small length scales (Frankel and Clayton, 1986; Chemingui, 2001; Diggle and Ribeiro, 2007). Others have shown that Matérn models are more appropriate for modeling real velocity heterogeneities and scatter waves more realistically than the Gaussian model (Frankel and Clayton, 1986; Sato et al., 2012).

Figure B.9 plots normalized autocorrelation functions for these three covariance models generated with $r_H = 50$ m. The correlation decreases at short lags from Gaussian to Exponential to Matérn, increasing the roughness at these small length scales. The implementation of the Matérn model in GSTools is such that the shape-parameter (ν) will rescale the input length scale (i.e., r_H), so that the limit case for ν to infinity results in the Gaussian model with a finite length scale (GSTools, 2020 - pers. comm.). For this reason, as shown in Figure B.9, when $r_H = 50$ m is specified as the length scale, the model is scaled such that the integral scale is 56 m (unless the an integral scale = 50 m is specified). Figure B.10 plots one realization of the random field (with Seed = 1) for all three covariance models. Note that due to the particular numerical method used by GSTools to generate the random field (i.e., the Randomization Method; Heße et al., 2014) it is not possible to generate the 'same' random field with different small scale roughness (corresponding to different Covariance models) using a seed; for this reason, sufficient realizations were analyzed, and mean and standard deviation of IMs were computed. As discussed in Appendix B.4, 30 realizations are sufficient for these IMs to converge. Figure B.10 clearly illustrates that the Exponential and Matérn models produce significantly more

roughness at small length scales in the randomized velocity model. While the difference in small-scale roughness between the Exponential and Matérn models is visible, it is subtle.

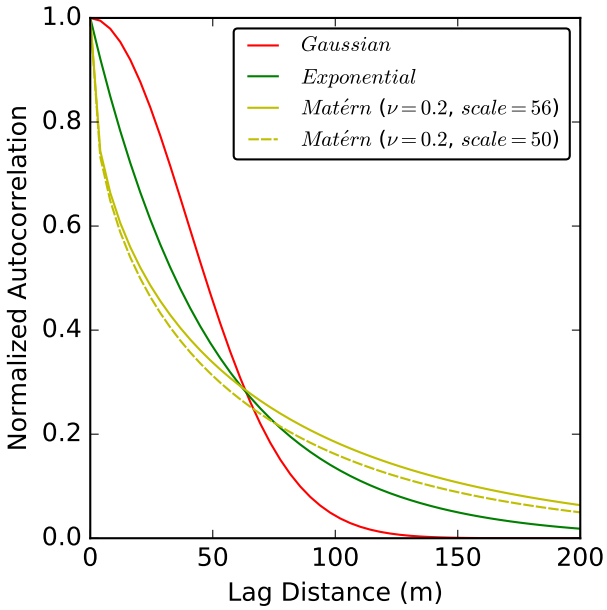

Figure B.9: Normalized Auto-Correlation functions for three different covariance models: Gaussian, Exponential, and Matérn ($\nu = 0.2$). $r_H = 50$ m and $a_{H/V} = 10$.

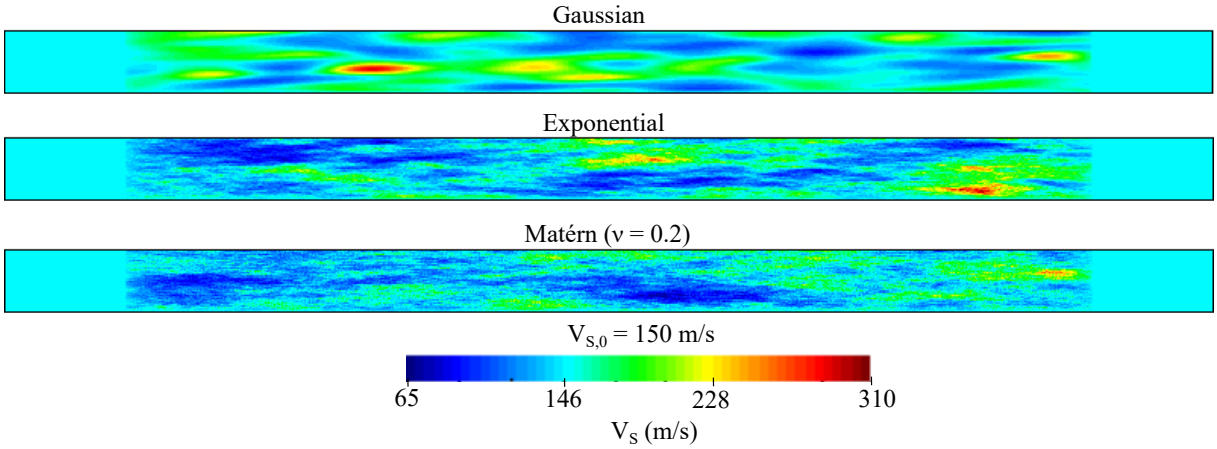

Figure B.10: Example of V_S random fields generated using three different covariance models: Gaussian, Exponential, and Matérn ($\nu = 0.2$). Seed = 1, $V_{S,0} = 150$ m/s, $\sigma_{lnVs} = 0.175$, $r_H = 50$ m and $a_{H/V} = 10$.

Median and standard deviation of transfer functions are plotted in Figure B.11. For all three covariance models, the amplification and standard deviation at f_0 are approximately equal, and slightly less than the $1D_{Det}$ amplification. Most notably, high frequencies are scattered more for the Exponential and Matérn models, resulting in an increase in the variance and decrease

in the median of transfer functions for $f > 8$ Hz. This is reasonable as these models exhibit increasingly more roughness at smaller length scales (see Fig. B.10), and, therefore, would be expected to scatter high frequencies more effectively. On the contrary, the Gaussian model reduces peak amplifications at the second and third mode frequencies.

Results can be further scrutinized by looking at median and standard deviation of other IMs in Figure B.12. The fundamental frequency (f_0) and amplification at f_0 ($AF(f_0)$), peak ground acceleration (PGA), spectral acceleration at $1/f_0$ ($SA(T_0)$), and Arias intensity in horizontal ($I_{a,Hor}$) and vertical components ($I_{a,Vert}$) are plotted for all three covariance models. These $\overline{IM}$ are normalized by the respective value from $1D_{Det}$ analysis, except for ($I_{a,Vert}$) which does not exist for $1D_{Det}$ and so it is normalized by the value for the Gaussian model. Consistent with observations from median transfer function in Figure B.11, f_0 and $AF(f_0)$ are not significantly influenced by the choice of covariance model. Peak ground acceleration is reduced for Exponential and Matérn models which is expected due to the reduction in high-frequency content observed in $\overline{TF}$. Interestingly, $I_{a,Vert}$ is significantly higher (60% higher) for the Matérn models suggesting that the scattering of waves induced by these models generates more vertical motion than the Gaussian model.

Based on these results, the Matérn model with $\nu = 0.5$ (i.e., the Exponential model) was chosen for final production analyses as it is more effective in scattering high frequencies. The difference between $\nu = 0.2$ and $\nu = 0.5$ is insignificant for this application and likely well within the uncertainty in identifying random field input parameters for real geologic deposits.

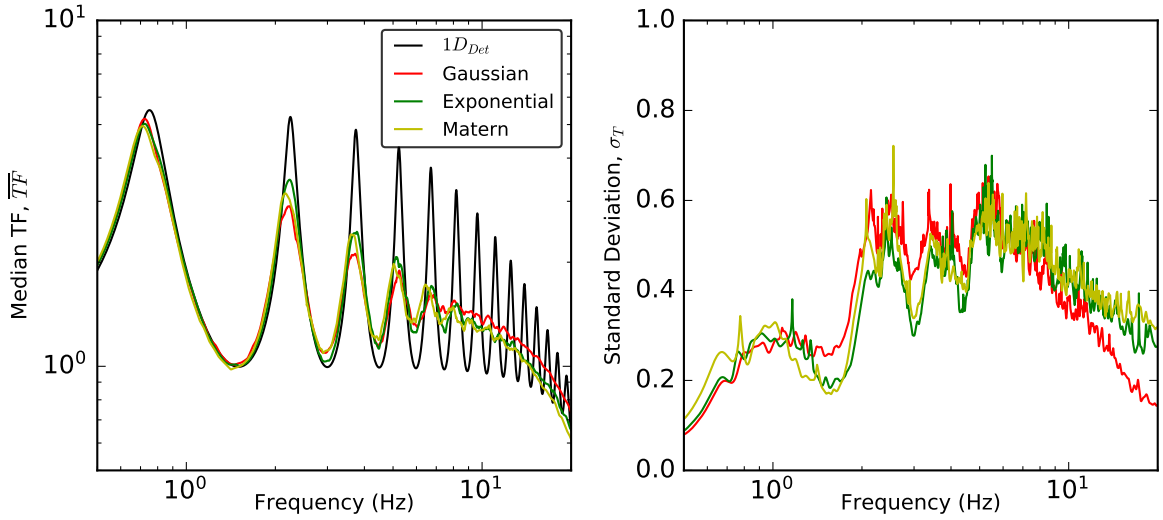

Figure B.11: Mean and standard deviation of transfer functions for 30 realizations comparing between different covariance models for random field generation. $V_{S,0} = 150$ m/s, $\sigma_{lnVs} = 0.175$, $r_H = 50$ m and $a_{H/V} = 10$.

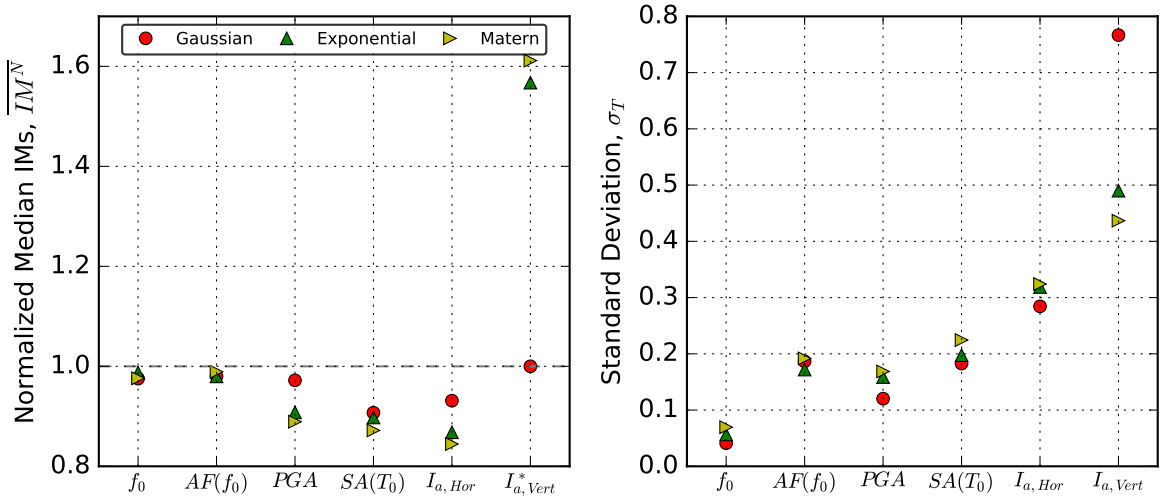

Figure B.12: Median and standard deviation of IMs from 30 realizations comparing between different covariance models for random field generation. $V_{S,0} = 150$ m/s, $\sigma_{lnVs} = 0.175$, $r_H = 50$ m and $a_{H/V} = 10$. * Note: Vertical Arias intensity ($I_{a,Vert}$) is not normalized by $1D_{Det}$ as the 1D analysis does not have a vertical component of motion, therefore, the values are normalized by $I_{a,Vert}$ of the Gaussian model.

B.4 Convergence of IMs

Bootstrap sampling was used to test that the main IMs investigated in this study converge within the number of random field realizations analyzed for each parameter permutation. For

a permutation with $V_{S,0} = 150$ m/s, $\sigma_{lnVs} = 0.175$, $r_H = 50$ m and $a_{H/V} = 10$, 500 realizations of the random field were generated and used for site-response analysis. From these 500 realizations, 1,000 bootstrap samples, allowing replacement, of N number of realizations were randomly selected. N was increased incrementally from 1 realization up to 100 realizations in each bootstrap sample. Median and standard deviation of IMs (e.g, $\overline{f_0}$ and σ_{T,f_0}) are computed for each bootstrap sample of N realizations. $std[ln(\overline{IM})]$ and $std[ln(\sigma_T)]$ are then taken as the standard deviations of these values across all 1,000 bootstrap samples.

The results of this convergence study are summarized in Figure B.13, which plot the variation in $std[ln(IM)]$ as the size of each bootstrap sample (i.e., number of realizations) increases. As expected, as the number of realizations in each sample increases, the standard deviation of each $\overline{IM}$ and σ_T across all bootstrap samples decreases. This variability decreases rapidly initially and then stabilizes, nearly asymptotically. Median IMs (e.g., $\overline{f_0}$ and $\overline{PGA}$), especially those corresponding to modal frequencies, converge quickly, nearly reaching their asymptotic value within 10 realizations. Total standard deviations of IMs (e.g., σ_{T,f_0} and $\sigma_{T,PGA}$) take more realizations to converge and converge to a higher value. Based on these results, the use of 30 realizations appears to give a stable estimate of medians and standard deviations of IMs. All final production analyses are based on 30 realizations.

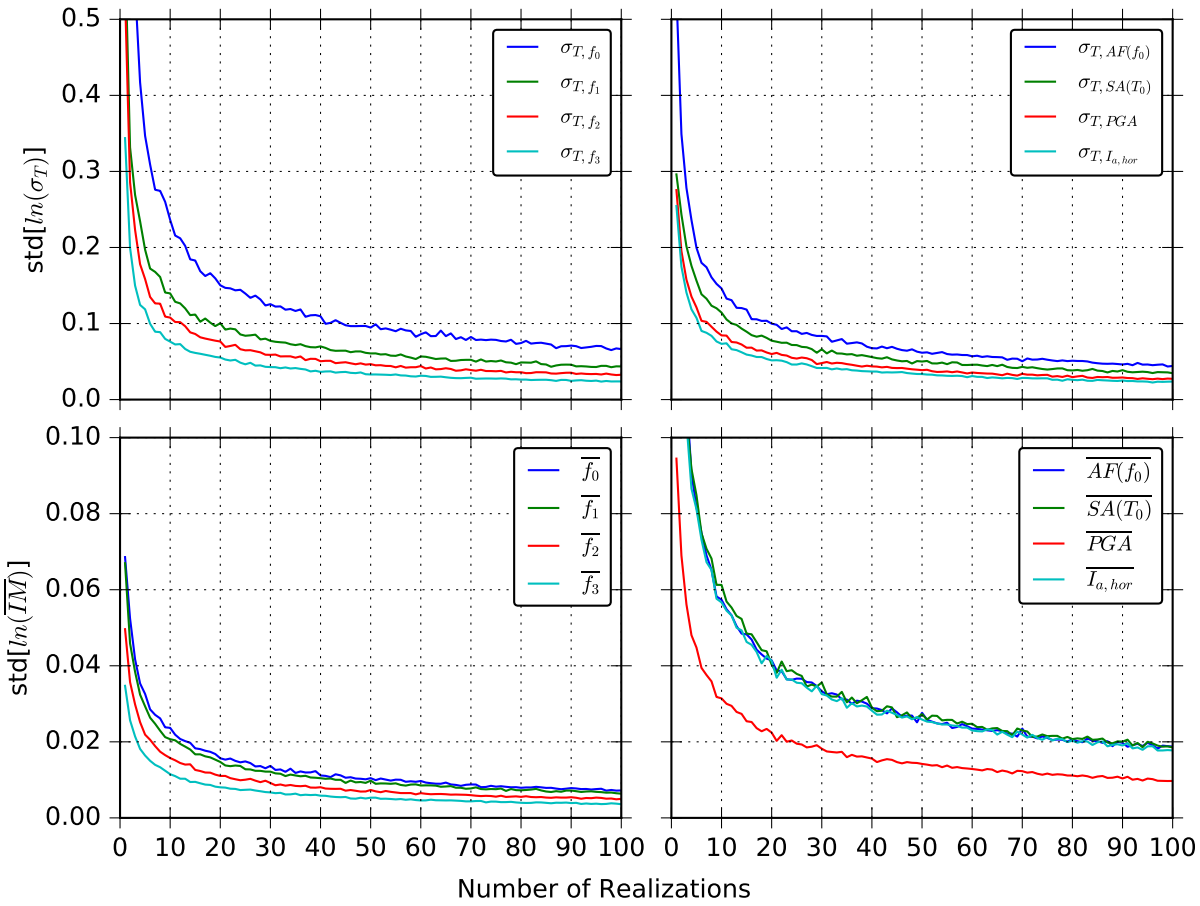

Figure B.13: Convergence of various IMs tested using bootstrap sampling with 1,000 bootstrap samples. This plots the standard deviation of each $\overline{IM}$ and σ_T across all bootstrap samples as the number of random field realizations increases.

B.5 Additional Figures to Supplement Discussion

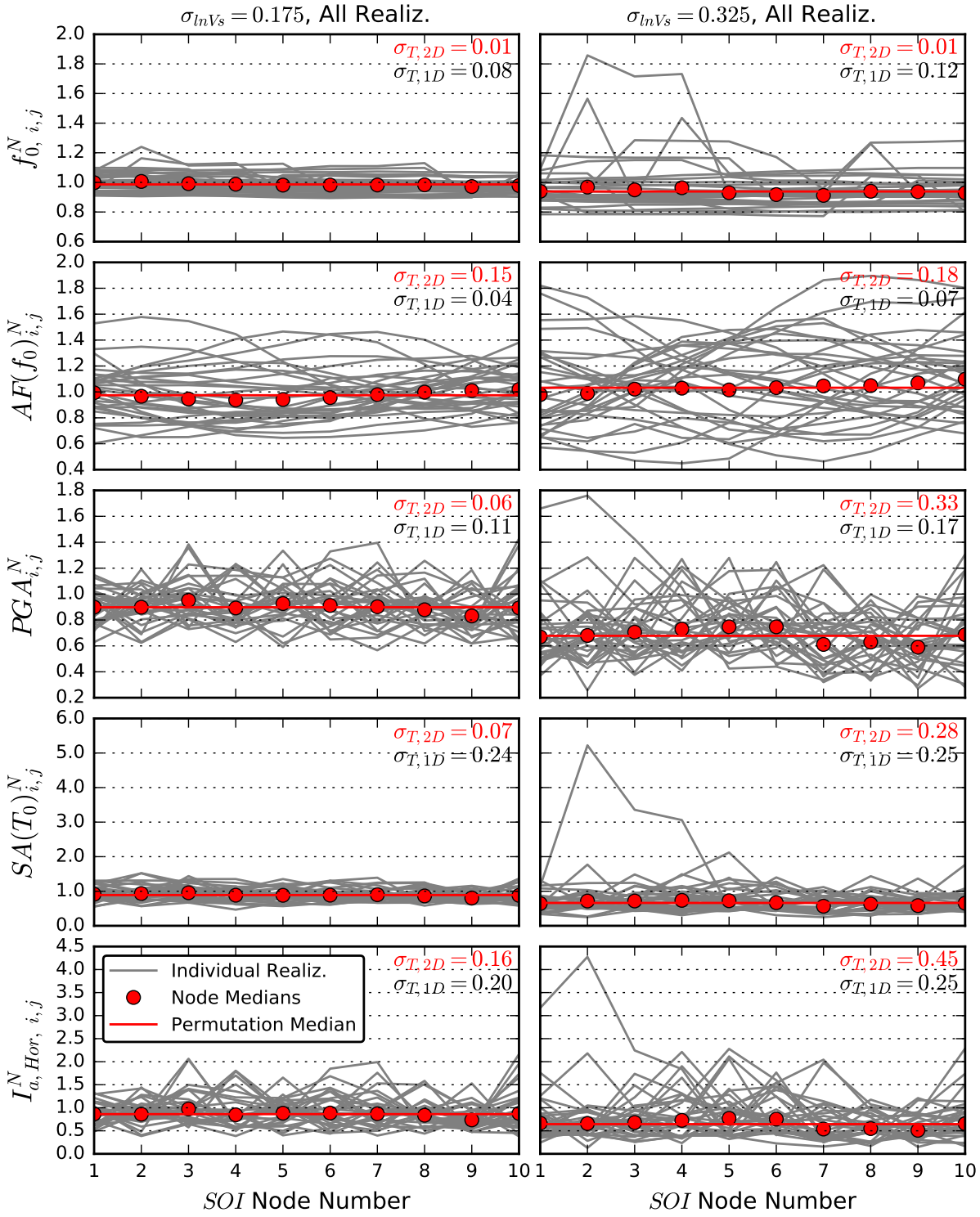

Figure B.14: Normalized IMs as a function of SOI node location for all realizations of permutations with $\sigma_{lnVs} = 0.175$ (left) and 0.325 (right). The median for all nodes and realizations (i.e., the permutation median) is compared to the median for all realizations at each individual node. For both permutations, $V_{S,0} = 150$ m/s, $r_H = 50$ m and $a_{H/V} = 10$

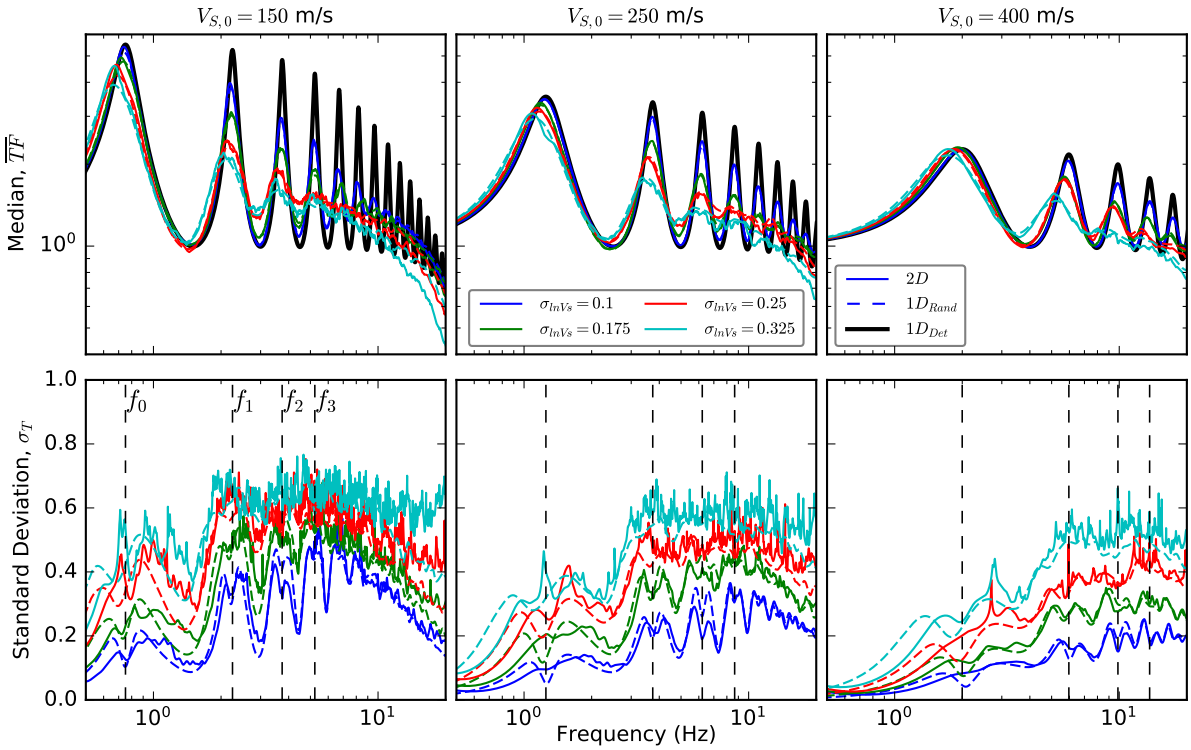

Figure B.15: Comparison of 2D and $1D_{Rand}$ median transfer functions and total standard deviations for various values of σ_{lnVs} with $V_{S,0}$ = 150, 250, and 400 m/s. Other random field parameters are $r_H = 50$ m, and $a_{H/V} = 10$.

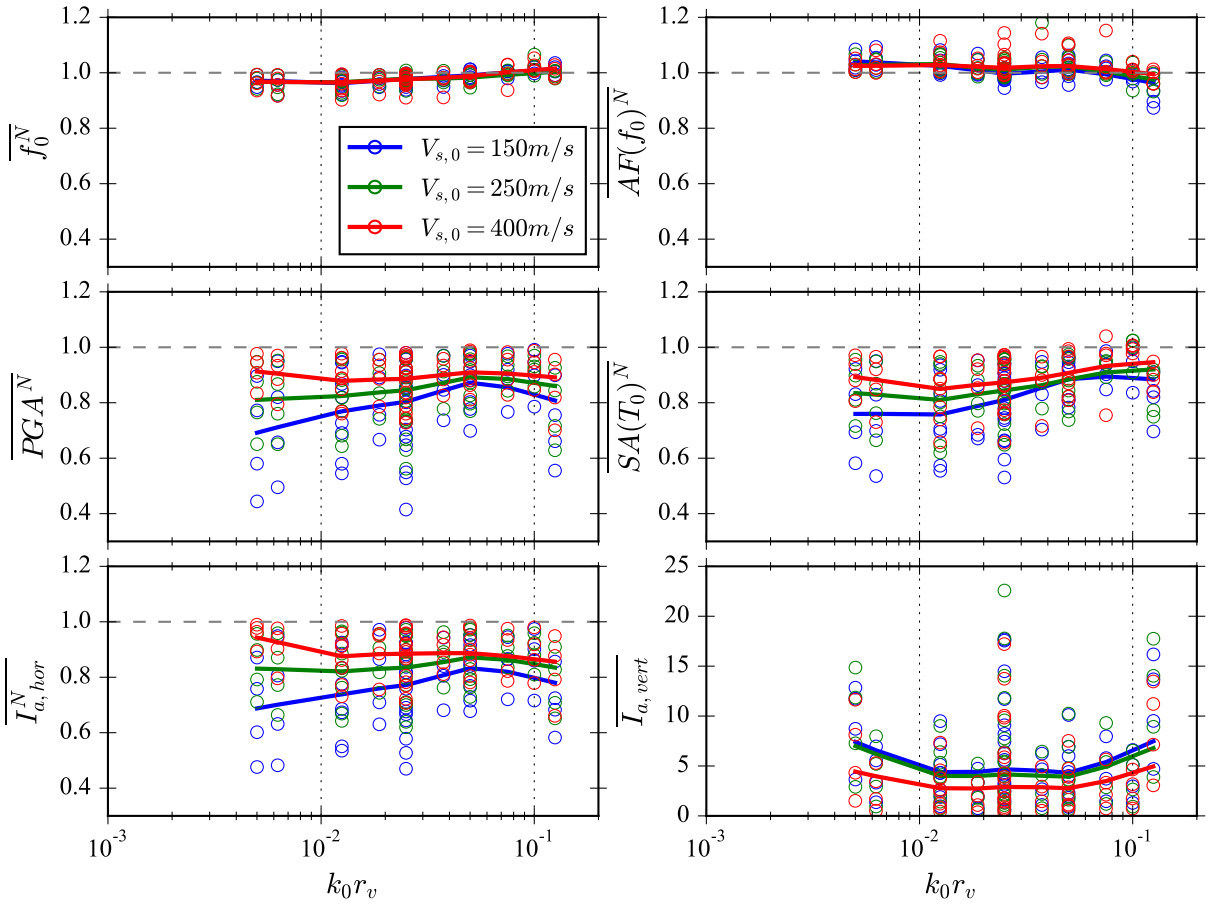

Figure B.16: Normalized median IMs for all permutations plotted as a function of $k_0 r_V$ and color-coded by $V_{S,0}$. Note that $I_{a,vert}$ is not normalized as there is no vertical component to $1D_{Det}$ analysis.

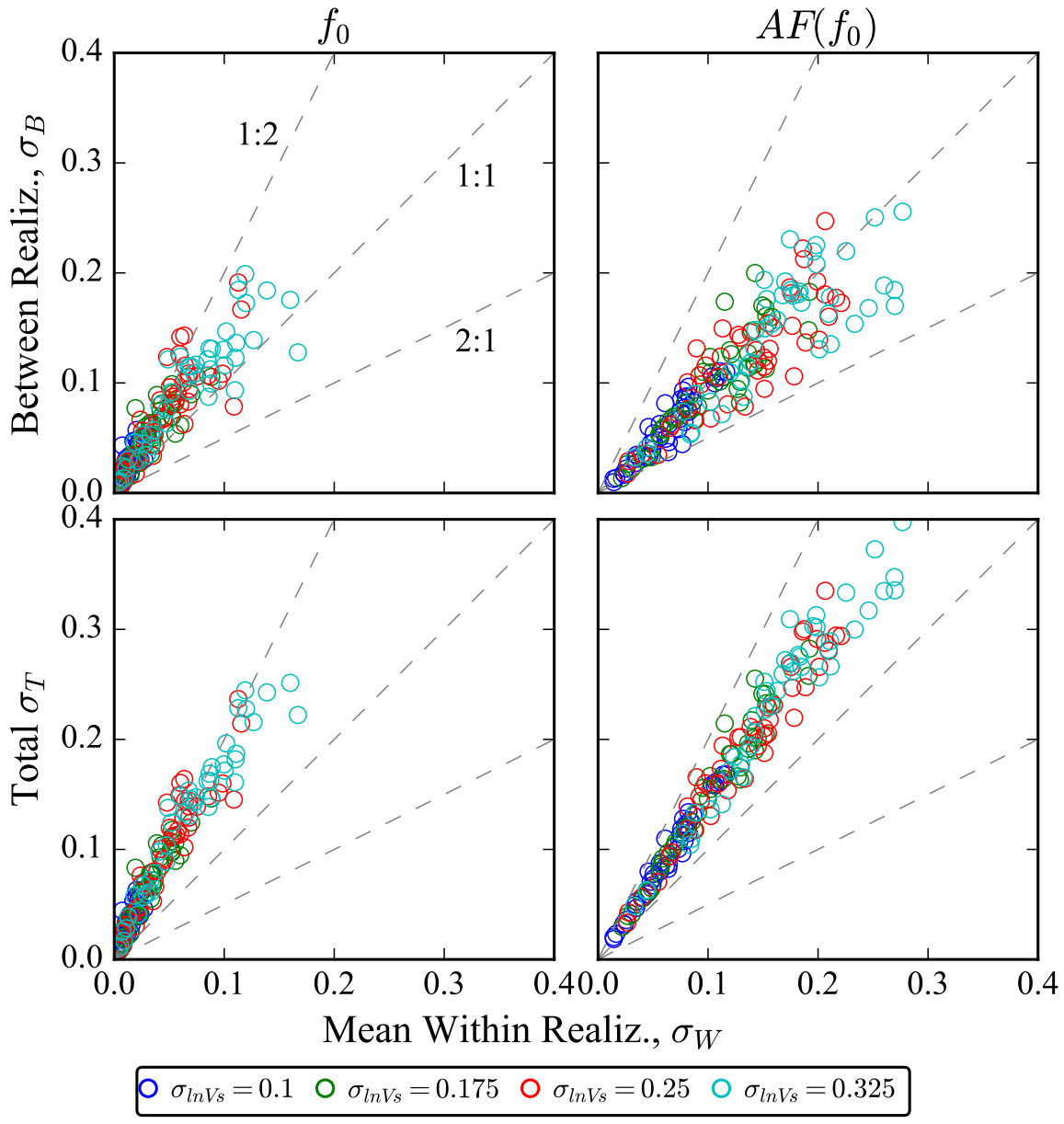

Figure B.17: Comparison of mean within-realization standard deviation to between-realization (top) and total (bottom) standard deviations from all permutations for f_0 (left) and $AF(f_0)$ (right).

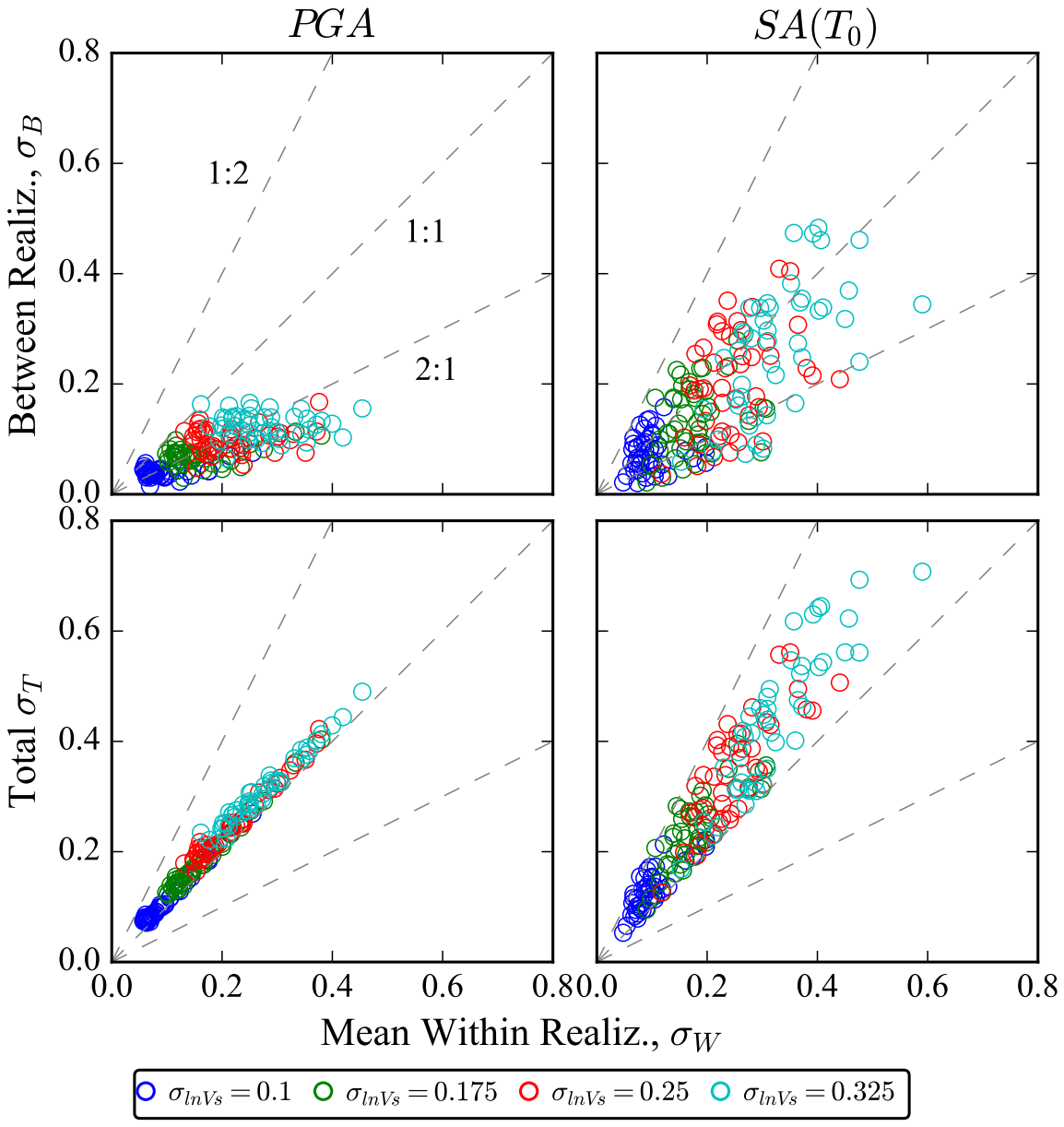

Figure B.18: Comparison of mean within-realization standard deviation to between-realization (top) and total (bottom) standard deviations from all permutations for *PGA* (left) and $SA(T_0)$ (right).

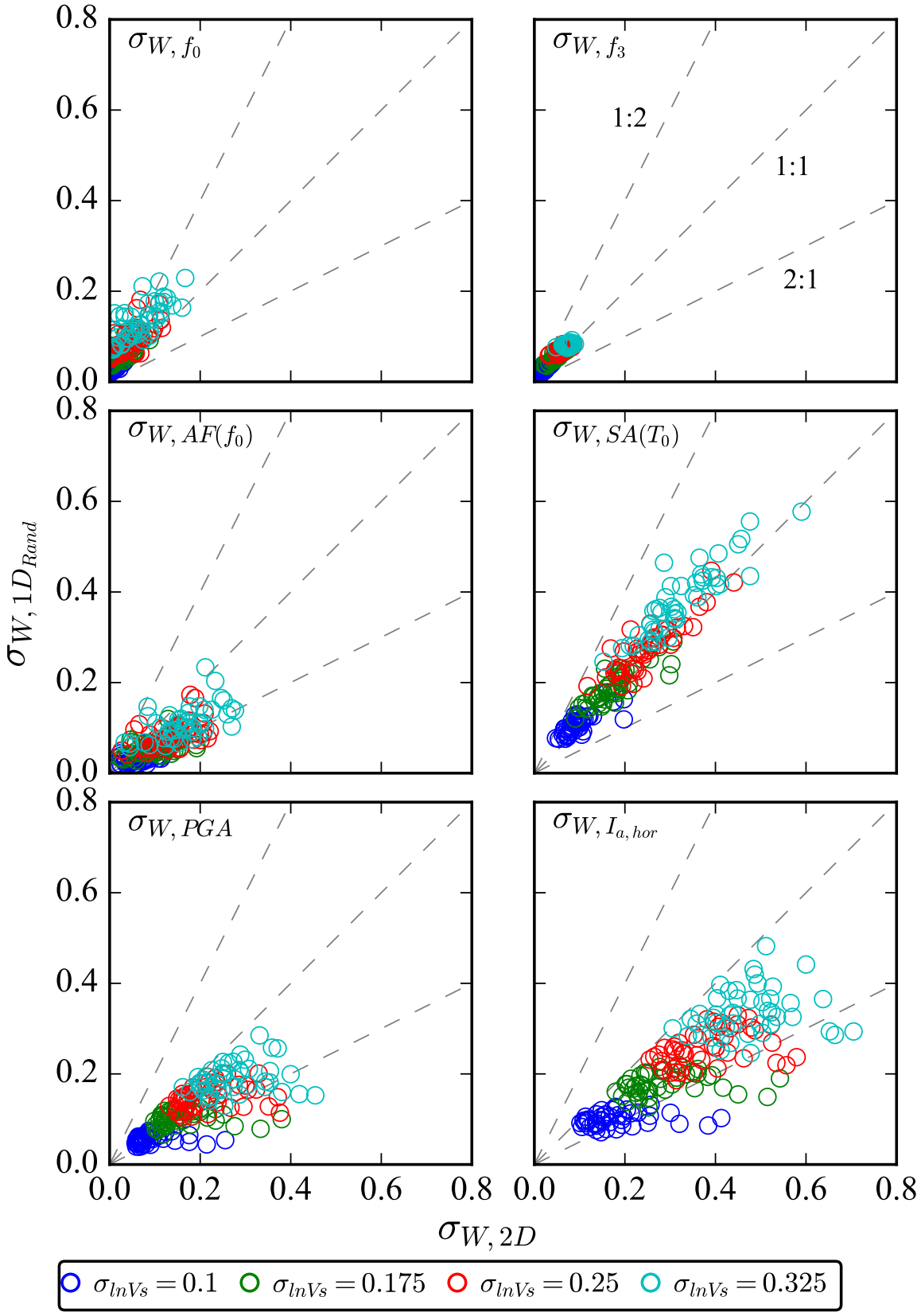

Figure B.19: Comparison of mean within-realization lognormal standard deviations between 2D and $1D_{Rand}$ analyses for all permutations..

Appendix C

Appendix to Chapter 4

C.1 Summary

These appendices contain additional figures, with interpretation, to supplement the discussion in Chapter 4, and are referenced throughout the chapter. Appendix C.2 explains in detail and verifies the frequency domain analyses for 2D models, Appendix C.3 checks the sensitivy of ETFs to smoothing, Appendix C.4 briefly compares results from 2D models with rigid and compliant bases, and Appendix C.5 provides additional figures to supplement the discussion throughout the text. Finally, V_S profiles, and median transfer functions and spectral acceleration residuals are provided in Appendix C.6.

- **VERIFICATION OF FREQUENCY-DOMAIN 2D ANALYSES**
- **SENSITIVITY OF MEDIAN AND STANDARD DEVIATION OF ETFS TO SMOOTHING**
- **COMPARISON OF 2D TRANSFER FUNCTIONS FROM RIGID AND COMPLIANT BASE MODELS**
- **ADDITIONAL FIGURES TO SUPPLEMENT DISCUSSION**
- **SHEAR WAVE VELOCITY PROFILES, TRANSFER FUNCTIONS, AND ADDITIONAL METADATA FOR ALL SITES**

C.2 Verification of Frequency-Domain 2D Analyses

The computational demand of running 30 realizations for every permutation of random field parameters (e.g., $\sigma_{lnVs} = 0.15$ and 0.25, rigid and compliant base) is large, therefore, running each of these models for every ground motion in the database becomes very computationally expensive. For this reason, the fidelity of frequency domain analyses for 2D models with wave scattering was assessed. To evaluate this, all ground motions were run in the time domain for one realization of one site. Then, a reference ground motion, with the highest T_{max}, was chosen to compute a transfer function (surface motion over incident motion at the base) for frequency domain analyses of all remaining ground motions. Surface accelerations and IMs were compared between the frequency domain solution and the time domain calculations. An example of this comparison for one ground motion is in Figure C.1. As shown in Figure C.1, the resulting surface acceleration and IMs are essentially the same for time domain and frequency domain calculations, with IMs generally being within 1-2% of each other at all recorder nodes.

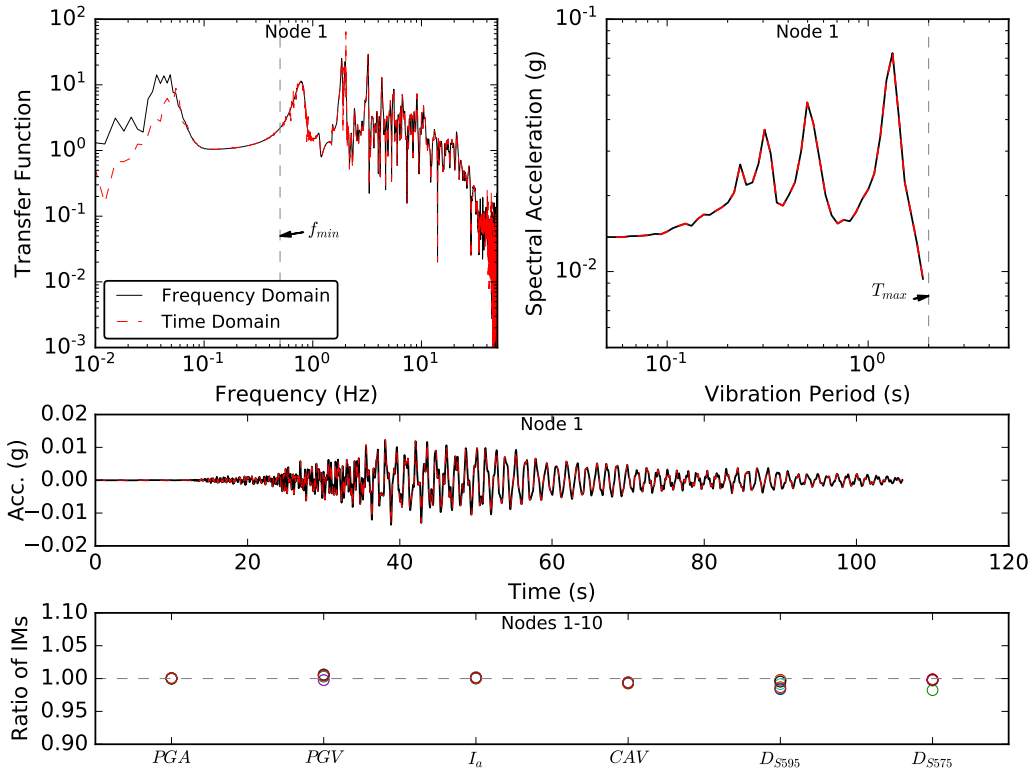

Figure C.1: Example verification of the 2D frequency domain analysis with time domain analysis by comparing within transfer functions, and surface ground accelerations and spectral accelerations for Node 1. Ratios of other surface IMs for all 10 nodes are also shown. (Site 1 - Event 6)

C.3 Sensitivity of median and standard devations of ETFs to smoothing

To thoroughly understand the influence of the smoothing on median and standard deviations of TF, ETFs were calculated in various ways using Konno-Ohmachi smoothing with bandwidth coefficients (b-values) ranging from 20 to 100, as well as with no smoothing. ETFs were computed in three ways, by: Method (1) smoothing each FAS before computing TF, Method (2) smoothing each GM component TF, and Method (3) only smoothing the median and standard deviations for "visual presentation". It was found that all three methods produce equivalent medians, provided that FAS and TFs are smooth in log space of Fourier amplitudes or amplification factors, respectively. However, the standard deviations can be significantly underpredicted if smoothing is applied to FAS or individual TFs (i.e., Methods 1 and 2).

Figure C.2 compares methods 1 and 3, described directly above for computing smoothed median and standard deviations of ETFs with many different b-values for the smoothing model. It shows that low b-values can result in excessive smoothing which can obscure details of the site response, such as the double peak amplification observed at f_0 for Site 21 - Treasure Island (Fig. C.2). With heavy smoothing, the peaks are significantly reduced and can even be "out of phase" with non-smoothed curves at higher modes. Based on these results, this study has adopted smoothing only the median and standard deviation values (Method 3) with a b-value of 100 for both ETF and theoretical transfer functions (TTF). For calculation of intensity measures (IMs) related to transfer functions, such as f_0 and $AF(f_0)$, transfer functions were computed by smoothing individual FAS (Method 1) with $b = 100$.

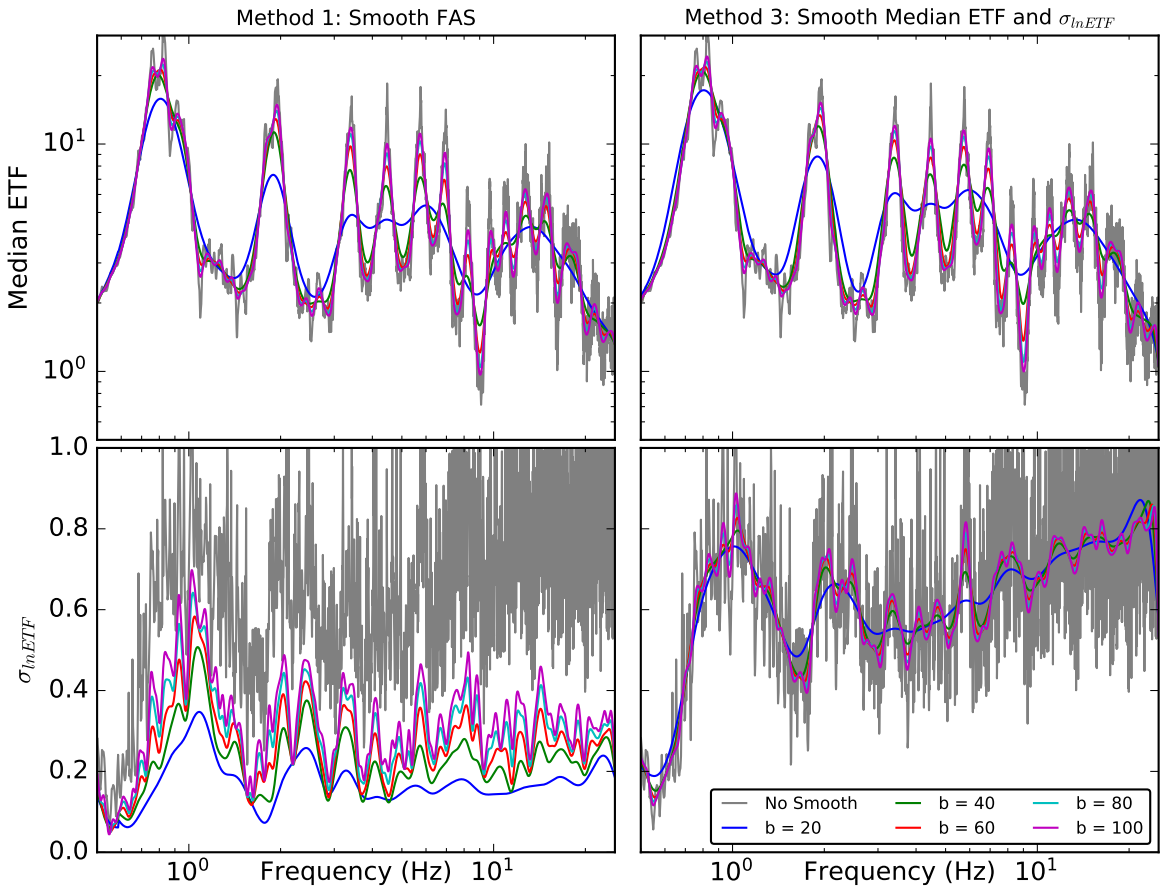

Figure C.2: Example of computing ETF median and standard deviation using different smoothing coefficient (b-values) by smoothing each individual FAS (left) and smoothing only the median and standard deviations (right). Site 21: Treasure Island

C.4 Comparison of 2D Transfer Functions from Rigid and Compliant Base Models

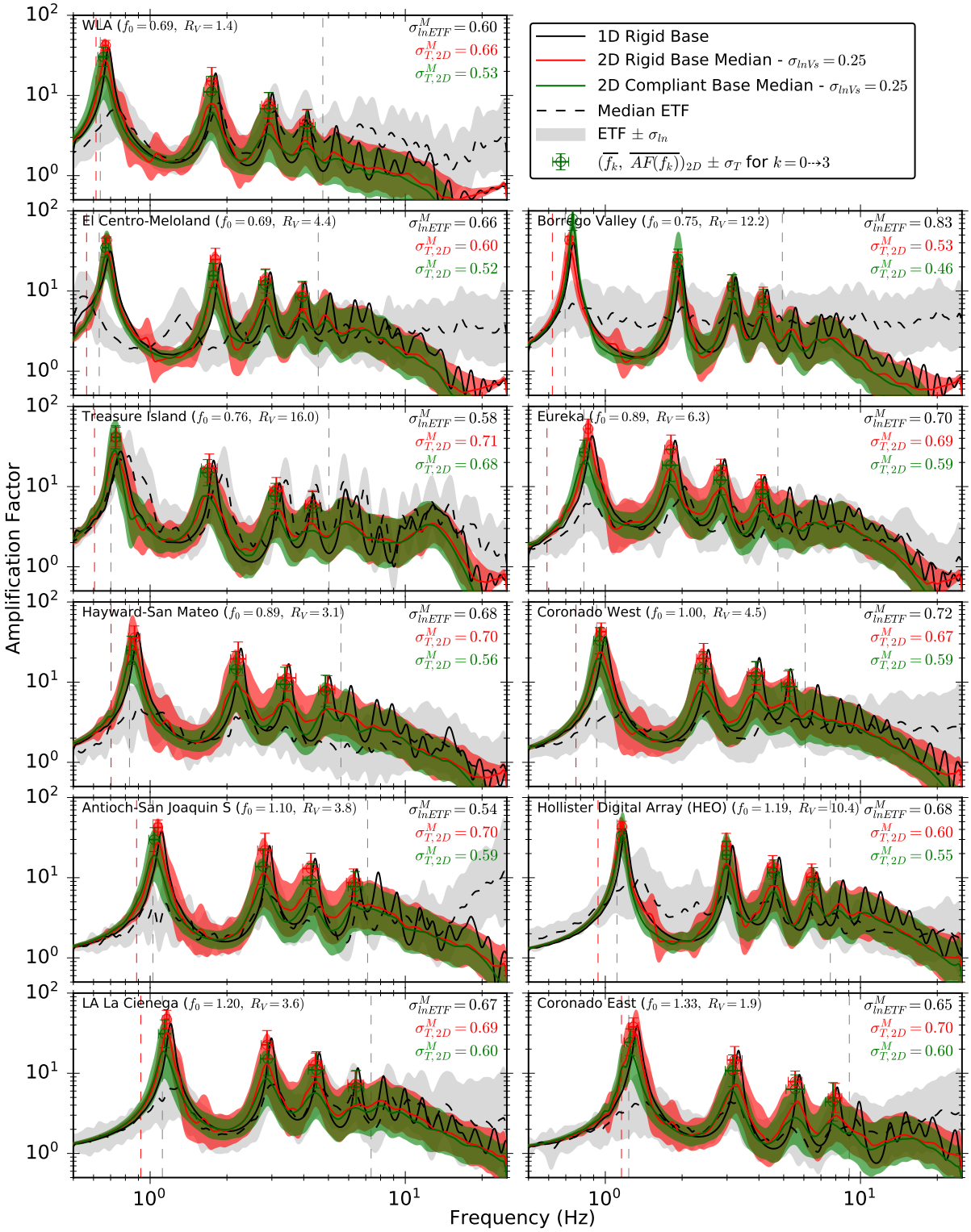

Figure C.3: Comparison of ETF to TTF from 1D and 2D analyses using a rigid base with the recorded DH motion and a compliant base with the computed incident motion.

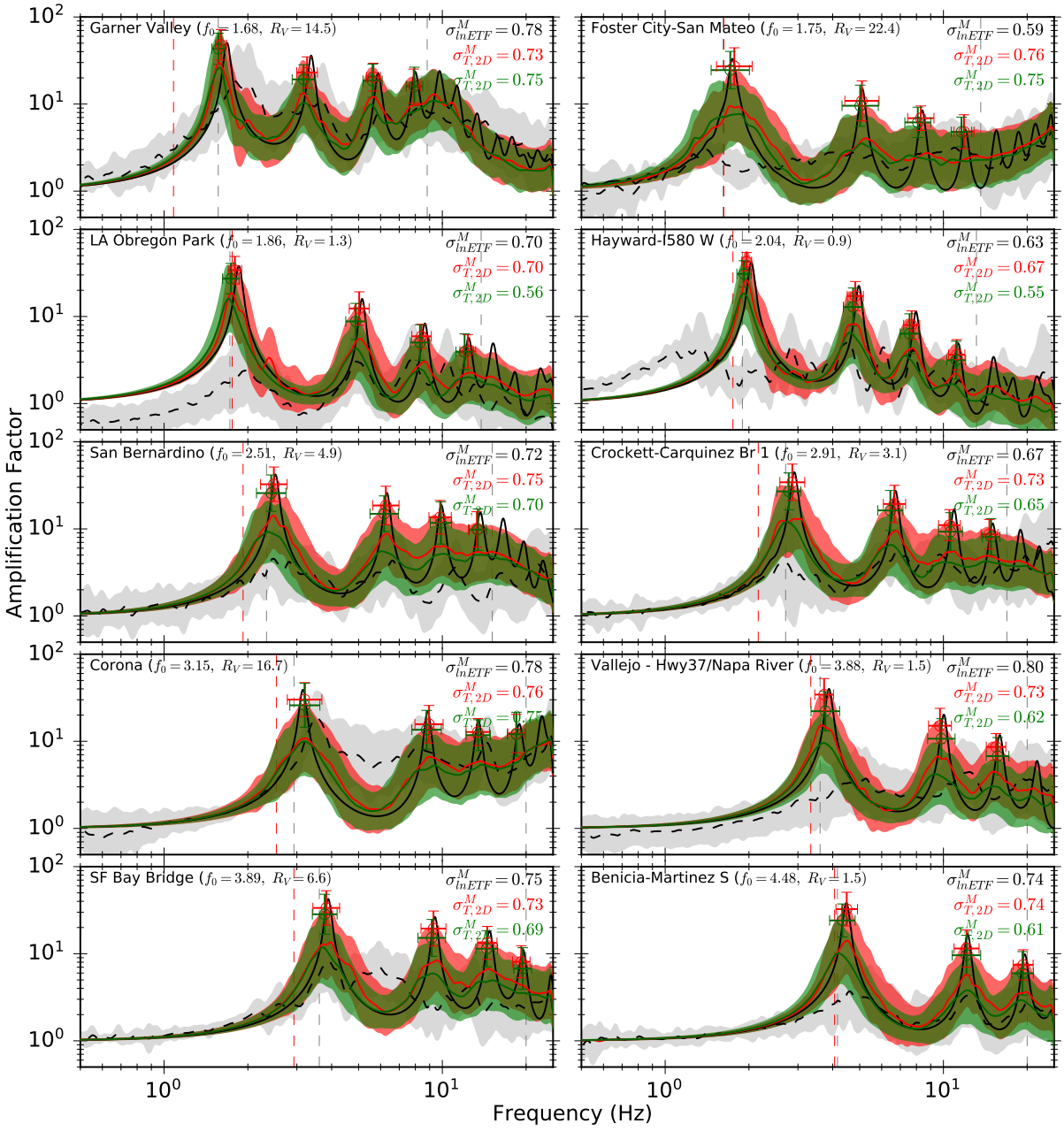

Figure C.3: Continued.

C.5 Additional Figures to Supplement Discussion

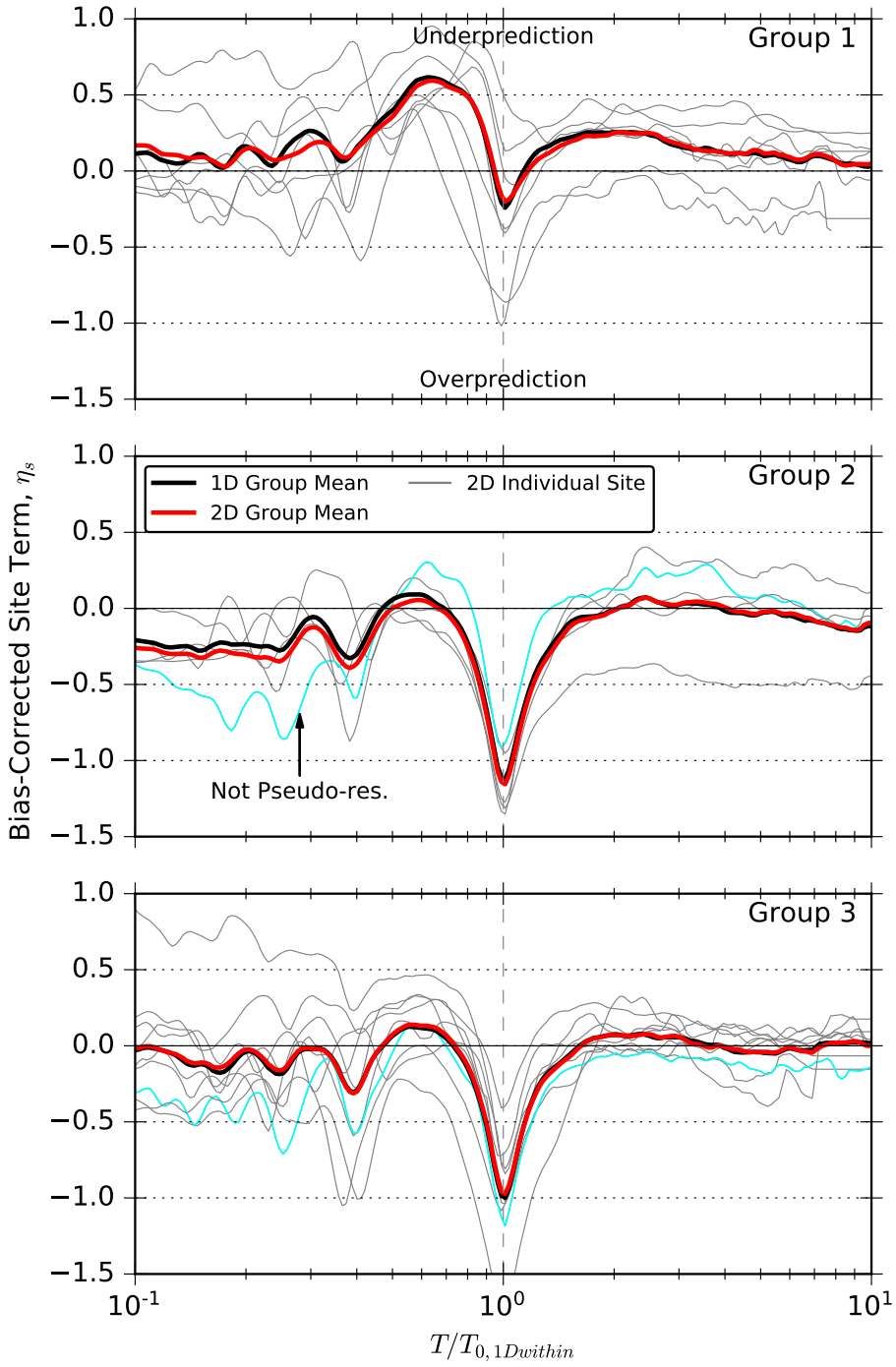

Figure C.4: Bias-corrected site terms of spectral accelerations versus normalized period $T/T_{0,1Dwithin}$ for 1D and 2D analyses. The 1D analyses are rigid-base models with the recorded within (i.e., downhole) input motion, and 2D analyses are compliant-base models with the derived incident motion. All sites are divided by groups (Table 4.1) and group averages are plotted along with individual site residuals.

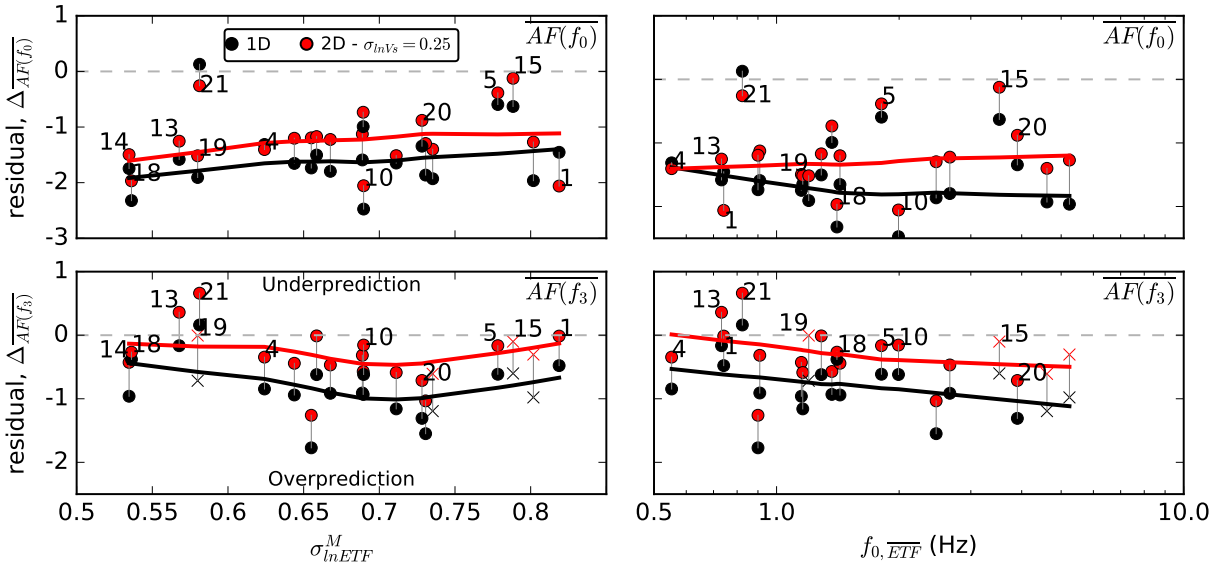

Figure C.5: Total residuals of $\overline{AF(f_0)}$ (top) and $\overline{AF(f_3)}$ (bottom) for 1D and 2D analyses as a function of σ^M_{ETF} (left) and $f_{0,\overline{ETF}}$ (right). 2D analysis is for a compliant base with $\sigma_{lnVs} = 0.25$. Residuals are computed using medians of amplification factors from individual TTF and ETF peaks. For sites with an 'x' symbol in $AF(f_3)$ plots, $AF(f_2)$ residuals are plotted because $f_3 > 20$ Hz or there is a large discrepancy between $f_{3,\overline{ETF}}$ and $f_{3,\overline{TTF}}$ (only site 19, see Sec. 4.3.1.2).

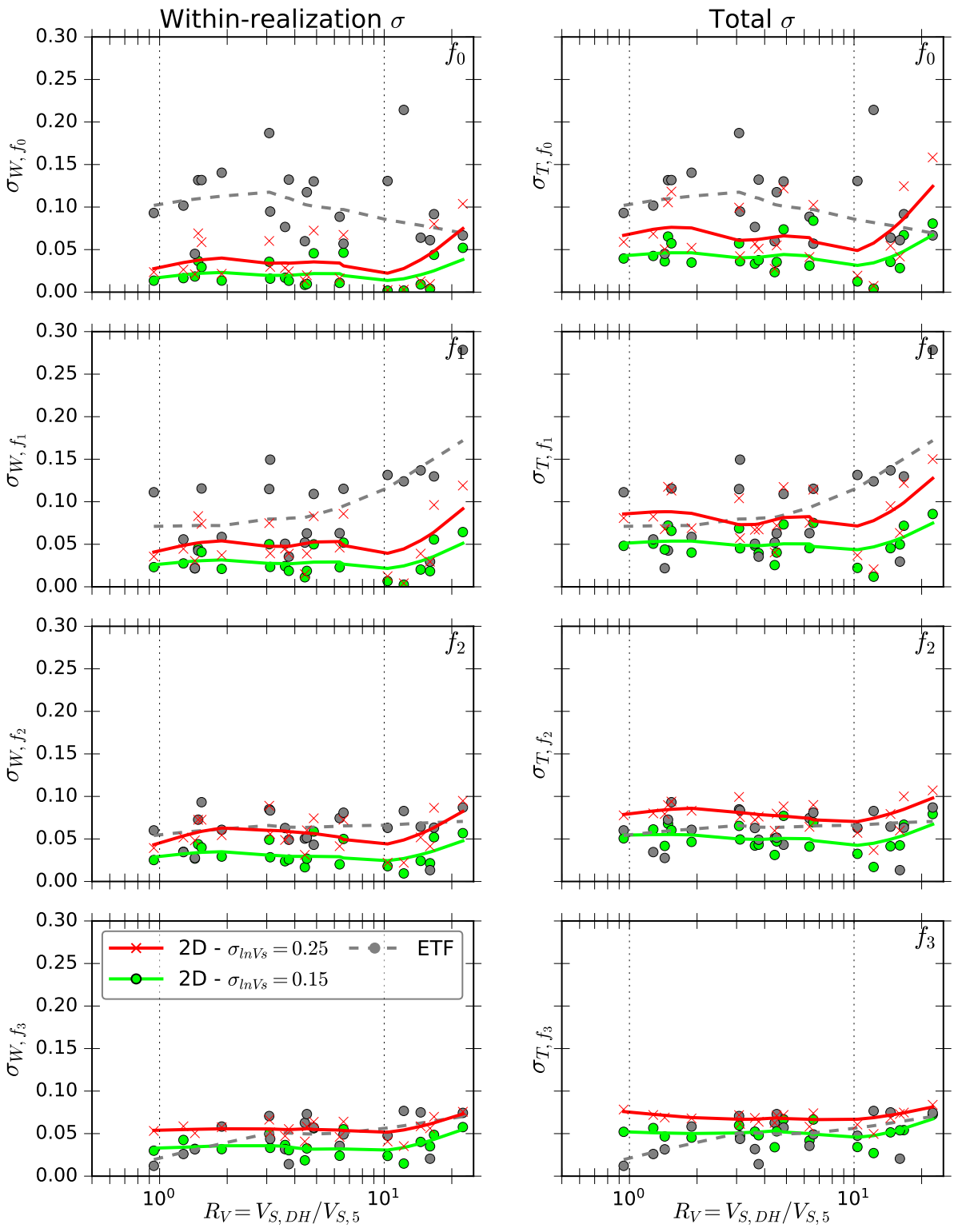

Figure C.6: Within-realization (σ_W; left) and total (σ_T; right) standard deviations for f_0 to f_3 as a function of R_V

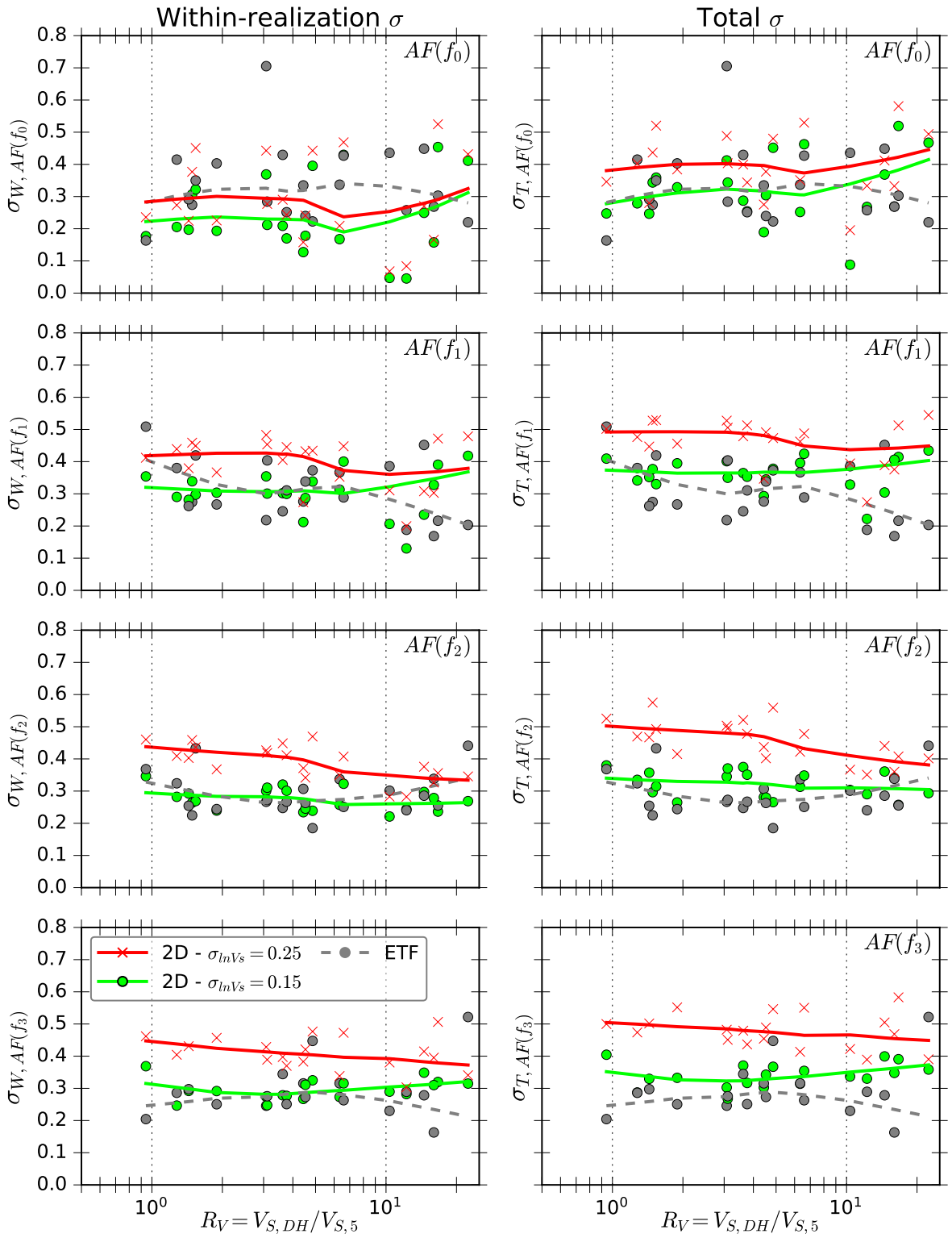

Figure C.7: Within-realization (σ_W; left) and total (σ_T; right) standard deviations for $AF(f_0)$ to $AF(f_3)$ as a function of R_V

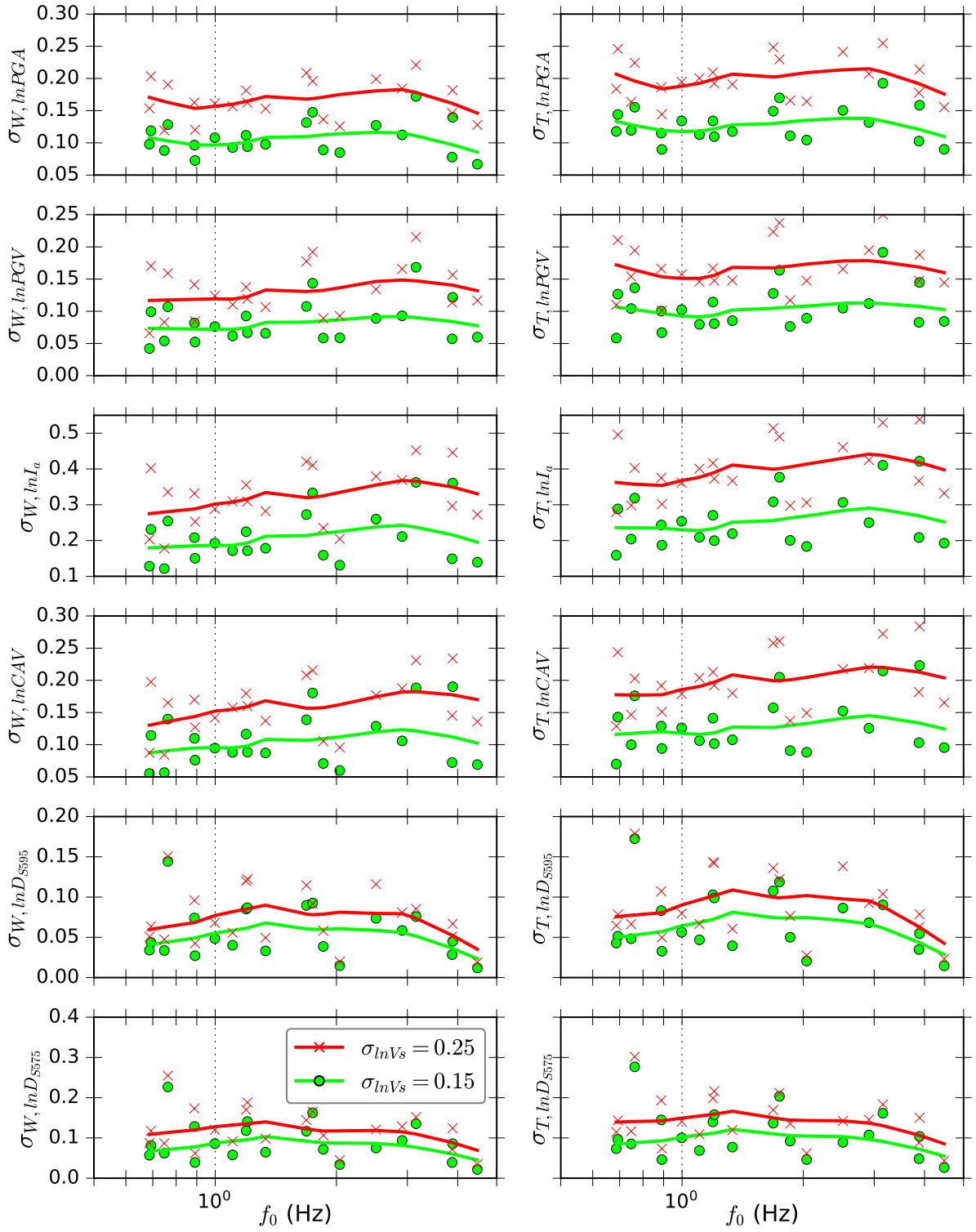

Figure C.8: Within-realization (σ_W; left) and total (σ_T; right) standard deviations for all IMs as a function of f_0.

C.6 Shear Wave Velocity Profiles, Transfer Functions, SA Residuals, and Additional Metadata for All Sites

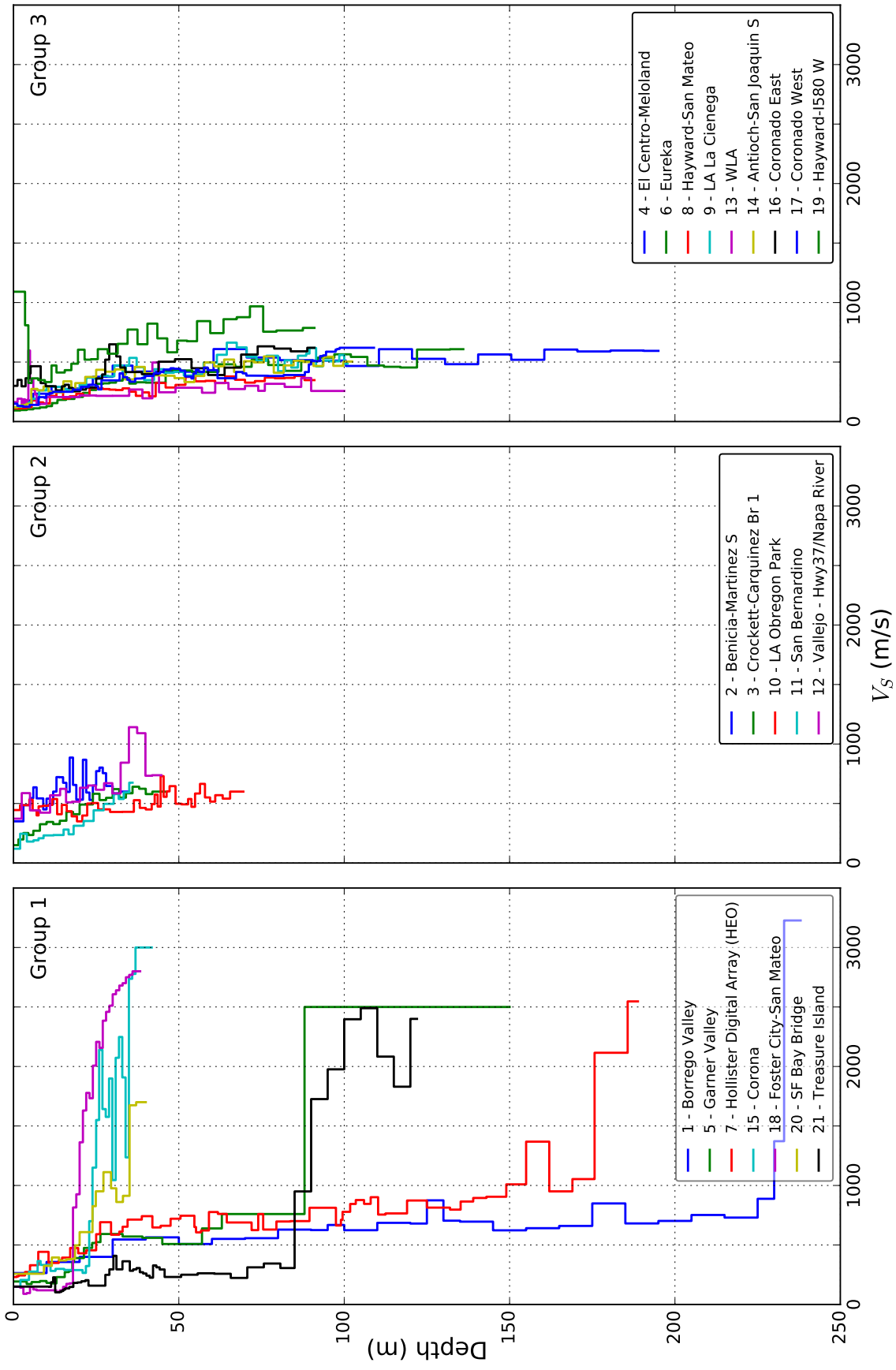

Figure C.9: V_S profiles for all sites sorted by group number.

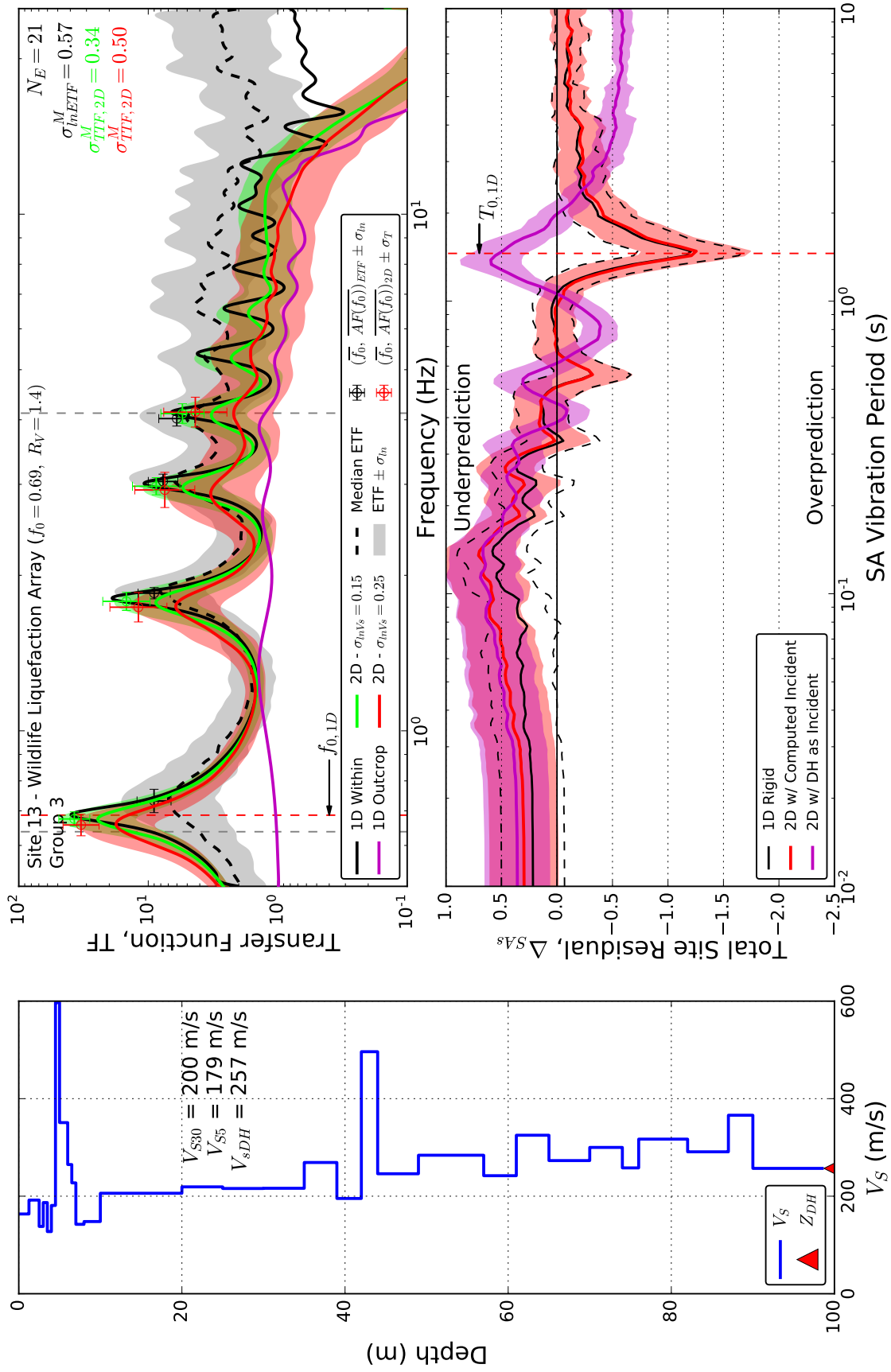

Figure C.10: V_S profile, transfer functions, and SA residuals for Site 13.

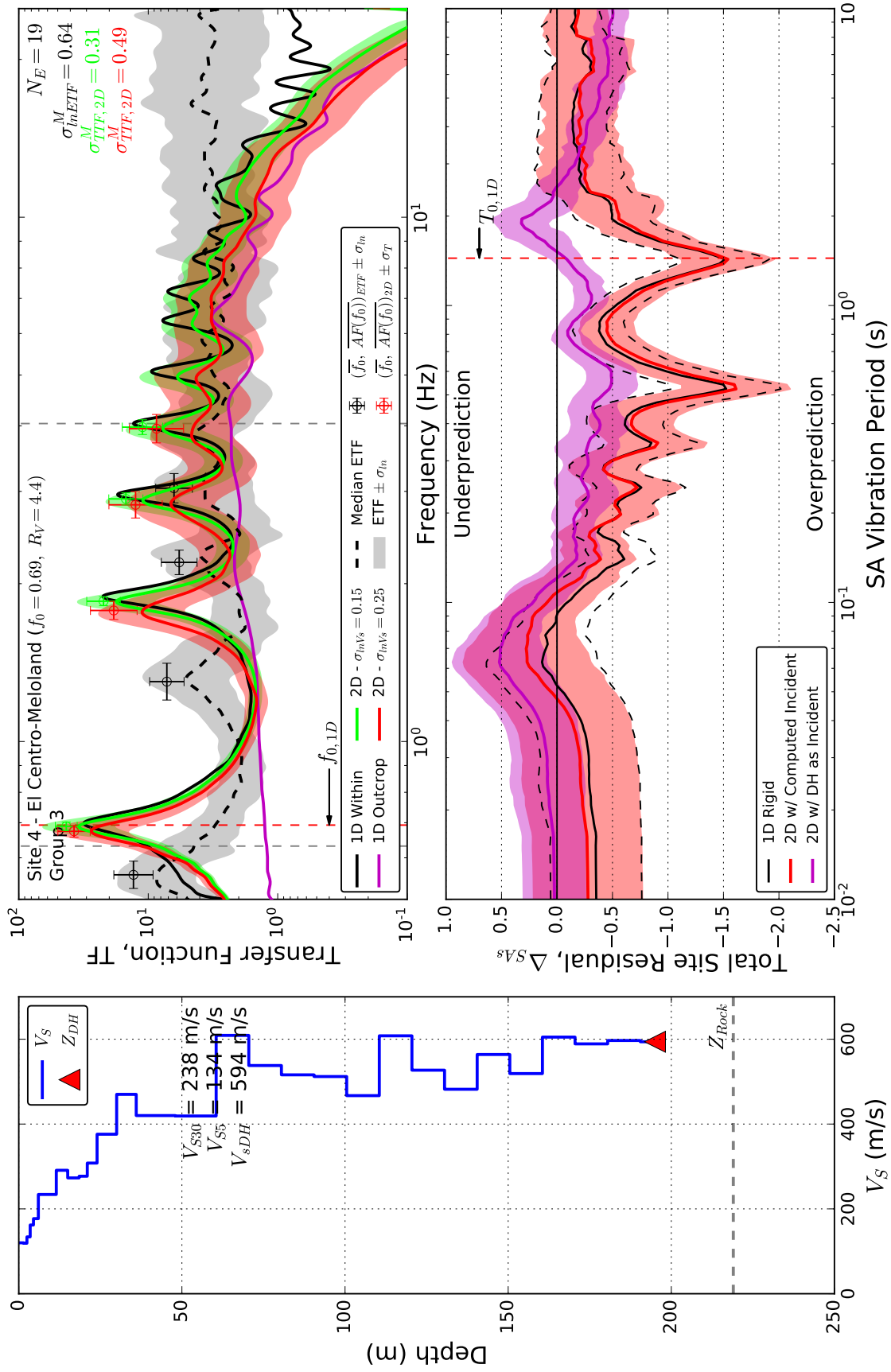

Figure C.11: V_S profile, transfer functions, and SA residuals for Site 4.

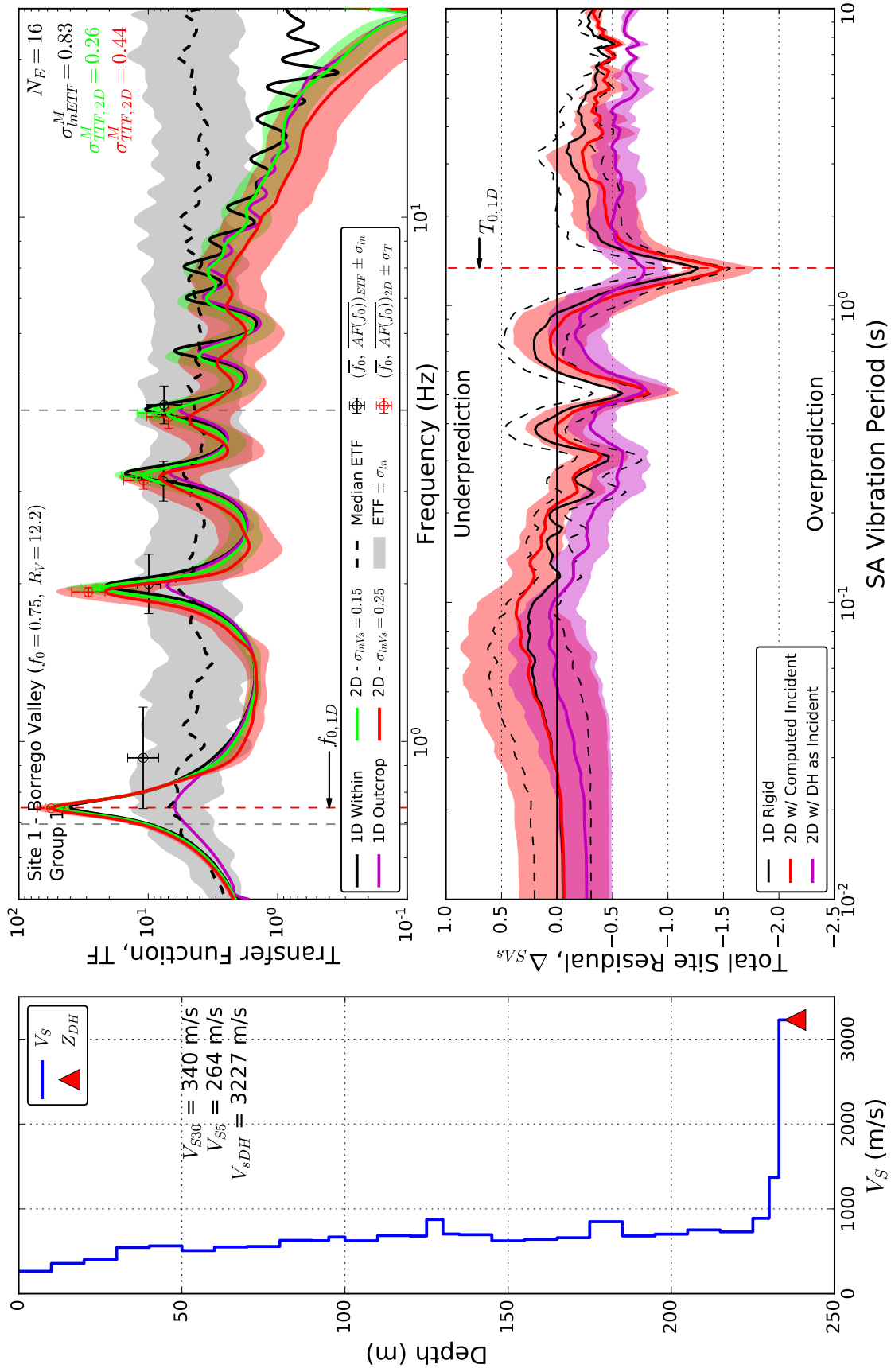

Figure C.12: V_S profile, transfer functions, and SA residuals for Site 1.

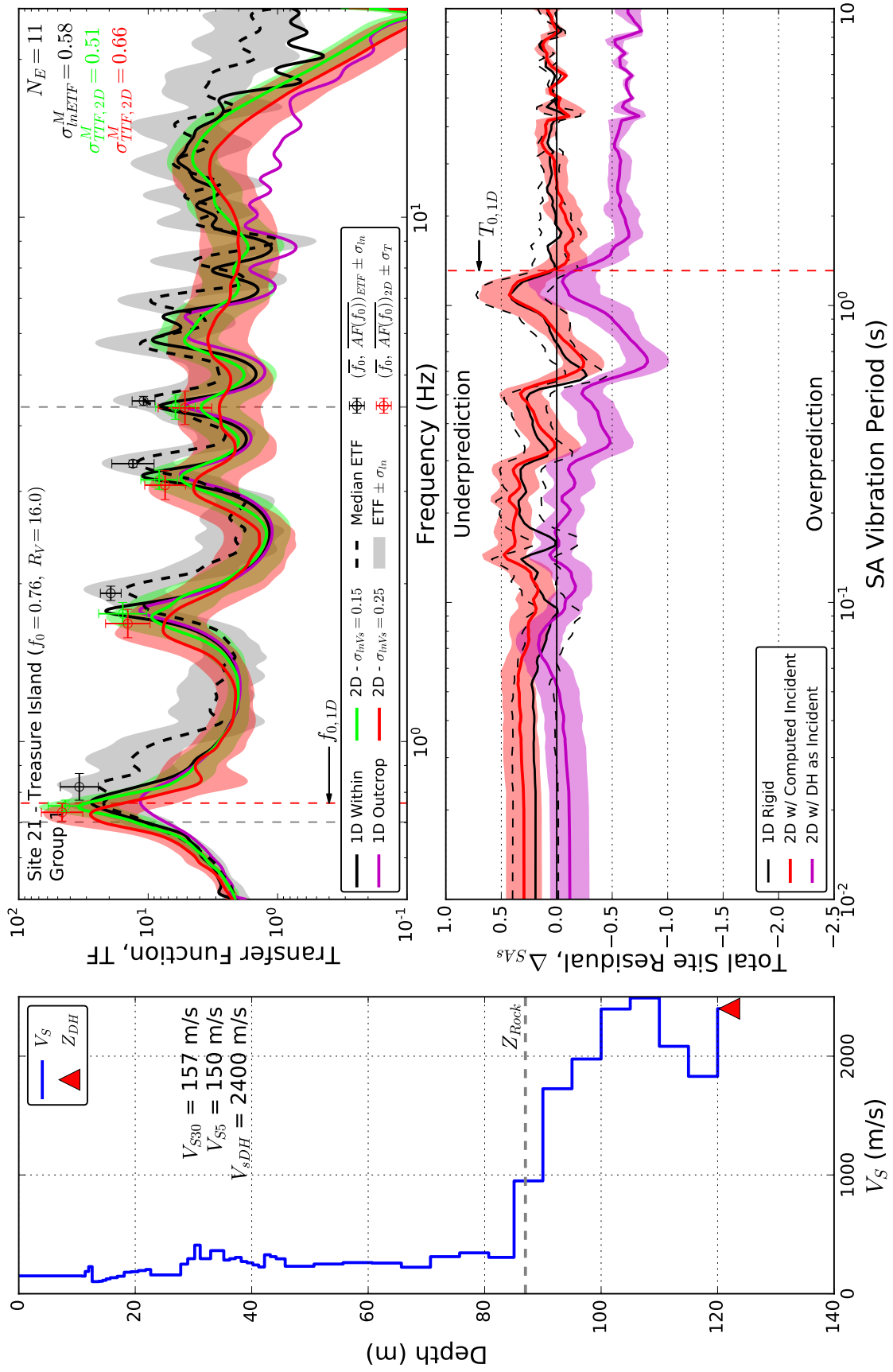

Figure C.13: V_S profile, transfer functions, and SA residuals for Site 21.

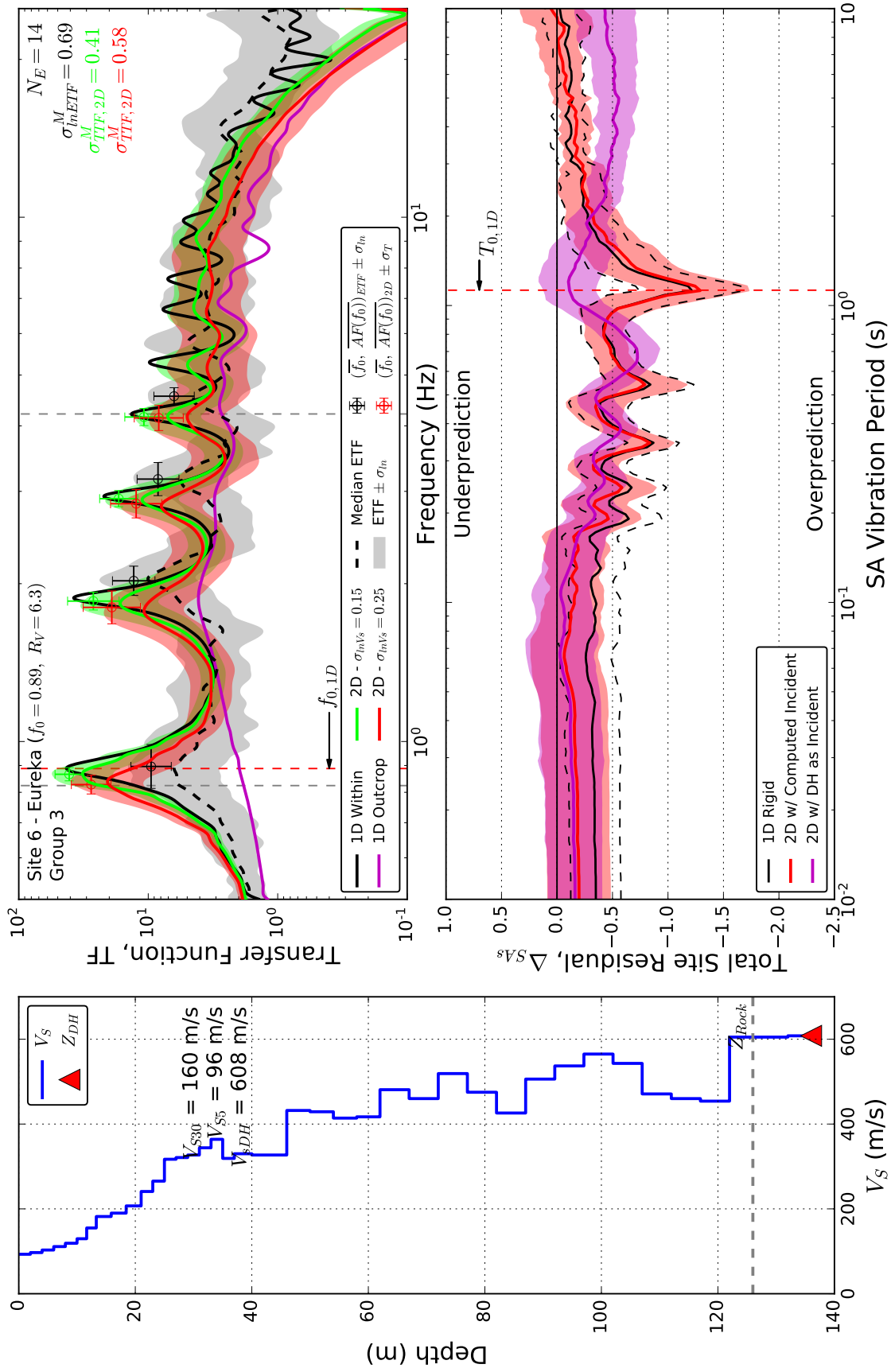

Figure C.14: V_S profile, transfer functions, and SA residuals for Site 6.

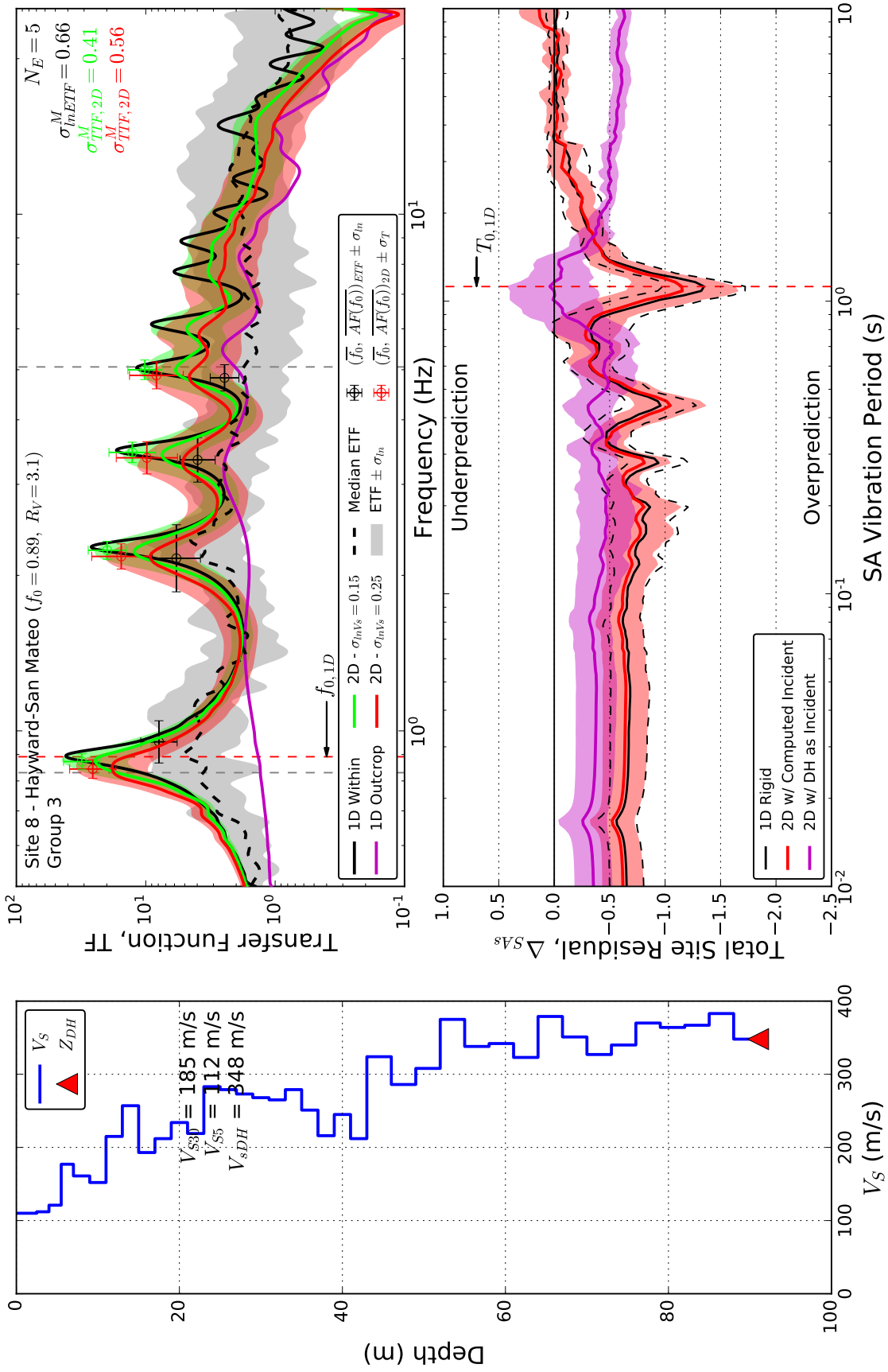

Figure C.15: V_S profile, transfer functions, and SA residuals for Site 8.

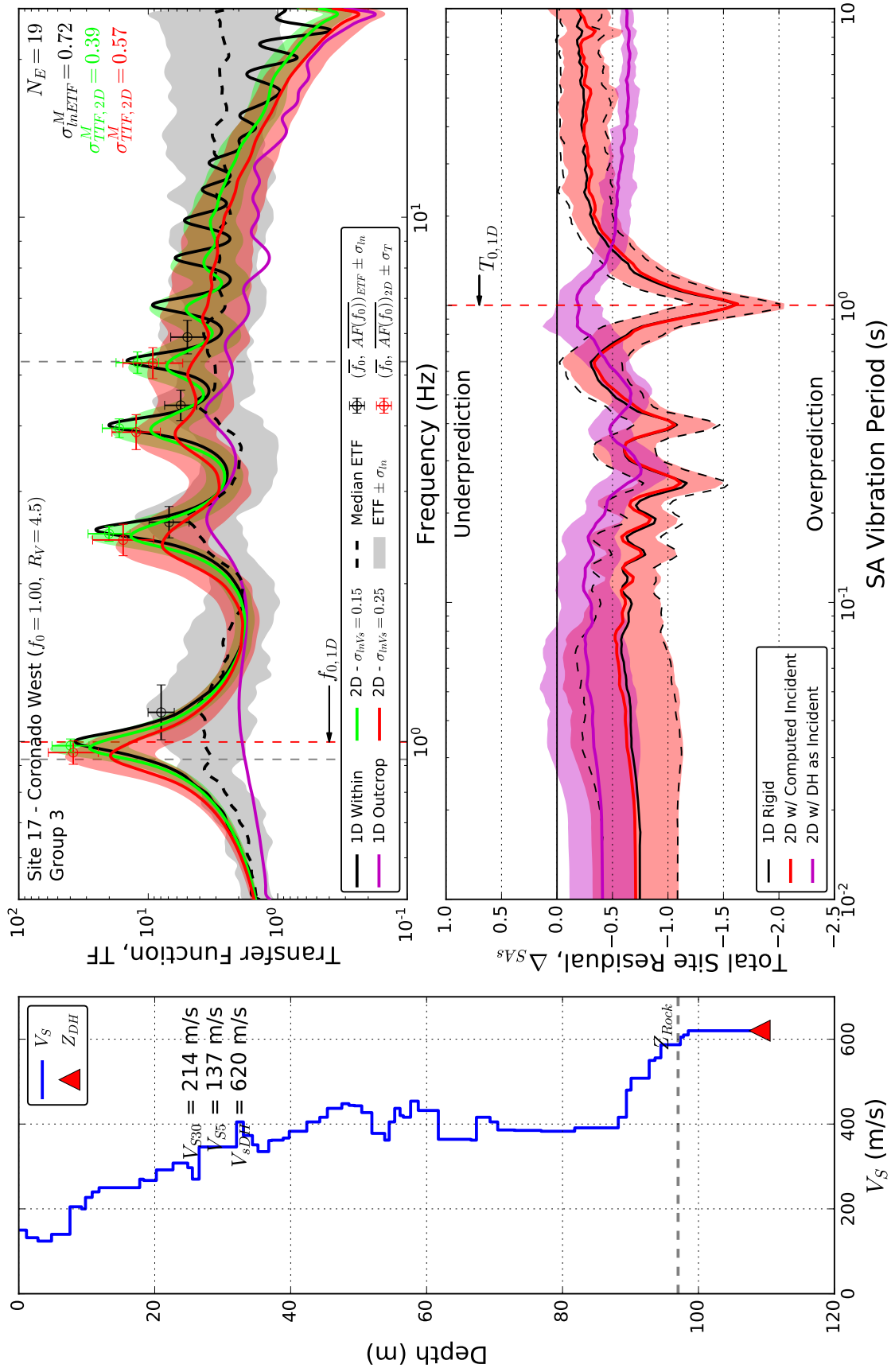

Figure C.16: V_S profile, transfer functions, and SA residuals for Site 17.

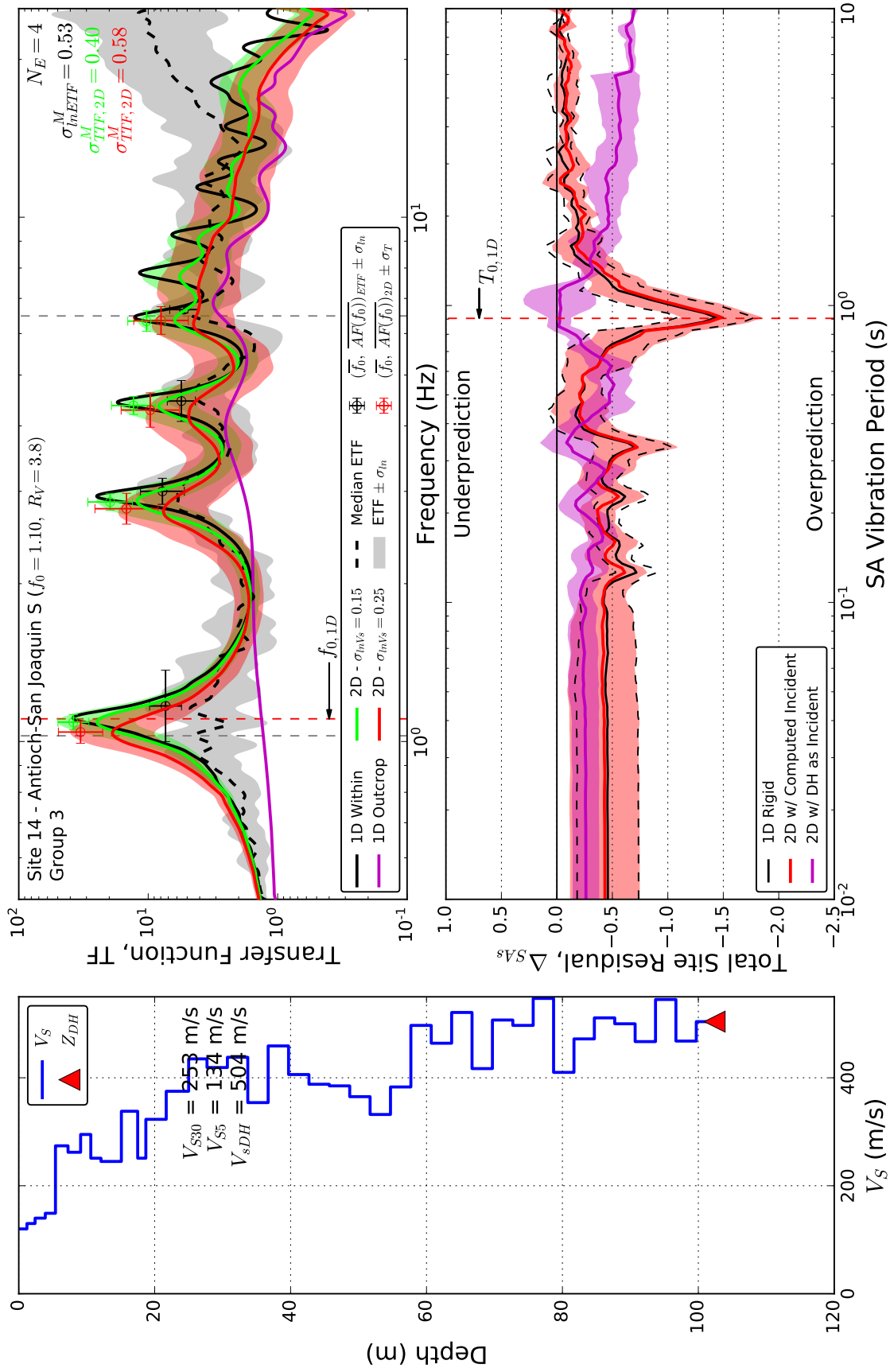

Figure C.17: V_S profile, transfer functions, and SA residuals for Site 14.

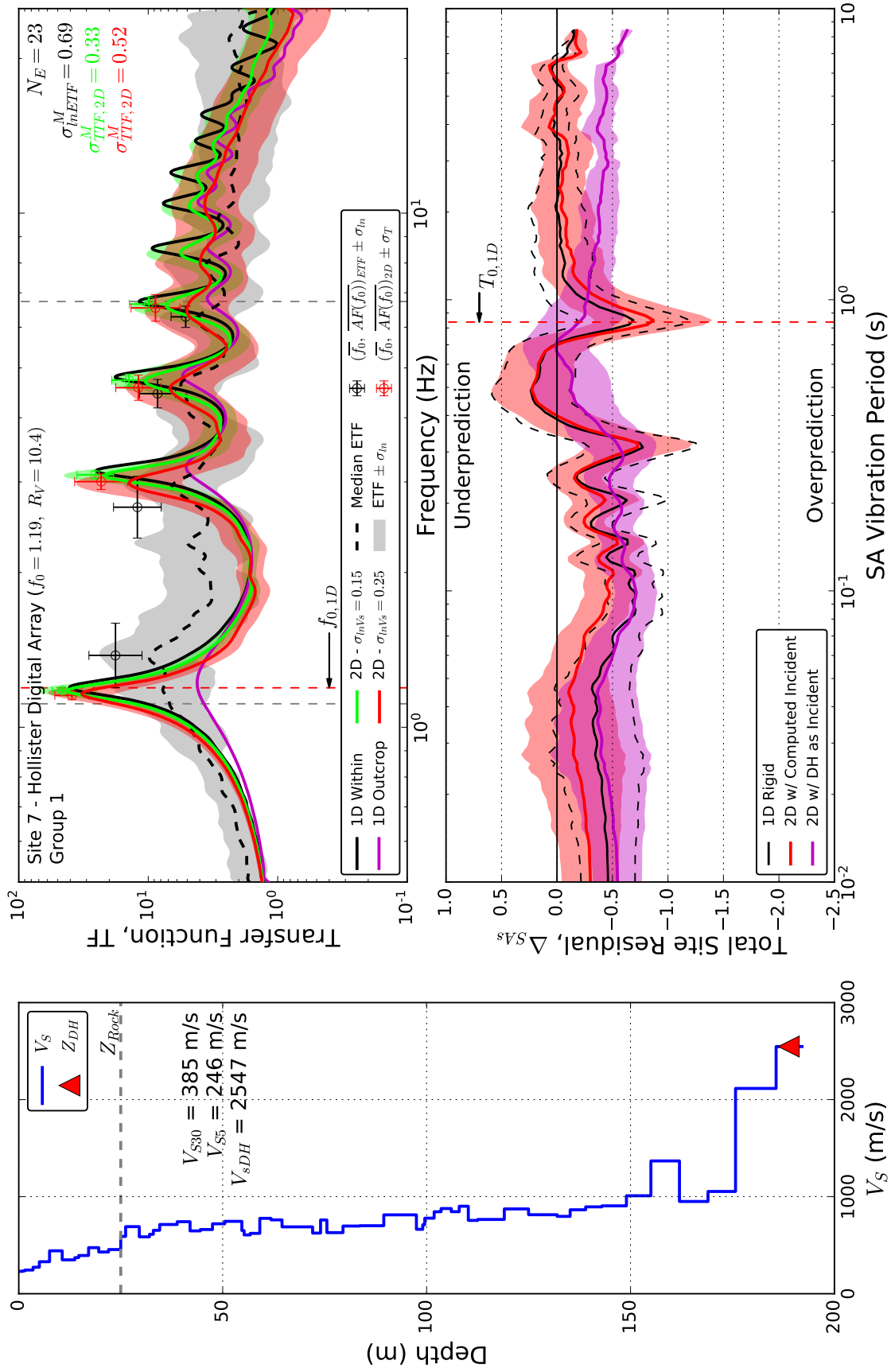

Figure C.18: V_S profile, transfer functions, and SA residuals for Site 7.

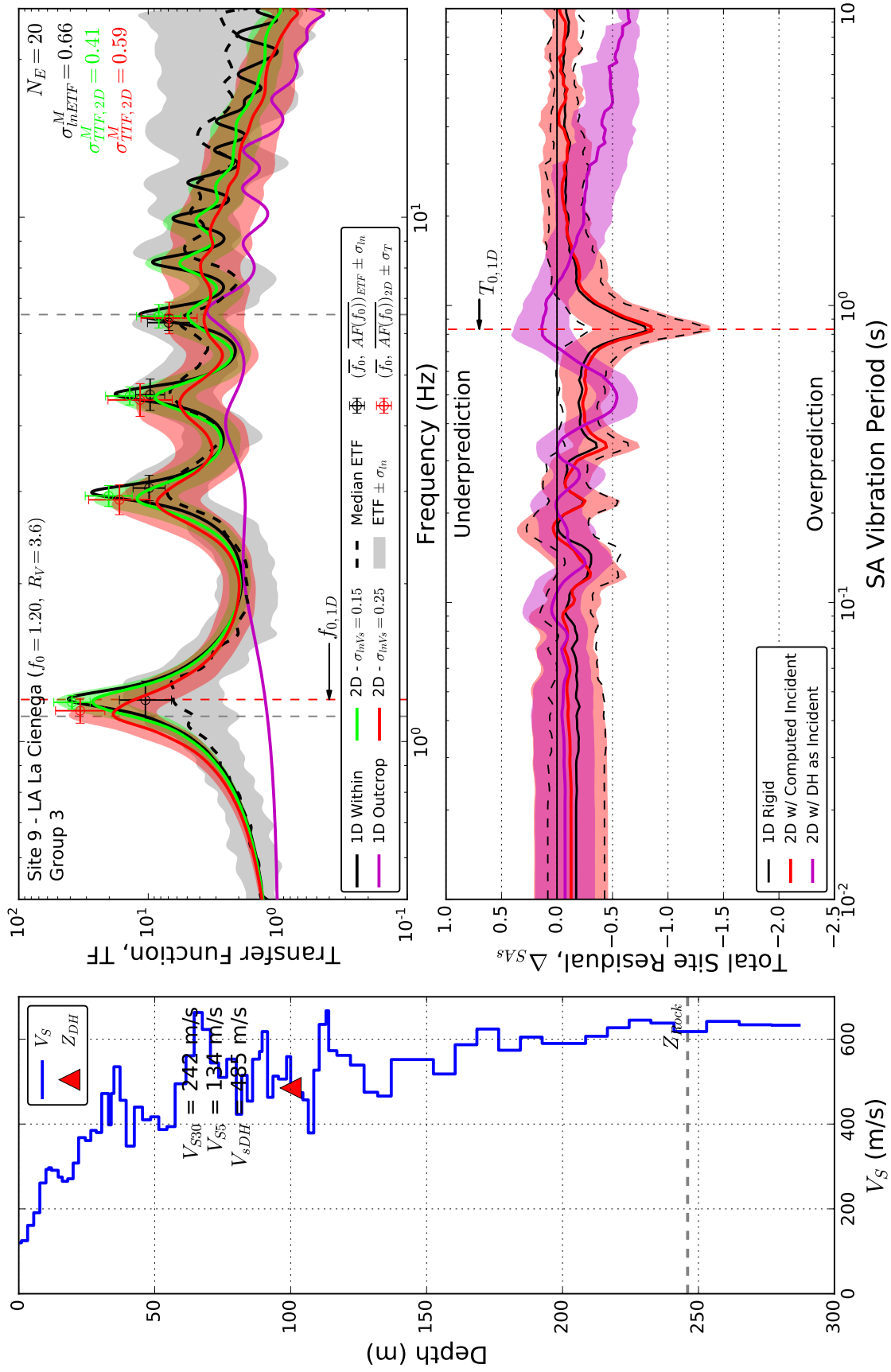

Figure C.19: V_S profile, transfer functions, and SA residuals for Site 9.

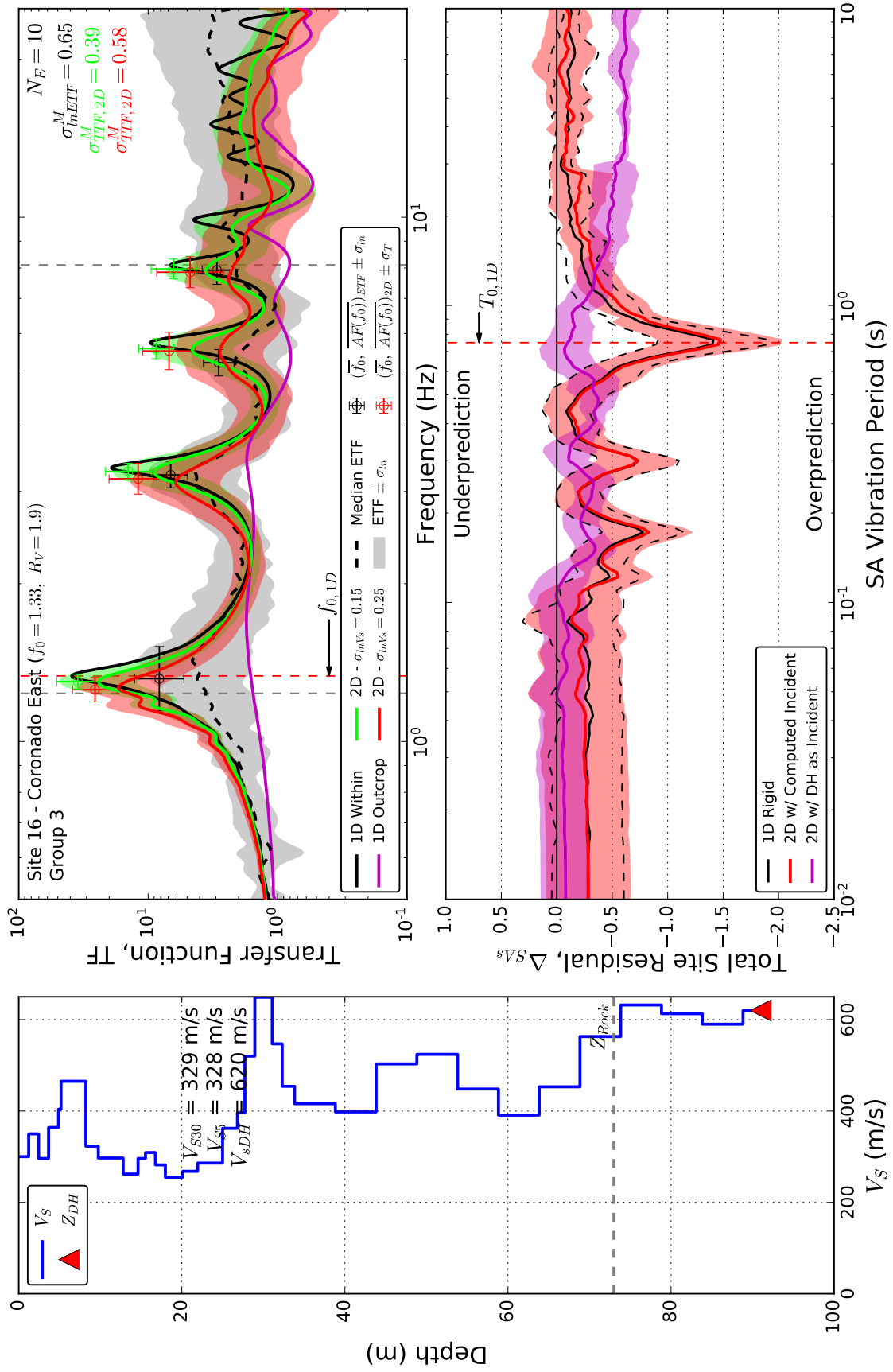

Figure C.20: V_S profile, transfer functions, and SA residuals for Site 16.

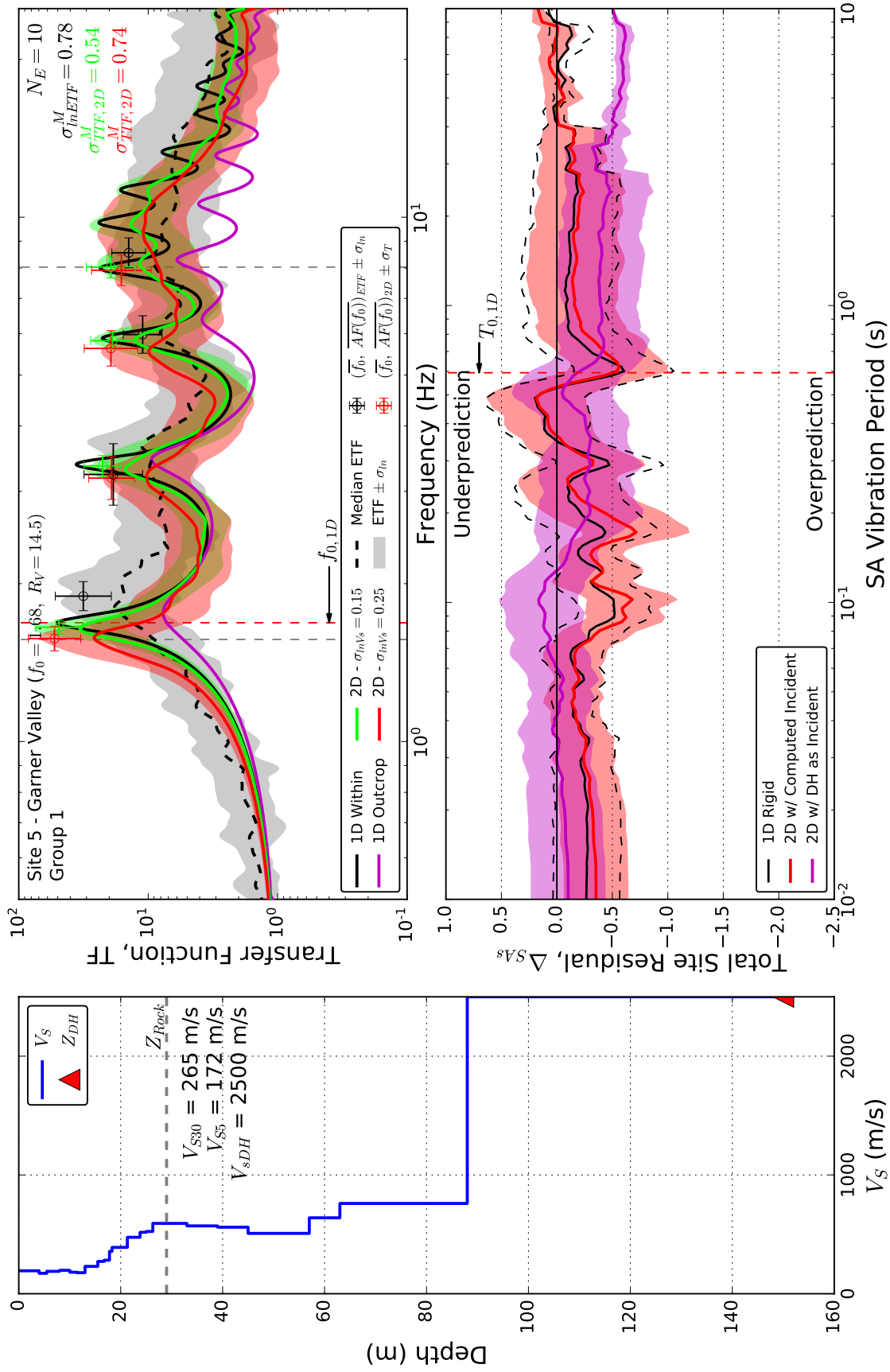

Figure C.21: V_S profile, transfer functions, and SA residuals for Site 5.

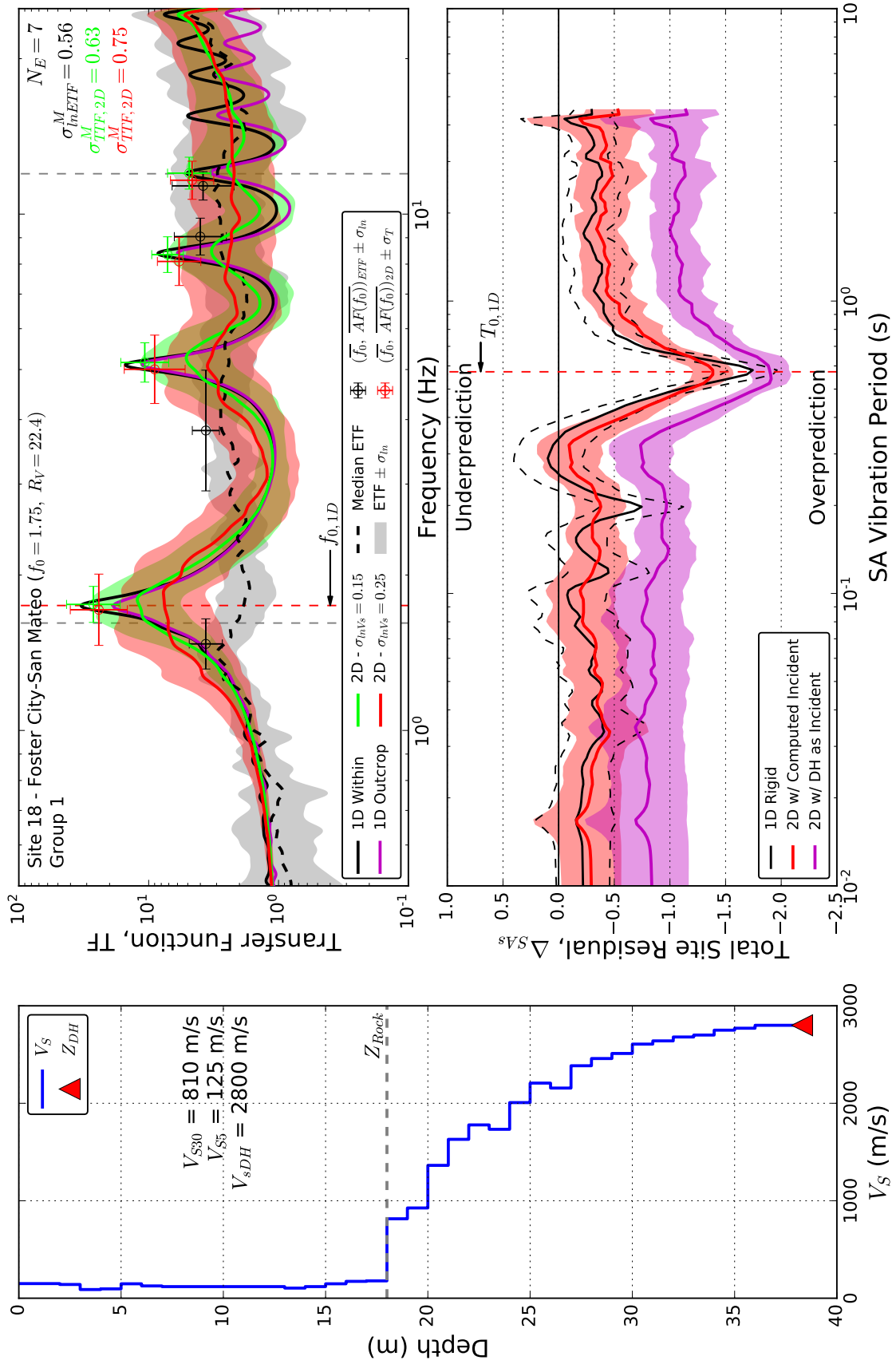

Figure C.22: V_S profile, transfer functions, and SA residuals for Site 18.

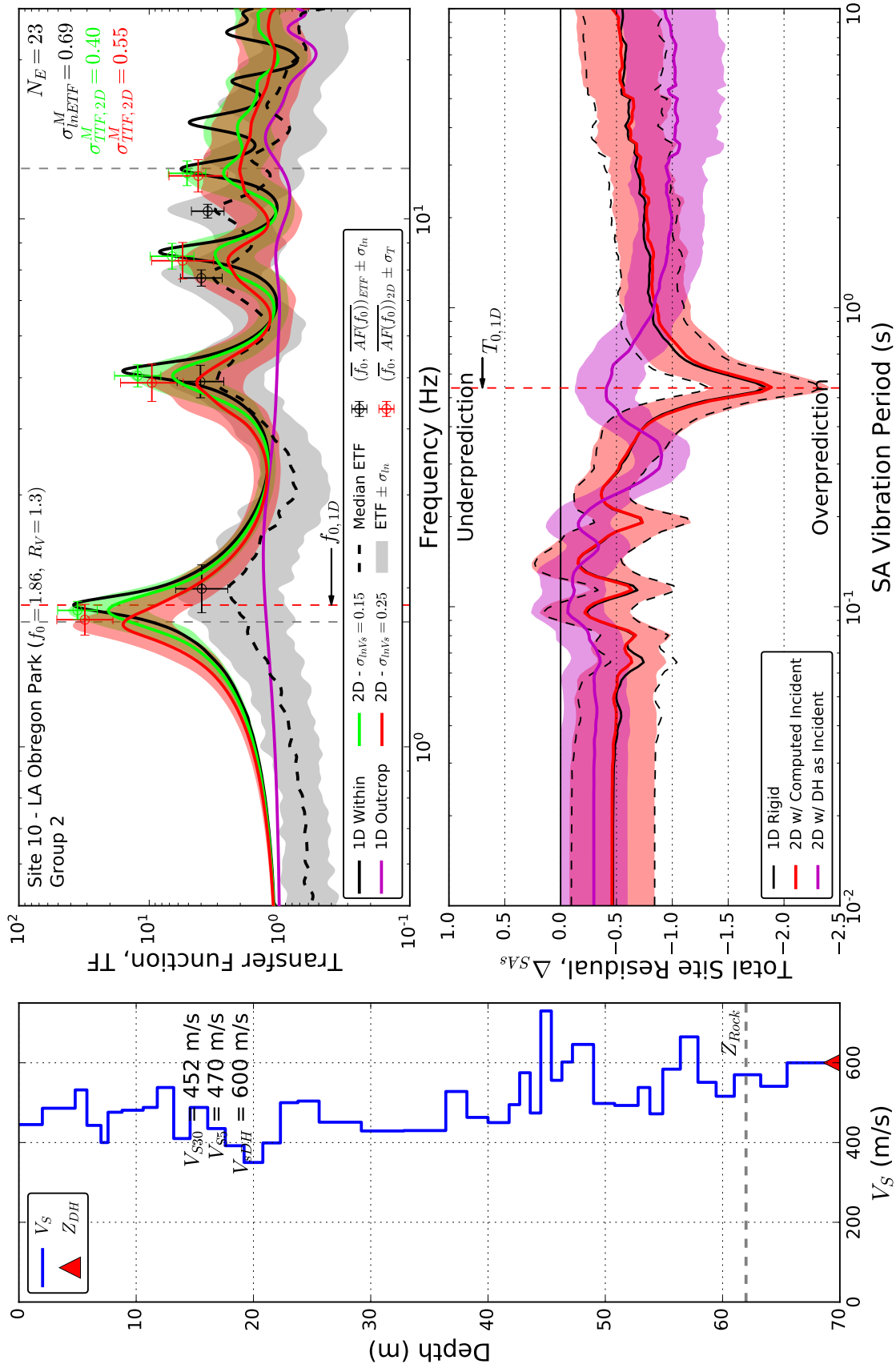

Figure C.23: V_S profile, transfer functions, and SA residuals for Site 10.

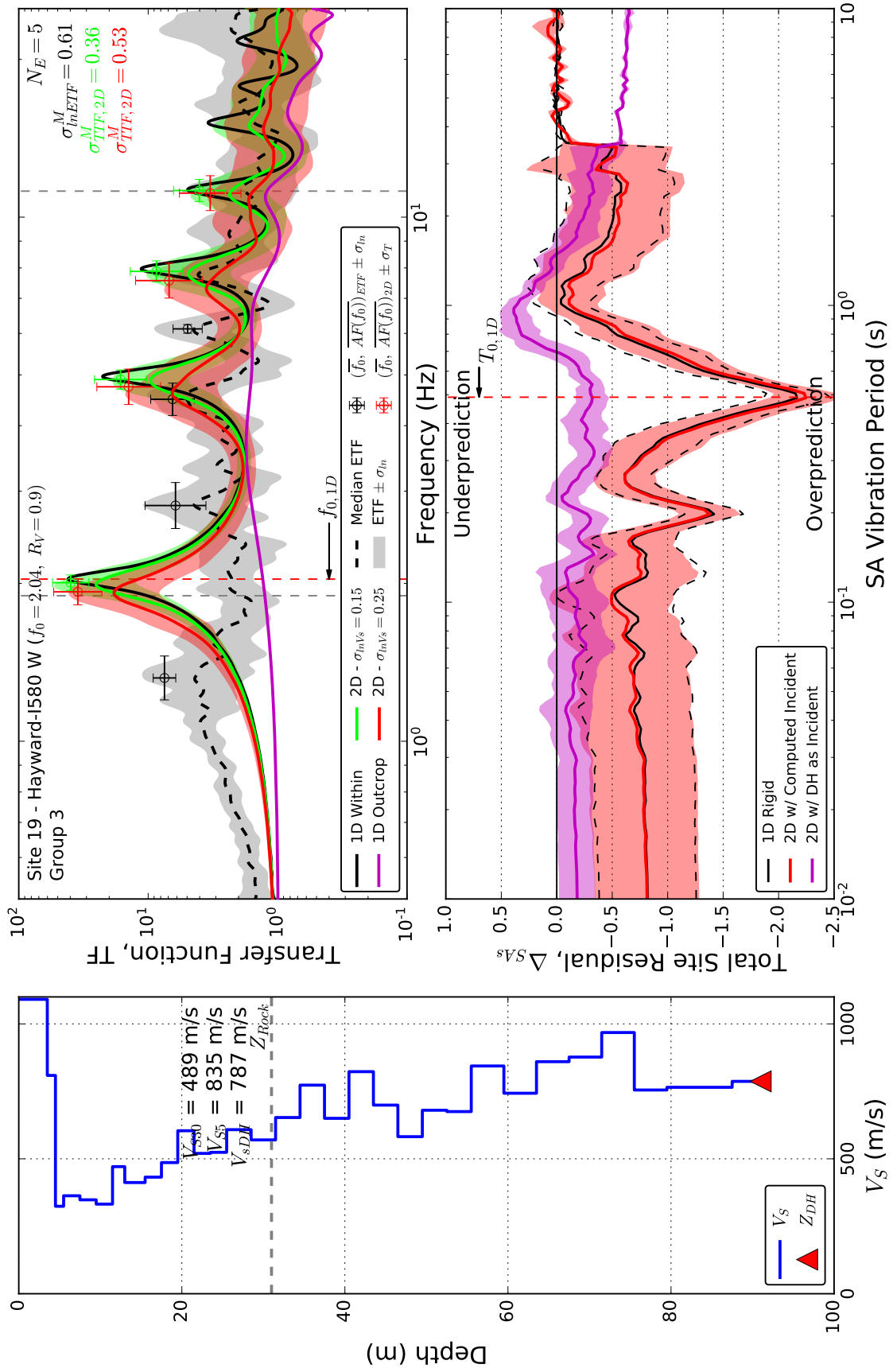

Figure C.24: V_S profile, transfer functions, and SA residuals for Site 19.

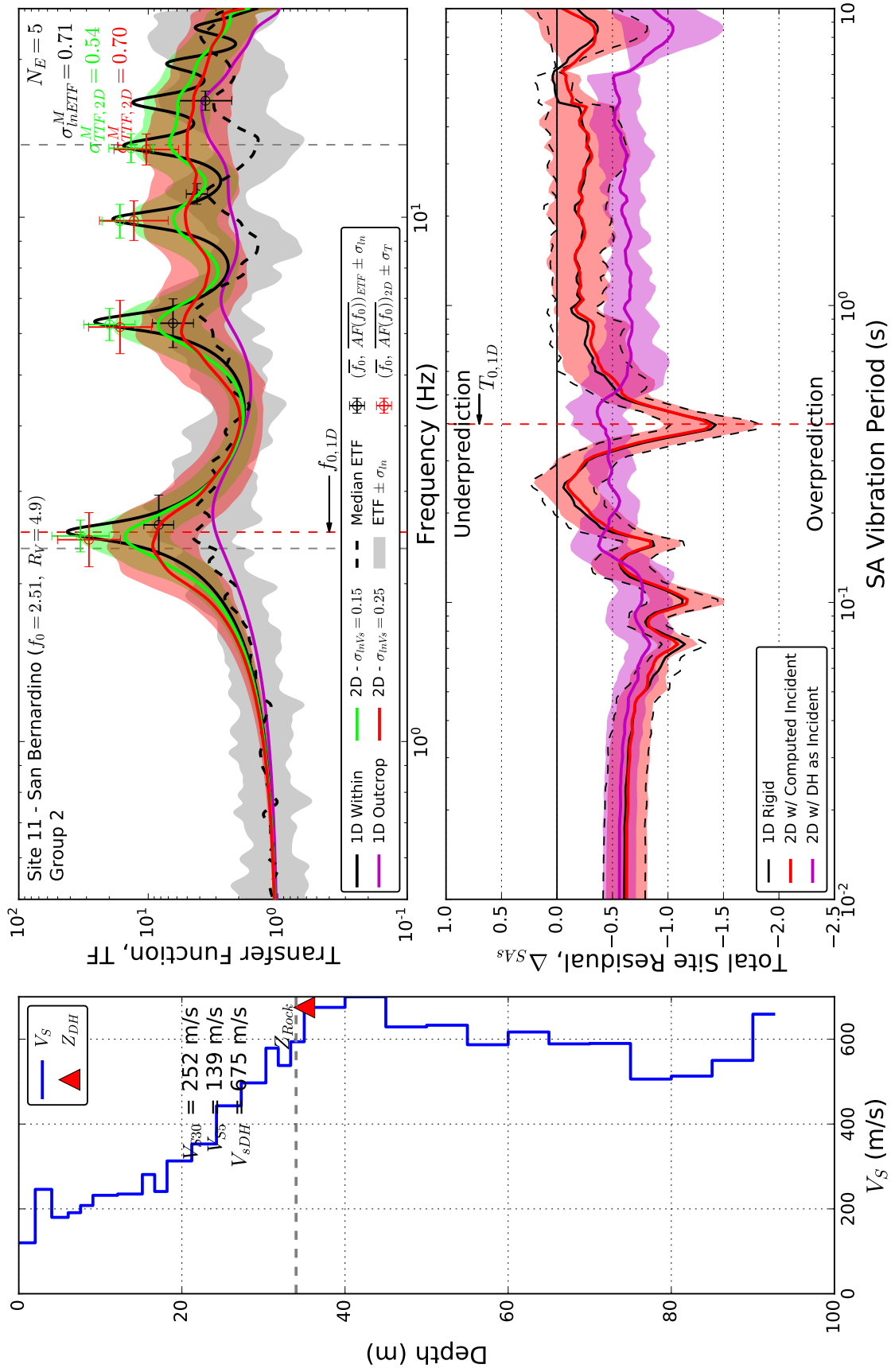

Figure C.25: V_S profile, transfer functions, and SA residuals for Site 11.

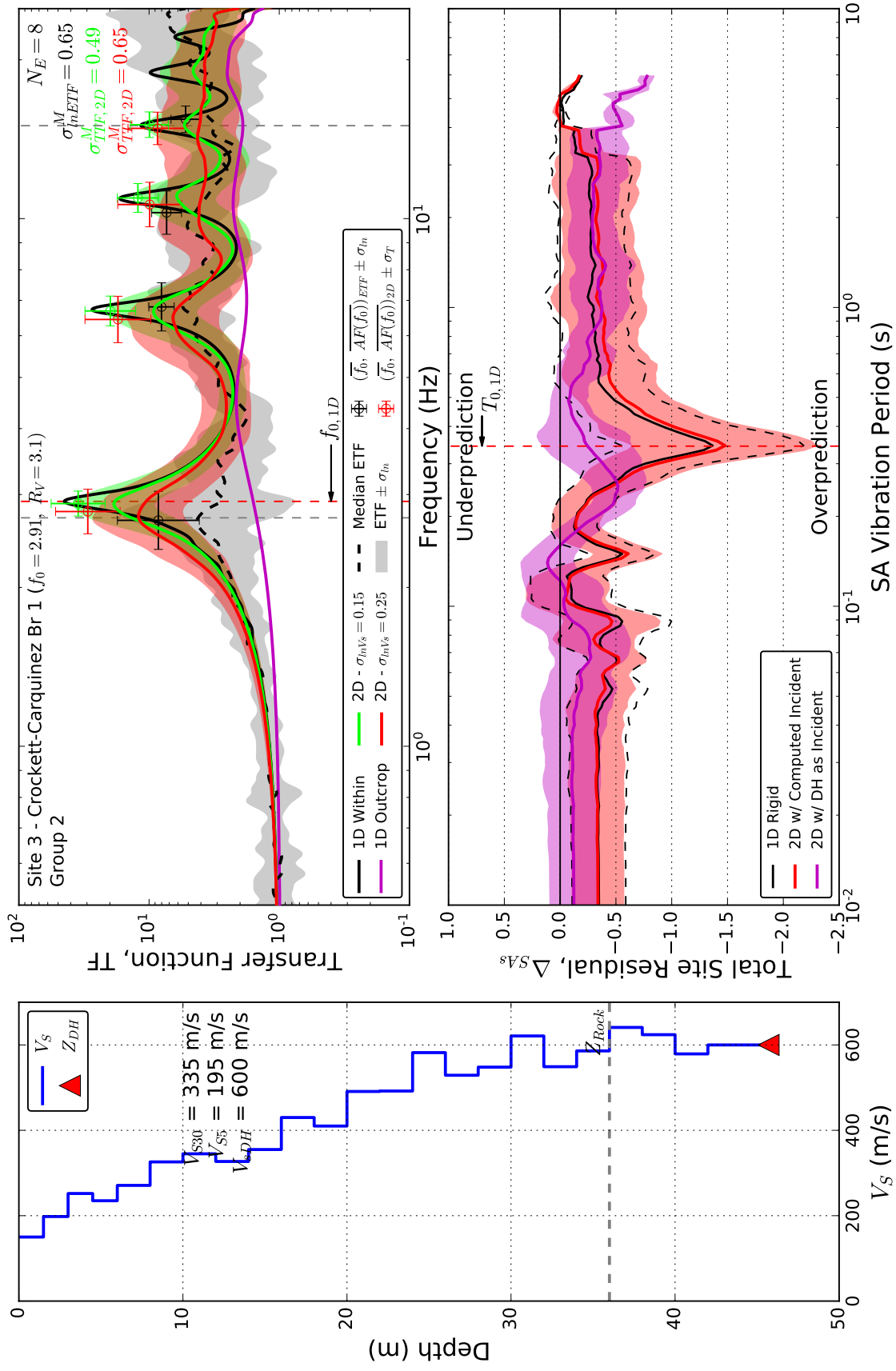

Figure C.26: V_S profile, transfer functions, and SA residuals for Site 3.

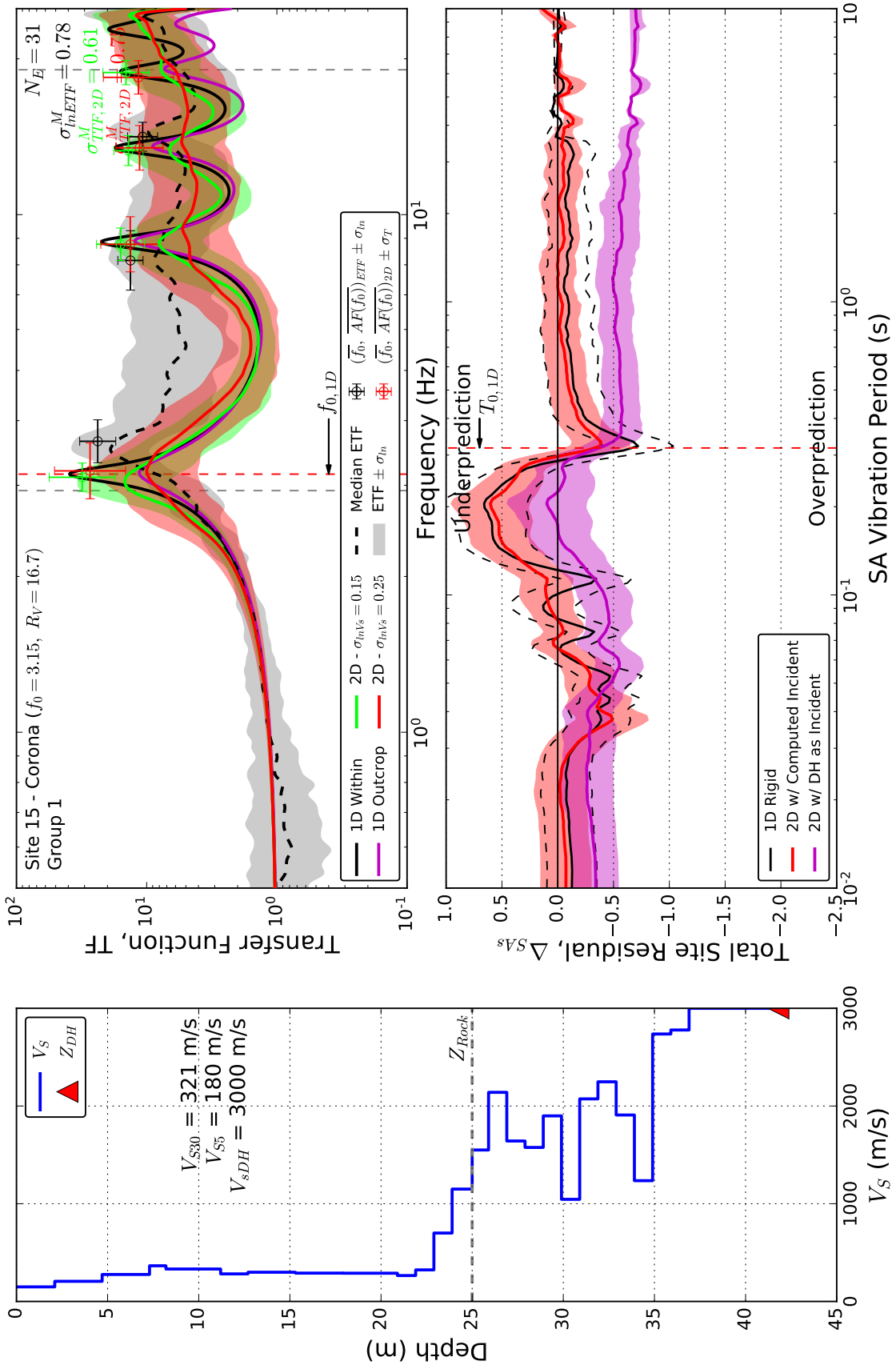

Figure C.27: V_S profile, transfer functions, and SA residuals for Site 15.

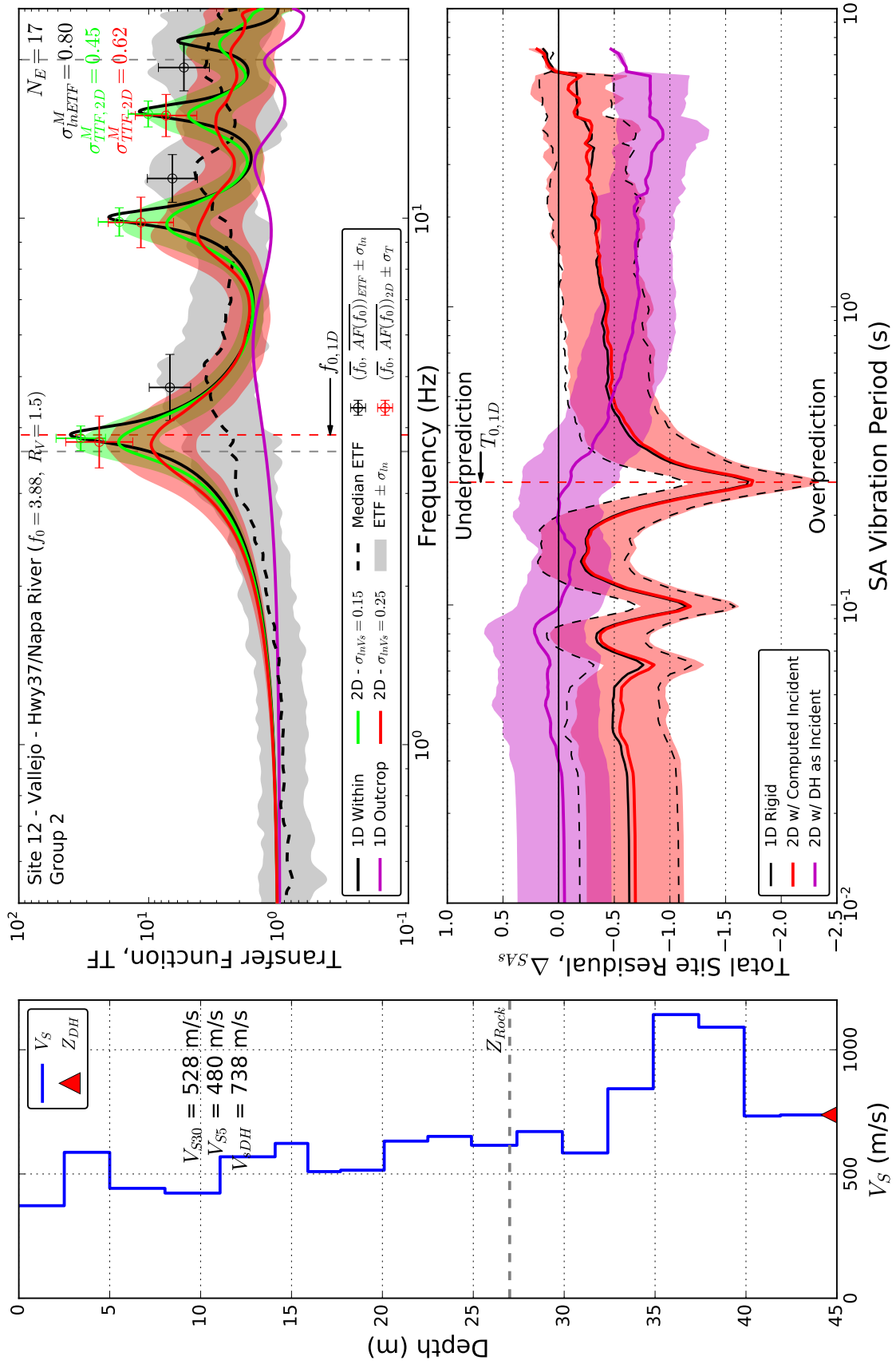

Figure C.28: V_S profile, transfer functions, and SA residuals for Site 12.

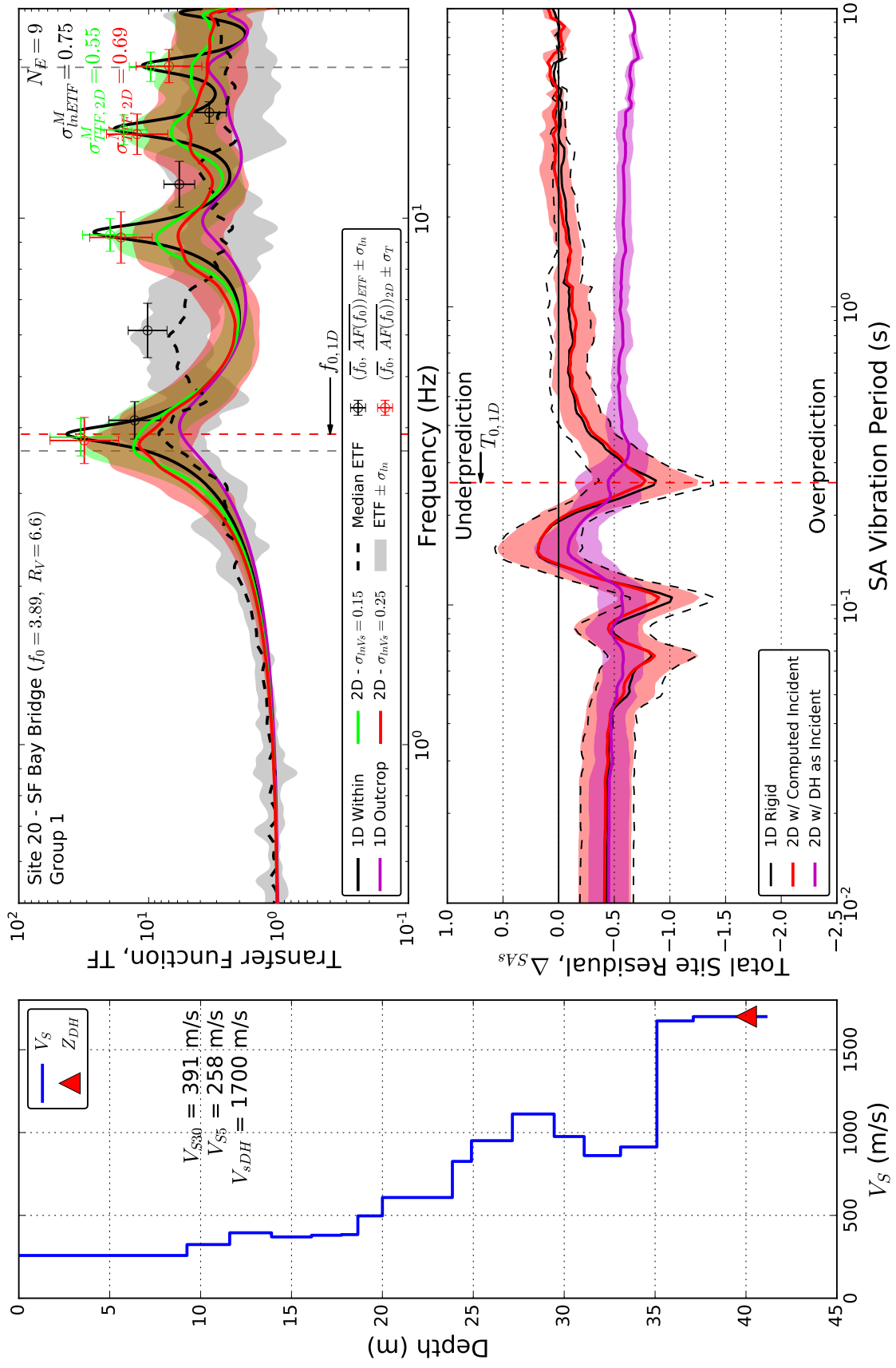

Figure C.29: V_S profile, transfer functions, and SA residuals for Site 20.

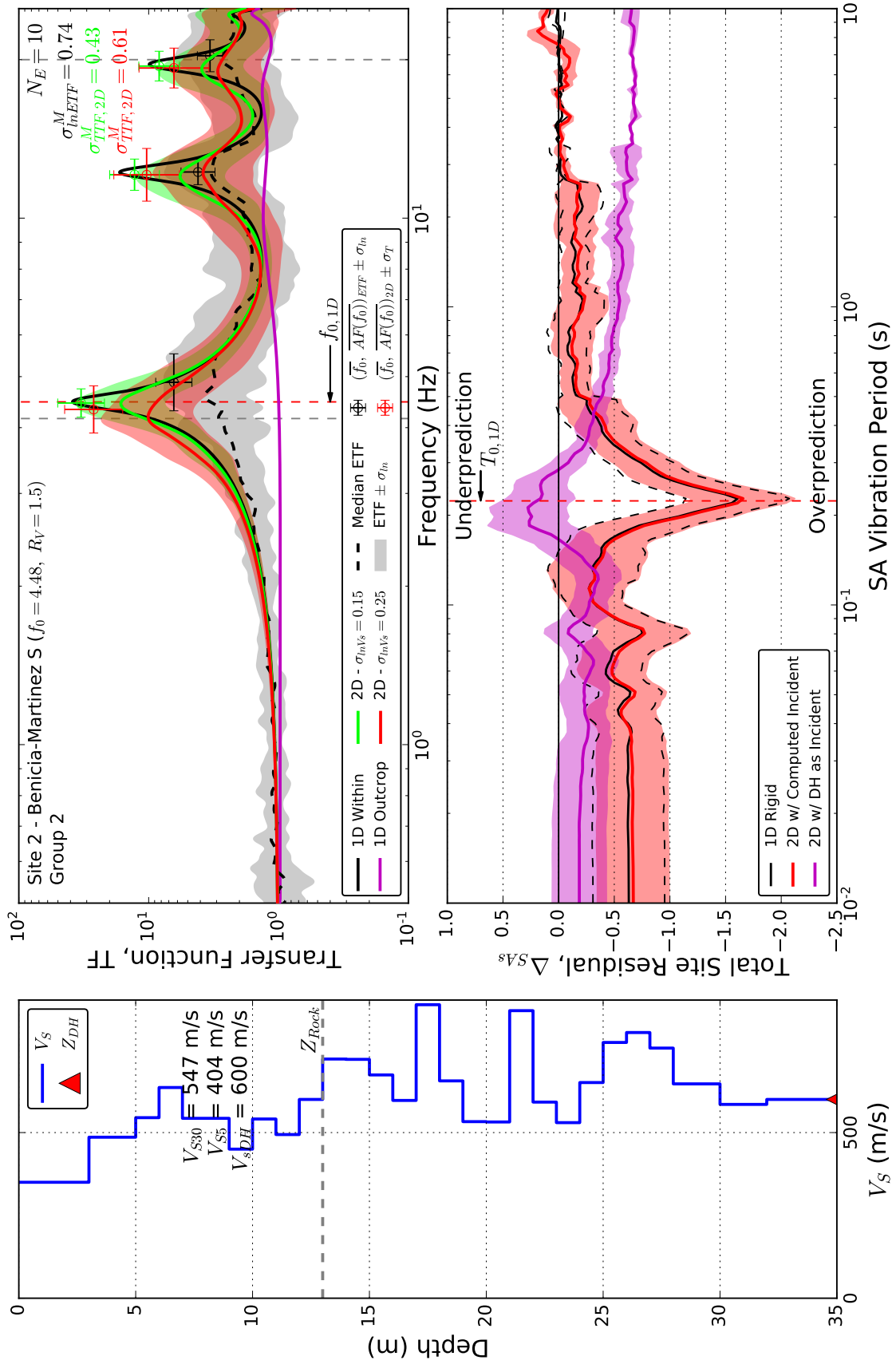

Figure C.30: V_S profile, transfer functions, and SA residuals for Site 2.

Bibliography

Afshari, K. and Stewart, J. (2019). Insights from California Vertical Arrays on The Effectiveness of Ground Response Analysis with Alternative Damping Models. *Bulletin of the Seismological Society of America*, 109(4):1250–1264.

Afshari, K., Stewart, J., and Steidl, J. (2018). California Ground Motion Vertical Array Database. DesignSafe-CI PRJ-1968. Accessed Aug. 10, 2019.

Afshari, K. and Stewart, J. P. (2017). Small-Strain Damping For Ground Response Analysis as used In Non-Ergodic Hazard Analysis - Lessons from California Recordings. Technical report, UCLA, retrieved from https://escholarship.org/uc/item/7cx9x9mc.

Afshari, K., Stewart, J. P., and Steidl, J. H. (2019). California ground motion vertical array database. *Earthquake Spectra*, 35(4):2003–2015.

Al Atik, L., Abrahamson, N., Bommer, J. J., Scherbaum, F., Cotton, F., and Kuehn, N. (2010). The Variability of Ground-Motion Prediction Models and its Components. *Seismological Research Letters*, 81(5):794–801.

Ancheta, T. D., Stewart, J. P., and Abrahamson, N. A. (2011). Engineering Characterization of Earthquake Ground Motion Coherency and Amplitude Variability. Technical report.

Anderson, J. G. and Brune, J. N. (1999). Probabilistic seismic hazard analysis without the ergodic assumption. *Seismological Research Letters*, 70(1):19–28.

Assimaki, D. (2004). *Topography Effects in the 1999 Athens Earthquake: Engineering Issues in Seismology*. Phd thesis, Massachusetts Institute of Technology.

Assimaki, D., Pecker, A., Popescu, R., and Prevost, J. (2003). Effects of Spatial Variability of Soil Properties on Surface Ground Motion. *Journal of Earthquake Engineering*, 7(Special Issue 1):1–44.

Atkinson, G. M. (2006). Single-station sigma. *Bulletin of the Seismological Society of America*, 96(2):446–455.

Bates, D., , Mächler, M., Bolker, B., and Walker, S. (2015). Fitting Linear Mixed-Effects Models Using lme4. *Journal of Statistical Software*, 67(1):1–48.

Bazzurro, P. and Cornell, A. (2004). Ground-motion amplification in nonlinear soil sites with uncertain properties. *Bulletin of the Seismological Society of America*, 94(6):2090–2109.

Beavan, J., Fielding, E., Motagh, M., Samsonov, S., and Donnelly, N. (2011). Fault Location and Slip Distribution of the 22 February 2011 Mw 6.2 Christchurch, New Zealand, Earthquake from Geodetic Data. *Seismological Research Letters*, 82:789–799.

Beavan, J., Motagh, M., Fielding, E. J., Donnelly, N., and Collett, D. (2012). Fault Slip Models of the 2010-2011 Canterbury, New Zealand, Earthquakes from Geodetic Data and Observations of Postseismic Ground Deformation. *New Zealand Journal of Geology and Geophysics*, 55:207–221.

Bielak, J., Loukakis, K., Hisada, Y., and Yoshimura, C. (2003). Domain Reduction Method for Three-Dimensional Earthquake Modeling in Localized Regions, Part I: Theory. *Bulletin of the Seismological Society of America*, 93(2):817–824.

Bolton Seed, H., Romo, M. P., Sun, J., Jaime, A., and Lysmer, J. (1987). Relationships between soil conditions and earthquake ground motions in Mexico City in the earthquake of Sept. 19, 1985 - Report No. UCB/EERC-87/15. Technical report, Earthqauke Engineering Research Center.

Bombasaro, E. and Kasper, T. (2016). Evaluation of Spatial Soil Variability in the Pearl River Estuary using CPTU Data. *Soils and Foundations*, 56(3):496–505.

Bong, T. and Stuedlein, A. W. (2017). Spatial Variability of CPT Parameters and Silty Fines in Liquefiable Beach Sands. *Journal of Geotechnical and Geoenvironmental Engineering*, 143(12):04017093.

Bonilla, L. F., Steidl, J. H., Gariel, J. C., and Archuleta, R. J. (2002). Borehole response studies at the Garner Valley Downhole Array, Southern California. *Bulletin of the Seismological Society of America*, 92(8):3165–3179.

Boore, D. M. (2007). Notes on relating density to velocity for use in site amplification calculations.

Boore, D. M., Gibbs, J. F., and Joyner, W. B. (2020). Damping Values Derived from Surface-Source, Downhole-Receiver Measurements at 22 Sites in the San Francisco Bay Area of Central California and the San Fernando Valley of Southern California. *Bulletin of the Seismological Society of America*.

Bora, S. S., Scherbaum, F., Kuehn, N., and Stafford, P. (2016). On the Relationship between Fourier and Response Spectra: Implications for the Adjustment of Empirical Ground-Motion Prediction Equations (GMPEs). *Bulletin of the New Zealand Society for Earthquake Engineering*, 106(3):1235–1253.

Bradley, B. (2013). A New Zealand-Specific Pseudospectral Acceleration Ground-Motion Prediction Equation for Active Shallow Crustal Earthquakes Based on Foreign Models. *Bulletin of the Seismological Society of America*, 103:1801–1822.

Bradley, B. and Cubrinovski, M. (2011). Near-Source Strong Ground Motions Observed in the 22 February 2011 Christchurch Earthquake. *Bulletin of the New Zealand Society for Earthquake Engineering*, 44(4):181–194.

Bradley, B., Jeong, S., and Razafindrakoto, H. (2015). Strong Ground Motions from the 2010-2011 Canterbury Earthquakes and the Predictive Capability of Empirical and Physics-Based Simulation Models. In *Tenth Pacific Conference on Earthquake Engineering*. November 6-8, Sydney, Australia.

Bradley, B. A. (2012). New Zealand Journal of Geology and Geophysics Ground motions observed in the Darfield and Christchurch earthquakes and the importance of local site response effects Ground motions observed in the Darfield and Christchurch earthquakes and the importance of local site response effects.

Bradley, B. A. (2015). Systematic Ground Motion Observations in the Canterbury Earthquakes and Region-Specific Non-Ergodic Empirical Ground Motion Modeling. *Earthquake Spectra*, 31(3):1735–1761.

Bradley, B. A., Quigley, M. C., Van Dissen, R. J., and Litchfield, N. J. (2014). Ground motion and seismic source aspects of the canterbury earthquake sequence. *Earthquake Spectra*, 30(1):1–15.

Bradley, B. A., Razafindrakoto, H. N. T., and Polak, V. (2017a). Ground Motion Observations from the 14 November 2016 Mw 7.8 Kaikora, New Zealand Earthquake and Insights from Broadband Simulations. *Seismological Research Letters*, 88(3).

Bradley, B. A., Wotherspoon, L. M., and Kaiser, A. E. (2017b). Ground motion and site effect observations in the wellington region from the 2016 Mw7.8 Kaikōura, New Zealand earthquake. *Bulletin of the New Zealand Society for Earthquake Engineering*, 50(2):94–105.

Brando, G., Pagliaroli, A., Cocco, G., and Di Buccio, F. (2020). Site effects and damage scenarios: The case study of two historic centers following the 2016 Central Italy earthquake. *Engineering Geology*, 272:105647.

Brown, L., Beetham, R., Paterson, B., and Weeber, J. (1995). Geology of Christchurch, New Zealand. *Environmental & Engineering Geoscience*, 1:427–488.

Browne, G. H., Field, B. D., Barrell, D. J., Jongens, R., Bassett, K. N., and Wood, R. A. (2012). The geological setting of the Darfield and Christchurch earthquakes. *New Zealand Journal of Geology and Geophysics*, 55(3):193–197.

Cabas, A., Rodriguez-Marek, A., and Bonilla, L. F. (2017). Estimation of Site-Specific Kappa (κ_0)-Consistent Damping Values at KiK-Net Sites to Assess the Discrepancy between

Laboratory-Based Damping Models and Observed Attenuation (of Seismic Waves) in the Field. *Bulletin of the Seismological Society of America*, 107(5):2258–2271.

Campbell, K. W. and Bozorgnia, Y. (2014). NGA-West2 Ground Motion Model for the Average Horizontal Component of PGA, PGV, and 5% Damped Linear Acceleration Response Spectra. *Earthquake Spectra*, 30(3):1087–1115.

Chavan, D., G., M., and Prashant, A. (2017). Seismic analysis of nailed soil slope considering interface effects. *Soil Dynamics and Earthquake Engineering*, 100:480–491.

Chemingui, N. (2001). Modeling 3-D anisotropic fractal media. *Stanford Exploration Project*, Report 80.

Chen, Y.-H. and Tsai, C.-C. P. (2002). A new method for estimation of the attenuation relationship with variance components. *Bulletin of the Seismological Society of America*, 92(5):1984–1991.

Cheng, T., Cox, B. R., Vantassel, J. P., and Manuel, L. (2020). A statistical approach to account for azimuthal variability in single-station HVSR measurements. *Geophysical Journal International*, 223(2):1040–1053.

Cheng, T., Hallal, M. M., Vantassel, J. P., and Cox, B. R. (2021). Estimating Unbiased Statistics for Fundamental Site Frequency Using Spatially Distributed HVSR Measurements and Voronoi Tessellation. *Journal of Geotechnical and Geoenvironmental Engineering*, 147(8):04021068.

Chin, C. Y., Kayser, C., and Pender, M. (2016). Seismic Earth Forces against Embedded Retaining Walls: Insights from Numerical Modelling. *Bulletin of the Seismological Society of America*, 49(2).

Ching, J., Wu, T. J., Stuedlein, A. W., and Bong, T. (2018). Estimating horizontal scale of fluctuation with limited CPT soundings. *Geoscience Frontiers*, 9(6):1597–1608.

Chiou, B. S. J. and Youngs, R. R. (2008). An NGA Model for the average horizontal component of peak ground motion and response spectra. *Earthquake Spectra*, 24(3):173–215.

Cubrinovski, M., Bray, J. D., Taylor, M., Giorgini, S., Bradley, B. B. A., Wotherspoon, L., and Zupan, J. (2011). Soil Liquefaction Effects in the Central Business District during the February 2011 Christchurch Earthquake. *Seismological Research Letters*, 82(6):893–904.

Cubrinovski, M., Winkley, A., Haskell, J., Palermo, A., Wotherspoon, L., Robinson, K., Bradley, B., Brabhaharan, P., and Hughes, M. (2014). Spreading-Induced Damage to Short-Span Bridges in Christchurch, New Zealand. *Earthquake Spectra*, 30(1):57–83.

Darendeli, M. B. (2001). Development of a New Family of Normalized Modulus Reduction and Material Damping Curves. Technical report.

de la Maza, G., Williams, N., Saez, E., Rollins, K., and Ledezma, C. (2017). Liquefaction-Induced Lateral Spread in Lo Rojas, Coronel, Chile: Field Study and Numerical Modeling. *Earthquake Spectra*, 33(1):219–240.

de la Torre, C., Bradley, B. A., and McGann, C. R. (2021). 2D Geotechnical Site-Response Analysis including Soil Heterogeneity and Wave Scattering. *Submitted: Earthquake Spectra*.

de la Torre, C., McGann, C. R., Bradley, B. A., and Pletzer, A. (2019). 3D Seismic Site Response with Soil Heterogeneity and Wave Scattering in OpenSees. In *The 1st Eurasian Conference on OpenSEES: OpenSEES Days Eurasia*, pages 255–262.

de la Torre, C. A., Bradley, B. A., and Lee, R. L. (2020). Modeling nonlinear site effects in physics-based ground motion simulations of the 2010–2011 Canterbury earthquake sequence. *Earthquake Spectra*, 36(2):856–879.

Deschenes, M., Wood, C., Wotherspoon, L., Bradley, B., and Thomson, E. (2018). Development of deep shear wave velocity profiles in the Canterbury Plains, New Zealand. *Earthquake Spectra*, In Press.

Diggle, P. J. and Ribeiro, P. J. (2007). *Model-based Geostatistics*. Springer, Lancaster, UK.

El Haber, E., Cornou, C., Jongmans, D., Youssef Abdelmassih, D., and Lopez-Caballero, F. (2019). Influence of 2D Heterogeneous Elastic Soil Properties on Ground Surface Motion Spatial Variability. *Soil Dynamics and Earthquake Engineering*, 123:75–90.

Elgamal, A., Yan, L., Yang, Z., and Conte, J. (2008). Three-Dimensional Seismic Response of Humboldt Bay Bridge-Foundation-Ground System. *Journal of Geotechnical and Geoenvironmental Engineering*, 137(7):1165–1176.

Fenton, G. A. (1999). Estimation for Stochastic Soil Models. *Journal of Geotechnical and Geoenvironmental Engineering*, 125(6):470–485.

Frankel, A. and Clayton, R. W. (1986). Finite Difference Simulations of Seismic Scattering Implications for the Propagation of Short-Period Seismic Waves in the Crust and Models of Crustal Heterogeneity. *Journal of Geophysical Research*, 91(B6):6465–6489.

Gibbs, J. F., Boore, D. M., Joyner, W. B., and Fumal, T. E. (1994). The attenuation of seismic shear waves in quaternary alluvium in Santa Clara Valley, California. *Bulletin of the Seismological Society of America*, 84(1):76–90.

Gobbi, S., Lopez-Caballero, F., and Forcellini, D. (2017). Numerical Analysis of Soil Liquefaction Induced Failure of Embankments. In *6th ECCOMAS Thematic Conference on Computational Methods in Structural Dynamics and Earthquake Engineering*.

Graves, R. and Pitarka, A. (2010). Broadband Ground-Motion Simulation Using a Hybrid Approach. *Bulletin of the Seismological Society of America*, 100(5A):2095–2123.

Graves, R. and Pitarka, A. (2015). Refinements to the Graves and Pitarka (2010) Broadband Ground-Motion Simulation Method. *Seismological Research Letters*, 86(1):75–80.

Griffiths, S., Cox, B. R., Rathje, E. M., and Teague, D. (2016a). Mapping Dispersion Misfit and Uncertainty in VS Profiles to Variability in Site Response Estimates. *Journal of Geotechnical and Geoenvironmental Engineering*, 142(11):1–16.

Griffiths, S., Cox, B. R., Rathje, E. M., and Teague, D. P. (2016b). Surface-Wave Dispersion Approach for Evaluating Statistical Models That Account for Shear-Wave Velocity Uncertainty. *Journal of Geotechnical and Geoenvironmental Engineering*, 142(11):1–16.

GSTools (2020). Personal Communication through GitHub; https://github.com/GeoStat-Framework/GSTools.

Hallal, M. M. and Cox, B. R. (2021a). An H/V geostatistical approach for building pseudo-3D Vs models to account for spatial variability in ground response analyses Part I: Model development. *Earthquake Spectra*.

Hallal, M. M. and Cox, B. R. (2021b). An H/V geostatistical approach for building pseudo-3D Vs models to account for spatial variability in ground response analyses Part II: Application to 1D analyses at two downhole array sites. *Earthquake Spectra*.

Hartzell, S., Alena, L., Frankel, A., Williams, R., Odum, J., Stephenson, W., and Silva, W. (2002). Simulation of Broadband Ground Motion Including Nonlinear Soil Effects for a Magnitude 6.5 Earthquake on the Seattle Fault, Seattle, Washington. *Bulletin of the Seismological Society of America*, 92(2):831–853.

Hashash, Y. M. A. and Park, D. (2001). Viscous Damping Formulation and High Frequency Motion Propagation in Nonlinear Site Response Analysis. *Soil Dynamics and Earthquake Engineering*, 22(7):611–624.

Heße, F., Prykhodko, V., Schlülter, S., and Attinger, S. (2014). Generating randomfields with a truncated power-law variogram:A comparison of several numerical methods. *Environmental Modelling & Software*, 55:32–48.

Holzer, T., Bennet, M., Noce, T., and Tinsley, J. (2005). Shear-Wave Velocity of Surficial Geologic Sediments in Northern California: Statistical Distributions and Depth Dependence. *Earthquake Spectra*, 21(1):161–177.

Huang, D., Wang, G., Du, C., and Jin, F. (2019). Seismic Amplification of Soil Ground with Spatially Varying Shear Wave Velocity Using 2D Spectral Element Method. *Journal of Earthquake Engineering*, pages 1–16.

Idris, I. M. (1993). Assessment of Site Response Analysis Procedures. Technical report, Report to National Institute of Standards and Technology, Gaithersburg, Maryland, Dept. of Civil & Environmental Eng., Univ. of California, Davis.

Idriss, I. M. and Boulanger, R. W. (2008). *Soil Liquefaction During Earthquakes*. Earthquake Engineering Research Insitute, Monograph-12, Oakland, California, USA.

Jeong, S. and Bradley, B. (2017a). Amplification of Strong Ground Motions at Heathcote Valley during the 2010-2011 Canterbury Earthquakes: Observation and 1D Site Response Analysis. *Soil Dynamics and Earthquake Engineering*, 100.

Jeong, S. and Bradley, B. (2017b). Amplification of Strong Ground Motions at Heathcote Valley during the 2010-2011 Canterbury Earthquakes: The Role of 2D Non-Linear Site Response. *Bulletin of the Seismological Society of America*, 107(5).

Jeong, S. and Bradley, B. (2017c). Amplification of Strong Ground Motions at Heathcote Valley during the 2010-2011 Canterbury Earthquakes: The Role of 2D Non-Linear Site Response. *Bulletin of the Seismological Society of America*, 107(5).

Kaklamanos, J., Baise, L. G., Thompson, E. M., and Dorfmann, L. (2015). Comparison of 1D linear, equivalent-linear, and nonlinear site response models at six KiK-net validation sites. *Soil Dynamics and Earthquake Engineering*, 69:207–219.

Kaklamanos, J., Bradley, B. A., Thomson, E., and Baise, L. (2013). Critical Parameters Affecting Bias and Variability in Site-Response Analyses Using KiK-net Downhole Array Data. *Bulletin of the Seismological Society of America*, 103(3):1733–1749.

Karimi, Z. and Dashti, S. (2016). Numerical and Centrifuge Modeling of Seismic Soil–Foundation–Structure Interaction on Liquefiable Ground. *Journal of Geotechnical and Geoenvironmental Engineering*, 142(1):04015061.

Kawase, H. and Matsuo, H. (2004). 3 th World Conference on Earthquake Engineering AMPLIFICATION CHARACTERISTICS OF K-NET, KIK-NET, AND JMA SHINDOKEI NETWORK SITES BASED ON THE SPECTRAL INVERSION TECHNIQUE.

Kokusho, T. (2017). *Innovative Earthquake Soil Dynamics*. Taylor & Francis Group, London, UK, 1 edition.

Kramer, S. (1996). *Geotechnical Earthquake Engineering*. Prentice Hall, Upper Saddle River, New Jersey, USA.

Kwok, A., Stewart, J. P., Hashash, Y. M. A., and Matasovic, N. (2007). Use of Exact Solutions of Wave Propagation Problems to Guide Implementation of Nonlinear Seismic Ground Re-

sponse Analysis Procedures. *Journal of Geotechnical and Geoenvironmental Engineering*, 133(11):1385–1398.

Lee, R., Bradley, B., Ghisetti, F., and Thomson, E. (2017a). Development of a 3D Velocity Model of the Canterbury, New Zealand, Region for Broadband Ground-Motion Simulation. *Bulletin of the Seismological Society of America*, 107(5):2131–2150.

Lee, R. L., Bradley, B. A., Graves, R. W., Rodriguez-Marek, A., and Stafford, P. J. (2018). Investigation of Systematic Effects Through Ground Motion Simulation of Small-to-Moderate Magnitude Earthquakes. *Bulletin of the Seismological Society of America*, In Press.

Lee, R. L., Bradley, B. A., and McGann, C. R. (2017b). 3d models of quaternary-aged sedimentary successions within the canterbury, new zealand region. *New Zealand Journal of Geology and Geophysics*, 60(4):320–340.

Lee, R. L., Bradley, B. A., Stafford, P. J., Graves, R. W., and Rodriguez-Marek, A. (2020). Hybrid broadband ground motion simulation validation of small magnitude earthquakes in Canterbury, New Zealand. *Earthquake Spectra*, 36(2):673–699.

Lee, R. L., Bradley, B. A., Stafford, P. J., Graves, R. W., and Rodriguez-Marek, A. (2021). Hybrid Broadband Ground Motion Simulation Validation of Small Magnitude Active Shallow Crustal Earthquakes in New Zealand. *Earthquake Spectra (submitted)*.

Li, G., Motamed, R., and Dickenson, S. (2018). Evaluation of one-dimensional multi-directional site response analyses using geotechnical downhole array data in California and Japan. *Earthquake Spectra*, 34(1):349–376.

Lin, P., Chiou, B., Abrahamson, N., Walling, M., Lee, C., and Cheng, C. (2011). Repeatable Source, Site, and Path Effects on the Standard Deviation for Empirical Ground-Motion Prediction Models. *Bulletin of the Seismological Society of America*, 101(5):2281–2295.

Lloret-Cabot, M., Fenton, G., and Hicks, M. (2014). On the estimation of scale fluctuations in geostatistics. *Georisk*, 8(2):129–140.

Lopez-Caballero, F. and Modaressi-Farahmand-Razavi, A. (2010). Assessment of Variability and Uncertainty Effects on the Seismic Response of a Liquefiable Soil Profile. *Soil Dynamics and Earthquake Engineering*, 30:600–613.

Mazzoni, S., McKenna, F., Scott, M., and Fenves, G. (2007). *OpenSees Command Language Manual*. http://opensees.berkeley.edu/OpenSees/manuals/usermanual OpenSeesCommandLanguageManual.pdf.

McGann, C. and Arduino, P. (2011). Dynamic 2d effective stress analysis of slope. `https://opensees.berkeley.edu/wiki/index.php/Site_Response_Analysis_of_a_Layered_Soil_Column_(Total_Stress_Analysis)`.

McGann, C. and Arduino, P. (2015). Dynamic 2d effective stress analysis of slope. `http://opensees.berkeley.edu/wiki/index.php/Dynamic_2D_Effective_Stress_Analysis_of_Slope`.

McGann, C., Arduino, P., and Mackenzie-Helmwein, P. (2012). Stabilized Single-Point 4-Node Quadrilateral Element for Dynamic Analysis of Fluid Saturated Porous Media. *Acta Geotechnica*, 7(4):297–311.

McGann, C. R., Bradley, B., and Cubrinovski, M. (2017). Development of regional V_{s30} model and typical V_S profiles for Christchurch, New Zealand from CPT data and region-specific CPT-V_s correlation. *Soil Dynamics and Earthquake Engineering*, 95:48–60.

McKenna, F. (2011). OpenSees: A framework for earthquake engineering simulation. *Computing in Science and Engineering*, 13(4):58–66.

Müller, S. and Schüler (2020). GeoStat-Framework/GSTools. Zenodo. https://doi.org/10.5281/zenodo.1313628.

Nour, A., Slimani, A., Laouani, N., and Afra, H. (2003). Finite Element Model for the Probabilistic Seismic Response of Heterogeneous Soil Profile. *Soil Dynamics and Earthquake Engineering*, 23:331–348.

Oth, A. and Kaiser, A. (2014). Stress Release and Source Scaling of the 2010-2011 Canterbury, New Zealand Earthquake Sequence from Spectral Inversion of Ground Motion Data. *Pure and Applied Geophysics*, 171:2767–2782.

Passeri, F., Foti, S., Cox, B. R., Eeri, . M., and Rodriguez-Marek, A. (2019). Influence of Epistemic Uncertainty in Shear Wave Velocity on Seismic Ground Response Analyses. *Earthquake Spectra*.

Pilz, M. and Cotton, F. (2019). Does the One-Dimensional Assumption Hold for Site Response Analysis? A Study of Seismic Site Responses and Implication for Ground Motion Assessment Using KiK-Net Strong-Motion Data. *Earthquake Spectra*, 35(2):883–905.

Popescu, R. (1995). *Stochastic Variability of Soil Properties, Data Analysis, Digital Simulation, Effects on System Behaviour*. Phd thesis, California Polytechnic State University, San Luis Obispo.

Popescu, R., Prevost, J., and Deodatis, G. (1997). Effects of Spatial Variability on Soil Liquefaction: Some Design Recommendations. *Geotechnique*, 47(5):1019–1036.

Quigley, M. C., Hughes, M. W., Bradley, B. A., van Ballegooy, S., Reid, C., Morgenroth, J., Horton, T., Duffy, B., and Pettinga, J. R. (2016). The 2010-2011 Canterbury Earthquake Sequence: Environmental Effects, Seismic Triggering Thresholds, and Geologic Legacy. *Tectonophysics*, 672/673:228–274.

Ramirez, J., Barrero, A., Chen, L., Dashti., S., Ghofrani, A., Taiebat, M., and Arduino, P. (2018). Site Response in a Layered Liquefiable Deposit: Evaluation of Different Numerical Tools and Methodologies with Centrifuge Experimental Results. *Journal of Geotechnical and Geoenvironmental Engineering*, 144(10):04018073.

Rathje, E. M., Kottke, A. R., and Trent, W. L. (2010). Influence of Input Motion and Site Property Variabilities on Seismic Site Response Analysis. *Journal of Geotechnical and Geoenvironmental Engineering*, 136(4):607–619.

Razafindrakoto, H. and Bradley, B. (2016). YouTube Video: 14 February 2016 Christchurch NZ Earthquake (Mw5.8) Simulation. $https://www.youtube.com/watch?v=JtT_tT6NoEk$.

Razafindrakoto, H., Bradley, B., and Graves, R. (2016). Broadband Ground Motion Simulations of the 2010-2011 Canterbury Earthquake Sequence. In *2016 New Zealand Society of Earthquake Engineering Conference*. April 1-3, Christchurch, New Zealand.

Razafindrakoto, H. N. T., Bradley, B. A., and Graves, R. W. (2018). Broadband Ground-Motion Simulations of the 2011 M_W6.2 Christchurch, New Zealand, Earthquake . *Bulletin of the Seismological Society of America*, 108(4):2130–2147.

Régnier, J., Bonilla, L. F., Bard, P. Y., Bertrand, E., Hollender, F., Kawase, H., . . . , and Watanabe, K. (2016). Internal Benchmark on Numerical Simulations for 1D Nonlinear Site Response (PRENOLIN): Verification Phase Based on Canonical Cases. *Bulletin of the Seismological Society of America*, 106(5):2112–2135.

Restrepo, D., Taborda, R., and Bielak, J. (2012). Three-Dimensional Nonlinear Earthquake Ground Motion Simulations in the Salt Lake Basin Using the Wasatch Front Community Velocity Model. Technical report, USGS Award G10AP00077.

Ricker, N. (1943). Further Developments in the Wavelet Theory of Seismogram Structure. *Bulletin of Seismological Society of America*, 33(3):197–228.

Robertson, P. K. and Wride, C. E. (1998). Evaluation of Cyclic Liquefaction Potential Using the Cone Penetration Test. *Canadian Geotechnical Journal*, 35:442–459.

Rodríguez-Castellanos, A., Sánchez-Sesma, F. J., Luzón, F., and Martin, R. (2006). Multiple Scattering of Elastic Waves by Subsurface Fractures and Cavities. *Bulletin of the Seismological Society of America*, 96(4A):1359–1374.

Rodriguez-Marek, A., Bommer, J. J., Youngs, R. R., Crespo, M. J., Stafford, P. J., and Bahrampouri, M. (2021). Capturing epistemic uncertainty in site response. *Earthquake Spectra*, 37(2):921–936.

Roten, D., Cui, Y., Olsen, L., Day, S. M., Withers, K., Savran, W. H., Wang, P., and Mu, D. (2016). High-Frequency Nonlinear Earthquake Simulations on Petascale Heterogeneous Supercomputers. In *2016 Conference for High Performance Computing, Networking, Storage and Analysis*. November 13-18, Salt Lake City, Utah, USA.

Roten, D., Olsen, K., and Pechman, J. (2012). 3D Simulations of M 7 Earthquakes on the Wasatch Fault, Utah, Part II: Broadband (0-10 Hz) Ground Motions and Nonlinear Soil Behavior. *Bulletin of the Seismological Society of America*, 102(5):2008–2030.

Sato, H., C, F. M., and Maeda, T. (2012). *Seismic Wave Propagation and Scattering in the Heterogeneous Earth*. Springer, Berlin, Heidelberg, New York, 2 edition.

Schnabel, P. B., Lysmer, J., and Seed, H. B. (1972). SHAKE A Computer Program for Earthquake Response Analysis of Horizontally Layered Sites. Technical report, Report No. EERC 72 - 12. College of Engineering, University of California, Berkeley.

Stewart, J. P. and Afshari, K. (2021). Epistemic uncertainty in site response as derived from one-dimensional ground response analyses. *Journal of Geotechnical and Geoenvironmental Engineering*, 147(1):04020146.

Stewart, J. P., Afshari, K., and Goulet, C. A. (2017). Non-ergodic site response in seismic hazard analysis. *Earthquake Spectra*, 33:1385–1414.

Stewart Annie On-Lei Kwok, J. P., Hashash, Y. M., Pyke Lafayette, R., Zhiliang Wang, C., and Yang, Z. (2008). Benchmarking of Nonlinear Geotechnical Ground Response Analysis Procedures.

Stolte, A. C. and Cox, B. R. (2019). Towards consideration of epistemic uncertainty in shear-wave velocity measurements obtained via seismic cone penetration testing (SCPT). 57:48–60.

Taborda, R. and Bielak, J. (2013). Ground-Motion Simulations and Validation of the 2008 Chino Hills, California, Earthquake. *Bulletin of the Seismological Society of America*, 103(1).

Taborda, R., Bielak, J., and Restrepo, D. (2012). Earthquake Ground-Motion Simulation including Nonlinear Soil Effects under Idealized Conditions with Application to Two Case Studies. *Seismological Research Letters*, 83(6).

Tao, Y. and Rathje, E. (2020a). Taxonomy for evaluating the site-specific applicability of one-dimensional ground response analysis. *Soil Dynamics and Earthquake Engineering*, 128:105865.

Tao, Y. and Rathje, E. (2020b). The importance of distinguishing pseudoresonances and outcrop resonances in Downhole array data. *Bulletin of the Seismological Society of America*, 110(1):288–294.

Tao, Y. and Rathje, E. M. (2019). Insights into Modeling Small-Strain Site Response Derived from Downhole Array Data. *Journal of Geotechnical and Geoenvironmental Engineering*, 145(7):1–15.

Teague, D. P. and Cox, B. R. (2016). Site Response Implications Associated with using Non-Unique V_S Profiles from Surface Wave Inversion in Comparison with Other Commonly used Methods of Accounting for V_S Uncertainty. *Soil Dynamics and Earthquake Engineering*, 91:87–103.

Teague, D. P., Cox, B. R., and Rathje, E. M. (2018). Measured vs. predicted site response at the Garner Valley Downhole Array considering shear wave velocity uncertainty from borehole and surface wave methods. *Soil Dynamics and Earthquake Engineering*, 113:339–355.

Thompson, E. M., Baise, L. G., Kayen, R. E., and B., G. B. (2009). Impediments to Predicting Site Response: Seimic Property Estimation and Modeling Simplifications. *Bulletin of the Seismological Society of America*, 99(5):2927–2949.

Thompson, E. M., Baise, L. G., Tanaka, Y., and Kayen, R. E. (2012). A Taxonomy of Site Response Complexity. *Soil Dynamics and Earthquake Engineering*, 41:32–43.

Thomson, E. M., Bradley, B. A., and Lee, R. L. (2020). Methodology and computational implementation of a New Zealand Velocity Model (NZVM2.0) for broadband ground motion simulation. *New Zealand Journal of Geology and Geophysics*, 63(1):110–127.

Toksöz, M., Dainty, A., Reiter, E., and Wu, R.-S. (1988). A Model for Attenuation and Scattering in the Earth's Crust. *Pure and Applied Geophysics*, 128(1/2):81–100.

Toro, G. (1995). Probabilistic Models of Site Velocity Profiles for Generic and Site-Specific Ground-Motion Amplification Studies. Technical report, Technical Report No. 779574. Upton N.Y.: Brookhaven National Laboratory.

Ulmer, K. J., Rodriguez-Marek, A., and Green, R. A. (2021). Accounting for Epistemic Uncertainty in Site Effects in Probabilistic Seismic Hazard Analysis. *Bulletin of the Seismological Society of America*, 111(4):2005–2020.

van Ballegooy, S., Malan, P., Lacrosse, V., Jacka, M. E., Cubrinovski, M., Bray, J. D., O'Rourke, T. D., Crawford, S. A., and Cowan, H. (2014). Assessment of Liquefaction-Induced Land Damage for Residential Christchurch. *Earthquake Spectra*, 30(1):31–55.

Van Houtte, C. (2017). Performance of Response Spectral Models against New Zealand Data. *Bulletin of the New Zealand Society for Earthquake Engineering*, 250(1):21–38.

Vucetic, M. and Dobry, R. (1991). Effect of soil plasticity on cyclic response. *Journal of Geotechnical Engineering*, 117(1):89–107.

Vytiniotis, A., Panagiotidou, A., and Whittle, A. (2019). Analysis of seismic damage mitigation for a pile-supported wharf structure. *Soil Dynamics and Earthquake Engineering*, 119:21–35.

Wang, Y. (2015). Frequencies of the Ricker Wavelet. *Geophysics*, 80(2):A31–A37.

Wills, C. and Clahan, K. (2006). Developing a Map of Geologically Defined Site-Condition Categories for California. *Bulletin of the Seismological Society of America*, 96(4A):1483–1501.

Wotherspoon, L., Orense, R., Bradley, B., Cox, B., Wood, C., and Green, R. (2014). Geotechnical Characterisation of Christchurch Strong Motion Stations. Technical report, Earthquake Commission Report, Project No. 12/629, Version 2.0 - October 2014.

Wu, H., Masaki, K., Irikura, K., and José Sánchez-Sesma, F. (2017). Application of a simplified calculation for full-wave microtremor H/V spectral ratio based on the diffuse field approximation to identify underground velocity structures. *Earth, Planets and Space*, 69:162.

Wu, R.-S. and Aki, K. (1988). Introduction: Seismic Scattering in Three-dimensionally Heterogeneous Earth. *Pure and Applied Geophysics*, 128(1/2):1–6.

Yang, Z., Elgamal, A., and Parra, E. (2003). Computational Model for Cyclic Mobility and Associated Shear Deformation. *Journal of Geotechnical and Geoenvironmental Engineering, ASCE*, 129(12):1119–1127.

Yee, E., Stewart, J. P., and Tokimatsu, K. (2011). Nonlinear Site Response and Seismic Compression at Vertical Array Strongly Shaken by 2007 Niigata-ken Chuetsu-oki Earthquake - PEER Report No. 2011/107. Technical report, Pacific Earthquake Engineering Research Center.

Yee, E., Stewart, J. P., and Tokimatsu, K. (2013). Elastic and Large-Strain Nonlinear Seismic Site Response from Analysis of Vertical Array Recordings. *Journal of Geotechnical and Geoenvironmental Engineering*, 139(10):1789–1801.

Yoshimura, C., Bielak, J., Hisada, Y., and Fernandez, A. (2003). Domain Reduction Method for Three-Dimensional Earthquake Modeling in Localized Regions, Part II: Verification and Applications. *Bulletin of the Seismological Society of America*, 93(2):825–840.

Zalachoris, G. and Rathje, E. M. (2015). Evaluation of One-Dimensional Site Response Techniques Using Borehole Arrays. *Journal of Geotechnical and Geoenvironmental Engineering*, 141(12).

Zhang, Y., Conte, J., Yang, Z., Elgamal, A., Bielak, J., and Acero, G. (2008). Two-Dimensional Nonlinear Earthquake Response Analysis of a Bridge-Foundation-Ground System. *Earthquake Spectra*, 24(2):343–386.

Zhang, Y., Yang, Z., Bielak, J., Conte, J., and Elgamal, A. (2003). Treatment of Seismic Input and Boundary Conditions in Nonlinear Seismic Analysis of a Bridge Ground System. In *16th ASCE Engineering Mechanics Conference*.